UNIVERSITÀ DEGLI STUDI
DI MODENA E REGGIO EMILIA

Dottorato di ricerca in Industrial and Environmental Engineering

Ciclo XXXVIII

High Velocity Oxygen Fuel (HVOF) Spraying of High-Entropy Alloy (HEA)-Based Coatings

Candidato: Luca Bortolotti

Relatore (Tutor): Prof. Giovanni Bolelli

Correlatore (Co-Tutor): Prof. Luca Lusvarghi

Coordinatore del Corso di Dottorato: Prof. Alberto Muscio

Contents

“You cannot describe passion,

you can only live it”

Summary

This thesis addresses one of the most pressing challenges in contemporary surface engineering: the design, development, and characterization of high-performance thermal spray coatings that are entirely free of cobalt and tungsten, yet capable of providing wear and corrosion protection comparable to or exceeding that of conventional Co- and W-based systems, while simultaneously addressing environmental, health, and supply-chain concerns associated with critical raw materials (CRMs). Across multiple industrial sectors including energy, aerospace, automotive, marine engineering, mining, and heavy machinery; metallic components are routinely subjected to extreme mechanical and chemical conditions, where abrasive, adhesive, and erosive wear processes interact with localized corrosion phenomena such as pitting, crevice, and intergranular attack. These processes result in premature component failure, unexpected maintenance shutdowns, and significant economic losses, motivating the need for advanced surface protection strategies. Thermal spray technologies, and particularly high-velocity methods such as High Velocity Oxy-Fuel (HVOF) and High Velocity Air-Fuel (HVAF), have emerged as industrially mature and versatile solutions capable of producing dense, adherent, low-porosity coatings over large and geometrically complex surfaces. In current practice, WC–CoCr and Cr3C2–NiCr coatings, as well as Stellite-type Co-based alloys, serve as benchmarks for severe abrasive and sliding wear and are increasingly favored as environmentally safer alternatives to hard chromium plating due to REACH regulations. However, the reliance on cobalt and tungsten is constrained by their classification as critical raw materials by the European Commission, reflecting both economic importance and supply vulnerability, while cobalt compounds are recognized as carcinogenic and mutagenic and hexavalent chromium is subject to strict regulatory control. Consequently, there is an urgent demand for new coating systems that minimize or eliminate CRMs without sacrificing functional performance.

High-entropy alloys (HEAs), also known as multi-principal element alloys, represent a transformative approach in alloy design and are particularly promising for CRM-free coatings. Typically composed of five or more elements in near-equiatomic ratios, HEAs often crystallize into simple FCC or BCC solid solutions, with properties arising from high configurational entropy, lattice distortion, sluggish diffusion, and the so-called cocktail effect, though the contribution of these mechanisms is highly composition-dependent. HEAs offer high hardness and strength via solid-solution and lattice distortion strengthening, enhanced corrosion and oxidation resistance when elements such as Cr and Al are incorporated, and

excellent thermal stability over broad temperature ranges, making them ideal candidates for protective coatings. In parallel, the literature has explored various strategies for reducing or eliminating CRMs in conventional cermet systems, including substituting cobalt binders with Fe- or Ni-based matrices, replacing WC with alternative carbides such as TiC, NbC, or complex (Ti,Mo)(C,N) solid solutions, and developing advanced cermets that balance ceramic reinforcement with alternative metallic binders. Previous studies have demonstrated that TiC- or NbC-based HVOF coatings with NiCr or FeCrAl matrices can approach Cr_3C_2–NiCr performance under certain conditions, but they often suffer from intrinsic brittleness and limited toughness, particularly under sliding or impact wear, highlighting the need for metallic matrices capable of delivering high hardness, ductility, and fracture toughness without CRMs.

Within this context, the overarching objective of this PhD research was to design, deposit, and characterize high-performance HVOF coatings that are fully free of cobalt and tungsten, while matching or surpassing the mechanical, tribological, and corrosion properties of conventional Co- and W-based coatings. Two complementary material families were developed:

- Metallic HEA coatings, including the equiatomic CrMnFeCoNi Cantor alloy as a reference, and a cobalt-free Al_x(CrMnFeNi) series with x = 0, 10, and 14 at.%, where increasing Al content enables phase evolution from FCC to dual FCC/BCC to predominantly BCC/B2, thereby increasing hardness at the expense of ductility;
- HEA–TiC cermet coatings, in which HEA matrices are reinforced with 60 vol.% TiC to produce hardmetal-like microstructures, with four matrices explored, including Cantor+60TiC, Al_0(CrMnFeNi)+60TiC, Al_{14}(CrMnFeNi)+60TiC, and AlCuCrFeNi+60TiC.

Powders were produced by high-energy ball milling, enabling rapid compositional screening and cost-effective development, sieved to −45/+10 µm, and deposited via HVOF onto grit-blasted AISI 304 stainless steel substrates under systematically optimized parameters to ensure uniform thickness, minimize oxidation, and avoid powder overheating.

Extensive characterization included particle size distribution analysis, XRD with Rietveld refinement, SEM/EDX of polished cross-sections, Vickers microhardness and high-speed nanoindentation mapping with Gaussian mixture model analysis, tribological evaluation via

ball-on-disc sliding (ASTM G99) and steel-wheel abrasion, and electrochemical corrosion testing in 3.5 wt.% NaCl. Metallic HEA coatings exhibited dense, low-porosity microstructures with phase evolution consistent with Al content: Cantor and Al_0 coatings were predominantly FCC, Al_{10} formed dual FCC/BCC structures, and Al_{14} transitioned to BCC/B2. Mechanical evaluation revealed that hardness increased with Al content, with FCC matrices providing the best balance between hardness and toughness, while BCC-rich phases offered higher hardness but increased brittleness. Corrosion testing indicated that oxide content was the main determinant of current density, with all metallic HEAs achieving corrosion resistance comparable to stainless steel or Ni-based overlays.

HEA–TiC cermet coatings showed uniform TiC dispersion, with Cantor+60TiC and Al_0+60TiC exhibiting TiC_{1-x} formation and Al14+60TiC displaying the highest oxidation, whereas AlCuCrFeNi+60TiC demonstrated minimal oxidation and excellent carbide stability. Nanoindentation revealed four distinct mechanical populations: soft FCC metallic phases, hard BCC-rich phases, intermediate interfacial zones, and very hard TiC particles. Sliding wear performance was lower than that of WC–CoCr and the best (Ti,Mo)(C,N)–Ni systems due to interfacial fatigue and crack initiation, whereas high-stress abrasion showed that Cantor+60TiC and AlCuCrFeNi+60TiC matched or approached Cr_3C_2–NiCr, with AlCuCrFeNi+60TiC performing exceptionally well due to its ductile FCC matrix and low oxide content. Corrosion performance was generally suitable for industrial applications, with oxide content again dominating behaviour.

Overall, the research demonstrates that fully CRM-free metallic HEAs and HEA–TiC cermets can provide corrosion resistance, hardness, and abrasive wear performance comparable to conventional Co- and W-based coatings, while dual-phase FCC/BCC matrices offer the optimal balance between toughness and hardness. The study establishes practical design guidelines for CRM-free coatings, including controlled phase engineering via Al content and valence electron concentration (VEC), optimization of TiC volume fraction (~60 vol.%) for hardmetal-like performance, minimization of oxidation through tailored HVOF/HVAF parameters, and the application of advanced micromechanical characterization to guide microstructural refinement. By integrating sustainable materials design, industrially mature deposition processes, and comprehensive tribo-corrosion characterization, this work provides a viable pathway for the development of high-performance, environmentally responsible, and supply-secure thermal spray coatings suitable for demanding industrial applications.

Summary (Italian version)

Questa tesi affronta una delle sfide attualmente più rilevanti nell'ingegneria delle superfici: la progettazione, lo sviluppo e la caratterizzazione di rivestimenti thermal spray ad alte prestazioni, completamente privi di cobalto e tungsteno, ma capaci di garantire una protezione dall'usura e dalla corrosione pari o superiore a quella dei tradizionali sistemi basati su Co e W. L'obiettivo è simultaneamente quello di mitigare le problematiche ambientali, sanitarie e di supply-chain associate alle Critical Raw Materials (CRMs).

In numerosi settori industriali (tra cui energia, aerospazio, automotive, ingegneria navale, estrattiva e macchinari pesanti) i componenti metallici operano in condizioni estremamente severe. Processi di usura abrasiva, adesiva e erosiva interagiscono con fenomeni di corrosione come pitting, crevice e attacco intergranulare, provocando guasti prematuri, fermi manutentivi imprevisti e significative perdite economiche. Questi scenari rendono indispensabile l'impiego di strategie avanzate ingegneria delle superfici.

Le tecnologie di thermal spray, in particolare i processi ad alta velocità come High Velocity Oxy-Fuel (HVOF) e High Velocity Air-Fuel (HVAF), rappresentano oggi soluzioni mature e versatili, in grado di produrre rivestimenti densi, aderenti e a bassa porosità su superfici estese o geometricamente complesse. Attualmente, i rivestimenti WC–CoCr, Cr_3C_2–NiCr e le leghe Co-based tipo Stellite costituiscono i benchmark per condizioni di severa usura e sono sempre più adottati come alternative più sicure alla cromatura dura, anche in risposta alle normative REACH. Tuttavia, la dipendenza da cobalto e tungsteno risulta critica in quanto entrambi sono classificati come CRMs dalla Commissione Europea, mentre i composti del Co sono cancerogeni e mutageni, e il Cr^{6+} è soggetto a stringenti regolamentazioni. Di conseguenza, vi è un urgente bisogno di rivestimenti che riducano o eliminino l'impiego di CRMs senza compromessi prestazionali.

In questo contesto, le High-Entropy Alloys (HEAs) rappresentano un paradigma innovativo nella progettazione delle leghe metalliche e un'opzione particolarmente promettente per rivestimenti CRM-free. Costituite tipicamente da cinque o più elementi in rapporti quasi equiatomici, le HEA formano spesso soluzioni solide FCC o BCC, con proprietà influenzate da high configurational entropy, lattice distortion, sluggish diffusion e dal cosiddetto cocktail effect, sebbene l'entità di ciascun meccanismo dipenda fortemente dalla composizione. Le HEA offrono durezza e resistenza elevate per effetto del solid-solution strengthening e del lattice distortion, ottima resistenza alla corrosione e all'ossidazione quando presenti

elementi come Cr e Al, e stabilità termica su ampi intervalli di temperatura. Parallelamente, la comunità scientifica ha investigato strategie per ridurre o eliminare i CRMs nei cermet convenzionali, tra cui l'impiego di matrici Fe- o Ni-based al posto del Co, la sostituzione del WC con carburi alternativi (TiC, NbC, o sistemi complessi tipo (Ti,Mo)(C,N)), e lo sviluppo di cermet avanzati in cui il rinforzo ceramico sia opportunamente bilanciato con leganti metallici alternativi. Sebbene alcuni rivestimenti HVOF a base di TiC o NbC con matrici NiCr o FeCrAl abbiano dimostrato prestazioni comparabili ai Cr_3C_2–NiCr in determinate condizioni, la loro tenacità limitata sotto sliding o impatti rimane una criticità, sottolineando la necessità di matrici metalliche dure, duttili e tenaci, ma prive di CRMs.

Alla luce di queste considerazioni, l'obiettivo principale di questa ricerca di dottorato è stato progettare, depositare e caratterizzare rivestimenti HVOF totalmente privi di Co e W, mantenendo o superando le prestazioni meccaniche, tribologiche e anti-corrosive dei rivestimenti convenzionali. Sono state sviluppate due famiglie complementari:

- Rivestimenti metallici HEA, comprendenti la lega equiatomica CrMnFeCoNi (Cantor alloy) come riferimento, e una serie cobalt-free Al_x(CrMnFeNi) con x = 0, 10 e 14 at.%, in cui l'aumento del contenuto di Al induce una transizione di fase da FCC a FCC/BCC fino a BCC/B2, incrementando la durezza a scapito della duttilità;
- Cermet HEA–TiC, costituiti da matrici HEA rinforzate con 60 vol.% TiC, comprendenti quattro sistemi: Cantor+60TiC, Al_0(CrMnFeNi)+60TiC, Al_{14}(CrMnFeNi)+60TiC e AlCuCrFeNi+60TiC.

Le polveri sono state prodotte tramite high-energy ball milling, setacciate a −45/+10 μm e successivamente depositate via HVOF su substrati in acciaio inossidabile AISI 304 sabbiati, con parametri ottimizzati per ottenere spessori uniformi, ridurre l'ossidazione e prevenire il surriscaldamento delle particelle.

La caratterizzazione ha incluso analisi della particle size distribution, XRD con Rietveld refinement, osservazioni SEM/EDX, microdurezza Vickers, high-speed nanoindentation mapping con analisi tramite Gaussian Mixture Model, test tribologici ball-on-disc (ASTM G99), test di abrasione con ruota d'acciaio e prove di corrosione elettrochimica in soluzione di NaCl al 3,5%. I rivestimenti HEA metallici hanno mostrato microstrutture dense e a bassa porosità, con una chiara evoluzione di fase correlata al contenuto di Al: Cantor e Al_0 prevalentemente FCC, Al_{10} presenta una struttura duale FCC/BCC, mentre Al_{14} mostra un assetto BCC/B2. La durezza aumentava con il contenuto di Al, con le matrici FCC che

offrivano il miglior compromesso hardness–toughness, mentre le matrici ricche in BCC garantivano maggiore durezza ma anche maggiore fragilità. La resistenza alla corrosione è risultata fortemente influenzata dal contenuto di ossidi, con tutte le HEA che hanno mostrato prestazioni comparabili a quelle dell'acciaio inossidabile o dei rivestimenti Ni-based.

I cermet HEA–TiC hanno mostrato una dispersione omogenea del TiC. Cantor+60TiC e Al_0+60TiC hanno evidenziato formazione di TiC_{1-x}, mentre Al_{14}+60TiC è risultato il più ossidato; al contrario, AlCuCrFeNi+60TiC ha mostrato minima ossidazione ed eccellente stabilità dei carburi. La nanoindentazione ha identificato quattro fasi con dverse proprietà meccaniche: fasi FCC morbide, fasi ricche in BCC più dure, zone intermedie e particelle di TiC molto dure. Le prestazioni di resistenza all'usura strisciante sono risultate inferiori a quelle dei sistemi WC–CoCr e dei migliori (Ti,Mo)(C,N)–Ni, principalmente per fenomeni di fatica e iniziazione di cricche. Tuttavia, sotto condizioni di usura abrasiva, i sistemi Cantor+60TiC e AlCuCrFeNi+60TiC hanno eguagliato o avvicinato le prestazioni dei Cr_3C_2–NiCr, con AlCuCrFeNi+60TiC che si è distinto grazie alla matrice duttile FCC e al basso contenuto di ossidi. Anche la resistenza a corrosione è risultata adeguata ad applicazioni industriali.

Nel complesso, questa ricerca dimostra che HEA metalliche e cermet HEA–TiC completamente CRM-free possono raggiungere resistenza alla corrosione, durezza e prestazioni in usura abrasiva comparabili ai rivestimenti convenzionali a base di Co e W. Le matrici dual-phase FCC/BCC rappresentano il miglior compromesso tra tenacità e durezza. Il lavoro fornisce inoltre linee guida pratiche per la progettazione di rivestimenti CRM-free, includendo l'ingegnerizzazione controllata delle fasi tramite contenuto di Al e Valence Electron Concentration (VEC), l'ottimizzazione del TiC intorno al 60 vol.% per prestazioni simili agli hardmetal, la minimizzazione dell'ossidazione tramite parametri HVOF/HVAF dedicati e l'impiego di tecniche avanzate di micromeccanica per guidare il miglioramento microstrutturale.

Integrando una progettazione sostenibile dei materiali, processi di deposizione industrialmente maturi e una caratterizzazione tribo-corrosiva completa, questo lavoro offre un percorso concreto verso lo sviluppo di rivestimenti thermal spray ad alte prestazioni, più sostenibili, più sicuri e meno dipendenti da risorse critiche, idonei per applicazioni industriali molto impegnative.

Aim of the PhD reserch

Wear and corrosion remain critical engineering challenges across industrial sectors, significantly undermining the longevity, safety, and efficiency of mechanical components. These degradation mechanisms are responsible for billions of euros in losses annually due to equipment failure, unscheduled maintenance, and decreased operational reliability. Common wear modes include abrasive wear (caused by hard particles or protuberances), adhesive wear (due to surface interaction and material transfer), and erosive wear (from high-velocity particle impact). Corrosion phenomena such as pitting, crevice corrosion, intergranular attack, and galvanic corrosion further compromise structural integrity, especially in chemically aggressive or high-humidity environments[1].

Europe's manufacturing sector covering critical domains such as aerospace, energy, automotive, marine, and heavy engineering is under intensifying pressure to improve both productivity and environmental performance. With sustainability regulations tightening and customer expectations for reliability growing, the industry must adopt more effective strategies to extend component life and minimize lifecycle costs[2].

To address these challenges, advanced surface engineering techniques have come to the forefront, particularly thermal spray coating technologies. These methods offer a powerful, flexible means to deposit protective coatings that enhance wear resistance, corrosion resistance, and thermal stability. Unlike bulk material substitution, which is often cost-prohibitive or impractical, coatings can be tailored to impart specific surface properties while preserving the underlying substrate[3].

Among thermal spray processes, the High-Velocity Oxy-Fuel (HVOF) technique has gained prominence due to its ability to produce dense, adherent coatings with low oxide content and excellent mechanical performance. This capability is particularly vital when applying hardmetal coatings such as WC-Co and Cr_3C_2-NiCr, which provide excellent sliding and abrasive wear resistance[4].

However, the use of materials such as cobalt (Co) and hexavalent chromium (Cr^{6+})—common in many traditional coating systems—raises health and environmental concerns. Both substances are subject to strict regulation under the European Union's REACH framework due to their carcinogenic and toxic properties[5,6]. The industry is thus increasingly driven to find safer and more sustainable alternatives.

In parallel, the European Commission has identified cobalt, tungsten, and other elements used in hardmetal coatings as Critical Raw Materials (CRMs) due to their economic

importance and high supply risk[7]. This has led to a concerted push toward minimizing the reliance on these materials while maintaining or enhancing functional performance.

In this context, the development of High Entropy Alloys (HEAs)—a new class of materials composed of multiple principal elements in near-equiatomic ratios—has emerged as a promising strategy. HEAs exhibit exceptional mechanical, chemical, and thermal properties, making them attractive candidates for next-generation protective coatings. When applied using HVOF, these high-entropy hardmetal coatings show promise in surpassing traditional systems in terms of both durability and resistance to harsh environments[8,9].

The study focused on the synthesis and evaluation of coatings produced from custom-designed powders developed through High Energy Ball Milling (HEBM). These experimental powders were tailored in collaboration with MBN Nanomaterialia (Carbonera, Italy), a company actively engaged in R&D for advanced powder materials. The powders underwent comprehensive characterization using techniques such as laser diffraction for particle size analysis, scanning electron microscopy (SEM) combined with energy-dispersive X-ray spectroscopy (EDS) for morphological and compositional assessment, X-ray diffraction (XRD) for phase identification, and simultaneous thermogravimetric and differential thermal analysis (TG-DTA) to assess thermal stability.

Coatings were applied onto AISI 304 stainless steel substrates using a High Velocity Oxy-Fuel (HVOF) system (Diamond Jet 2600 Hybrid). Three distinct sets of spraying parameters (run 1, run 2, and run 3) were investigated by varying spray distance, powder feed rate, and the oxygen-to-hydrogen fuel ratio.

Subsequent analysis was performed on the coatings to determine their microstructure, phase composition, mechanical and tribological properties, and corrosion resistance. Tribological behavior was assessed through pin-on-disk and steel-wheel abrasion tests, while electrochemical polarization techniques were used to evaluate corrosion performance. Conventional coatings composed of WC-CoCr and Cr_3C_2-NiCr were used as reference benchmarks.

The experimental compositions investigated included a High Entropy Alloy (HEA) system, both in its pure form and reinforced with 60 vol% titanium carbide (TiC) as a hard phase. These compositions were processed via HEBM and subsequently deposited using the HVOF technique.

Introduction

This chapter provides a comprehensive overview of metallic surface protection via surface engineering, with a focus on the latest developments in thermally sprayed coatings for wear and corrosion resistance. Particular emphasis is placed on High-Velocity Oxy-Fuel (HVOF) and High-Velocity Air-Fuel (HVAF) technologies, which are the core deposition techniques used in this thesis to produce hardmetal coatings. The role of tungsten and cobalt in these coatings is discussed in light of their functional importance, supply risk within the European Union, and growing concerns related to toxicity and environmental sustainability.

Surface Engineering

Surface engineering is a multidisciplinary field dedicated to enhancing the performance of material surfaces and components. Its primary objectives include extending service life and improving chemical, mechanical, and optical properties, all while maintaining economic feasibility and environmental sustainability[10]. Across nearly all industrial sectors, components are routinely subjected to harsh chemical, mechanical, or thermal conditions. These aggressive environments inevitably lead to material degradation, often described as the gradual loss of performance in an engineered system. Even minor material loss due to wear can compromise the functionality or reliability of a component. Corrosion, which results from electrochemical reactions that dissolve or oxidize metal surfaces, can initiate pits or cracks and ultimately lead to structural failure[11,12].

The interaction between wear and corrosion frequently accelerates the rate of degradation, substantially shortening the service life of components. Research indicates that abrasive wear alone is responsible for nearly half of all industrial wear-related problems[1]. Moreover, the combined effects of wear and corrosion contribute to economic losses totaling hundreds of billions of euros each year[13]. To counter these issues, modern engineering relies heavily on surface protection techniques. These may involve altering the surface itself through integral coatings or applying a separate protective layer, known as a discrete coating, to safeguard the component against environmental damage.

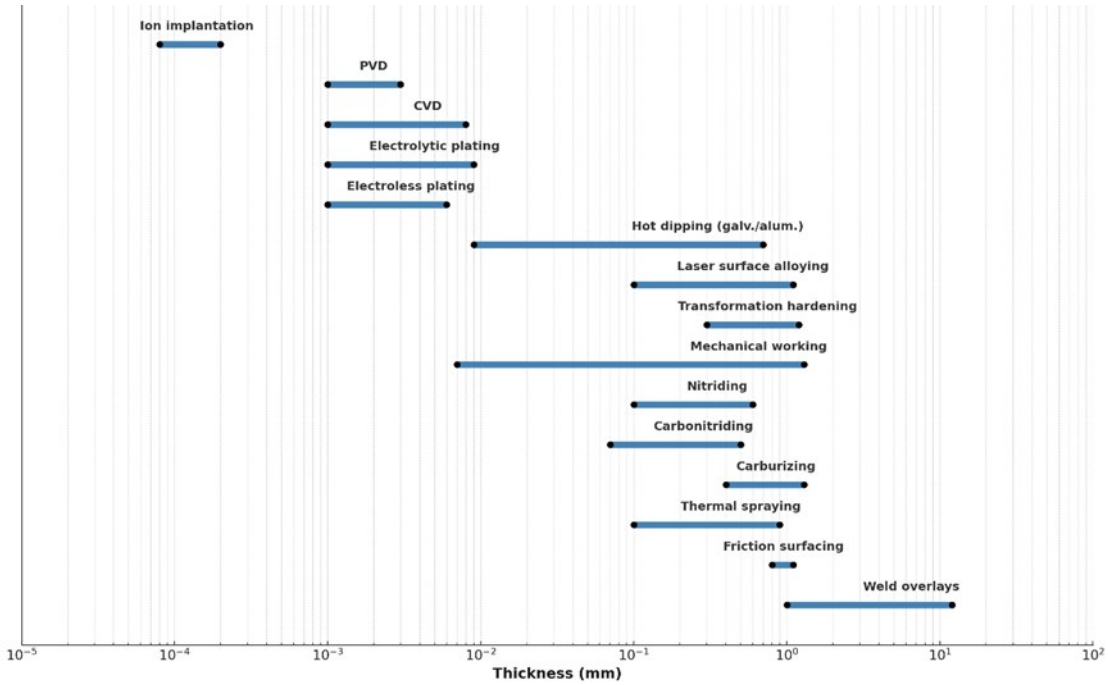

Figure 1: Modified Thickness Ranges by Surface Engineering Techniques.

Selecting an appropriate surface treatment requires careful consideration of several interrelated factors, including the intended application and service conditions, the nature and geometry of the substrate material, and any relevant environmental constraints. Additionally, the choice must account for the coating's composition and thickness, as well as the desired mechanical and chemical performance. Among the many available technologies, thermal spray processes are particularly notable for their versatility and scalability. These methods offer the capability to deposit coatings ranging in thickness from just a few micrometers to several millimeters, making them highly adaptable to a wide array of industrial needs.

Thermal spray methods are widely adopted in sectors such as energy, aerospace, transportation, and manufacturing. Applications include ball valves, turbine blades, shafts, and forming rolls, where wear or corrosion resistance is critical (Figure 2). These methods allow for high deposition rates and a wide choice of feedstock materials including metals, ceramics, and composites.

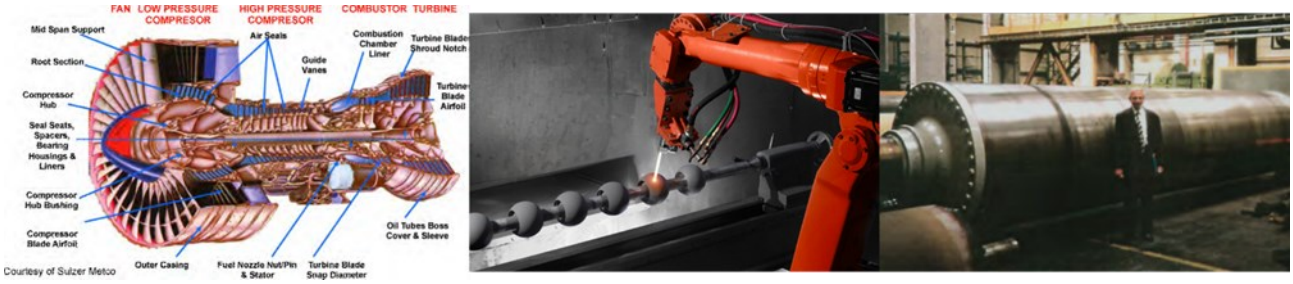

Figure 2: Industrial applications of thermal spray[14].

1. Overview of Thermal Spray Techniques

Thermal spray technologies encompass a range of processes used to deposit protective coatings by propelling finely divided material, typically in powder or wire form, onto substrates. These coatings are engineered to enhance surface properties such as wear resistance, corrosion protection, and thermal insulation without altering the bulk characteristics of the underlying component. Each thermal spray method operates under specific conditions of temperature and particle velocity, which fundamentally influence the microstructure, adhesion, and overall performance of the resulting coating[3,15].

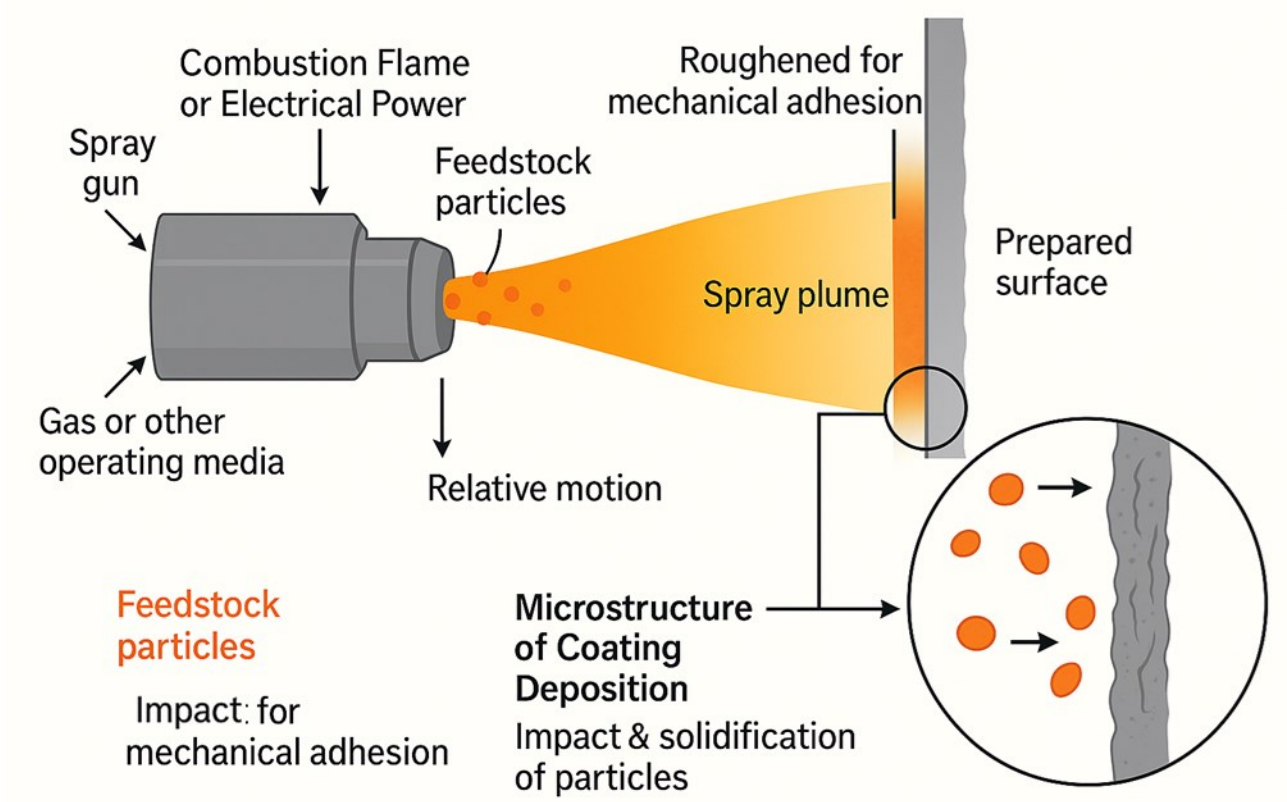

Figure 3: Diagram of a thermal spray process: hot, fast-moving gas melts the powder, which hits the surface and forms a coating[16].

Among the earliest and simplest methods is flame spraying, which involves melting the feedstock material in an oxy-fuel flame and using compressed air to project it toward the target surface. Although relatively low in cost and easy to operate, flame spraying generally produces coatings with higher porosity and weaker adhesion, limiting its use to basic anti-corrosion applications[3].

Atmospheric plasma spraying (APS) employs an electric arc to generate a high-temperature plasma jet capable of melting a wide variety of materials, including ceramics and refractory compounds. While APS can achieve coatings with good thickness and coverage, oxidation and relatively high porosity remain concerns due to the exposure to ambient atmosphere

during spraying[15]. These drawbacks are mitigated in vacuum plasma spraying (VPS) or low-pressure plasma spraying (LPPS), where the process takes place in a controlled, low-pressure environment. These techniques yield dense, oxidation-free coatings suitable for demanding aerospace and biomedical applications but come at significantly higher operational costs[3].

Electric arc wire spray, which uses an electric arc to melt two converging wires and propels the molten droplets using compressed gas, provides a high deposition rate and is widely adopted for protective metallic coatings on large steel structures. However, it is limited to electrically conductive materials and often results in rougher, less dense coatings compared to powder-based methods[15].

Among the most widely adopted advanced techniques is High-Velocity Oxy-Fuel (HVOF) spraying. In this process, combustion of oxygen with a hydrocarbon fuel generates a supersonic gas jet that accelerates powder particles toward the substrate at velocities exceeding 500 m/s. The relatively moderate particle temperature, typically not far to the melting point of many feedstocks, combined with extremely high kinetic energy, leads to the formation of dense, well-adhered coatings with low porosity and limited oxidation. HVOF is particularly effective for depositing hardmetal coatings such as WC-Co and Cr_3C_2-NiCr, which are extensively used in aerospace, power generation, and heavy machinery applications where both wear and corrosion resistance are critical[3,15].

A closely related and increasingly preferred alternative is High-Velocity Air Fuel (HVAF) spraying. Like HVOF, HVAF uses a combustion-driven jet to propel particles at high velocities, but it substitutes air for oxygen and operates at lower combustion temperatures—typically in the range of 1,900–2,100 °C. This reduction in thermal load significantly minimizes oxidation and phase degradation of sensitive materials like tungsten carbides, while still achieving particle velocities comparable to or even exceeding those in HVOF. HVAF coatings thus often exhibit superior hardness, toughness, and long-term stability in aggressive environments, with lower operational costs and improved environmental safety [17,18].

In contrast to both HVOF and HVAF, Cold Spray operates in a completely solid-state regime. Particles are not melted but rather accelerated to very high velocities (up to 1,200 m/s) using a high-pressure, high-velocity stream of compressed gas, typically helium or nitrogen. Upon impact, severe plastic deformation results in bonding through solid-state mechanisms. The key advantage of cold spray lies in its low operating temperature, generally below 500 °C, which prevents oxidation, phase transformations, and thermal stresses. This makes it ideal

for oxygen-sensitive materials and repair applications involving lightweight alloys, titanium, copper, and even some polymers. However, the process is largely limited to ductile materials and requires substantial gas consumption[19,20].

A consolidated comparison of the main thermal spray processes, including their typical particle velocities and temperatures, is shown below to highlight the relationship between processing parameters and the nature of coatings produced.

Table 1: Velocity and temperature of the main used thermal spray processes[3,11,19].

Process	Particle Velocity (m/s)	Particle Temperature (°C)
Flame Spray	50–100	2,500–3,000
Arc Wire Spray	100–150	~4,000 (local arc)
APS	200–500	Up to 15,000 (plasma core)
VPS/LPPS	300–600	Similar to APS
HVOF	500–900	2,500–3,000
HVAF	800–1,000+	1,900–2,100
Cold Spray	300–1,200	<500

This comparison underscores why techniques like HVOF, HVAF, and Cold Spray are of industrial relevance: they offer precise control over coating properties, low oxide content, and high mechanical integrity. Their role becomes even more strategic in contexts where regulatory constraints increasingly limit the use of hazardous materials such as hexavalent chromium (Cr^{6+}) and cobalt, and where there's a push to minimize reliance on critical raw materials[21]. In this light, modern thermal spray technologies provide both a technological and environmental pathway forward for next-generation manufacturing.

1.1. HVOF

High-Velocity Oxy-Fuel (HVOF) spraying has become a reference process in the field of thermal spray technologies, particularly when the application requires coatings with superior mechanical strength, minimal oxidation, and extremely low porosity. HVOF operates through the combustion of a fuel, such as propane, hydrogen, or kerosene, with pure oxygen in a high-pressure combustion chamber. This reaction generates a stream of hot gases that is accelerated through a de Laval nozzle to supersonic speeds. Feedstock powders, typically metals, alloys, or cermets, are injected into this high-velocity flow, gaining momentum and thermal energy before impacting the target substrate. Unlike other high-temperature spray processes, HVOF relies predominantly on kinetic energy rather than heat to achieve bonding. The particles generally are in a molten semi-molten or even solid state upon impact, which helps to preserve the original material phases and enhances coating integrity through plastic deformation and mechanical interlocking[3, 22, 23].

The principal advantage of HVOF lies in its capacity to produce dense, tightly bonded coatings with porosity values commonly below 1% and bond strengths often exceeding 70 MPa. These characteristics are essential for components exposed to high mechanical loads, abrasive environments, or corrosive media. The low thermal exposure also significantly limits the formation of oxide inclusions or deleterious secondary phases, a particularly important factor when spraying oxygen-sensitive feedstocks like tungsten carbide. The resulting microstructure is typically lamellar, with minimal interlamellar gaps and high homogeneity, which translates directly into enhanced wear resistance, corrosion protection, and thermal stability[3, 24].

A wide range of feedstock materials can be used in HVOF spraying, allowing tailored solutions for specific industrial needs. Tungsten carbide-based systems, such as WC-Co and WC-CoCr, are among the most widely adopted. WC-12Co and WC-17Co compositions offer high hardness and erosion resistance and are extensively used in oil and gas, mining, and aerospace applications[25]. The addition of chromium to the binder phase, as in WC-CoCr, enhances corrosion resistance without sacrificing toughness. Another common class of feedstock is chromium carbide-based systems, particularly Cr_3C_2-NiCr, which are preferred for high-temperature oxidation and corrosion environments, including turbine components and heat exchangers. Nickel-based superalloys, such as Inconel 625 and Hastelloy, provide oxidation and sulfidation resistance at elevated temperatures, while stainless steel powders (e.g., 316L, AISI 304) are often used for chemical and marine

applications [20, 26]. Iron-based materials and self-fluxing Ni-Cr-B-Si alloys also find use in wear-resistant coatings, especially when post-fusing is possible[27].

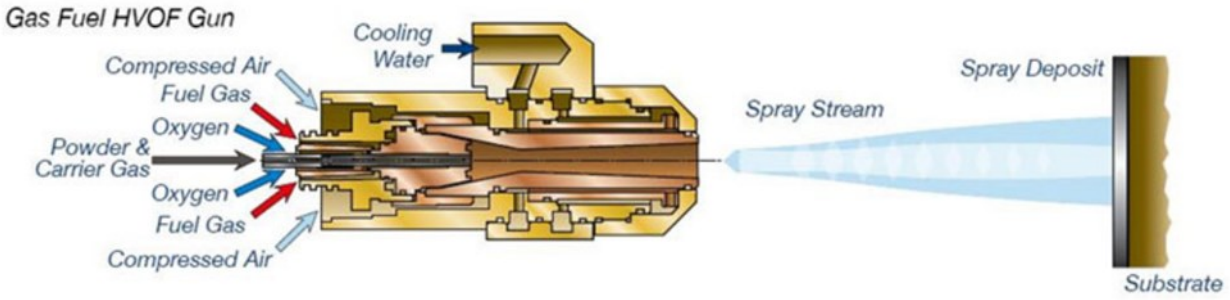

Figure 4: General Schematic of a gaseous-fuelled HVOF gun[28].

The morphology and mechanical characteristics of HVOF and HVAF coatings have been extensively documented. Coatings composed of WC-based cermets typically reach hardness levels exceeding 1,200 HV, which makes them suitable for highly abrasive conditions. Chromium carbide coatings, while slightly less hard, offer superior performance at high temperatures due to better chemical stability. As shown in Figure y, the microstructure of an HVAF-sprayed WC-Co coating is dense, with a nearly pore-free appearance and uniformly distributed hard phases[28, 24]. These attributes translate directly into extended service life for coated components, reduced maintenance intervals, and lower total lifecycle costs.

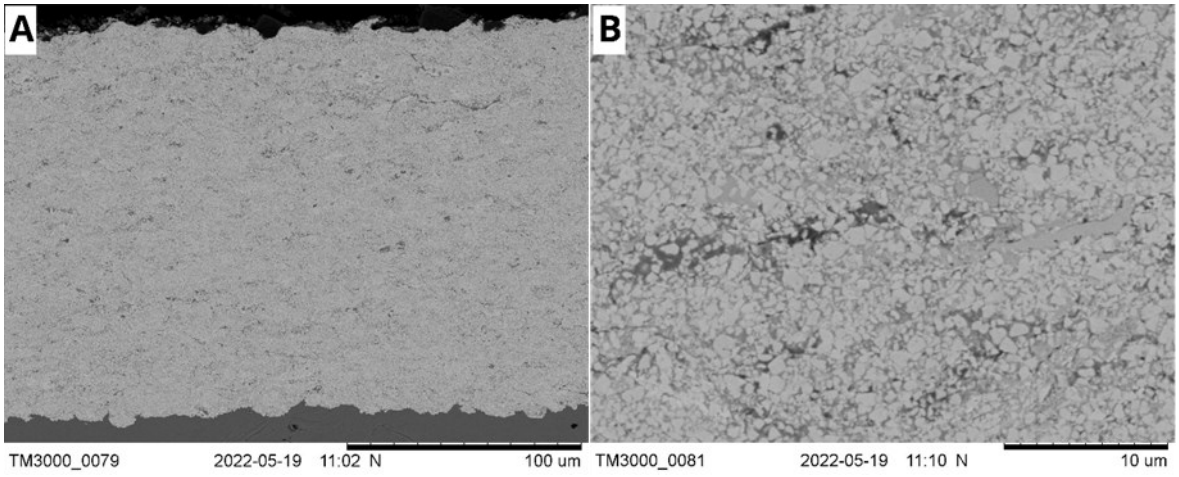

Figure 5: SEM image of a WC-Co HVAF coating showing dense structure and minimal porosity[29].

Careful control of process parameters is essential to achieving optimal coating quality. Variables such as the fuel-to-oxygen ratio, combustion pressure, particle injection method, standoff distance, and powder feed rate must be finely tuned. Even slight deviations in gas flow rate or flame geometry can significantly affect particle velocity and temperature, thereby influencing coating adhesion, hardness, and surface roughness. Additionally, the choice of

powder morphology, angular versus spherical, agglomerated versus monolithic, can affect the deposition efficiency and splat morphology[30].

HVOF's industrial success is also linked to its adaptability. It can be used to coat complex geometries, internal surfaces, or localized areas, thanks to developments in robotic torch manipulation and in situ diagnostic systems. In sectors such as aerospace, power generation, and hydraulic systems, HVOF coatings are now considered the standard solution for replacing environmentally hazardous plating methods such as hexavalent chromium, aligning with current European and international regulatory frameworks on critical raw materials and toxic substances[21].

In conclusion, HVOF spraying represents one of the most reliable and versatile technologies available for the production of high-performance coatings. Its ability to combine high deposition velocity with controlled thermal input makes it uniquely suited for applications demanding both mechanical and chemical durability. By leveraging advanced feedstock materials and increasingly precise process control, HVOF has established itself as an indispensable tool in modern surface engineering for critical components across multiple industries.

1.1.1. Feedstock Materials for HVOF Spraying

The selection of feedstock is paramount in achieving HVOF coatings with tailored performance and reliability. Traditional powder feedstocks typically produced via agglomeration, atomization, or spray-drying remain predominant, offering particle sizes from 5 to 45 µm. Spherical and agglomerated powders deliver consistent flowability and controlled in-flight behaviour, while nanostructured powders enable microstructural refinement and enhanced hardness, provided that feeding mechanisms are optimized to avoid clogging and backflow[30–32]. Recent studies on WC–Co powders confirm that feedstock morphology significantly influences decarburization resistance and coating cohesion[34].

For ultrafine coatings, suspension feedstocks, where nanoparticles are dispersed in liquid media, have been adapted to HVOF torch systems. While more common in suspension flame or plasma spraying, these systems have demonstrated the capacity to produce homogeneous, thin (<50 µm) depositions with controlled porosity. Challenges such as liquid evaporation and spray stability require careful tailoring of torch design and spray parameters[34, 35].

A groundbreaking evolution is found in polymer–ceramic filament feedstocks, developed by Sauter and collaborators[37]. These filaments, produced by extruding powders bound within a polymer matrix, are fed continuously into modified HVOF torches such as TopGun systems. During spraying, the polymer burns away, and ceramic or metallic particles form a dense, lamellar structure. Sauter's foundational work explores binder composition, filament tensile strength, and burnout behaviour, showing that filament-fed HVOF achieves coatings comparable to suspension-fed systems but with enhanced feed consistency [37]. Moreover, the comprehensive comparison by[38] between APS, suspension HVOF, and filament HVOF for nichrome coatings revealed that filament-fed HVOF strikes an optimal balance, producing coatings with moderate oxidation (42–54 vol %), superior microstructure, and thermal stability up to 700 °C, outperforming atmospheric plasma sprayed variants under the majority of test conditions.

Although wire and conventional filament feedstocks are uncommon in standard HVOF due to incompatibility with supersonic powder feeds, experimental prototypes utilizing cored-wire injection or hybrid torch designs have been explored[39]. These aim to combine the deposition efficiency of wire-based methods with the high kinetic energy of HVOF, though they remain primarily in research stages.

The interplay of feedstock properties: morphology, size distribution, binder system, and material composition; directly affects deposition efficiency, oxidation propensity, and final coating characteristics. Nanostructured powders and suspension systems promise high-performance coatings but demand precise spray control, while filament systems pioneered by Sauter offer a scalable pathway to finely structured coatings with industrial feed reliability. Continued development of these technologies will further expand the versatility of HVOF in advanced surface engineering applications.

1.1.2. Powder Feedstocks for HVOF Spraying

Among the various forms of feedstock applicable to thermal spray processes, powders represent the most mature and widely used category in High-Velocity Oxy-Fuel (HVOF) spraying. Their morphological, structural, and chemical characteristics have a decisive influence on coating quality, determining critical aspects such as flowability, deposition efficiency, porosity, hardness, phase retention, and oxidation behaviour during spraying. Several technologies are currently available for the production of powders tailored to HVOF, each offering specific advantages depending on the material system and final application[34], [40]–[43].

Table 2: Comparative Summary of Powder Production Methods for HVOF Feedstocks

Production Method	Typical Morphology	Materials	Advantages	Limitations	Reference
Gas Atomization	Spherical	Metals, alloys	Excellent flowability; low oxidation; fine microstructure	Costly setup; limited to metallic systems	[44], [45]
Agglomeration & Sintering	Rounded agglomerates	Hardmetals (WC–Co, Cr_3C_2–NiCr)	Homogeneous phase distribution; tailored composite design	Requires spray drying + sintering; risk of decarburization	[46], [47]
Fused and Crushed	Angular/irregular	Oxide ceramics (Al_2O_3, Cr_2O_3)	Simple; low-cost	Poor flowability; high surface oxidation; inconsistent size	[35], [46], [48], [49]
HEBM (High-Energy Ball Milling)	Irregular; dense composite	Cermets, hardmetal composites (WC–Ni)	Uniform phase dispersion; no sintering required	High contamination risk; low productivity	[44], [50], [51]
Mechanical Alloying	Similar to HEBM	Non-equilibrium alloys; nanocomposites	Formation of metastable phases; fine microstructure	Similar to HEBM; sensitive to process parameters	[48], [50]
Spray Drying (pre-sintering)	Porous granules	Precursor for agglomerated powders	Controlled granule size and binder content	Not a standalone process; requires post-sintering for HVOF	[40], [46]

Gas atomization is one of the most common and industrially scalable methods for producing metallic and alloy powders for HVOF. It consists in disintegrating a molten stream of metal using a high-pressure gas jet (typically argon or nitrogen), leading to rapid solidification and the formation of spherical or near-spherical particles. This morphology guarantees excellent flowability and minimizes clogging during feeding, making gas-atomized powders ideal for dense metallic coatings. Furthermore, the rapid solidification promotes homogeneous microstructures with fine grain sizes and low oxygen content[44], [45].

For composite or ceramic-based systems—such as WC–Co, Cr_3C_2–NiCr, or TiC–Ni—the most widely used production method is agglomeration and sintering. In this two-step process, fine powders are first agglomerated via spray drying into porous granules, and then thermally sintered to consolidate their structure. The resulting agglomerates are typically spherical or rounded and exhibit good flowability. This method allows a homogeneous

distribution of the hard phase within the binder and precise control over phase ratios. Agglomerated and sintered powders are particularly suitable for HVOF because they balance sprayability with mechanical integrity, ensuring adequate in-flight behaviour and microstructural cohesion in the coating[46], [47].

A more traditional method, often used for oxide ceramics, is the fused-and-crushed route. This process involves melting the material in an electric arc furnace, rapidly solidifying it, and then crushing the solid mass into particles of the desired size. While it is relatively cost-effective, the method generally produces angular and irregular particles with lower flowability and higher surface oxidation. Consequently, fused and crushed powders are less ideal for HVOF than for plasma spraying, where higher thermal energy can compensate for particle irregularity[35].

In systems where the metallic binder does not adequately wet the ceramic reinforcement, or where sintering fails to produce cohesive structures, High-Energy Ball Milling (HEBM) provides a solid-state alternative. This mechanical alloying technique uses high-speed milling to induce repeated fracturing and cold welding of powder particles. The result is a fine, homogeneous microstructure in which each particle contains the target composition. HEBM is particularly effective for composite materials such as WC–Ni or Fe-based cermets, where traditional sintering may lead to poor phase dispersion or segregation. Moreover, the mechanically deformed microstructure of HEBM powders enhances their reactivity and cohesion during spraying[50], [51].

Closely related to HEBM is mechanical alloying, which refers more broadly to solid-state reactions between dissimilar powders. It is often used to prepare non-equilibrium or metastable phases, including supersaturated solid solutions, amorphous alloys, and nanocomposites. The structural refinement achieved through mechanical alloying promotes improved hardness and thermal stability in the resulting coatings, though care must be taken to control contamination and excessive cold welding[50], [52].

Finally, spray drying is commonly employed as a precursor step for agglomerated-sintered feedstocks. It allows the formation of spherical granules from a slurry of particles dispersed in a liquid medium. The morphology, density, and internal porosity of spray-dried granules can be tailored by adjusting the drying rate, binder content, and solid loading. Although spray-dried powders require further sintering to be fully consolidated for HVOF, they provide an essential route for the pre-conditioning of feedstock mixtures, especially in multi-phase systems[40].

In conclusion, powder feedstocks for HVOF spraying are produced via a variety of methods, each tailored to the material chemistry and the intended coating function. Gas atomization offers high purity and flowability for metallic powders; agglomeration and sintering provide structured granules for hardmetal systems; fused-and-crushed methods serve ceramic needs; and high-energy mechanical techniques like HEBM enable innovative composite formulations. The continuous refinement of these technologies ensures the production of feedstocks that meet the increasingly stringent performance requirements of HVOF coatings across industrial sectors.

1.1.3. High-Energy Ball Milling for HVOF Powder Feedstocks

High-Energy Ball Milling (HEBM) is a solid-state powder processing technique increasingly employed in the development of composite feedstocks for HVOF spraying. Unlike conventional methods such as gas atomization or agglomeration–sintering, HEBM enables the formation of refined microstructures through repeated fracturing, cold welding, and mechanical alloying of particles under high-energy impacts. This process promotes a uniform dispersion of reinforcement phases within metallic matrices, stabilizes non-equilibrium structures, and reduces particle size, often into the submicron range. Particularly in systems where wetting between binder and hard phases is poor, HEBM proves advantageous by eliminating the need for liquid-phase sintering. The resulting powders exhibit improved chemical homogeneity, enhanced densification behaviour during spraying, and better resistance to in-flight phase degradation. For example, Pougoum et al. [51] reported that Fe_3Al-based powders reinforced with BN and prepared via HEBM produced HVOF coatings with up to tenfold improvement in wear resistance and significantly increased hardness compared to non-milled counterparts. These improvements are attributed to the refined grain structure and intimate bonding between phases introduced during the milling process. Consequently, HEBM stands as a versatile and scalable method for producing tailored powder feedstocks suitable for high-performance HVOF coatings in structural and wear-critical applications[50].

1.2. Wear and Corrosion Protection of Mechanical Components by Thermal Spray Coatings

The application of protective coatings remains one of the most widespread and effective strategies for improving the wear and corrosion resistance of mechanical components and tools. Today, thermal spray technologies continue to be widely adopted due to their relatively low cost, broad thickness range (from tens to hundreds of microns), and flexibility in coating complex geometries. These features have made thermal spray indispensable across various sectors, including aerospace, energy, advanced manufacturing, and electric mobility.

The key requirements for an effective protective coating include low porosity, strong adhesion to the substrate, and thermal compatibility between the coating and the substrate. Excessive mismatch in thermal expansion coefficients can lead to residual stresses that may cause coating delamination[53]. Therefore, selecting the appropriate coating material and deposition process (e.g., HVOF, HVAF, APS, Cold Spray) is critical to ensuring optimal performance[54], [55]. Emerging technologies and materials are on developing in the field of thermal spray such as: Suspension Plasma Spray (SPS), High-Entropy Alloy (HEA) spraying, and Solution Precursor Plasma Spray (SPPS). All of these are further expanding the application potential, enabling the deposition of nanostructured and multi-component coatings[56], [57].

In recent years, hybrid approaches combining thermal spray with additive manufacturing have also gained attention for the repair and customization of high-value components[58]. The integration of machine learning and real-time diagnostics into process control further improves reproducibility, quality, and the ability to tailor microstructures for specific applications[59]. These advancements are aligned with the broader goals of the Fourth Industrial Revolution, enabling intelligent manufacturing processes and highly engineered surfaces.

Thermal spray coatings are now increasingly being developed for multifunctional performance. In addition to wear and corrosion resistance, new formulations are targeting thermal insulation, electrical conductivity, bioactivity, or anti-fouling properties. This multifunctionality is particularly valuable in advanced applications such as biomedical implants, high-efficiency turbines, and hydrogen economy components. For instance, coatings with controlled porosity and tailored composition are being explored for solid oxide fuel cells and hydrogen separators.

Furthermore, the sustainability aspect of surface engineering is gaining growing importance. Thermal spray processes, when properly optimized, contribute to the extension of service life, reduction of raw material usage, and component remanufacturing. This makes them attractive within the context of circular economy and green manufacturing initiatives.

1.2.1. Conventional Compositions

The most common thermal spray materials used for abrasion, sliding, and corrosion protection include:

Hardmetals, such as WC- or Cr_3C_2-based systems with Co, Ni, or NiCr/CoCr binders[55], provide an excellent combination of ceramic hardness and metal toughness, making them highly effective in abrasive and impact environments;

Ceramic oxides, including Al_2O_3, TiO_2, and Cr_2O_3, are typically applied using APS and widely used across high-temperature applications. However, due to their porous and microcracked structures, these coatings often require sealing with polymeric resins to achieve effective corrosion protection[3], [60].

Metallic corrosion- and wear-resistant alloys, such as Inconel 625[61], [62], Hastelloy [63], and Stellite[64], are employed in highly corrosive environments. Superalloys like MCrAlY are still used in niche applications such as thermal barrier coatings due to their high-temperature oxidation resistance[65].

Hardmetal coatings offer the best performance in demanding environments due to their low porosity (especially when applied using HVOF or HVAF) and the synergistic effect between hard ceramic phases and the metallic matrix. Their main corrosion resistance limitation lies in potential galvanic coupling between the more noble ceramic phase and the metallic binder. In oxidizing conditions, Cr_3C_2-NiCr-based coatings demonstrate superior thermal stability up to 850 °C[66], whereas WC-Co-based systems are typically limited to around 500 °C.

1.2.2. WC-Based Compositions

Currently, as evidenced by both the scientific literature and industrial trends, the most effective and widely adopted hardmetal coating systems remain those based on WC-Co. These systems provide exceptional performance in wear and erosion resistance, with the exception of applications exceeding 450–500 °C, beyond which WC begins to oxidize rapidly. Feedstock powders are produced by agglomeration and sintering of WC with

metallic binders such as Co or Ni. Coating quality is strongly influenced by the pre-spray heat treatment and the internal cohesion of the powder particles[23], [66].

Cobalt remains the preferred binder due to its excellent wettability and compatibility with WC[67], although Ni-based binders offer better corrosion resistance at the expense of hardness[68]. The addition of chromium (as in WC-10Co4Cr) significantly enhances electrochemical corrosion resistance[69], [70] through the formation of stable passive films and corrosion-resistant η-phases[23], [71].

During spraying, careful control of parameters is crucial to minimize WC dissolution and decarburization, which can lead to the formation of brittle phases such as W_2C, W, and $Co_xW_yC_z$[72]–[74]. Microstructural evolution depends on the spraying technique: HVOF, despite its lower temperature compared to APS, can still cause some decarburization, whereas HVAF, with even lower flame temperatures and oxygen content, minimizes this effect[75].

The influence of the use of nanostructured WC particle size remains a topic of debate: some studies report beneficial effects[76], others detrimental[77], and some indicate negligible influence[34], [78]. Finer WC particles may increase wear and corrosion resistance but also enhance reactivity, thereby raising the risk of decarburization.

Advances in powder engineering, such as the use of spherical, nanostructured, or core-shell feedstocks, are now being explored to improve deposition efficiency, reduce decarburization, and optimize coating architecture. These engineered powders, combined with AI-driven process optimization, are pushing the boundaries of performance in critical sectors such as aerospace engines, oil and gas pipelines, and next-generation electric vehicles.

In conclusion, the continuous evolution in spray technologies (HVAF, SPS, SPPS, Cold Spray), advanced feedstocks, and real-time process control (including AI and diagnostics) is significantly expanding the capabilities of thermal spray coatings. These coatings are becoming key enablers in the ongoing industrial transition toward energy efficiency, durability, and sustainability for the next decade and beyond.

1.3. Critical Raw Materials (CRM) and Carcinogenic Substances

Concerns regarding the supply, economic volatility, and health impacts of tungsten (W) and cobalt (Co) have intensified over the past decade.

Since 2011, the European Commission has regularly updated its list of Critical Raw Materials (CRMs), identifying elements with high economic importance and significant supply risk. Both tungsten and cobalt have appeared in all updates, and they continue to appear on the latest (2023) CRM list due to:

Economic Importance (EI), tied to market instability and high price volatility. For example, Figure 6 illustrates extreme fluctuations in cobalt pricing from 2002 to 2020[79].

Supply Risk (SR), stemming from geopolitical concentration and resource accessibility, especially in conflict-affected or high-risk areas[7], [80].

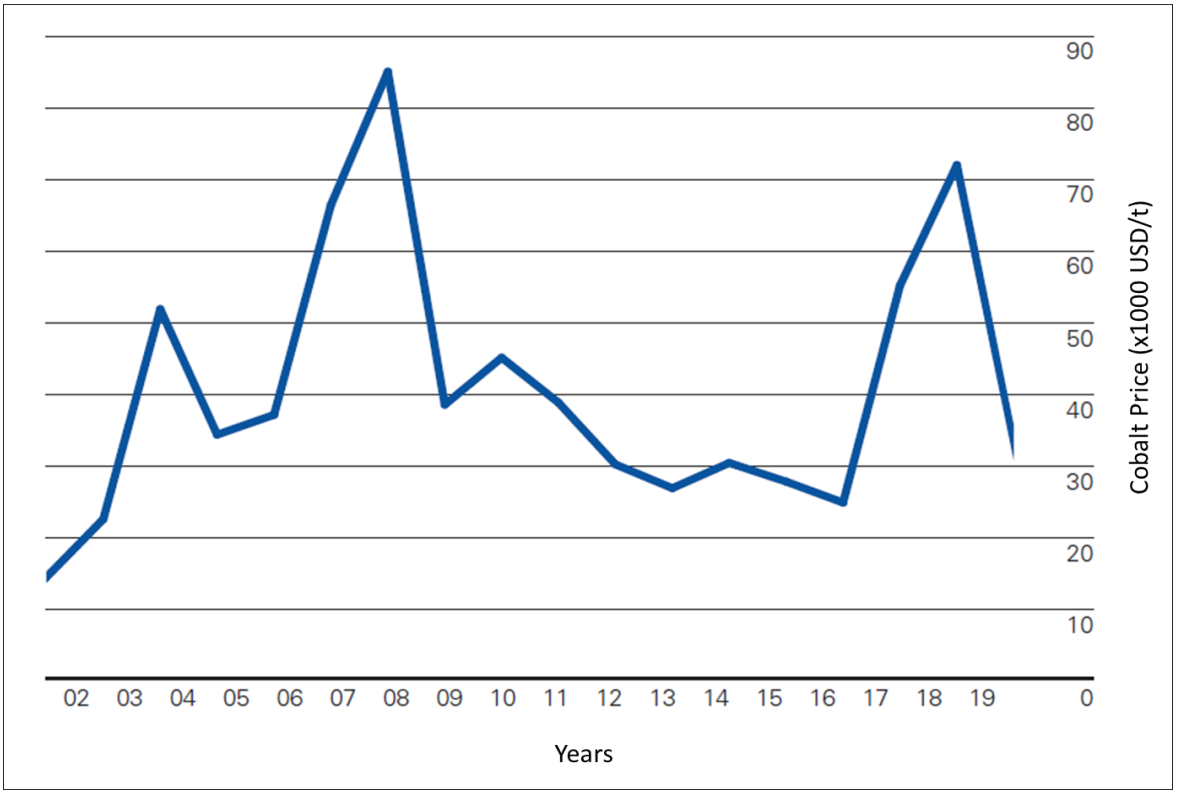

Figure 6: – Cobalt price evolution from 2000 to 2020 [79], [81].

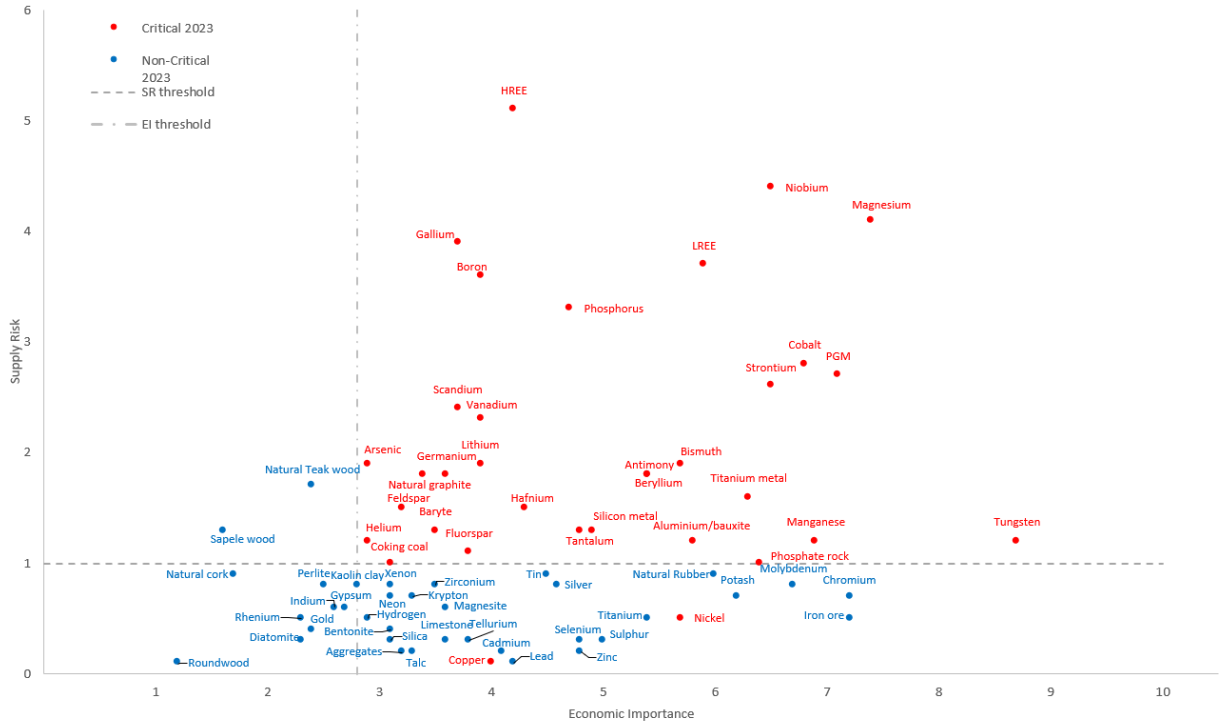

Figure 7: Criticality assessment based on EI and SR by the European Commission, 2023[82].

In Figure 7, materials positioned in the “critical zone” (EI ≥ 2.8, SR ≥ 1) are denoted in red. Both cobalt and tungsten meet these criteria. Furthermore, the sourcing of tungsten must comply with EU Regulation 2017/821, which mandates supply chain due diligence for imports from high-risk regions[80].

In addition to resource-related concerns, health and safety risks associated with cobalt have garnered attention. Cobalt and cobalt-based compounds, including metallic cobalt, salts, oxides, and hardmetals, are now classified as carcinogenic and mutagenic[83], [84]. Inhalation of cobalt powders is linked to acute and chronic respiratory diseases, including asthma, pulmonary fibrosis, and even lung cancer[85], [86]. Moreover, skin and eye irritation are common upon contact with cobalt powders[87]. As a result, cobalt has been officially classified by the European Chemicals Agency (ECHA) as a Category 1B carcinogen and mutagen[88].

In response, the EU is pursuing strategies focused on:

- Enhancing recycling efficiency (while recognizing that 100% CRM recovery is unachievable).
- Promoting substitution with more abundant or less hazardous materials.
- Encouraging innovation in secondary raw material processing.

These policies aim not only to secure resource independence but also to improve environmental and occupational safety, particularly in sectors such as thermal spraying, where powder handling and high-energy deposition processes are common.

1.3.1. Alternative Solutions to WC-Co-Based Coatings

Replacing WC-Co systems is a significant challenge due to their superior wear resistance and well-established industrial performance. Substitutes must offer a balanced compromise between mechanical performance, thermal stability, cost, and environmental safety. The most widely adopted CRM-free alternative is the Cr_3C_2–NiCr system, typically deposited via HVOF or HVAF. It is particularly suited for high-temperature wear applications due to better oxidation resistance and better thermal expansion compatibility with steel substrates[89], [90].

In a systematic comparison study[91], Cr_3C_2–NiCr coatings outperformed traditional metallic alloys and hard chrome at room temperature. However, under abrasive, erosive, or sliding wear conditions, WC-Co coatings still exhibited superior performance. Pure ceramic alternatives (e.g., Al_2O_3, TiO_2, Cr_2O_3) remain limited by inherent brittleness and porosity [82]. Recent research into ternary ceramic systems such as Al_2O_3–Cr_2O_3–TiO_2 has demonstrated improvements in wear resistance by tailoring oxide ratios—TiO_x reduces porosity, while Cr_2O_3 enhances wear resistance[92].

To guide further research, the following categorization outlines the primary strategies under investigation:

WC-FeCrAl: Iron acts as a WC grain growth inhibitor and improves hardness through carbon affinity during sintering. However, poor corrosion resistance limits broader use[93].

WC-Ni and WC-NiCr: Both commercial and experimental variants are being evaluated. While they offer CRM reduction, they fall short of WC-CoCr in wear resistance[94], [95].

WC–Cr_xC_y–Ni: Chromium carbides stabilize WC during spraying and enhance high-temperature oxidation resistance. HVOF and APS methods have shown improved tribological performance, particularly above 500 °C, though overall wear resistance remains inferior to WC-CoCr[96]–[98].

(Ti,Mo)(C,N)–Ni(Co): TiC-based systems offer high hardness, chemical stability, and lower density than WC, allowing potential economic advantages (lower powder mass for equal surface coverage). Mo enhances wettability; N facilitates grain refinement. Wear resistance

is intermediate between Cr_3C_2–NiCr and WC-Co, though brittleness remains a limiting factor[91], [99].

SiC–Ti and SiC–TiCr cermets: These compositions, processed via high-energy ball milling (HEBM), show competitive wear resistance at 400 °C. The in-situ formation of oxides enhances toughness and pore sealing[100].

TiC–FeCrAl (25 vol.% FeCrAl): Developed using HEBM, TiC is formed from Ti and graphite. FeCrAl is CRM-free, has low toxicity, and offers moderate corrosion resistance. At room temperature, wear performance surpasses Cr_3C_2–NiCr but remains below WC-CoCr. However, brittleness due to oxidation during cooling and poor corrosion resistance of FeCrAl (compared to NiCr or CoCr alloys) limit broader adoption[101].

The substitution of WC-Co coatings remains a technically complex and multidisciplinary challenge, requiring coordinated advancements in material science, process optimization, and environmental regulation. Although Cr_3C_2–NiCr and TiC-based systems represent promising directions, trade-offs in wear resistance, corrosion behavior, and mechanical properties must still be addressed. Future developments should prioritize CRM-free, non-toxic, and high-performance materials, with particular attention to recyclability and occupational safety within thermal spray environments.

1.4. High-entropy alloys

High-entropy alloys (HEAs), often called multi-principal element alloys (MPEAs), emerged in the early 2000s with the parallel proposals by Yeh et al. and Cantor et al., who independently argued for exploring the central, previously neglected region of the multicomponent alloy composition space[102], [103]. The intellectual thrust behind the concept was not merely to mix many elements, but to interrogate how high configurational disorder modifies the thermodynamics, defect landscapes, diffusion kinetics and ultimately the macroscopic properties of metallic solids.

1.4.1. Definition

HEAs are most commonly defined by composition: alloys that contain five or more principal elements, each present in the range of roughly 5–35 at.%[102]. Minor additions are permitted to tune properties, but the defining characteristic is the absence of a single dominant element and the presence of high configurational complexity[104]. Despite this compositional complexity, a striking experimental observation is that many HEAs crystallize as simple substitutional solid solutions with face-centered cubic (FCC) or body-centered cubic (BCC) lattices rather than as large families of ordered intermetallic phases [28]. The standard thermodynamic explanation attributes this tendency to the effect of configurational entropy at near-equiatomic compositions: the entropy term can become large enough to compensate enthalpic preferences for ordered compounds in the Gibbs free energy of mixing, making substitutional solid solutions competitive or even preferred.

Thermodynamically, the relevant condition is the minimization of the molar Gibbs free energy of mixing:

$$\Delta G_{mix} = \Delta H_{mix} - T\Delta S_{mix} \quad (1)$$

where $\Delta Hmix$ is the enthalpy of mixing, T the absolute temperature and $\Delta Smix$ the total entropy of mixing. The entropy of mixing contains several physically distinct contributions: configurational, vibrational, magnetic and electronic randomness; but the configurational term generally dominates for substitutional alloys and is therefore the customary proxy for $\Delta Smix$ in HEA discussions[105]. Invoking Boltzmann's combinatorial formulation, the configurational entropy per mole for an n n-component solid solution can be written as

$$\Delta S_{conf} = k \ln w \quad (2)$$

which, for ideal substitutional mixing, reduces to the familiar Gibbs expression

$$\Delta S_{conf} = -R \sum_{i=1}^{n} X_i \ln X_i \quad (3)$$

with R, the gas constant and X_i the mole fraction of element i. For an equiatomic alloy (X_i=1/n for all i) the expression simplifies to

$$\Delta S_{conf} = R \ln n \quad (4)$$

and thus increases monotonically with the number of components. The numerical values for $\Delta S_{conf}/R$ rapidly rise with n (Equation 1), so that, beyond a modest number of components, the entropy contribution $T\Delta S_{conf}$ becomes competitive with typical formation enthalpies of ordered compounds and can alter phase stability even at relatively low temperatures[105]. Yeh et al. used such considerations to classify alloys qualitatively as low-, medium- or high-entropy based on ΔS_{conf}, with the high-entropy regime taken as $\Delta S_{conf} \geq 1.5R$[104]. While this entropy-centric definition has proved useful as a heuristic, it must be employed with care because it implicitly assumes random occupation of lattice sites and other questionable assumptions. In practice, short-range order, clustering and phase separation reduce the configurational entropy relative to the ideal value, and the relative importance of entropy versus enthalpy depends strongly on temperature, strain energy and other contributions omitted by a simplified treatment[106].

1.4.2. Core effects

Four “core effects” have been commonly used to rationalize the distinctive behaviour of HEAs: the high-entropy effect, lattice distortion, sluggish diffusion and the so-called cocktail effect. These labels are intended as conceptual handles rather than sharp physical laws; each effect reflects an ensemble of microscopic phenomena whose relative importance depends on chemistry, structure and processing[104].

The high-entropy effect refers to the observation that large configurational entropy lowers the Gibbs free energy of disordered solid solutions relative to ordered intermetallics,

especially at elevated temperatures where the $-T\Delta S_{mix}$ term is large. A simplified thermodynamic comparison highlights the point: while elemental phases have negligible mixing enthalpies and entropies, intermetallic compounds typically have strongly negative ΔH_{mix} and low configurational entropy, and multicomponent solid solutions present intermediate enthalpies but much larger ΔS_{mix}. Consequently, for many combinations of elements the free energy of a disordered solid solution can be competitive with, or lower than, that of ordered compounds, and Miracle et al. estimated that configurational entropy can destabilize a nontrivial fraction of intermetallics (order 5–10% at room temperature and as much as 30–55% at 1500 K for some families)[105], [107]. The high-entropy effect therefore should be read as a thermodynamic tendency whose quantitative impact depends on the actual magnitudes of ΔH_{mix}, ΔS_{mix} and the temperature.

Lattice distortion in HEAs is a direct geometric consequence of placing atoms of different radii and bonding characteristics on a common lattice. Because in a multicomponent solid every atom has neighbours of multiple types, local bond lengths and local strain fields fluctuate at the atomic scale; these distortions are often sufficiently strong to influence mechanical strength (through solid-solution strengthening), electronic transport (via enhanced electron scattering), thermal transport (phonon scattering) and diffraction signatures (peak broadening and intensity reduction)[104], [108]–[111]. In extreme cases, very large size mismatch or incompatible local bonding preferences can make a crystalline lattice energetically unfavourable and lead to glass formation or amorphization.

The sluggish diffusion effect is an observed tendency for diffusion-controlled processes in many HEAs to proceed more slowly than in simpler alloys. One mechanistic explanation is that the lattice potential energy (LPE) landscape is highly heterogeneous: when an atom attempts to jump between neighbouring sites it experiences variations in site energy and jump barrier that are larger than in simpler alloys. Tsai et al. quantified this by comparing the mean difference in potential energy between adjacent sites (MD) and showed that in some HEAs the MD for a migrating atom can be substantially higher than in ternary alloys, producing effective atomic traps and higher activation energies for long-range diffusion[112]. The practical consequence of sluggish diffusion is twofold: it suppresses coarsening and phase separation (which can stabilise fine microstructures and metastable phases) and it makes HEAs effective as diffusion barrier materials in applications where interdiffusion must be minimized[102], [104], [113], [114].

The cocktail effect is a descriptive term emphasizing that the macroscopic properties of HEAs cannot be predicted by simple rule-of-mixtures arguments alone. Interactions among

constituent elements, emergent local environments, and the collective response of a highly disordered lattice produce properties that are often non-linear, sometimes synergistic and occasionally counterintuitive compared with the properties of the constituent elements taken separately[105], [115]. Treating each phase in a HEA as an “atomic-scale composite” helps to conceptualize how both average chemistry and fluctuations around that average determine strength, ductility, corrosion resistance and other functional responses.

Recent reviews have highlighted that the so-called “four core effects” of HEAs — namely the high-entropy effect, lattice distortion, sluggish diffusion, and the cocktail effect — should be considered more as conceptual frameworks than universally valid physical laws[104]. For instance, while the high-entropy effect can thermodynamically stabilise disordered solid solutions at high temperatures, and lattice distortion can influence mechanical and transport properties [104], [108]–[111], several studies have pointed out that the sluggish diffusion effect is not universally observed across all HEAs. Experimental and computational evidence suggests that diffusion rates do not systematically decrease with increasing alloy complexity, and that factors such as local lattice mismatch and specific chemistry play a more significant role than previously assumed [112]–[114]. Similarly, the cocktail effect, which reflects the non-linear combination of elemental properties in HEAs [105], [115], is recognized as a descriptive concept rather than a predictable rule.

More recent critical reviews reinforce this perspective. Miracle et al. examined the general validity of the four core effects and highlighted their limitations, noting that the influence of each effect strongly depends on chemistry, structure, and processing conditions[106]. Divinski et al. specifically questioned the “sluggish diffusion” effect, concluding that there is currently no experimental evidence supporting its universal applicability in HEAs[116]. Dąbrowa et al. provided an updated overview of diffusion studies in HEAs, confirming that the effect is often overstated and highly composition dependent[117]. Finally, Odetola et al. emphasized that thermodynamic and kinetic behaviours in HEAs do not always align with the assumptions underlying the core effects, particularly in multi-component systems[118].

Considering these observations, it is advisable to treat the “core effects” as starting hypotheses rather than proven governing laws: their actual influence is strongly dependent on alloy chemistry, phase constitution, processing history, and measurement conditions. This nuanced understanding helps frame the current work on HEA coatings, where composition, microstructure, and processing must be carefully optimized to achieve the desired mechanical and functional performance.

1.4.3. Taxonomy

Experimental and computational surveys have shown that HEAs cover a wide chemical space, but certain element classes appear recurrently. Miracle and Senkov's compilation of 408 HEAs shows that Al, Co, Cr, Cu, Fe, Mn, Ni, Ti and V are among the most frequently employed elements, a pattern that reflects both the availability of data for 3d transition metals and the technological interest in these chemistries[106]. Accordingly, two broad families are often discussed in the literature.

The most thoroughly studied family comprises HEAs formed predominantly from 3d transition metals (for instance the well-known CoCrFeMnNi Cantor alloy). Because these chemistries are conceptually close to conventional stainless steels and nickel-based superalloys, much of the early mechanistic understanding and processing know-how could be transferred and extended to the HEA context.

Refractory HEAs (RHEAs) are based on high-melting refractory elements such as Cr, Hf, Mo, Nb, Re, Ta, V, W and Zr, frequently alloyed with small concentrations of Al, Co, Ni, Ti or Si to tune phase stability and oxidation resistance. Introduced around 2010 by Senkov and co-workers, RHEAs are of particular interest because they can retain strength to temperatures where conventional nickel superalloys begin to soften, opening possibilities for high-temperature structural applications[119], [120].

1.4.4. Thermally Sprayed High-Entropy Alloy Coatings

Thermally sprayed coatings based on high-entropy alloys (HEAs) have emerged as a distinct and rapidly developing branch of surface engineering, bridging the compositional flexibility of multicomponent alloys with the cost-effective capability of thermal spray to deposit thick, functional layers. Since the first reports in the early 2000s and the first explicit studies addressing sprayed HEA feedstock and coatings, interest has accelerated because many HEA chemistries show combinations of high hardness, promising corrosion/oxidation behaviour and thermal stability that are attractive for protective and tribological applications. These advantages are realized only when the feeding powder, spray process, and post-processing are coherently selected and optimized to preserve or exploit HEA mechanisms (e.g., solid-solution formation, supersaturation, phase stability) under the extreme thermal and kinetic histories encountered in thermal spraying[121], [122].

Feedstock production and selection are central to the success of thermally sprayed HEA coatings because the powder's phase constitution, particle morphology and size distribution

determine how particles respond to the thermal plume or gas jet and thus which microstructures are achieved on the substrate. Three practical routes dominate current practice: gas atomization of pre-alloyed melts, mechanical alloying (MA) of elemental powders followed by consolidation/heat treatment, and blending of elemental or pre-alloy powders. Gas-atomized powders are typically spherical, chemically more homogeneous and scalable for industrial spraying; they are therefore the preferred route when process reproducibility and low porosity are required. Mechanical alloying produces finer, often nanocrystalline powders that can be attractive for certain microstructural effects but may suffer from irregular shapes and contamination if not carefully controlled. Blending is the simplest and cheapest but carries the highest risk of compositional inhomogeneity unless followed by appropriate thermal treatment. The literature consistently emphasizes gas atomization as the leading feedstock route for industrially relevant HEA thermal spray work, while noting that the final coating reflects a complex convolution of feedstock state and process parameters[121], [123].

Different thermal-spray processes impart markedly different thermal and kinetic histories to HEA particles and hence produce distinctive microstructures and property trade-offs. Atmospheric plasma spray (APS) exposes particles to extremely high temperatures and results in molten or partially molten droplets that form lamellar splats upon impact, but this route also promotes oxidation and intersplat porosity. High-velocity oxy-fuel (HVOF) and high-velocity air fuel (HVAF) produce higher particle velocities and lower in-flight dwell temperatures compared with APS, yielding denser coatings with reduced oxide content and typically higher as-applied hardness. Cold spray (CS) is a solid-state route: particles remain below melting and adhere by severe plastic deformation. Cold-sprayed HEA coatings can retain powder phases with minimal oxidation and low oxide inclusions, but bonding relies on ductility and particle deformation, placing constraints on some HEA chemistries or requiring process innovations (e.g., laser-assisted cold spray or warm spray variants). Detonation and flame spraying have also been used in specific studies. Thus, process selection must be driven by target properties: dense, low-oxide wear-resistant coatings are often best achieved by HVOF/HVAF; oxidation-sensitive chemistries benefit from cold/warm spray; APS remains useful for ceramic-rich or re-meltable systems and for subsequent laser remelting[121], [124], [125].

The microstructure of thermally sprayed HEA coatings is shaped by rapid solidification, splat formation, in-flight oxidation, and post-impact thermal diffusion. Typical as-sprayed structures are lamellar with inter-splat boundaries, oxide stringers (particularly in APS), and

discrete regions of compositional partitioning or nanoscale precipitates depending on cooling rates and alloy chemistry. Rapid quenching during splat solidification often results in supersaturated solid solutions and suppressed intermetallic formation relative to cast material; subsequent heat exposure or annealing can drive precipitation and decomposition toward the equilibrium phases. Importantly, identical HEA nominal chemistries prepared from different powder routes or deposited by different spray techniques can yield substantially different phase constitutions: spherical gas-atomized powders sprayed by HVOF often produce homogeneous, dense BCC/FCC solid solutions, whereas MA powders sprayed by APS can present micro-segregation and a higher oxide fraction. Understanding and controlling these splat-scale phenomena is crucial to tuning hardness, toughness and high-temperature stability[121], [123].

The mechanical and tribological performance of thermally sprayed HEA coatings is typically superior to many conventional sprayed alloys, but performance depends strongly on microstructural state. HVOF-deposited HEA coatings frequently report the highest as-applied hardness owing to a dense, low-porosity lamellar structure and retained supersaturation; however, hardness is not solely a function of density: solid-solution strengthening, precipitation, and severe lattice distortion from multielement mixing all contribute. APS coatings can show lower hardness and higher scatter because of residual porosity and oxides, yet specific APS + post-laser or annealing sequences can restore or even improve performance by homogenizing composition and reducing porosity. Cold spray coatings may achieve good ductility and toughness with competitive wear resistance due to work-hardening and refined grain structures induced by severe plastic deformation, but their hardness can be lower than optimized HVOF counterparts unless post-treatments are applied. Quantitative comparisons in the literature underline that HVOF gives the best compromise for high hardness and low oxide fraction in many HEA systems, while CS excels where preservation of oxygen-sensitive elements is critical[116], [119].

Corrosion and high-temperature oxidation behaviour in sprayed HEA coatings have been investigated for several chemistries and processes; results are chemistry- and process-dependent. APS coatings often incorporate oxides that influence the electrochemical response, sometimes degrading the corrosion resistance versus bulk cast HEAs because porosity and oxide heterogeneities act as sites for localized attack. A clear example is FeCoNiCrAl APS coatings, where aluminium’s affinity for oxygen leads to Al-rich oxide regions and associated localized corrosion patterns unless the process is tuned to minimize oxidation. Conversely, HVOF-deposited HEA coatings designed with sufficient Al and Cr

have demonstrated oxidation resistance comparable to or better than conventional MCrAlY bond coats in some studies, and selected HEA compositions used as bond coats have endured extended high-temperature oxidation and thermal cycling with promising results. Cold-sprayed HEA layers, by limiting in-flight oxidation, can offer favourable corrosion/oxidation resistance but may still require post-deposition treatments to close pores and stabilize the microstructure for long-term high-temperature use[124], [126], [127].

A particularly active application area is the use of HEAs as metallic bond coats for thermal barrier coating (TBC) systems. Compared with conventional MCrAlY bond coats, HEA bond coat concepts aim to combine compositional flexibility (to favour the formation of continuous α-Al_2O_3 / protective TGO layers and to slow detrimental interdiffusion) with enhanced mechanical properties and phase stability at higher temperatures. Experimental work has shown that properly designed HEA bond coats deposited by HVOF or APS can sustain long isothermal exposures and hundreds of thermal cycles with no catastrophic failure, although internal oxidation and TGO characteristics must be carefully studied and engineered. The potential of HEA bond coats is therefore high, but practical adoption requires rigorous qualification and understanding of TGO growth, CTE compatibility, and thermal cycling behaviour[121], [126].

Despite encouraging results, several practical challenges impede straightforward industrial deployment of thermally sprayed HEA coatings. First, powder production cost and compositional control (especially for gas-atomized pre-alloyed powders containing refractory or low-vapor-pressure elements) are very high. Second, oxidation during high-temperature spray processes can alter intended chemistries and produce oxide defects; this can be mitigated by using inert shrouds, reducing dwell times, selecting HVAF/HVOF or cold spray, or by post-deposition laser re-melting and vacuum annealing. Third, achieving reliable adhesion and low porosity with brittle or complex HEA chemistries is sometimes difficult; process windows, substrate pre-treatment and grit-blast standards need to be optimized. Finally, the multiplicity of alloying elements complicates the thermodynamic prediction of phase formation during the non-equilibrium rapid solidification of splats, and CALPHAD-assisted design combined with targeted experiments has been recommended to reduce empirical trial-and-error. Overall, the key to overcoming these challenges lies in an integrated approach that couples feedstock engineering, process selection, and post-treatment with computational alloy design[121]–[123].

Future directions for sprayed HEA coatings include systematic exploration of gas-atomized pre-alloyed powders for industrial-scale HVOF/HVAF spraying, more studies on solid-state

cold/warm spray for oxygen-sensitive chemistries, coupling of CALPHAD thermodynamic predictions with spray process models to anticipate phase evolution, and development of HEA bond coat standards for TBC qualification. Additional promising avenues are hybrid routes such as APS followed by laser remelting to heal porosity and homogenize microstructure, compositional gradient (functionally graded) HEA coatings, and HEA-based composite coatings in which ceramic reinforcements are embedded to tailor wear or thermal properties. The literature and recent review efforts emphasize that the field is moving rapidly from fundamental demonstrations toward targeted qualification for demanding environments (tribological, corrosive, or high-temperature) but that standardized feedstock and process databases are still needed to accelerate adoption[121], [122].

1.5. Alternative solutions to Co-based coatings

The development of alternative protective coatings to replace conventional Co- and W-based systems represents one of the main current challenges in the field of surface engineering. The motivation for this research arises both from the high supply risk and cost associated with these critical raw materials (CRMs), and from growing concerns regarding their toxicity and environmental impact [88], [128], [121], [129].

All coatings were deposited using High Velocity Oxy-Fuel (HVOF) spraying on stainless-steel substrates [130], [131]. The main aim of the deposition strategy was to ensure reproducible coating microstructures and to allow systematic investigation of the effects of composition and phase constitution on coating performance.

The coatings were characterised through a combination of microstructural, mechanical, tribological and corrosion analyses. Phase composition and microstructure were assessed by X-ray diffraction, SEM/EDX, and EBSD, while chemical composition, porosity, and thickness were quantified using gas analysis and image-based methods[130], [131].

Mechanical properties were evaluated via microhardness and nanoindentation mapping, as well as scratch testing to assess adhesion and fracture resistance. Tribological behaviour was studied through ball-on-disc sliding and high-stress abrasion tests [130], [131], whereas corrosion resistance was investigated using potentiodynamic polarisation and post-test microstructural analysis [130], [131]

Overall, this characterisation approach was designed to link composition and microstructure to functional performance in terms of hardness, wear, and corrosion resistance, providing a framework for comparison with conventional WC-Co/Cr and Stellite-type coatings [121], [129] and highlighting the potential advantages of CRM-free HEA and HEA–TiC coatings.

The overall goal of this work is therefore to design, deposit, and characterise new high-performance coatings that are completely free of cobalt and tungsten, while maintaining or even improving the mechanical, tribological, and corrosion properties of traditional Stellite and WC-Co/Cr systems. At the same time, the aim is to develop coatings that are more sustainable and recyclable, in line with current circular-economy objectives.

To achieve these goals, two complementary families of materials were developed and investigated:

- Metallic high-entropy alloy (HEA) coatings, designed as direct metallic substitutes for Ni- and Co-based overlays, and

- HEA-based cermet coatings, obtained by reinforcing the same HEA matrices with TiC ceramic particles to achieve hardmetal-like microstructures combining high hardness and wear resistance.

Both families were specifically tailored for High Velocity Oxy-Fuel (HVOF) deposition and conceived to allow a systematic study of the relationships between composition, phase constitution, and functional performance.

1.5.1. Route 1: Metallic coatings

Based on the evidence available in the scientific literature, two distinct HEA systems were selected for investigation.

The first is the equiatomic Cr–Mn–Fe–Co–Ni alloy, commonly known as the Cantor alloy. This material is one of the most representative and extensively studied HEAs, characterised by a stable single-phase face-centred cubic (FCC) structure[132]. Due to its well-documented mechanical and corrosion properties and the fact that it has already been successfully deposited and evaluated as a thermal-spray coating by several authors, the Cantor alloy was considered a reliable reference material for this work. However, it is important to underline that the alloy still contains a significant fraction of cobalt, which, although lower than in conventional Stellite alloys, remains a limiting factor when the goal is to minimise the use of CRMs.

The second selected system is the $Al_x(Cr_{20}Mn_{25}Fe_{40}Ni_{15})_{100-x}$ alloy, previously investigated in[133]. Unlike the Cantor alloy, this system is entirely cobalt-free, and both its phase constitution and mechanical behaviour can be systematically tuned by varying the aluminium content. In this work, three compositions were considered, corresponding to x = 0, 10 and 14, referred to hereafter as Al_0(CrMnFeNi), Al_{10}(CrMnFeNi), and Al_{14}(CrMnFeNi), respectively.

The composition with x = 0 forms a single-phase FCC solid solution, typically associated with high ductility but lower hardness. Conversely, the Al-containing variants (x = 10 and 14) are expected to develop dual-phase microstructures composed of a disordered body-centred cubic (BCC) solid solution and an ordered intermetallic B2 phase. Such a phase assemblage usually results in increased hardness at the expense of ductility, which makes these alloys particularly interesting for wear-resistant coating applications.

The rationale behind the selection of this alloy family can be summarised in three main points:

- The complete absence of cobalt, which directly addresses the issue of CRM dependency and related cost and health concerns.
- The relatively high iron content, which helps to reduce production costs and improve sustainability.
- The systematic control of phase constitution through Al addition, enabling a detailed investigation of structure–property relationships in HEA coatings.

1.5.2. Route 2: Cermet coatings

The second research route focused on the development of HEA-based cermets, in which the metallic HEA matrices from Route 1 were used as binders for a ceramic hard phase, with the aim of obtaining hardmetal-type coatings characterised by high wear resistance.

Four matrix compositions were selected, chosen to represent a wide range of phase constitutions and mechanical behaviours:

- CrMnFeCoNi + 60 vol.% TiC, hereafter Cantor+60TiC.
- $Cr_{20}Mn_{25}Fe_{40}Ni_{15}$ + 60 vol.% TiC, hereafter Al0(CrMnFeNi)+60TiC.
- $Al_{14}(Cr_{20}Mn_{25}Fe_{40}Ni_{15})_{86}$ + 60 vol.% TiC, hereafter Al14(CrMnFeNi)+60TiC.
- $Al_{0.5}CrCuFeNi_2$ + 60 vol.% TiC, hereafter AlCuCrFeNi+60TiC.

Within the $Al_x(Cr_{20}Mn_{25}Fe_{40}Ni_{15})_{100-x}$ family, only the boundary compositions x = 0 and x = 14 were selected, as they represent two opposite structural conditions: a fully FCC solid solution and a dual BCC/B2 microstructure[133].

In addition, the $Al_{0.5}CrCuFeNi_2$ alloy [134] was included because, despite its relatively high Al content (~9 at.%), it remains predominantly FCC-stabilised due to its high valence electron concentration (VEC > 8) and φ ≈ 20 [135]. This provides a useful comparison with the Al-rich Cr–Mn–Fe–Ni systems, where increasing Al promotes the formation of BCC/B2 phases.

All HEA matrices were reinforced with 60 vol.% TiC, a fraction chosen based on previous studies on TiC- and NbC-based hardmetals with simpler metallic binders (Ni-Cr, Fe-Cr-Al, etc.), which demonstrated that this value offers the best compromise between hardness and fracture resistance. Higher TiC contents generally cause excessive brittleness, whereas lower ones fail to provide sufficient reinforcement[99], [101], [136], [137].

The powders were produced by high-energy ball milling (HEBM) with in-situ TiC synthesis, followed by classification into an HVOF-grade particle size range (−45/+10 μm). This procedure ensures a fine and homogeneous dispersion of TiC within the metallic matrix before spraying.

2. Experimental Procedure

This chapter presents a systematic account of all coating compositions investigated within the framework of the present Ph.D. research, with particular emphasis on strategies aimed at reducing the dependence on Critical Raw Materials (CRMs) and mitigating their associated hazardousness. A detailed description is provided of the thermal spraying processes employed, together with the deposition parameters optimized to ensure reliable and reproducible coating fabrication.

To evaluate the functional performance of the developed coatings, an extensive experimental campaign was conducted, encompassing micromechanical, tribological, and corrosion resistance tests. All testing procedures were selected and performed in strict accordance with ASTM standards, thereby guaranteeing methodological consistency, reliability of the data, and comparability with the state of the art. The experimental design was conceived to generate a comprehensive performance profile of the coatings under conditions representative of their potential applications.

Post-test analyses were primarily devoted to the identification and classification of the prevailing wear mechanisms and corrosion morphologies observed in the coated systems. This approach enabled not only a deeper understanding of the coatings' degradation pathways but also the establishment of direct comparisons with the scientific and technical literature available on analogous classes of protective coatings, thus situating the present results within a consolidated research context.

In addition, the chapter provides an exhaustive description of the experimental methodologies adopted for both the manufacturing processes and the subsequent characterization of feedstock powders and deposited coatings. These procedures, discussed in detail in dedicated sections, represent the methodological backbone of the research and form the basis for the critical evaluation of the coatings' properties and their technological relevance.

2.1. Feedstock Powders and characterization

All feedstock powders employed in this research were produced by mechanical alloying (MA), a well-established and extensively validated method for the synthesis of high-entropy alloys (HEAs)[138]. While gas atomization represents the most typical route for producing metallic powders, including HEAs, mechanical alloying was specifically chosen in this study to reduce production costs and accelerate the development of experimental powders. This approach allows rapid exploration of different compositions and phase constitutions, providing a practical balance between material performance and experimental flexibility, particularly in the early stages of coating development. In this case, MA was conducted through a proprietary high-energy ball milling (HEBM) process, starting from elemental powders of the respective alloying elements. The resulting MA powders were subsequently subjected to a classification procedure, involving sieves and cyclone separators, in order to obtain a fraction with particle sizes in the −45 +10 μm range for high-velocity oxy-fuel (HVOF) spraying.

The particle size distributions of all classified feedstock materials were verified by laser scattering analysis (Mastersizer 2000, Malvern Panalytical Ltd., Malvern, UK). Measurements were conducted using ultrasonication in a wet dispersion cell (Hydro-2000) in order to promote deagglomeration and ensure accurate characterization.

The phase composition of the powders was determined by X-ray diffraction (XRD) using Cu-Kα radiation (X'Pert PRO and Empyrean, Malvern Panalytical B.V., Almelo, NL). Diffraction patterns were recorded within the $20° < 2\theta < 85°$ range, thus enabling the identification of both major crystalline phases and potential secondary constituents formed during mechanical alloying.

Further insight into the microstructure and chemical composition of the powders was obtained by means of scanning electron microscopy (SEM) (Nova NanoSEM 450, FEI – Thermo Fisher Scientific, Eindhoven, NL) combined with energy-dispersive X-ray spectroscopy (EDX) (Quantax-200 microanalysis system equipped with an XFlash6|10 detector, Bruker Nano GmbH, Berlin, Germany). For metallographic preparation, the powders were embedded in a two-component epoxy resin, which was then cured at room temperature. The mounted samples were ground sequentially with silicon carbide (SiC) abrasive papers (grit sizes ranging from P400 to P4000), followed by polishing steps using polycrystalline diamond suspensions (3 μm average particle size) on woven cloth and colloidal silica suspensions on non-woven cloth. Since the metallic powders imparted

sufficient electrical conductivity to the epoxy matrix, no additional metallization (e.g., gold or carbon coating) was required prior to SEM observation.

Quantitative chemical analyses were carried out by acquiring three independent EDX spectra from representative areas imaged at 400× magnification. The analyses were performed at an acceleration voltage of 15 kV with a live counting time of 60 s. Carbon and oxygen were excluded from direct quantification, as both elements were present not only in the powders but also in the epoxy resin. Instead, their concentrations were measured separately: carbon was quantified by the oxygen combustion method (TCH600, LECO Corporation, St. Joseph, MI, USA), whereas oxygen and nitrogen were determined via the inert gas fusion technique (CS230, LECO Corporation). The elemental concentrations obtained from EDX were subsequently renormalized to 100% by incorporating the measured C, O, and N values, following the procedure detailed in [136].

2.2. Coating Deposition

Coatings were deposited on AISI 304 stainless steel plates (60 × 25 × 3 mm). Prior to deposition, the substrates were grit-blasted with brown alumina particles of median size 300 µm (d50) using a handheld blasting unit operated at 5.5 bar, yielding a surface roughness of approximately Sa ≈ 7 µm. The plates were subsequently cleaned in an ultrasonic acetone bath to remove residual grit and contaminants, dried with compressed air, and stored in an oven at 60 °C to minimize moisture uptake prior to spraying.

Depositions were performed using a Diamond Jet 2600 HVOF system (Oerlikon Metco, Westbury, NY, USA) equipped with a DJ8W torch and a pressurized gravimetric 9MPE-DJ powder feeder. The torch was mounted on an X–Y translation system and traversed across a rotating mandrel holding the plates. The mandrel rotation and horizontal traverse speed of the torch were adjusted to achieve a relative torch–substrate velocity of 750 mm/s and a pitch distance of 5 mm (spindle rotational speed 90 rpm and axial feed rate 448 mm/min). Each deposition cycle comprised three torch passes applied in an alternating back-and-forth motion in the X direction with the same start and end points during the coating process, and 13 cycles were carried out in total. A 20 s pause was introduced between cycles to allow substrate cooling, while fixed compressed air jets were directed at the substrates to further control temperature and limit overspray accumulation.

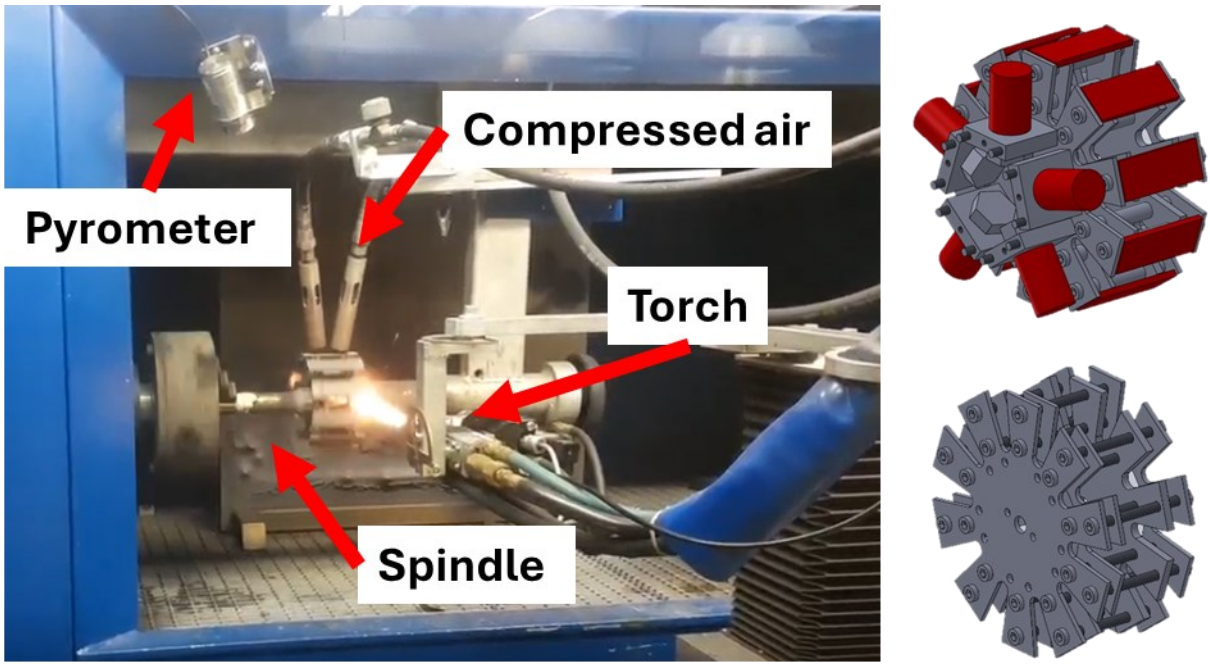

Figure 8: HVOF gun - Diamond Jet 2600 system (spraying booth is installed in Ecor International to Schio in Italy). In the right side 2 configuration of the new sample holder designed by me for CoBRAIN project.

Prior to coating, one 3-pass cycle without powder feed and without cooling was performed to preheat the substrates. Deposition commenced once the powder feed rate stabilized within ±4 g/min of the target value, typically within 1 min.

During deposition, the surface temperature was monitored using an infrared pyrometer (OPTRIS CTLaser, Luchsinger srl, Curno, Italy) positioned outside the torch scan track to avoid artefacts from the spray plume.

For each powder, three depositions were performed under different parameter sets, denoted as “Run 1” to “Run 3,” corresponding to progressively higher H_2 and O_2 flow rates, as summarized in Table 3. All other parameters were held constant.

Deposition efficiency was determined by weighing three plates before and after deposition using an electronic balance (accuracy ±0.01 g). The mass gain of each plate (Δm_plate) was calculated as the difference between the final and initial weight.

The total mass of powder directed toward each plate (m_powder) was calculated from the powder feed rate ($\dot{m}$, in g/min) multiplied by the effective spraying time per plate (t_spray). The spraying time was derived from the process kinematics, taking into account the relative gun-to-substrate velocity (v), the pitch distance between adjacent passes (p), the effective coating width, the number of passes per cycle (n_p), and the total number of deposition cycles (n_c). In practice, the time required to complete one pass was obtained from the ratio between the scan length and the relative velocity, and the total spraying time was computed as the product of the time per pass, the number of passes per cycle, and the number of cycles.

The deposition efficiency (DE) was then calculated as:

$$\mathrm{DE}(\%) = \frac{\Delta m_{\mathrm{plate}}}{m_{\mathrm{powder}}} \times 100$$

where Δm_plate is the mass gain of the substrate and m_powder is the total mass of powder delivered toward the plate during deposition.

For reference, commercial WC-CoCr (Woka 3652, Oerlikon Metco WOKA GmbH, Barchfeld, Germany [139], *Density 5 g/cm³)* and Stellite-6 powders (Amperit 344.088, Höganäs, Laufenburg, Germany) were also deposited on the same substrates with the parameters listed in *Table 3*. The resulting coatings were used as a benchmark.

Table 3: HVOF deposition parameters for all powders.

Parameter setting	**Run 1**	**Run 2**	**Run 3**	**Stellite-6**	**WC-CoCr**
O_2 pressure (psi / MPa)	170 / 1.20				
O_2 flow rate (SLPM)	201	214	228	214	234
H_2 pressure (psi / MPa)	140 / 0.98				110/0.97
H_2 flow rate (SLPM)	574	635	656	635	666
Air pressure (psi / MPa)	100 / 0.7				
Air flow rate (SLPM)	274			313	235
Stoichiometric ratio	0.9	0.86	0.87	0.88	0.85
Powder feed rate (g/min)	20			60	
Standoff distance (mm)	250				240
Torch-substrate speed (mm/s)	750				
Pitch distance (mm)	5			6	
N° of passes per cycle	3				
N° of deposition cycles	13			9	8
N° of pre-heating cycles	1				
Pause between cycles (s)	20				
Sample holder diameter (mm)	160				

2.3. Coatings characterization

2.3.1. Microstructure and phase composition

The microstructural characteristics and chemical composition of the coatings, both on the surface and in cross-section, were investigated by scanning electron microscopy. Observations were carried out using a field emission gun SEM (Nova NanoSEM 450, FEI – Thermo Fisher Scientific, Eindhoven, NL) equipped with energy-dispersive X-ray (EDX) spectroscopy (Quantax200 EDX microanalysis system with XFlash6|10 detector, Bruker Nano GmbH, Berlin, Germany). Preparation of coated samples for cross-sectional observation followed standard metallographic procedures: samples were sectioned by precision cutting, embedded in fenolic resin to ensure mechanical stability, and subsequently ground with SiC abrasive papers of increasing grit size (from P400 to P4000). Final polishing was performed sequentially with a polycrystalline diamond suspension (3 μm average particle size) and colloidal silica. Afterwards, samples were ultrasonically cleaned in acetone, dried with compressed air, and mounted on standard aluminium stubs using conductive adhesive tapes[136], [140]. No metallization was applied to the sample surfaces, since the powder-loaded resin used for mounting was electrically conductive, while the phenol-based resin exhibited sufficient intrinsic conductivity.

The quantitative chemical composition of powders and coatings was determined by acquiring three EDX spectra on 400× cross-sectional views, operating at an acceleration voltage of 15 kV and a live time of 60 s. Quantification was carried out using the Esprit 2.1 software, applying the φ-ρ-Z correction method. Porosity measurements were performed by image analysis on eight backscattered electron micrographs acquired at 3000×, using a Matlab routine (R2024a – The MathWorks Inc., USA). Coating thickness was evaluated from 400× micrographs by means of ImageJ software (NIH, Bethesda, MA, USA).

The crystalline phase composition of the coatings was examined by X-ray diffraction (XRD) using an X'Pert PRO and Empyrean diffractometer (Malvern Panalytical, Almelo, NL). Analyses were conducted with Cu-Kα radiation generated by a tube operated at 40 kV and 40 mA, over the angular range $20° < 2\theta < 85°$. Prior to measurement, coating surfaces were ground with diamond-based abrasive papers (P120, P400, P600), then polished with pads and polycrystalline diamond suspensions (9 μm and 3 μm average particle size), followed by final polishing with a cloth and 3 μm polycrystalline diamond suspension. Phase identification was performed using X'Pert HighScore Plus software (version 5.1, Malvern Panalytical) [141] in combination with the ICDD PDF-4 database. Semi-quantitative phase

analysis was carried out through Rietveld refinement using the GSAS-EXPGUI package[142], [143], with structural models retrieved from the Crystallography Open Database (COD) [144]. Peak profiles were fitted with a pseudo-Voigt function (“type 2” profile shape model in GSAS[142]). Refinement included unit cell parameters and scale factors for each phase, together with the background (modelled as a shifted Chebyshev function with nine terms) and the zero shift.

2.3.2. Micromechanical testing

Cross-sections polished as described in Section 2.3.1 were also used to measure the microhardness of the coatings by depth-sensing micro-indentation (Micro-Combi Tester, Anton Paar Tritec, Corcelles, CH). Measurements were performed with a Vickers indenter under a 3 N applied load, using loading and unloading times of 30 s each and a 15 s hold at maximum load. The indentation curves were analysed according to the Oliver–Pharr method, in compliance with ISO 14577. For each sample, twenty indents were performed, and the resulting values were reported as mean ± standard deviation.

In addition to conventional micro-indentation, high-speed nanoindentation mapping [145] was carried out across the coating thickness, from the substrate to the outer surface, in order to map the mechanical properties and their local heterogeneity. This technique, which is based on the standard Oliver–Pharr procedure[146], incorporates significant improvements in hardware, electronics, and data acquisition, enabling rapid measurements with load–unload cycles as short as 1 to 5 seconds. High-speed mapping was performed with a G200 nanoindenter (KLA Corporation, Oak Ridge, TN, USA) equipped with a standard Berkovich indenter. The lateral extension and number of indents per sample were adjusted according to the balance between time and resolution, as detailed in Table 4. To avoid overlap of plastic zones, indent spacing was set to at least ten times the indentation depth, in accordance with the recommendations of Vignesh et al. and Phani et al. [147], [148]. Before mapping, grid continuous stiffness measurements were performed on each specimen to calibrate the load–displacement response, which was then used to determine the appropriate target load for the load-controlled mapping experiments. The selected parameters are listed in Table 4.

Table 4: High-speed nanoindentation mapping parameters.

Sample	**Target load (mN)**	**X Size (µm)**	**Y Size (µm)**	**Number of indents**	**Average depth (nm)**
Cantor	10	225	225	8100	240
Cantor+60TiC	2.3	200	280	56000	83
Al_0(CrMnFeNi)	8	440	184	15360	238
Al_0(CrMnFeNi)+ 60TiC	3	120	120	14400	96
Al_{10}(CrMnFeNi)	8	441	207	17280	236
Al_{14}(CrMnFeNi)	12	200	200	6400	260
Al_{14}(CrMnFeNi)+60TiC	3.5	242	273	65502	114
AlCuCrFeNi+60TiC	3	150	150	22500	95

Machine compliance and the indenter area function were calibrated using the same high-speed protocol applied for the actual indentation maps. After testing, the hardness data from the nanoindentation maps were processed using a Gaussian Mixture Model (GMM) algorithm to identify the mechanical phase composition of the coatings. This statistical approach, which assumes a normal distribution of the components, enabled the deconvolution of the hardness dataset through an expectation–maximization protocol.

Scratch testing was also performed on surfaces of the cermet coatings, ground and polished following the same procedure adopted for XRD analysis (Section 2.3.1). Tests were carried out with the Micro-Combi Tester using a conical diamond indenter (120° opening) with a spherical tip of 100 µm radius. For each sample, six scratch tracks were executed under a linearly increasing load ranging from 0.02 mN to 30 N, over a track length of 6 mm at a constant speed of 6 mm/min. The resulting tracks were examined by optical microscopy at 200× magnification to determine failure modes and to identify the critical loads associated with their onset. Complementary instrumental signals, including acoustic emission, tangential force (and corresponding friction coefficient), as well as total and residual penetration depths measured through pre- and post-scans with the same indenter at 0.02 N, were also acquired and used to support the identification of the critical loads.

Multi-cycle spherical nanoindentations were made on the same polished cross-sections using an NHT3 indenter (Anton Paar Tritec) equipped with a spherical diamond indenter with

a tip radius of 20 μm. The indentation protocol involved 25 loading / partial unloading cycles, with a quadratic increment of the peak load from 30 mN to 400 mN, unloading to 20% of each peak load, 10 s loading and unloading time in each cycle, 15 s hold at each maximum load, and 1 s pause between cycles. At least 20 multi-cycle indentations were performed on each sample.

The data were analysed to extract the indentation modulus (EIT) of each cycle.

The plane-strain indentation modulus (E^*) was computed as:

$$E^* = S/(2a_{eff})$$

where:

S = unloading slope, obtained by fitting the unloading portion of each cycle with a power-law and taking the first derivative at the beginning of unloading, according to the usual Oliver-Pharr analysis method.

a_{eff} = effective contact radius at the maximum load of each cycle = $\sqrt{2 \cdot R \cdot h_C - h_C^2}$

R = indenter radius

h_C = contact depth at the maximum load of each cycle, obtained via the Oliver–Pharr method.

In a spherical indentation experiment, the sample only starts to plasticize for sufficiently high loads. The E^* values obtained before the complete plasticization of the contact are unreliable, because all analysis models rely on the assumption of full plasticization during loading. Therefore, all the data points at contact depths below the level at which the slope of the E^* versus h_C trend was <0.5° were discarded. In fact, E^* should be independent of the contact depth when the condition for the applicability of the above equations is met, i.e. full plasticization of the contact region during loading.

To identify the true value of the indenter radius R at each contact depth h_C, accounting for deviations from the nominally ideal spherical geometry, the following approach was employed. First, the profile of the indenter was verified by optical profilometry in structured illumination mode (Confosurf profilometer, Confovis GmbH, Jena, Germany, installed on a Nikon Eclipse L150VN optical microscope operated with a 50× objective). By fitting the overall profile to a spherical shape, the radius was verified as 20 μm, however the profile was not completely spherical next to the tip due to fabrication imperfections. A calibration was therefore performed against a fused silica standard, performing multicycle indentations

and reversing the indentation modulus relation to obtain a_{eff} as a function of the h_C value at each cycle. The data were fitted to a polynomial relation.

When analysing the indentation data from the test samples, R was obtained from the fitting curves for h_C values within the contact depth range for the calibration. For h_C > 4 μm the radius was assumed to coincide with the nominal value of 20 μm. For intermediate h_C values, R was computed as a linear interpolation between 20 μm and the value at the maximum h_C attained in the calibration.

2.3.3. Wear testing

Ball-on-disc sliding wear tests were performed in unidirectional rotating mode according to ASTM G99, using the same polished samples prepared for XRD analyses and scratch testing. The counterparts consisted of 3 mm-diameter Al_2O_3 spheres, operated under an applied load of 10 N and a sliding distance of 5000 m for cermet, 5 N and 1000 m for metal coatings, a relative sliding speed of 0.4 m/s, and a track radius of 7 mm. These test parameters were selected because they generate sufficiently severe contact conditions to highlight possible mechanical issues within the coatings (e.g., lamellar delamination). Al_2O_3 was chosen as counterpart material because it is both hard and chemically inert, thereby simulating sliding against hardened surfaces or surfaces containing hard asperities, while minimizing (though not entirely eliminating) the tribo-chemical interactions that could otherwise complicate the interpretation of the results.

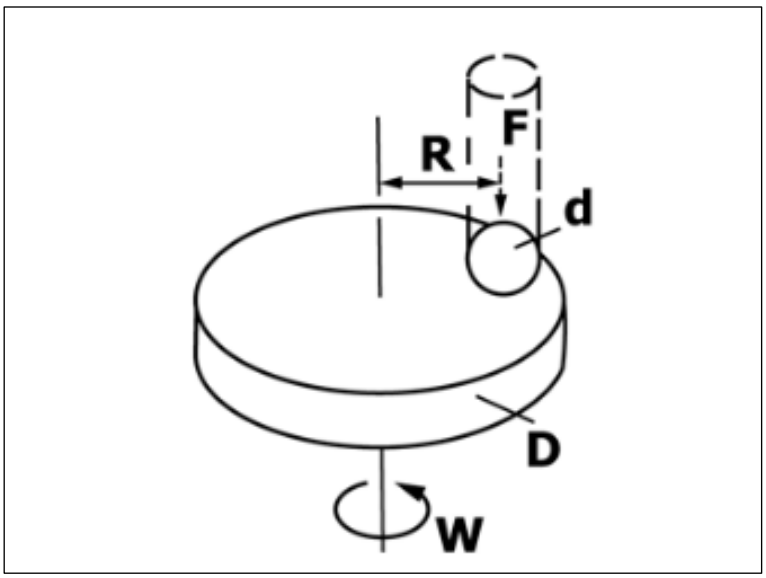

Figure 9: schematic diagram of ball-on-disk experimental set-up[149].

At least two wear tests were carried out on each sample. The friction coefficient was continuously measured during testing using a load cell. The volumetric wear loss of the counterpart ball was quantified by measuring the diameter of the circular wear scar with an optical microscope (Olympus GS30) and subsequently calculating the volume of the corresponding spherical cap. The volumetric wear loss of the coatings was instead determined using a structured illumination microscopy technique (ConfoSurf profilometer, Confovis GmbH, Jena, Germany), integrated with a Nikon Eclipse LV150N optical microscope equipped with a 10× objective. For each wear track, four profiles were acquired at angular positions spaced 90° apart along the circular path. For each position, the volume of the wear-groove sector was calculated with respect to the mean plane of the external unworn surface. The obtained sector volume was divided by the corresponding arc length to determine the average cross-sectional area of the groove, and this value was then multiplied by the total sliding track length to obtain the overall wear volume.The wear volumes were then converted into specific wear rates, calculated according to the relation $K = V/(F_N \cdot L)$, where V is the volumetric wear loss, F_N = normal force, L = total sliding distance.

High-stress abrasion tests were performed on as-deposited cermet plates using a steel-wheel apparatus (AP87, Ceramic Instruments, Sassuolo, Italy). In high-stress abrasion applications, unpolished specimens are typically employed, as low surface roughness is not generally required. During testing, the plates were pressed against a 200 mm-diameter Fe360A steel wheel with a normal load of 40.2 N. The wheel, rotating at 87 rpm, dragged along a tangential flow of FEPA80 Al_2O_3 abrasive (≈180 μm average particle size), supplied through an adjustable orifice at a controlled outflow rate of 110 g/min. A total of 100 wheel revolutions were performed for each test. A minimum of three abrasion tests were carried out for each coating. The volumetric wear loss of the abraded samples was measured by acquiring the wear track profiles using the same ConfoSurf profilometer mounted on the Nikon Eclipse LV150N optical microscope. Measurements were conducted in focus variation mode with a 5× objective and a ring-light illumination source, the latter chosen to compensate for the roughness of the abraded surfaces and the reduced numerical aperture of the objective. For each sample, a strip 2 mm in width was acquired along the entire length of the wear track. The wear volume of this strip was calculated with respect to the mean plane of the external unworn surface. The resulting value was then rescaled to the total nominal track width of 10 mm by multiplying the measured strip volume by a factor of five.

High-stress abrasion tests were not performed on metallic coatings for two main reasons. First, metallic overlays are generally not intended for service under the severe abrasion conditions reproduced by the steel-wheel test, making the results of such a test poorly representative of their typical operating environments. Second, it is well established that the steel-wheel configuration produces significant artefacts when applied to metallic materials: the severe contact conditions promote the excessive embedding of Al_2O_3 abrasive fragments into the metallic surface, artificially increasing the apparent wear resistance. This artefact does not occur in ceramic and cermet coatings, whose hardness and microstructure prevent such anomalous particle incorporation.

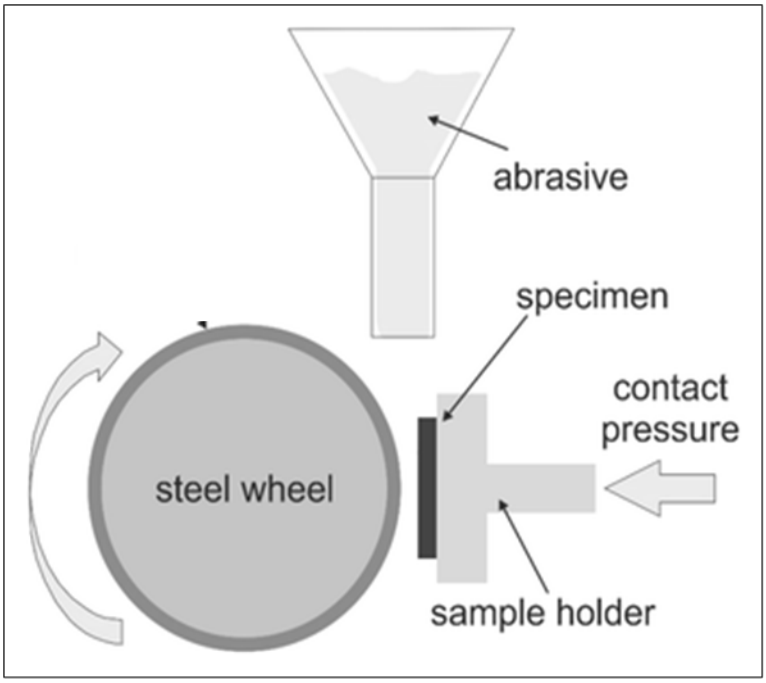

Figure 10: Schematic configuration of steel wheel abrasion test.

The surfaces and cross-sections of the worn samples, subjected to ball-on-disc and steel-wheel abrasion tests, were examined by SEM + EDX using the same equipment described in (2.3.1). Worn surfaces were observed at an inclination angle of 45° to achieve a clearer view of their morphology. Cross-sections prepared by metallographic cutting were hot mounted in transparent acrylic resin to facilitate the identification of the wear track. The grinding and polishing procedure was the same as reported in (2.3.1). In this case, the resin-mounted samples were sputter-coated with an ~10 nm-thick Au layer to ensure the required electrical conductivity.

2.3.4. Electrochemical corrosion testing

Electrochemical polarization tests were carried out on the polished surfaces of the coated samples, prepared as described in (2.4.1). A three-electrode cell was employed, consisting of the sample as the working electrode (exposed surface area: 1 cm²), an Ag/AgCl/KCl(sat.) reference electrode, and a Pt mesh counter electrode. The cell was filled with 300 mL of a 3.5% (wt./vol.) NaCl aqueous solution at room temperature under aerated conditions. After immersion for one hour, the samples were polarized from the open circuit potential (OCP) to –400 mV vs. OCP and subsequently swept from –400 mV vs. OCP to +1600 mV vs. OCP at a scan rate of 0.5 mV/s, to obtain the complete electrochemical polarization curve. Measurements were performed using a VersaStat 3 potentiostat (Ametek – Princeton Applied Research, USA). Two repetitions were conducted for each coating type.

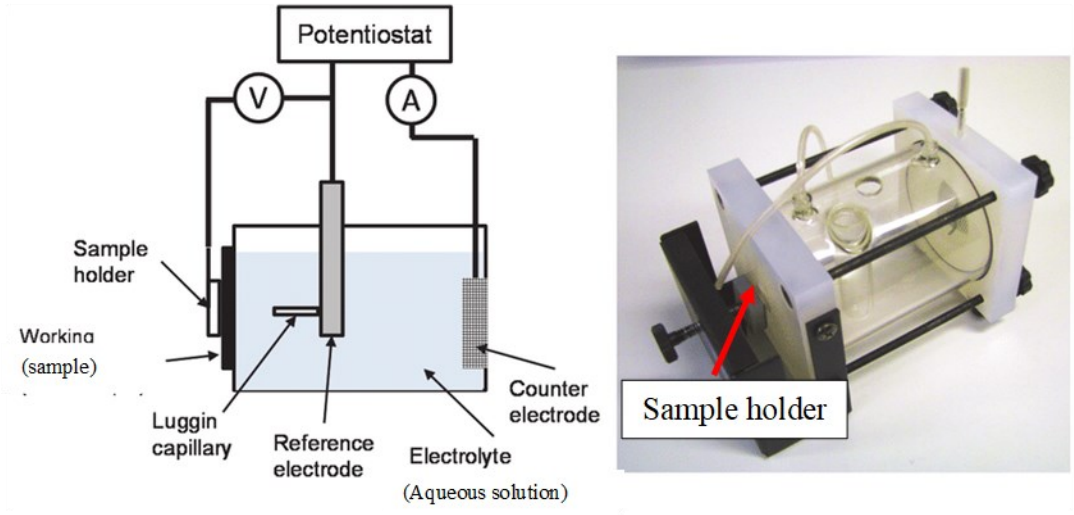

Figure 11: Scheme and picture of electrochemical cell.

The corrosion potential (E_{Corr}) and corrosion current density (I_{Corr}) were determined from the polarization curves using the Tafel extrapolation method, by fitting linear regions of the anodic and cathodic branches at overpotentials of at least |50| mV from the equilibrium potential.

After testing, the corroded samples were hot-mounted in acrylic resin as described in (2.3.3), ground and polished as in (2.3.1), and examined by SEM + EDX to evaluate the extent of corrosion damage across the cross-section.

For selected samples (see 3.6.b.), chronoamperometric tests were also conducted in the same 3.5% (wt./vol.) NaCl aqueous solution using the experimental setup described above. As before, the samples were allowed to stabilize in contact with the test solution for 1 hour, after which they were first polarized cathodically from the open-circuit potential

(OCP) to –0.4 V vs. OCP, ensuring that the initial surface condition matched that at the beginning of the electrochemical polarization sweep. Subsequently, the sample was polarized to a fixed potential, which was maintained for 3 hours while continuously monitoring the current flowing through the system (1 acquisition per second). The potential values were chosen so that the samples were polarized to overpotentials of +0.15 V, +0.20 V, and +0.25 V above their OCP value established after the cathodic pre-polarization.

Cross-sections of the samples after both electrochemical polarization and chronoamperometric testing, as well as selected surfaces after chronoamperometric testing, were examined by scanning electron microscopy (SEM: Quanta-200 and Nova NanoSEM 450, FEI Thermo Fisher Scientific, Eindhoven, NL) equipped with energy-dispersive X-ray (EDX) detectors (INCA, Oxford Instruments Analytical, Abingdon, UK; and Quantax-200 with X|Flash10 detector, Bruker Nano GmbH, Berlin, Germany). The samples were hot-mounted in a transparent acrylic resin using a mounting press, sectioned with a metallographic cutting disk, ground with SiC abrasive papers (P400 to P4000), and polished with a 3 μm polycrystalline diamond slurry followed by colloidal silica. Resin-mounted specimens were then sputter-coated with an approximately 10 nm Au layer to ensure adequate electrical conductivity.
Compound identification on the surfaces of samples subjected to chronoamperometric tests was further performed by micro-Raman spectroscopy (LabRAM HR Evolution, Horiba Jobin-Yvon) and X-ray Photoelectron Spectroscopy (XPS). Raman spectra were collected using a Nd:YAG laser (532 nm wavelength, 100 mW maximum output), with the beam attenuated to 10% of full power and focused onto the sample through a 100× objective. The signal was dispersed using a 600 g/mm diffraction grating and detected with a CCD camera equipped with a Peltier cooling system. Spectra consisted of 6 accumulations (for wear tracks) or 10 accumulations (for corroded surfaces), each with a 20 s acquisition time. XPS analyses were carried out using a custom-built system with a Mg-Kα X-ray source (photon energy 1253.6 eV) and a SPECS Phoibos HSA 3500 analyzer. The analysed area was approximately 1 mm² and located near the center of the tested surface. High-resolution spectra of all detectable elements were acquired with a 0.1 eV energy resolution. Binding energies for XPS interpretation were taken from the NIST XPS database[150].

3. Results and discussions

To facilitate clarity and readability, the presentation of results has been organized into two main sections, distinguishing metallic coatings (a. Metallic coatings) from cermet coatings (b. Cermet coatings). This division reflects not only the different nature of the investigated systems but also the specific characterization approaches adopted for each category.

Metallic coatings are primarily employed for their corrosion resistance and chemical stability, making them suitable for applications in marine environments, chemical processing equipment, and energy systems where protection against aggressive atmospheres is crucial. Accordingly, their characterization focused on phase constitution, microstructural features, and electrochemical behaviour.

Cermet coatings, on the other hand, are designed to combine high hardness and wear resistance with adequate toughness, which makes them particularly effective in severe mechanical environments. Typical applications include components exposed to abrasive or erosive conditions, such as turbine blades, valves, mining tools, and automotive parts. Their evaluation therefore required extended tribological and mechanical characterization, in addition to microstructural analysis.

This structure enables a more systematic discussion of the findings, allowing the reader to follow the rationale of the study while appreciating the differences in behaviour and performance between metallic and cermet-based protective solutions.

3. a. Metallic coatings

3.1. a. Size distribution, microstructure, and phase composition of the powders

All the powders exhibited very similar particle size distributions, which are quantitatively summarized in Table 5 through the 10th, 50th, and 90th percentile values. Overall, the distributions were found to be only slightly coarser than the nominal −45 + 10 µm range specified in 2.1. This small deviation is consistent with typical feedstock preparation by high-energy ball milling and subsequent classification, and it does not hinder the suitability of the powders for HVOF spraying.

Such granulometric characteristics ensure adequate flowability during powder feeding and stable in-flight behaviour, both of which are essential for achieving uniform deposition and consistent coating microstructures. In this sense, the values reported in Table 5 confirm that all feedstock powders were appropriately tailored for thermal spray processing and fall within the optimal range required for the HVOF technique.

Table 5 presents the characteristic percentile values of the particle size distributions for the HEBM feedstock powders, providing a reliable basis for subsequent correlation between powder properties and coating performance.

Table 5: Density by helium pycnometry and characteristic values (10th, 50th, and 90th percentiles) of the size distributions of the HEBM feedstock powders.

Powder	**Density [g/cm^3]**	**d_{10} [µm]**	**d_{50} [µm]**	**d_{90} [µm]**
Cantor	7.69	16	33	59
Al_0(CrMnFeNi)	7.65	21	37	61
Al_{10}(CrMnFeNi)	7.09	15	31	60
Al_{14}(CrMnFeNi)	6.86	15	31	56

The chemical composition determined by EDX analysis, reported in Table 6, showed that all powders generally matched their nominal alloy compositions, except for manganese. In most cases, the measured Mn content was lower than expected, which may indicate either a partial loss of this element during the powder preparation process or limitations in its quantitative detection by EDX. The only exception to this trend was the annealed Cantor powder, in which the manganese concentration was consistent with the nominal composition.

For all other principal alloying elements, the measured concentrations were in good agreement with the designed stoichiometries, thereby confirming the reliability of the powder preparation route.

Furthermore, traces of silicon were detected in some samples, as reported in Table 6. However, these are most likely artefacts rather than actual constituents of the powders. The presence of Si can be attributed to residual particles from the colloidal silica suspension used during the final polishing step of the samples, as described in 2.1. These particles may have become trapped in the resin between the powder grains, producing spurious EDX signals.

Table 6: Chemical composition of HEA powders and coatings (mass%, normalized to 100: mean ± standard deviation) measured by EDX analysis on areas imaged at 400×, and by inert gas fusion (oxygen, nitrogen) and oxygen combustion (carbon) for the powders.

Element	**Cantor**				
	Nominal	*Powder*	*HVOF*		
			Run1	*Run2*	*Run3*
Oxygen	-	0.15±0.07	11.16±0.24	10.89±0.76	12.19±0.51
Nitrogen	-	0.17±0.01	-	-	-
Carbon	-	0.28±0.01	-	-	-
Aluminum	-	0.17±0.02	0.11±0.07	0.15±0.09	0.15±0.12
Silicon	-	1.46±0.08	0.51±0.04	0.43±0.04	0.50±0.02
Chromium	18.54	20.02±0.04	17.38±0.20	17.54±0.27	17.27±0.18
Manganese	19.59	16.96±0.03	15.09±0.11	14.76±0.23	14.50±0.23
Iron	19.91	19.00±0.03	17.80±0.10	18.08±0.10	17.56±0.13
Cobalt	21.02	20.53±0.10	18.88±0.16	19.08±0.16	18.79±0.29
Nickel	20.93	21.26±0.08	19.08±0.34	19.06±0.26	19.03±0.24
Element	**Al_0(CrMnFeNi)**				
	Nominal	*Powder*	*HVOF*		
			Run1	*Run2*	*Run3*
Oxygen	-	0.55±0.01	10.34±0.10	9.95±0.30	8.98±0.12
Nitrogen	-	0.18±0.01	-	-	-
Carbon	-	0.04±0.01	-	-	-
Aluminum	-	0.20±0.06	0.17±0.06	0.23±0.10	0.23±0.11
Silicon	-	0.84±0.08	0.41±0.03	0.39±0.04	0.37±0.03
Titanium	-	0.14±0.08	0.12±0.04	0.08±0.03	0.09±0.02
Chromium	18.81	20.13±0.29	17.34±0.17	17.27±0.12	17.37±0.17
Manganese	24.85	18.37±0.35	19.12±0.12	19.06±0.15	19.69±0.14
Iron	40.41	43.14±0.26	38.21±0.17	38.52±0.21	38.61±0.18
Nickel	15.93	16.41±0.22	14.29±0.12	14.50±0.09	14.66±0.05
Element	**Al_{10}(CrMnFeNi)**				
	Nominal	*Powder*	*HVOF*		
			Run1	*Run2*	*Run3*
Oxygen	-	0.45±0.01	7.75±0.08	8.43±0.12	8.85±0.17
Nitrogen	-	0.18±0.05	-	-	-
Carbon	-	0.02±0.01	-	-	-
Aluminum	5.14	5.77±0.23	5.04±0.03	4.99±0.04	5.10±0.02
Silicon	-	1.06±0.30	0.20±0.02	0.15±0.03	0.21±0.02
Chromium	17.85	18.91±0.33	17.77±0.21	17.77±0.04	17.49±0.13
Manganese	23.57	18.80±0.03	17.56±0.21	17.07±0.27	16.69±0.16
Iron	38.33	39.33±0.20	37.30±0.19	37.26±0.08	37.30±0.07
Nickel	15.11	15.49±0.13	14.38±0.14	14.31±0.19	14.35±0.08
Element	**Al_{14}(CrMnFeNi)**				
	Nominal	*Powder*	*HVOF*		
			Run1	*Run2*	*Run3*
Oxygen	-	0.54±0.03	6.70±0.14	7.62±0.09	6.34±0.38
Nitrogen	-	0.18±0.01	-	-	-
Carbon	-	0.03±0.01	-	-	-
Aluminum	7.36	7.34±0.03	7.24±0.10	7.22±0.11	7.09±0.10
Silicon	-	1.07±0.14	0.16±0.02	0.15±0.02	0.19±0.01
Chromium	17.43	17.93±0.10	16.80±0.19	16.95±0.17	16.86±0.04
Manganese	23.02	19.43±0.38	17.40±0.33	16.56±0.06	18.22±0.22
Iron	37.44	39.19±0.39	37.79±0.42	37.59±0.17	37.50±0.21
Nickel	14.76	14.29±0.05	13.91±0.22	13.90±0.14	13.81±0.07

Table 7: Quantitative phase composition (in wt.%) of feedstock powders and coatings by Rietveld refinement of the XRD patterns

Sample	**FCC**	**BCC**	**MO**	**$M^{II}M^{III}_2O_4$**
Cantor powder	68.2±0.4	31.8±0.5	-	-
Cantor Run1 HVOF	74.3±0.1	-	7.1±0.6	18.6±0.4
Cantor Run2 HVOF	73.2±0.1	-	7.6±0.6	19.2±0.4
Cantor Run3 HVOF	73.8±0.1	-	7.5±0.6	18.7±0.5
Al_0(CrMnFeNi) Powder	66.0±0.3	34.0±0.3	-	-
Al_0(CrMnFeNi) Run1 HVOF	75.8±0.1	1.8±0.1	-	22.4±0.7
Al_0(CrMnFeNi) Run2 HVOF	73.2±0.1	1.5±0.1	-	25.4±0.6
Al_0(CrMnFeNi) Run3 HVOF	77.8±0.7	-	-	22.2±0.7
Al_{10}(CrMnFeNi) Powder	37.3±0.6	62.7±0.2	-	-
Al_{10}(CrMnFeNi) Run1 HVOF	51.7±0.2	34.3±0.2	-	14.0±0.6
Al_{10}(CrMnFeNi) Run2 HVOF	52.7±0.3	26.4±0.2	-	20.9±0.7
Al_{10}(CrMnFeNi) Run3 HVOF	55.9±0.2	23.3±0.2	-	20.8±0.5
Al_{14}(CrMnFeNi) Powder	42.9±0.7	57.1±0.3	-	-
Al_{14}(CrMnFeNi) Run1 HVOF	27.8±0.3	60.7±0.1	-	11.6±0.7
Al_{14}(CrMnFeNi) Run2 HVOF	30.4±0.3	54.1±0.1	-	15.4±0.7
Al_{14}(CrMnFeNi) Run3 HVOF	22.2±0.3	66.2±0.1	-	11.6±0.8

SEM micrographs shown in Figure 12A, C, E, and G reveal that the as-milled powder particles exhibited an irregular shape, with some particles displaying visible cracks. Upon closer examination in Figure 12B, D, F, and H, each particle was observed to consist of tightly adherent thin sheets of material. The particles contained a uniform distribution of sub-micrometric dark phases, which were rich in oxygen and occasionally contained traces of sulphur, as reported in Figure 13. Consistently, chemical analysis by inert gas fusion reported in Table 6 showed that all powders contained approximately 0.2 to 0.5 weight percent oxygen, along with 0.17 to 0.18 weight percent nitrogen.

The proportion of metallic elements within these oxide inclusions sometimes differed from the average composition of the alloy (Table 6). For example, spectra 1 and 4 in Figure 13C and spectrum 4 in Figure 13B showed a higher concentration of Mn than the corresponding base alloy. In a few cases, traces of sulphur were also detected (Figure 13A – spectrum 2; Figure 13C – spectra 1 and 6). These inclusions likely resulted from the fragmentation of oxidized shells on the surface of the original particles employed in the high-energy ball

milling process, and/or from the uptake of trace amounts of contaminants within the vials, despite the use of an inert atmosphere environment during the process.

Apart from these inclusions, the particles were chemically quite homogeneous, indicating extensive interdiffusion during HEBM. Nevertheless, a few regions exhibited different contrasts in backscattered electron imaging as seen in Figure 12B, D, F, and H. Figure 13 indicates that most of these areas were enriched in chromium, suggesting that chromium had more difficulty in diffusing together within the other alloy elements, although some regions were enriched in other elements, such as nickel.

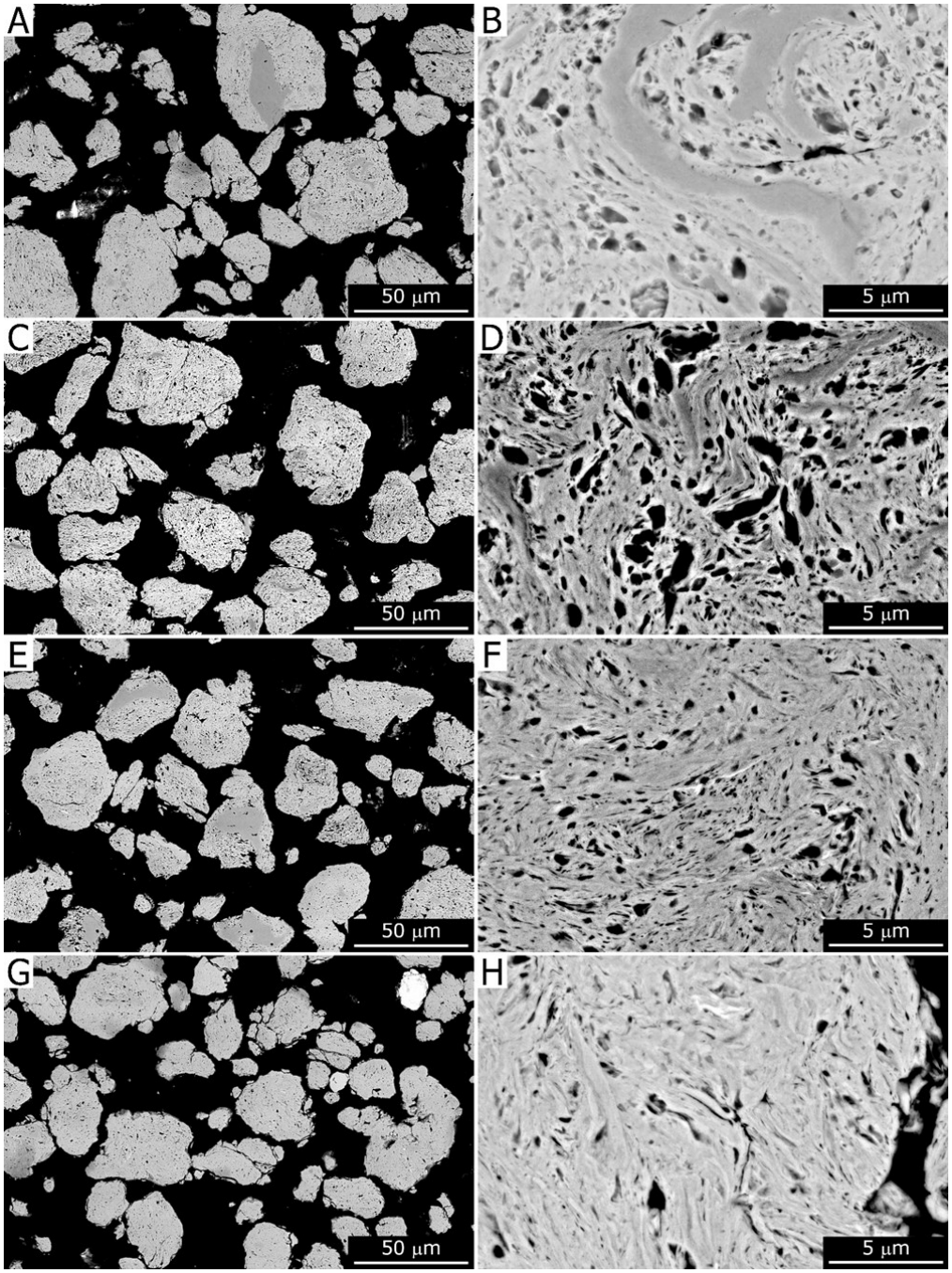

Figure 12: Cross-sectional SEM micrographs (backscattered electrons) of the Cantor (A, B), Al_0(CrMnFeNi) (C, D), Al_{10}(CrMnFeNi) (E, F), and Al_{14}(CrMnFeNi) (G, H) powders, HVOF spray-grade (A, C, E, G: overviews; B, D, F, H: details).

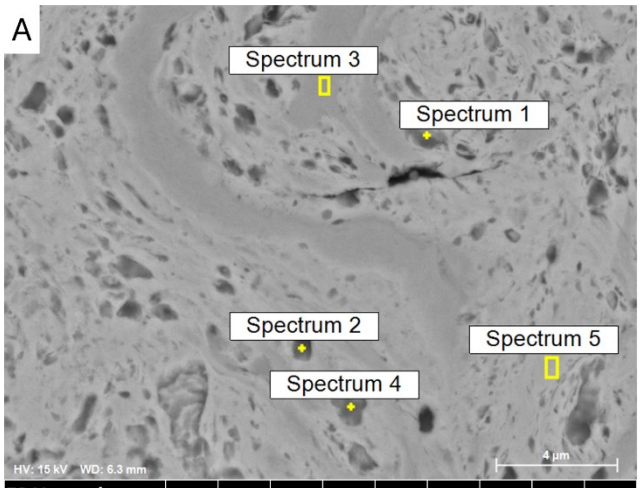

EDX results (wt.%)	O	Al	Si	S	Cr	Mn	Fe	Co	Ni
Spectrum 1	4.0	0.1	0.4	-	5.4	68.5	15.6	3.7	2.3
Spectrum 2	6.7	0.0	0.3	0.4	19.1	20.2	20.1	20.7	12.5
Spectrum 3	1.1	0.0	0.5	-	72.0	0.2	25.2	0.5	0.5
Spectrum 4	6.9	0.0	0.4	-	16.4	23.6	22.2	14.9	15.5
Spectrum 5	1.4	0.1	0.4	-	18.7	16.7	18.3	23.6	20.8

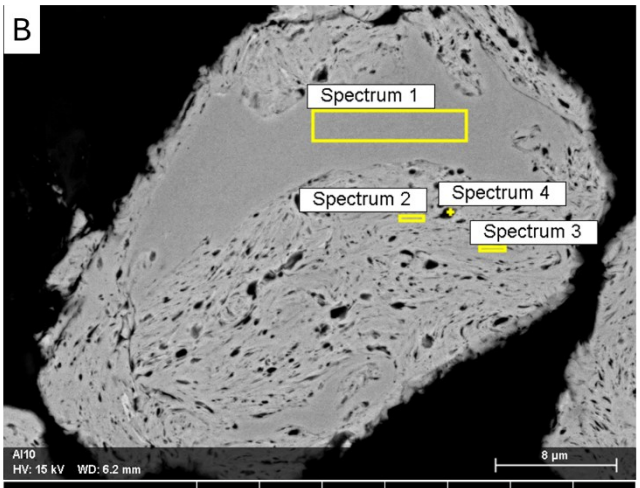

EDX results (wt.%)	O	Al	Si	Cr	Mn	Fe	Ni
Spectrum 1	1.3	-	0.4	74.3	-	23.6	0.4
Spectrum 2	1.0	5.8	0.2	17.7	20.7	38.8	15.7
Spectrum 3	1.1	1.5	0.5	60.3	3.4	28.8	4.4
Spectrum 4	8.2	2.7	6.0	11.7	23.5	33.0	14.9

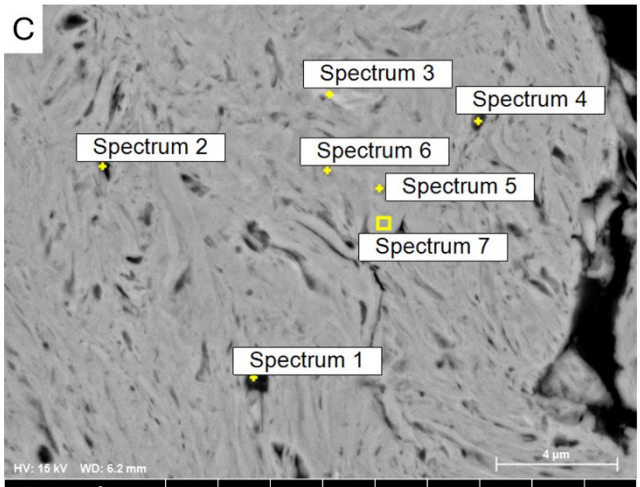

EDX results (wt.%)	O	Al	Si	S	Cr	Mn	Fe	Ni	Zn
Spectrum 1	9.4	3.4	0.3	0.3	13.4	33.4	29.7	10.0	0.2
Spectrum 2	2.1	4.0	0.5		16.0	11.1	52.4	13.8	
Spectrum 3	0.4	4.5	0.1		5.5	8.0	16.7	64.8	
Spectrum 4	5.2	5.3	3.8		14.2	22.2	35.2	14.2	
Spectrum 5	2.0	7.3	0.9		19.6	14.6	39.1	16.4	
Spectrum 6	2.8	8.3	0.1	0.4	10.3	24.8	40.2	13.1	
Spectrum 7	1.0	6.7	0.3		22.5	19.8	35.5	14.1	

Figure 13: Cross-sectional backscattered-electron SEM micrographs and quantitative EDX analyses of the feedstock powders: Cantor (A), Al_{10}(CrMnFeNi) (B) and Al_{14}(CrMnFeNi) (C).

XRD patterns shown in Figure 14 indicated that the as-milled powders, including the Cantor and Al_0(CrMnFeNi) compositions, contained the BCC phase, with all diffraction peaks appearing very broad. In contrast, the annealed Cantor powder shown in Figure 14A exhibited substantially sharper diffraction peaks. The intensity of the BCC peaks decreased relative to the as-milled powder as reported in Table 7, while weak diffraction peaks

corresponding to a tetragonal σ-phase appeared, with a quantified amount of approximately 6 wt.%.

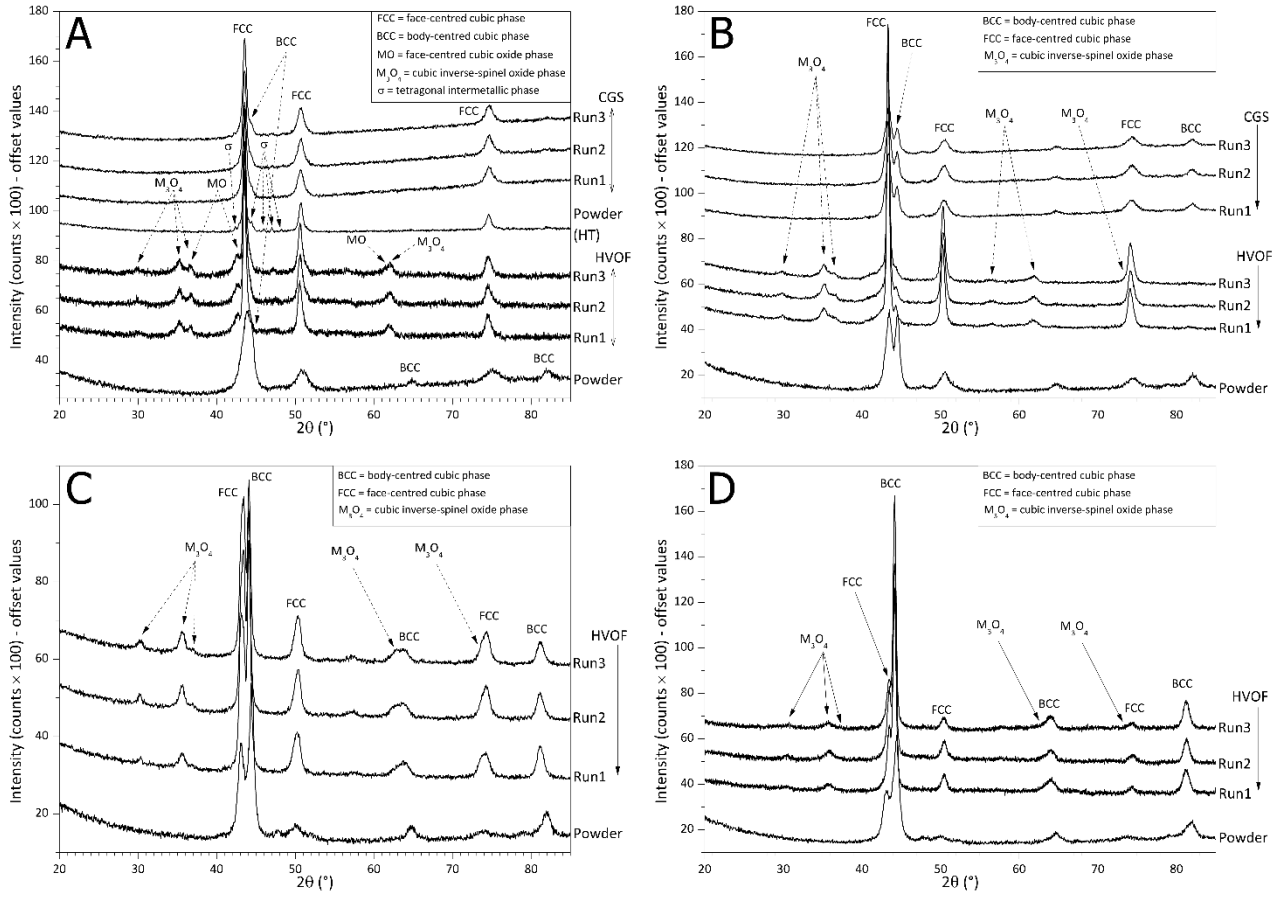

Figure 14: X-ray diffraction pattens of the feedstock powders and the coatings: Cantor (A), Al_0(CrMnFeNi) (B), Al_{10}(CrMnFeNi) (C), Al_{14}(CrMnFeNi) (D).

The structural and microstructural analyses of the powders confirmed that the high-energy ball milling (HEBM) process induced significant lattice strain and microstructural refinement. In the as-milled Cantor and Al_0(CrMnFeNi) powders, the presence of a body-centered cubic (BCC) phase alongside the expected face-centered cubic (FCC) structure suggests that the severe plastic deformation during HEBM partially destabilized the FCC lattice. This effect, together with incomplete interdiffusion, particularly of chromium, which tends to form BCC-rich regions, led to the coexistence of multiple phases, as evidenced by the broad diffraction peaks in Figure 14. The powder morphology also supported this interpretation: welded and deformed lamellae, as well as microcracks within particles, indicate repeated cycles of fracturing and cold-welding during milling. Furthermore, oxygen- and sulfur-containing inclusions likely originated from the fragmentation of native surface oxides or slight contamination during milling, as even trace amounts of oxygen in the inert-gas atmosphere can react with freshly exposed metallic surfaces.

3.2. a. Microstructure and phase composition of the coatings

The HVOF deposition of the four HEA powders resulted in reasonably high deposition efficiencies, ranging from 50% to 60%. These values were nonetheless lower than the approximately 68% efficiency obtained with the commercial Stellite-6 powder, as reported in Table 8. Quantitative results obtained from image analysis, also summarized in Table 8, indicated that the HVOF-deposited HEA coatings were very dense, with porosities often well below 1% and lower than those measured for the Stellite reference. The coatings produced by cold gas spraying exhibited similarly low porosities, generally below 1%.

The results further suggested that there were no major differences among the HVOF-sprayed coatings deposited using the same feedstock powder but under different process parameters. From the infrared pyrometer data, the maximum temperature (Tmax) reached during spraying was extrapolated. The results showed no significant differences among the different powders or between the various runs, with Tmax values ranging between 400 and 500 °C. A qualitative comparison of the microstructures of all coatings, as illustrated in Figure 15, Figure 16, Figure 17 and Figure 18, confirmed this observation. For this reason, only selected deposition conditions are presented in Figure 19A–H to facilitate comparison.

Table 8: Porosity, thickness, deposition efficiency and oxide inclusion content (mean ± standard deviation) of all the coatings according to image analysis, and deposition efficiency.

Sample ID	Porosity (vol.%)	Thickness [µm]	Thickness/pass [µm]	Deposition efficiency (%)	Oxide Inclusions (vol.%)
Cantor Run1	0.24±0.05	284±11	7.3	54.8	41.8±3.0
Cantor Run2	0.21±0.06	281±22	7.2	54.2	43.5±3.1
Cantor Run3	0.17±0.03	315±23	8.1	64.4	45.4±3.1
Al_0(CrMnFeNi) Run1	0.69±0.24	305±18	7.8	61.0	33.7±3.2
Al_0(CrMnFeNi) Run2	0.84±0.33	298±14	7.6	59.4	36.8±1.5
Al_0(CrMnFeNi) Run3	0.35±0.08	264±14	6.8	56.7	29.6±2.0
Al_{10}(CrMnFeNi) Run1	0.04±0.02	263±10	6.7	59.7	31.7±0.7
Al_{10}(CrMnFeNi) Run2	0.02±0.01	259±7	6.6	57.5	33.1±1.9
Al_{10}(CrMnFeNi) Run3	0.01±0.01	252±8	6.5	56.5	33.6±3.7
Al_{14}(CrMnFeNi) Run1	0.37±0.22	264±13	6.8	52.3	22.2±2.0
Al_{14}(CrMnFeNi) Run2	0.46±0.17	252±11	6.5	50.4	25.9±2.0
Al_{14}(CrMnFeNi) Run3	0.45±0.15	255±12	6.5	52.8	19.1±3.1
Stellite	0.94±0.51	523±21	19.4	68.4	4.3±1.2

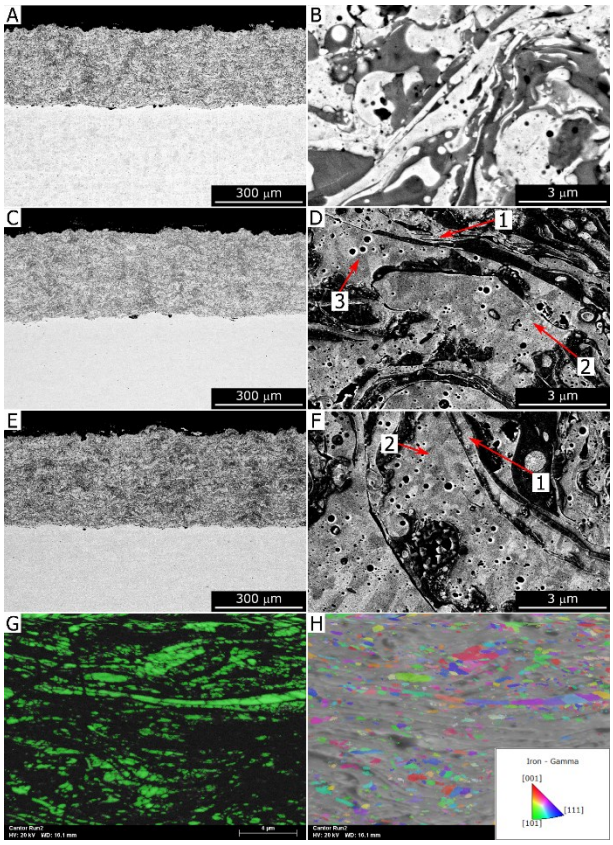

Figure 15: Cross-sectional backscattered-electron SEM micrographs of the HVOF Cantor Run1 (A, B), Run2 (C, D), and Run3 (E, F) coatings, and EBSD maps of the HVOF Cantor Run2 sample: phase map (G) and inverse pole figure along the x-direction – IPFX (H). Label 1 = columnar grains, 2 = fine equiaxed grains, 3 = coarser equiaxed grains.

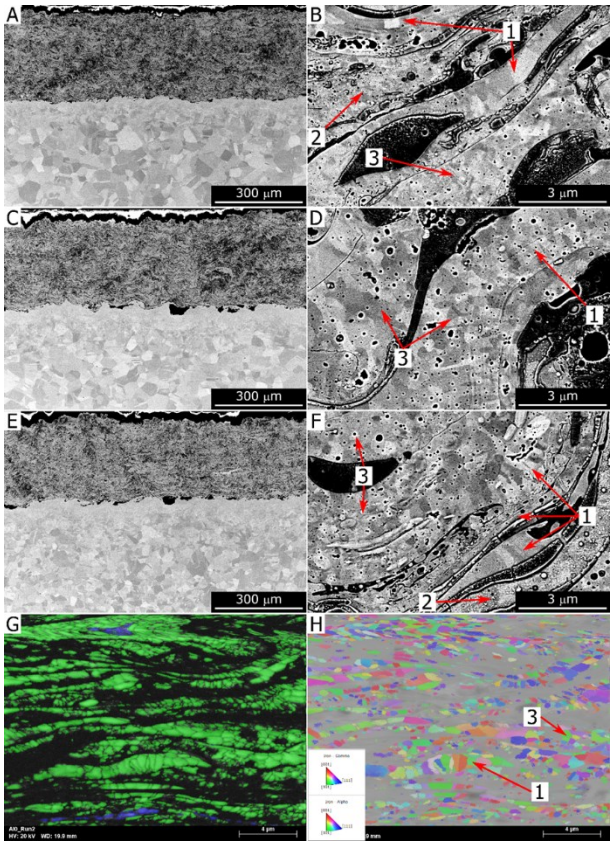

Figure 16: Cross-sectional backscattered-electron SEM micrographs of the HVOF Al_0(CrMnFeNi) Run1 (A, B), Run2 (C, D), and Run3 (E, F) coatings, and EBSD maps of the HVOF Al_0(CrMnFeNi) Run2 sample: phase map (G) and inverse pole figure along the x-direction – IPFX (H). Label 1 = columnar grains, 2 = fine equiaxed grains, 3 = coarser equiaxed grains.

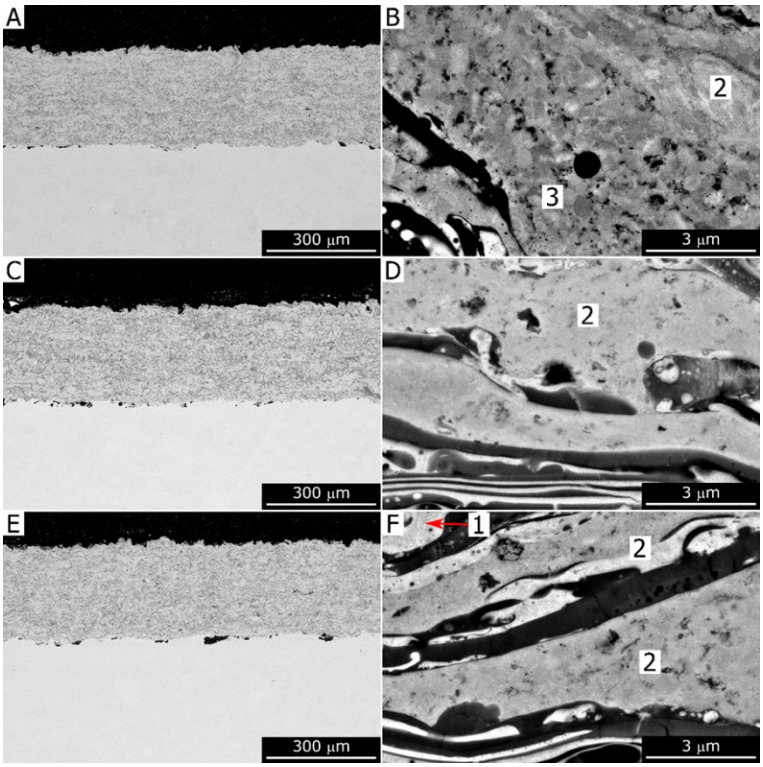

Figure 17: Cross-sectional backscattered-electron SEM micrographs of the HVOF Al_{10}(CrMnFeNi) Run1 (A, B), Run2 (C, D), and Run3 (E, F) coatings. Label 1 = columnar grains, 2 = fine equiaxed grains, 3 = coarser equiaxed grains.

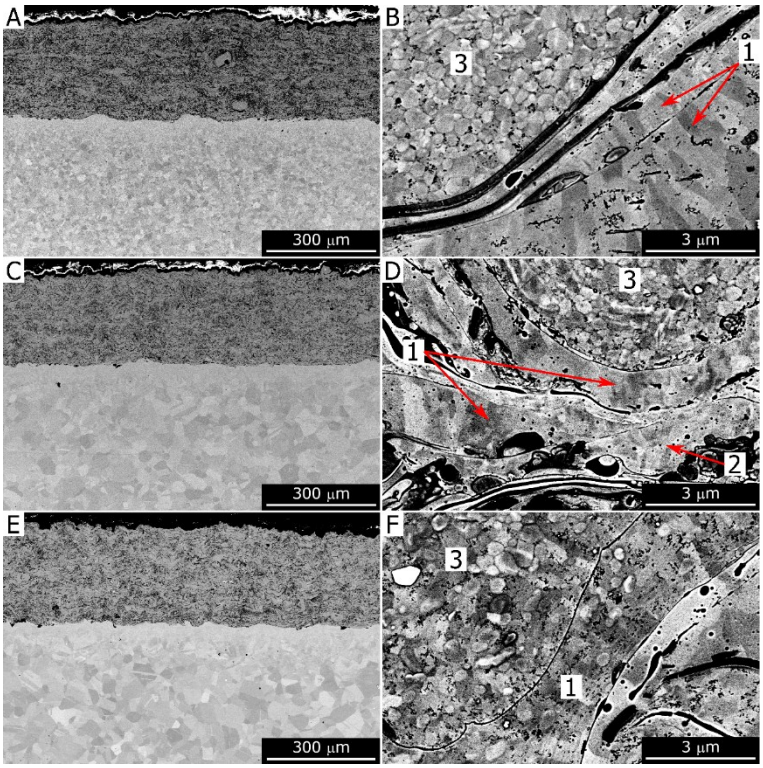

Figure 18: Cross-sectional backscattered-electron SEM micrographs of the HVOF Al_{14}(CrMnFeNi) Run1 (A, B), Run2 (C, D), and Run3 (E, F) coatings. Label 1 = columnar grains, 2 = fine equiaxed grains, 3 = coarser equiaxed grains.

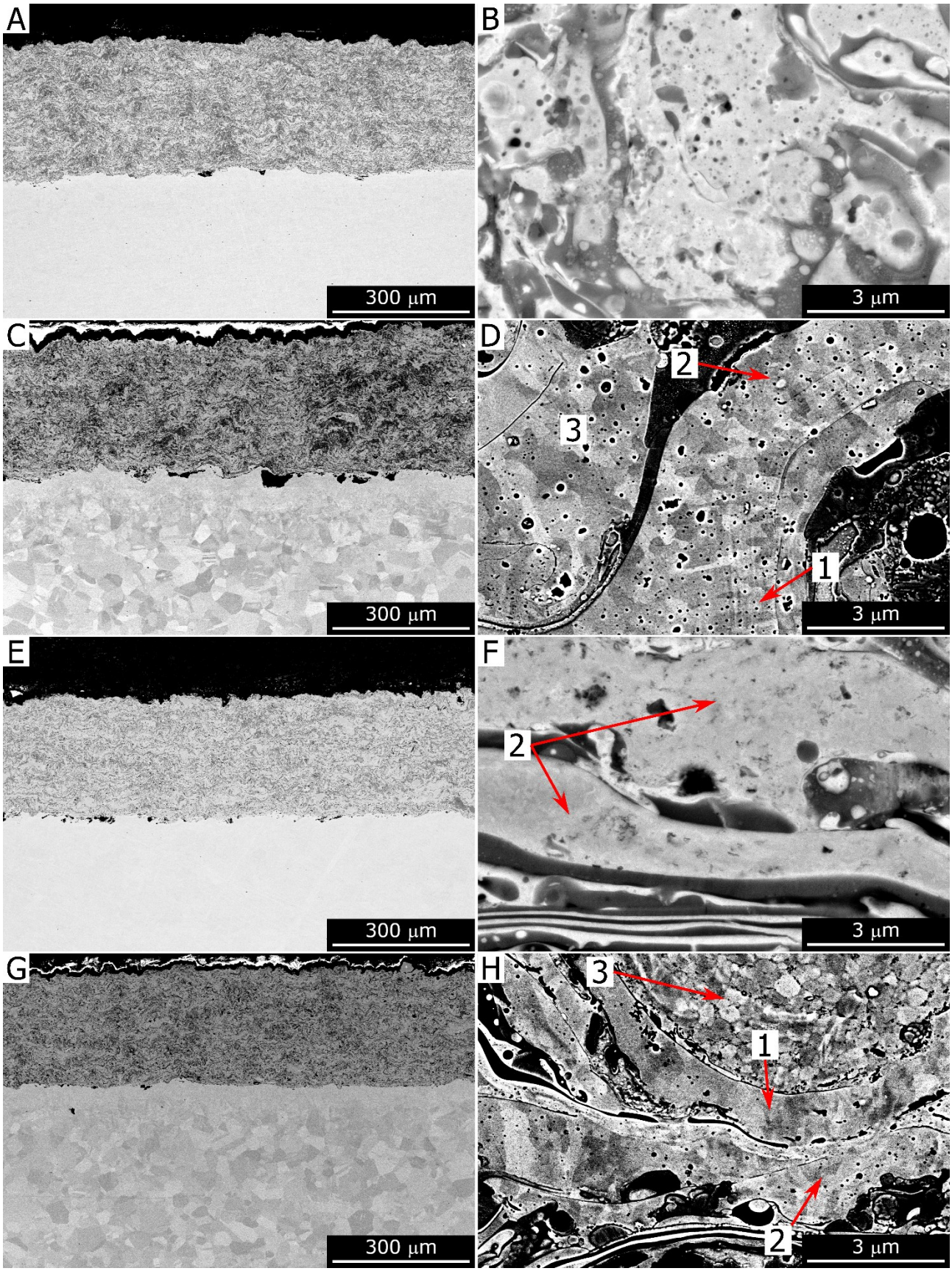

Figure 19: Cross-sectional backscattered-electron SEM micrographs of the HVOF Cantor Run2 (A, B), Al_0(CrMnFeNi) Run2 (C, D), Al_{10}(CrMnFeNi) (E, F), and Al_{14}(CrMnFeNi) (G, H) coatings. Label 1 = columnar grains, 2 = fine equiaxed grains, 3 = coarser equiaxed grains.

The HVOF-sprayed HEA coatings also contained a substantial amount of oxide inclusions. Image analysis performed on the SEM micrographs indicated that the oxide fraction ranged from approximately 20 to 45 volume percent, as reported in Table 8. Quantitative EDX analyses, summarized in Table 6, consistently showed oxygen contents ranging from 6 to 11 wt.%. Interestingly, the HVOF-sprayed Stellite coating exhibited a much lower oxide content of about 4 vol.%, along with a correspondingly lower oxygen content measured by quantitative EDX analysis, equal to 2.48 ± 0.19 wt.%.

A more detailed characterization of the oxides in the HVOF HEA coatings can be found in Figure 20, Figure 21, Figure 22 and Figure 23. EDX spectra revealed the formation of mixed oxides in the HVOF-sprayed Cantor coating, as shown in the Supplementary Material in Figure 20 (spectra 1 to 8), and in the HVOF-sprayed Al_0(CrMnFeNi) coating, illustrated in Figure 21 (spectra 1 and 3). In contrast, the HVOF-sprayed Al_{10}(CrMnFeNi) and Al_{14}(CrMnFeNi) coatings, presented in Figure 22 and Figure 23 respectively, exhibited two clearly distinguishable types of oxides. The Al-rich oxides, corresponding to spectra 4 to 6 in Figure 22 and spectrum 4 in Figure 23, displayed a darker contrast in backscattered electron imaging mode. Conversely, mixed oxides with lower aluminium content, corresponding to spectra 7 to 9 in Figure 22 and spectrum 5 in Figure 23, appeared brighter.

The oxides within the HVOF coatings also showed two distinct morphologies: elongated stringers located along the lamellar boundaries, and rounded inclusions embedded within the lamellae. Examples of these rounded inclusions can be observed in Figure 21 (spectrum 1) and Figure 22 (spectrum 9). A portion of the rounded oxide inclusions may have originated from oxides already present in the feedstock powders, as discussed previously. However, many of these inclusions likely formed as a result of in-flight oxidation during the spraying process. The amount and morphology of oxide inclusions varied with composition: mixed (Cr,Fe,Mn,Ni)-oxides dominated in the Cantor and Al_0(CrMnFeNi) coatings, while thin, Al-rich oxide stringers were more frequent in Al_{10} and Al_{14}(CrMnFeNi) coatings, likely contributing to their reduced overall oxygen content. The oxide morphologies, spherical intra-lamellar inclusions and elongated inter-lamellar stringers, correspond to oxidation both during flight and immediately after impact, consistent with literature on thermal spray oxidation mechanisms.

During flight, the temperature of the particles approached or even exceeded 2000 °C, allowing oxides that developed on the surface of molten droplets to exist in a liquid state. Turbulent flow within the molten metal could then drag these oxides into the interior of the droplet, leading to the mixing of two immiscible liquid phases of different densities, the

molten oxide and the molten metal. As a result, the oxides adopted a spherical morphology, as previously described in reference[151]. In contrast, the interlamellar stringers are believed to have originated either from oxide scales that formed in flight but were not drawn into the molten particle, or from post-impact oxidation of the solidified lamellae, also as described in reference[151].

Examining the microstructure of the metallic phase revealed two distinct features within the lamellae of the Al-containing coatings, namely Al_{10}(CrMnFeNi) and Al_{14}(CrMnFeNi). The darker phase, as shown in Figure 22 (spectrum 1) and Figure 23 (spectrum 1), was richer in aluminium, while the surrounding matrix, illustrated in Figure 22 (spectra 2 and 3) and Figure 23 (spectra 2 and 3), contained lower amounts of aluminium. It is likely that, in these two-phase systems, comprising a body-centered cubic (BCC) and a face-centered cubic (FCC) structure, as reported in Table 7, the Al-rich regions correspond to the BCC phase, whereas the Al-poor regions correspond to the FCC phase. This dual-phase structure, consistent with the thermodynamic tendency of Al to stabilize BCC lattices, persisted despite rapid cooling.

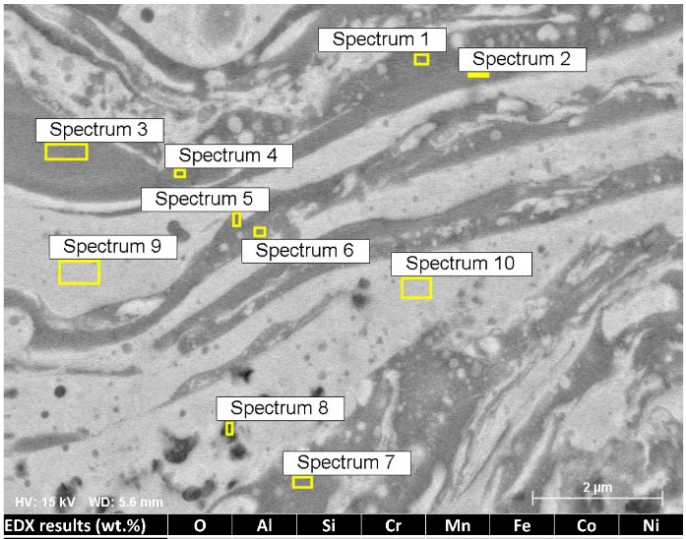

EDX results (wt.%)	O	Al	Si	Cr	Mn	Fe	Co	Ni
Spectrum 1	18.7	0.5	0.8	24.4	22.2	13.3	10.4	9.6
Spectrum 2	19.9	0.3	0.8	23.8	18.6	17.0	11.7	7.9
Spectrum 3	20.1	0.1	0.3	19.0	17.4	18.7	14.6	9.7
Spectrum 4	18.1	0.1	0.5	18.7	12.4	19.9	16.8	13.6
Spectrum 5	14.1	-	0.4	20.7	20.7	17.6	14.3	12.2
Spectrum 6	16.8	-	0.5	20.5	14.5	17.4	15.9	14.5
Spectrum 7	18.5	0.1	0.4	18.2	17.0	16.6	15.3	13.9
Spectrum 8	6.3	-	0.9	19.1	21.5	16.6	17.9	17.6
Spectrum 9	2.0	-	0.2	17.2	13.7	20.7	23.1	23.1
Spectrum 10	2.3	-	0.3	18.1	16.5	20.2	21.9	20.8

Figure 20: Cross-sectional backscattered-electron SEM micrograph of the HVOF Cantor Run2 coating with quantitative results from EDX analyses performed at the locations marked on the micrograph.

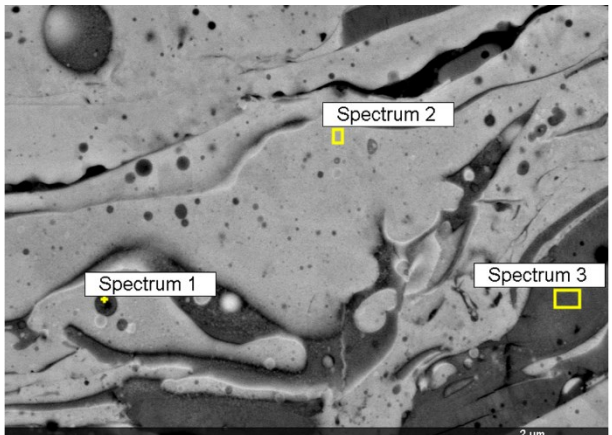

EDX results (wt.%)	O	Al	Si	Cr	Mn	Fe	Ni
Spectrum 1	13.7	0.5	0.2	18.6	16.2	37.5	13.4
Spectrum 2	2.8	0.1	0.1	14.3	8.2	54.1	20.5
Spectrum 3	27.5	0.2	0.2	16.6	14.7	35.2	5.6

Figure 21: Cross-sectional backscattered-electron SEM micrograph of the HVOF Al_0(CrMnFeNi) Run2 coating with quantitative results from EDX analyses performed at the locations marked on the micrograph.

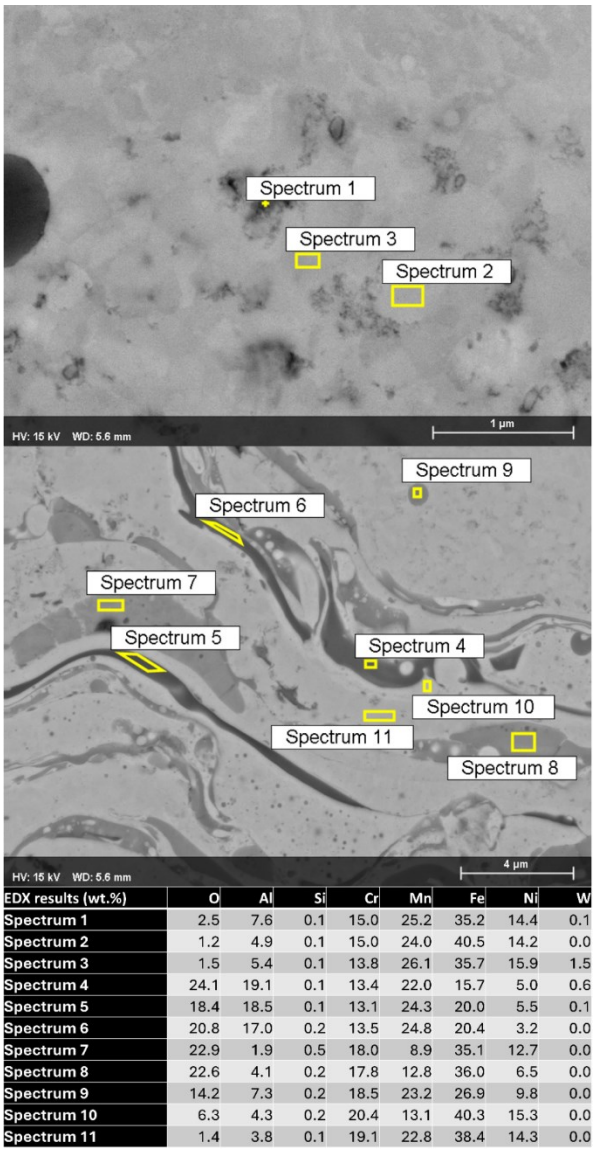

EDX results (wt.%)	O	Al	Si	Cr	Mn	Fe	Ni	W
Spectrum 1	2.5	7.6	0.1	15.0	25.2	35.2	14.4	0.1
Spectrum 2	1.2	4.9	0.1	15.0	24.0	40.5	14.2	0.0
Spectrum 3	1.5	5.4	0.1	13.8	26.1	35.7	15.9	1.5
Spectrum 4	24.1	19.1	0.1	13.4	22.0	15.7	5.0	0.6
Spectrum 5	18.4	18.5	0.1	13.1	24.3	20.0	5.5	0.1
Spectrum 6	20.8	17.0	0.2	13.5	24.8	20.4	3.2	0.0
Spectrum 7	22.9	1.9	0.5	18.0	8.9	35.1	12.7	0.0
Spectrum 8	22.6	4.1	0.2	17.8	12.8	36.0	6.5	0.0
Spectrum 9	14.2	7.3	0.2	18.5	23.2	26.9	9.8	0.0
Spectrum 10	6.3	4.3	0.2	20.4	13.1	40.3	15.3	0.0
Spectrum 11	1.4	3.8	0.1	19.1	22.8	38.4	14.3	0.0

Figure 22: Cross-sectional backscattered-electron SEM micrographs of the HVOF Al_{10}(CrMnFeNi) Run2 coating with quantitative results from EDX analyses performed at the locations marked on the micrographs.

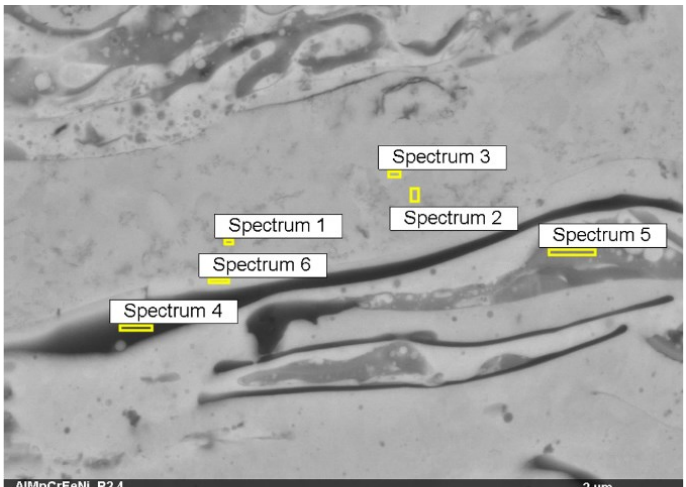

EDX results (wt.%)	O	Al	Si	Cr	Mn	Fe	Ni
Spectrum 1	2.1	8.8	0.2	21.7	20.3	33.8	13.0
Spectrum 2	1.4	7.2	0.2	15.8	23.1	37.2	15.1
Spectrum 3	1.3	6.8	0.2	18.2	21.1	39.7	12.8
Spectrum 4	22.0	28.4	0.1	12.6	13.7	18.2	5.1
Spectrum 5	21.0	7.9	0.2	15.7	9.7	33.2	12.4
Spectrum 6	6.2	10.6	0.2	20.1	17.9	33.5	11.4

Figure 23: Cross-sectional backscattered-electron SEM micrograph of the HVOF Al_{14}(CrMnFeNi) Run2 coating with quantitative results from EDX analyses performed at the locations marked on the micrograph.

The HVOF process fundamentally altered the structure of the feedstock powders by melting most of the particles and rapidly resolidifying them into lamellar splats.

The HVOF-sprayed coatings, illustrated in Figure 19B, D, F, and H as well as in Figure 15, Figure 16, Figure 17 and Figure 18, exhibited three distinct types of microstructural features. The first consisted of thin, spread-out lamellae, mostly displaying a columnar grain structure, as shown in Figure 19B, D, F, and H and in Figure 15, Figure 16, Figure 17 and Figure 18, identified as label 1. The second type comprised less-flattened lamellae that often contained small equiaxed grains, identified as label 2. The third type included poorly flattened or non-flattened particles characterized by coarse equiaxed grains, identified as label 3.

These features, illustrated in Figure 15 to Figure 23, reflect a gradient of solidification conditions, from planar to cellular growth regimes, driven by local temperature and impact dynamics. The extremely high cooling rates associated with HVOF spraying suppressed solute segregation and promoted solute trapping, resulting in chemically homogeneous metallic lamellae, especially evident in the Cantor coatings. In contrast, the Al-containing coatings exhibited two metallic phases with distinct contrasts in backscattered electron imaging: an Al-rich BCC phase and an Al-poor FCC phase.

The phase composition of the HVOF-sprayed coatings underwent significant changes compared to that of the corresponding feedstock powders. In the case of the HVOF-sprayed Cantor coatings, only the face-centered cubic (FCC) phase was detected, as shown in Figure 14A and summarized in Table 7, with no evidence of the body-centered cubic (BCC) phase that was originally present in the feedstock material. The HVOF-sprayed Al_0(CrMnFeNi) coatings were predominantly composed of the FCC phase, although a minor peak corresponding to the BCC phase was also observed, as reported in Figure 14B and Table 7. In the Al_{10}(CrMnFeNi) coatings, the X-ray diffraction patterns revealed similarly intense peaks for both the FCC and BCC phases, as illustrated in Figure 14C and Table 7. For the Al_{14}(CrMnFeNi) coatings, the BCC phase became predominant, accounting for most of the structure, while the FCC phase represented approximately 20 to 30 weight percent, as indicated in Figure 14D and Table 7.

In addition to the metallic phases, the XRD patterns of the HVOF-sprayed coatings displayed diffraction peaks corresponding to oxide phases. Spinel-type oxides with the general formula $M^{II}M^{III}{}_2O_4$, together with cubic MO oxides, were identified in the HVOF-sprayed Cantor coatings, as shown in Figure 14A and reported in Table 7. The Alx(CrMnFeNi) coatings exhibited only $M^{II}M^{III}{}_2O_4$-type oxides, as presented in Figure 14B to D and Table 7. The quantitative analysis further revealed that the amount of the $M^{II}M^{III}{}_2O_4$ oxide phase decreased progressively with increasing aluminium content in the alloy, from x = 0 to x = 14, as summarized in Table 7.

The phase composition of the HVOF-sprayed coatings closely approached the equilibrium phases expected near the alloy solidus temperatures, while reflecting the influence of rapid solidification. The Cantor and Al_0(CrMnFeNi) coatings were primarily FCC, with only minor traces of BCC, whereas the Al_{10}(CrMnFeNi) and Al_{14}(CrMnFeNi) coatings exhibited both FCC and BCC phases, the latter becoming predominant as aluminium content increased. The persistence of some FCC phase in the Al_{14}(CrMnFeNi) composition, despite equilibrium predictions favouring only BCC, suggests incomplete phase transformation due to kinetic constraints during the rapid solidification process. The evolution of the oxide composition, from mixed transition-metal oxides in the Cantor coating to Al-rich oxides in the Al-containing samples, is consistent with the higher affinity of aluminium for oxygen. However, the Al-rich oxides detected by SEM/EDX and their absence in the XRD patterns can be reconciled by considering several concurrent effects. The atomic scattering factor of aluminium is significantly lower than that of transition metals, resulting in intrinsically weak diffraction peaks for Al-rich phases. Moreover, these oxides are typically localized along lamellar

boundaries and form thin layers, so their overall volume fraction within the penetration depth of conventional XRD is likely too small to produce detectable reflections above the background. In addition, these Al-rich oxides often exhibit poor crystallinity or even an amorphous structure, leading to broad and low-intensity peaks that are difficult to distinguish in standard diffraction measurements.

All these factors: low scattering power of Al, surface localization, and limited crystallinity; are consistent with local EDX observations showing Al- and O-enriched regions surrounding the lamellae. This experimental picture supports the proposed mechanism whereby the formation of Al-rich oxides along lamellar boundaries acts as an effective barrier to oxygen diffusion, thereby protecting the transition metals from extensive oxidation and reducing the overall fraction of spinel-type oxides (MM_2O_4) observed in the Al-containing coatings, such as Al_{14}.

3.3. a. Micro- and nano-mechanical properties

The Vickers microhardness measurements revealed distinct differences among the coatings, reflecting the influence of alloy composition and processing conditions on their mechanical response (Table 9). The HVOF-sprayed Cantor and Al_{14}(CrMnFeNi) coatings exhibited the highest hardness values, ranging between approximately 500 and 570 HV, while slightly lower hardness values were recorded for the Al_0(CrMnFeNi) and Al_{10}(CrMnFeNi) coatings, in the range of 430–470 HV and 480–500 HV, respectively. The HVOF-sprayed Stellite reference coating displayed somewhat higher hardness than the HEA-based coatings, consistent with its cobalt-rich matrix and lower ductility. These results suggest that increasing aluminium content leads to moderate variations in hardness, likely associated with changes in phase composition, solid-solution strengthening, and microstructural refinement induced by the spraying process.

Table 9: Vickers microhardness (HV) by depth-sensing Vickers micro-indentation, elastic modulus (EIT) by spherical nano indentation.

Sample ID	$HV_{0.3}$	E_{IT} [GPa]
Cantor Run1	531±29	171±5
Cantor Run2	516±29	162±4
Cantor Run3	533±38	161±6
Al_0(CrMnFeNi) Run1	464±28	157±5
Al_0(CrMnFeNi) Run2	435±37	159±4
Al_0(CrMnFeNi) Run3	436±22	162±4
Al_{10}(CrMnFeNi) Run1	487±16	137±5
Al_{10}(CrMnFeNi) Run2	494±35	146±5
Al_{10}(CrMnFeNi) Run3	508±25	148±4
Al_{14}(CrMnFeNi) Run1	501±24	164±4
Al_{14}(CrMnFeNi) Run2	574±31	169±3
Al_{14}(CrMnFeNi) Run3	574±63	168±3
Stellite	584±65	212±6

To obtain a more detailed characterization of the micromechanical properties of the coatings and to probe the intrinsic hardness and modulus of the individual phases, nanoindentation mapping was performed on selected HVOF-sprayed samples, as described in section 2.3.2 Since no significant variations were observed among coatings produced under different process parameters, only one representative sample was analysed for each alloy composition. The low indentation load enabled high spatial resolution, allowing the local mechanical properties of distinct microstructural constituents to be resolved.

The resulting hardness maps (Figure 24) clearly reflected the heterogeneous lamellar microstructure typical of the HVOF-sprayed coatings. Harder regions corresponded to oxide

inclusions, whereas softer areas were associated with the metallic matrix within the lamellae. Fluctuations in hardness at the intra-lamellar level were also evident. As illustrated in Figure 25, some indentations within the oxide regions did not yield reliable load–displacement curves, likely due to the brittle nature and limited thickness of these features.

The data were further analysed through distribution plots representing the fraction of measurement points within specific hardness and modulus intervals. Fitting Gaussian functions to these distributions (Figure 25 and Figure 26) allowed identification of distinct mechanical sub-populations within the coatings, each corresponding to a specific microstructural phase. The mean and standard deviation of hardness and elastic modulus for each sub-population were extracted from the fitted curves. There is no guarantee that a "mechanical phase" identified by this fitting process matched exactly with an actual phase identified by structural and microstructural investigations, but the good spatial matching between microstructural features and distinct hardness values seen in Figure 25 suggests that an association is possible.

As summarized in Table 10, all HVOF-sprayed coatings exhibited at least one sub-distribution with an average hardness above 10 GPa, confirming the presence of hard, oxide-rich regions embedded in a softer metallic matrix. Depending on the composition, either two (e.g., HVOF Cantor Run 2) or three (e.g., Al-containing coatings) mechanical sub-distributions were observed. While the hardness differences among the sub-distributions were clearly distinguishable, the corresponding variations in elastic modulus were comparatively smaller and often within the same standard deviation range.

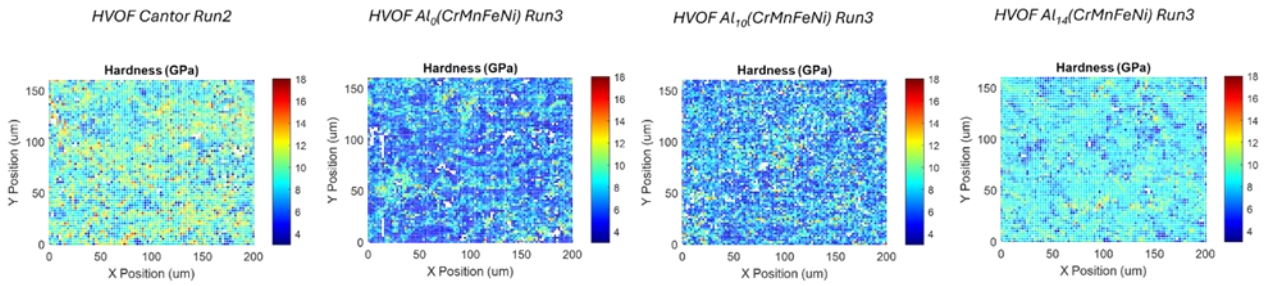

Figure 24: Hardness maps obtained from high-speed nanoindentation with 2.5 µm spacing between indents. Note: The represented areas are cropped from the actual map sizes, and all samples have been standardized to the same region of interest (ROI) to illustrate comparative differences effectively

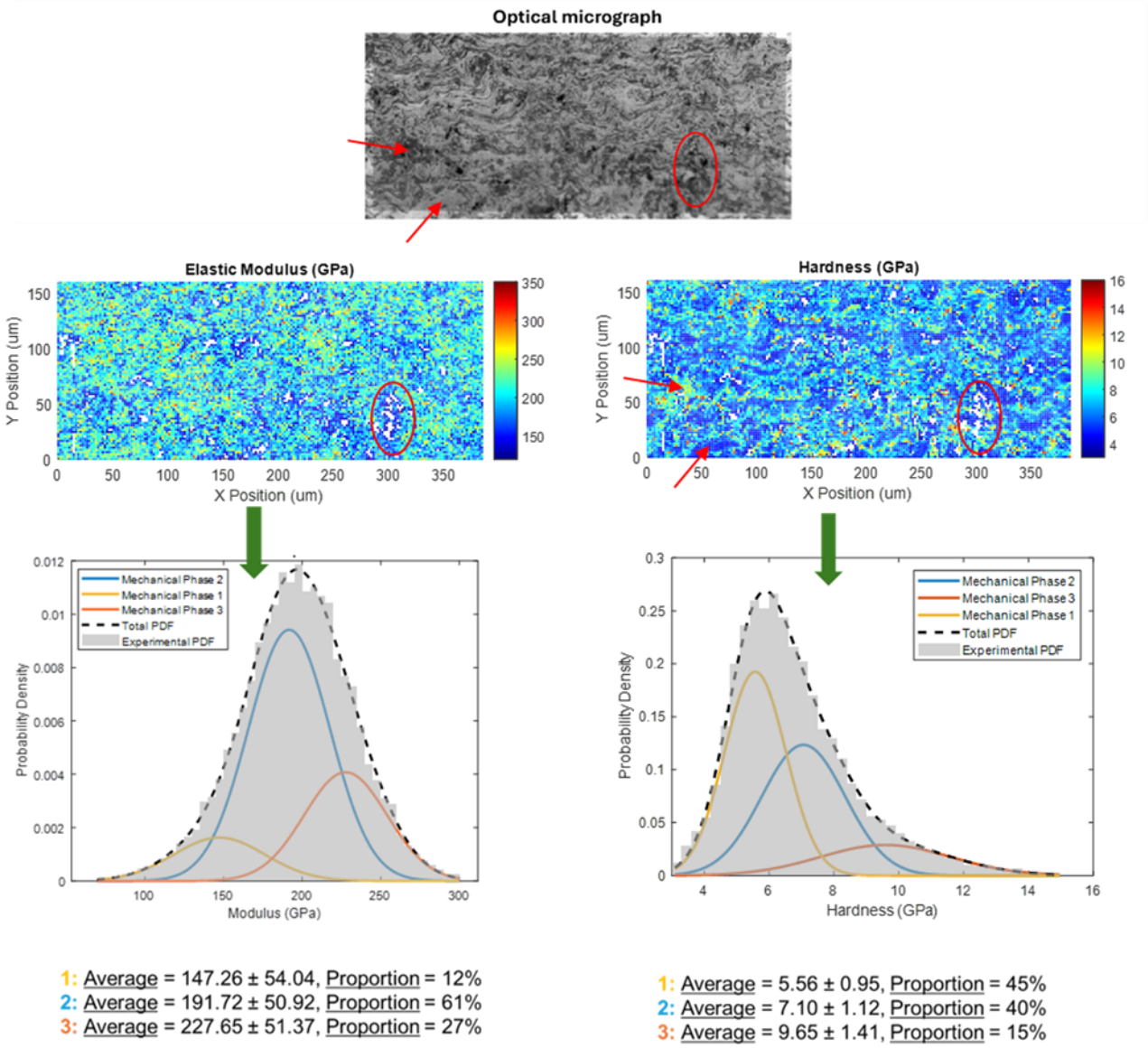

Figure 25: Example of nanoindentation results for the HVOF-sprayed Al_0(CrMnFeNi) Run3 coating. Optical micrograph of the indented area, along with maps of elastic modulus and indentation hardness, and the corresponding distribution plots. The distributions were fitted with Gaussian sub-distributions to determine the average hardness and elastic modulus (± standard deviation) associated with each mechanical phase. The circled regions mark extremely brittle oxide areas that fractured during indentation and did not yield reliable measurements, while the arrows highlight the harder oxide inclusions and the softer metallic phases within the lamellar structure.

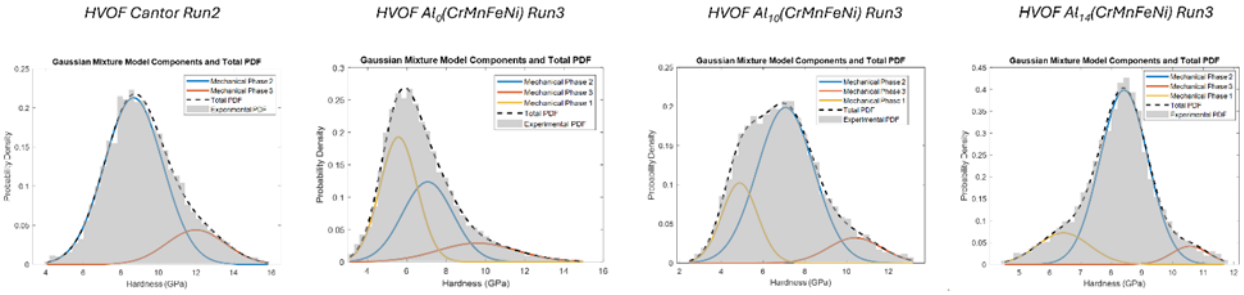

Figure 26: Distributive curves of indentation hardness obtained by high-speed nanoindentation for the analyzed samples. Each plot shows the histogram representing the fraction of indentations within specific hardness ranges, the overall fitted curve obtained using the Gaussian Mixture Model (GMM) algorithm, and the individual Gaussian components corresponding to distinct mechanical phase distributions.

Table 10: Results of least-squares fitting of the nanoindentation data distributions using Gaussian functions. For each identified distribution, the mean ± standard deviation is reported, and the percentage values in parentheses indicate the fraction of the total data associated with that distribution.

Sample	E_{IT} [GPa]			H_{IT} [GPa]		
	Phase 1	Phase 2	Phase 3	Phase 1	Phase 2	Phase 3
Cantor Run2	-	184±33 (27%)	203±25 (73%)	-	8.61±1.24 (83%)	12.03±1.26 (17%)
Al_0(CrMnFeNi) Run3	247±54 (14%)	192±51 (79%)	228±51 (7%)	5.56±0.95 (45%)	7.10±1.12 (40%)	9.65±1.41 (15%)
Al_{10}(CrMnFeNi) Run3	135±13 (18%)	172±21 (72%)	211±17 (10%)	4.87±0.92 (22%)	7.07±1.16 (67%)	10.45±1.13 (11%)
Al_{14}(CrMnFeNi) Run3	168±20 (8%)	202±18 (89%)	244±14 (3%)	6.43±0.92 (15%)	8.41±0.88 (78%)	10.57±0.77 (7%)

These observations can be further interpreted by considering the mechanical implications of the oxide inclusions and the multi-phase microstructure. Some of the interlamellar oxide inclusions present in the HVOF-sprayed HEA coatings likely fractured or collapsed during indentation, leading to a local reduction in the measured hardness and modulus. Nevertheless, many oxide inclusions exhibited extremely high hardness values, confirming that several of these oxides were dense and mechanically strong. This dual behaviour explains the coexistence of very hard and locally brittle regions within the coatings, as already highlighted by the nanoindentation maps (Figure 24 and Figure 25).

The distribution of indentation hardness values revealed the presence of distinct mechanical sub-populations within each coating. In the case of the HVOF-sprayed Cantor coating, two main hardness distributions were identified: a predominant one centered around 8.5 GPa, attributed to the FCC metallic matrix, and a secondary one at approximately 12 GPa, associated with the harder oxide inclusions. The high hardness of the matrix compared with that of the bulk Cantor alloy can be explained by the fine grain size and the presence of numerous nano-oxides acting as dispersion-strengthening particles.

The nanohardness values of both the FCC and BCC phases were significantly higher than those typically reported for bulk high-entropy alloys, which are generally in the range of 150–200 HV for FCC and 500–650 HV for BCC materials[152].

For the Al-containing coatings, three hardness sub-distributions were observed. The lowest hardness values (≈ 5.5–6.5 GPa) corresponded to the softer FCC phase, the intermediate ones (≈ 7–8 GPa) to the harder BCC phase, and the highest values (≈ 9.5–10.5 GPa) to dense, defect-free oxide inclusions. As the Al content increased, the fraction of data corresponding to the FCC phase decreased, while that of the BCC phase increased, in agreement with the phase evolution described before. Conversely, the fraction of data

associated with the hardest oxide inclusions diminished, consistent with the observed reduction in oxide volume fraction.

Overall, the micromechanical data confirm that the combination of metallic and oxide phases governs the mechanical response of the HVOF-sprayed HEA coatings. The strong, finely distributed oxides contribute significantly to hardness and work-hardening behaviour by impeding dislocation motion, while their brittle nature may locally limit ductility. These results highlight the complex balance between strengthening and embrittlement mechanisms induced by oxide formation and Al addition in these multicomponent systems.

3.4. a. Sliding wear behaviour

The specific wear rates of the HVOF-sprayed HEA coatings in the ball-on-disc tests (Figure 27A) spanned approximately one order of magnitude. These values were mainly grouped according to alloy composition, with no signific

ant influence from the deposition parameters. The specific wear rate increased progressively from Cantor coatings, which exhibited the lowest values of about 6–8 × 10^{-5} mm^3/(N·m), to the Al_0(CrMnFeNi) (~1 × 10^{-4} mm^3/(N·m)), Al_{10}(CrMnFeNi) (~2–5 × 10^{-4} mm^3/(N·m)), and Al_{14}(CrMnFeNi) (~5–8 × 10^{-4} mm^3/(N·m)) coatings. Similarly, the Cantor and Al_0(CrMnFeNi) coatings produced the lowest wear losses on the counterpart (Figure 27B), whereas the Al_{10}(CrMnFeNi) and Al_{14}(CrMnFeNi) coatings caused higher counterpart wear. In all cases, the wear rates of the balls were at least one order of magnitude lower than those of the coatings. Conversely, the steady-state friction coefficients followed an almost inverse trend (Figure 27C): the Cantor and Al_0(CrMnFeNi) coatings exhibited friction coefficients around 0.6, while slightly lower values, around 0.56, were recorded for the Al_{10}(CrMnFeNi) and Al_{14}(CrMnFeNi) coatings.

Stellite coating, used as a reference, displayed a lower specific wear rate than all the HEA-based coatings (~4 × 10^{-5} mm^3/(N·m), Figure 27A). It also caused lower counterpart wear (~2.3 × 10^{-7} mm^3/(N·m), Figure 27B) but exhibited a higher steady-state friction coefficient (~0.66, Figure 27C). These results are consistent with previous studies on HVOF-sprayed Stellite-6 coatings, which showed similar wear and friction behaviour under comparable test conditions[153]. The complete friction curves from all tests (Figure 28) confirmed that the HEA coatings, regardless of composition, reached steady-state friction rapidly, while the Stellite coating exhibited an initial transient stage of lower friction before stabilizing at higher values.

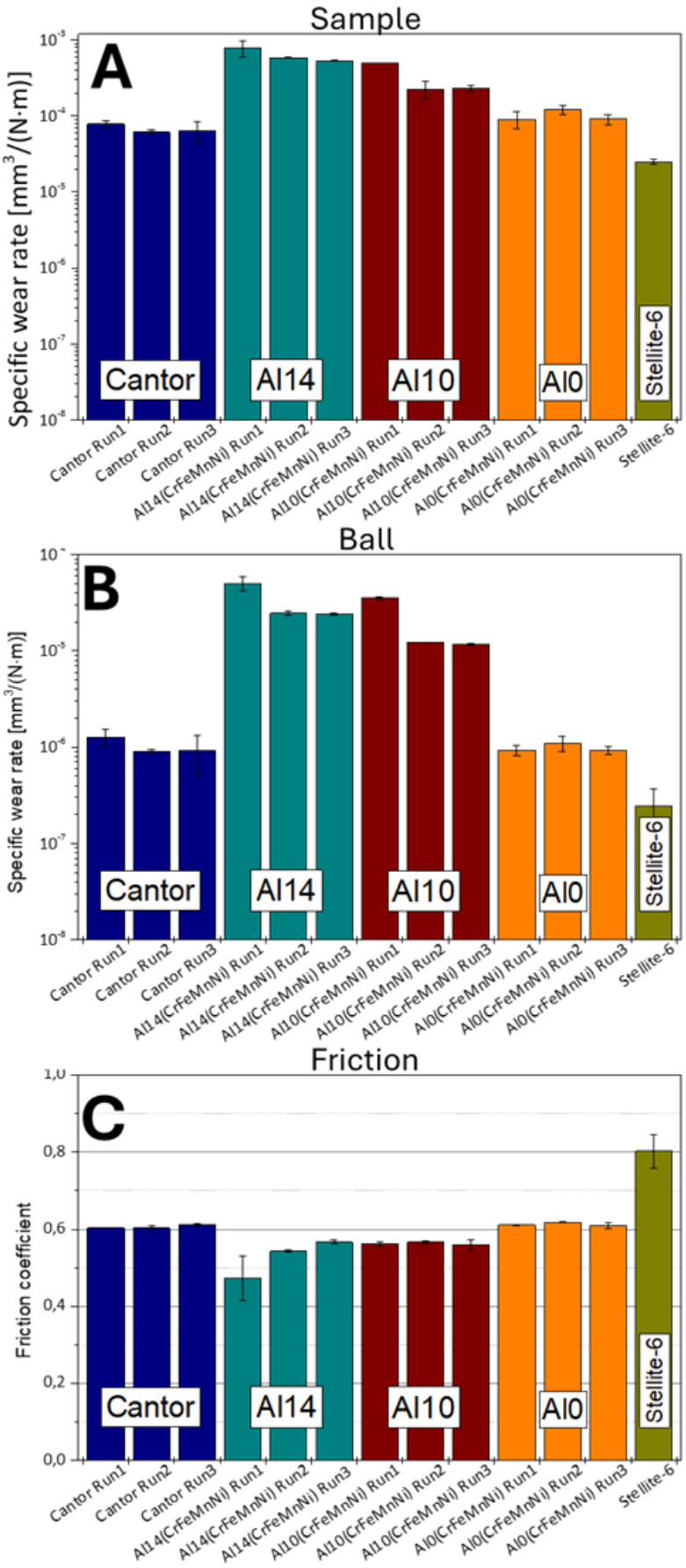
Sample
A
Specific wear rate [mm³/(N·m)]
Cantor
Al14
Al10
Al0
Stellite-6
Cantor Run1
Cantor Run2
Cantor Run3
Al14(CrFeMnNi) Run1
Al14(CrFeMnNi) Run2
Al14(CrFeMnNi) Run3
Al10(CrFeMnNi) Run1
Al10(CrFeMnNi) Run2
Al10(CrFeMnNi) Run3
Al0(CrFeMnNi) Run1
Al0(CrFeMnNi) Run2
Al0(CrFeMnNi) Run3
Stellite-6
Ball
B
Specific wear rate [mm³/(N·m)]
Friction
C
Friction coefficient
0,0
0,2
0,4
0,6
0,8
1,0

Figure 27: Quantitative results of the ball-on-disc sliding wear tests: specific wear rates of the coated samples (A) and the balls (B), and steady-state friction coefficients (C). Note: the tests on the HVOF-sprayed Cantor coatings were done over 5000 m to improve the accuracy of the results on account of the lower wear volume.

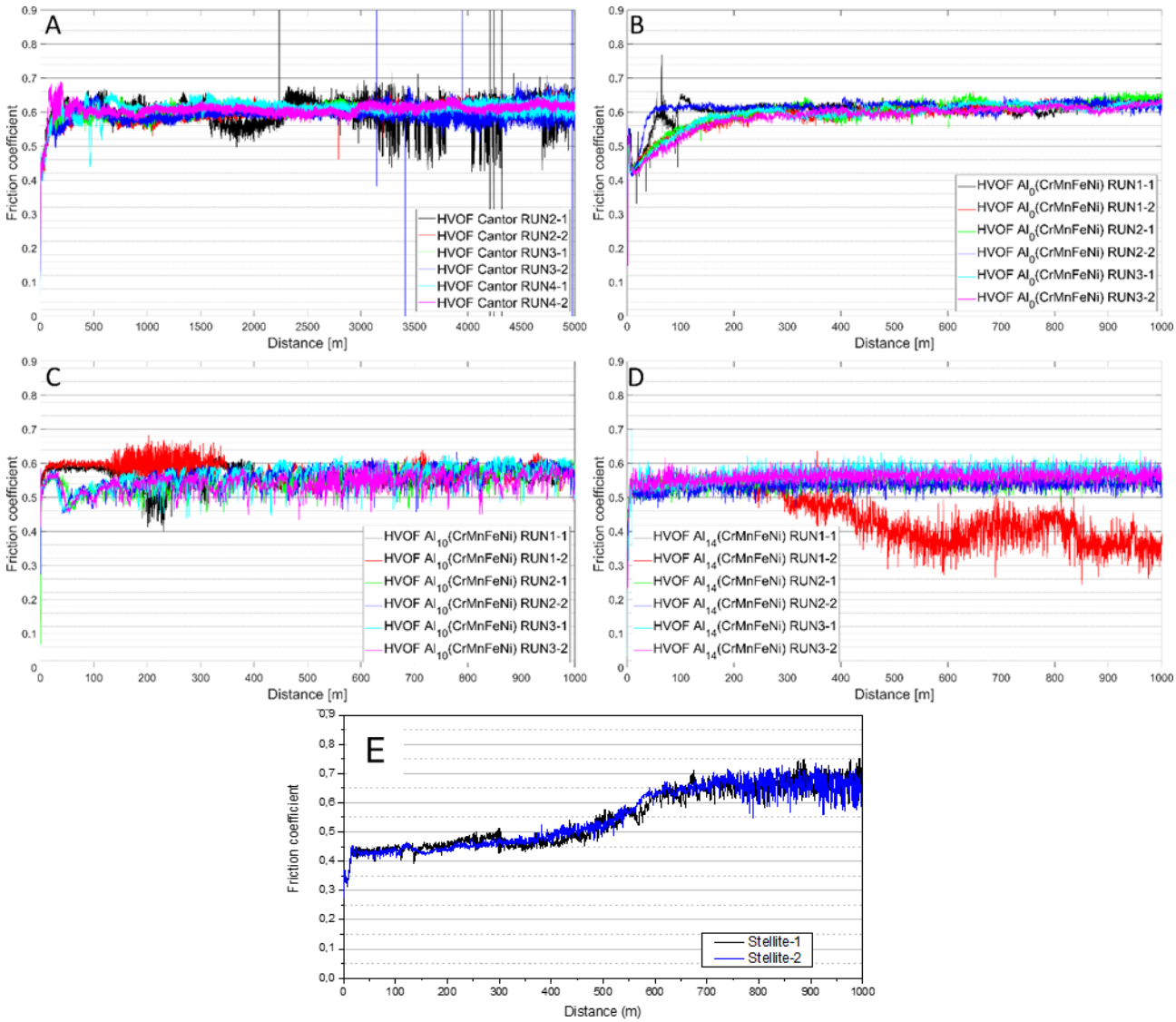

Figure 28: Friction curves of Cantor (A), Al_0(CrMnFeNi) (B), Al_{10}(CrMnFeNi) (C), Al_{14}(CrMnFeNi) (D) and Stellite reference (E) samples.

SEM micrographs of the worn surfaces of the HVOF-sprayed Cantor coatings revealed a combination of ductile tearing (Figure 29A, B, label 1) and oxidized clusters (darker contrast, label 2). On the corresponding ball surfaces, bright metallic transfer patches (Figure 30A, label 1) and dark oxidized debris (label 2) were observed. Cross-sectional images (Figure 31A) showed an irregular submicrometric layer of compacted oxidized debris partially covering the worn surface. In regions where the metallic surface was exposed (Figure 31B), the morphology was rough and irregular, showing signs of lip extrusion along the sliding direction (label 1). In several areas, oxide inclusions contained within the coating had emerged at the surface (Figure 31A, B, label 2).

For the HVOF Al_{10}(CrMnFeNi) (Figure 29C, D) and Al_{14}(CrMnFeNi) coatings (Figure 29E, F), coarser evidence of plastic flow was observed together with fewer oxidized clusters. Supplementary analyses (Figure 32) showed that the oxygen content detected along the worn surfaces decreased progressively with increasing Al content, with the highest oxygen levels found in the Cantor coatings. The counterpart surfaces after sliding against the Al-containing coatings (Figure 30B–D) were also covered with bright metallic transfer patches.

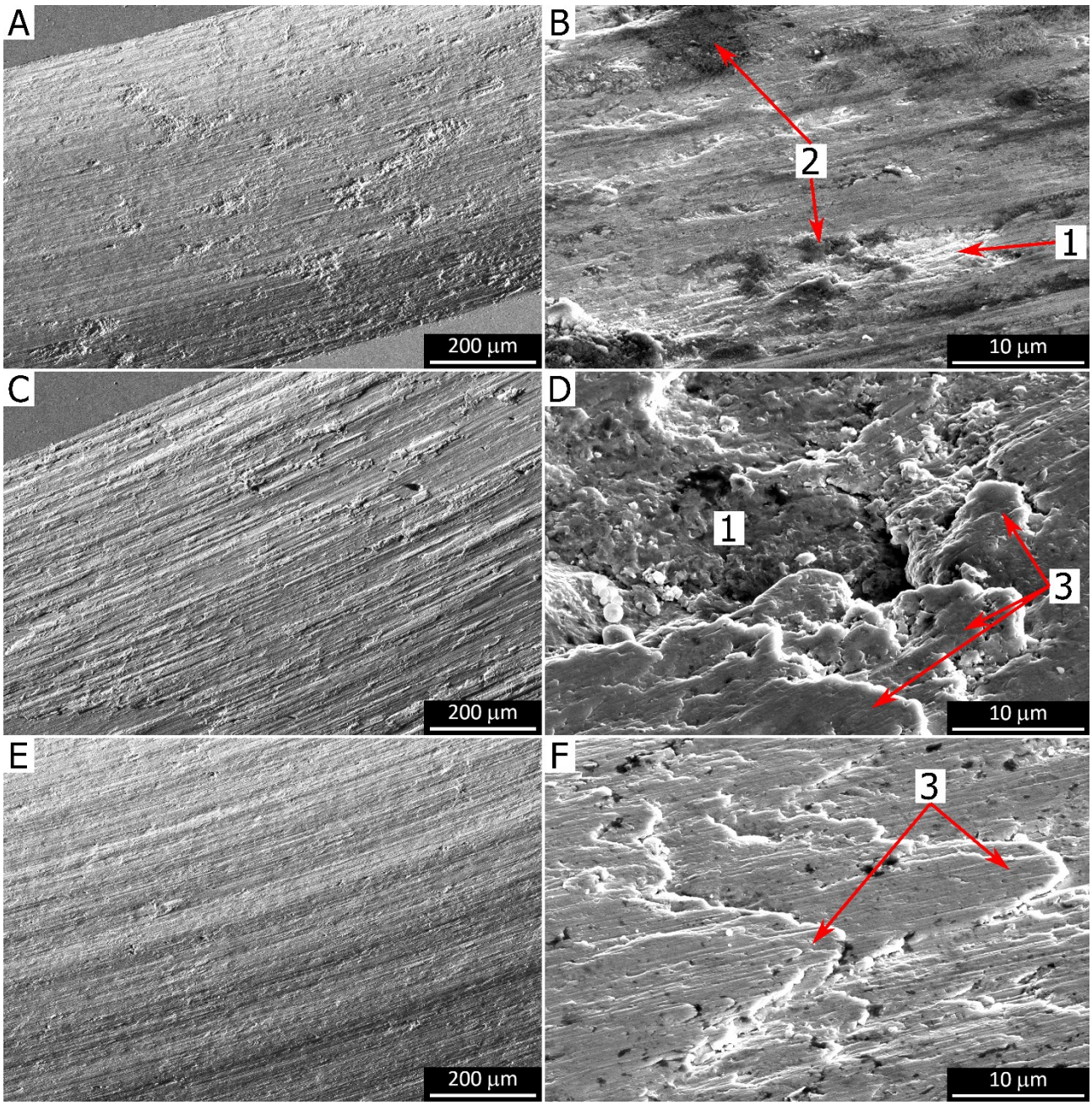

Figure 29: SEM micrographs (secondary electrons) of the ball-on-disc wear tracks on the HVOF-sprayed Cantor Run2 (A, B), Al_{10}(CrMnFeNi) Run3 (C, D), and Al_{14}(CrMnFeNi) Run3 (E, F) coatings. A, C, E: overviews; B, D, F: details. Labels: 1 = ductile tearing; 2 = tribo-oxidized clusters; 3 = plastic extrusion of lips.

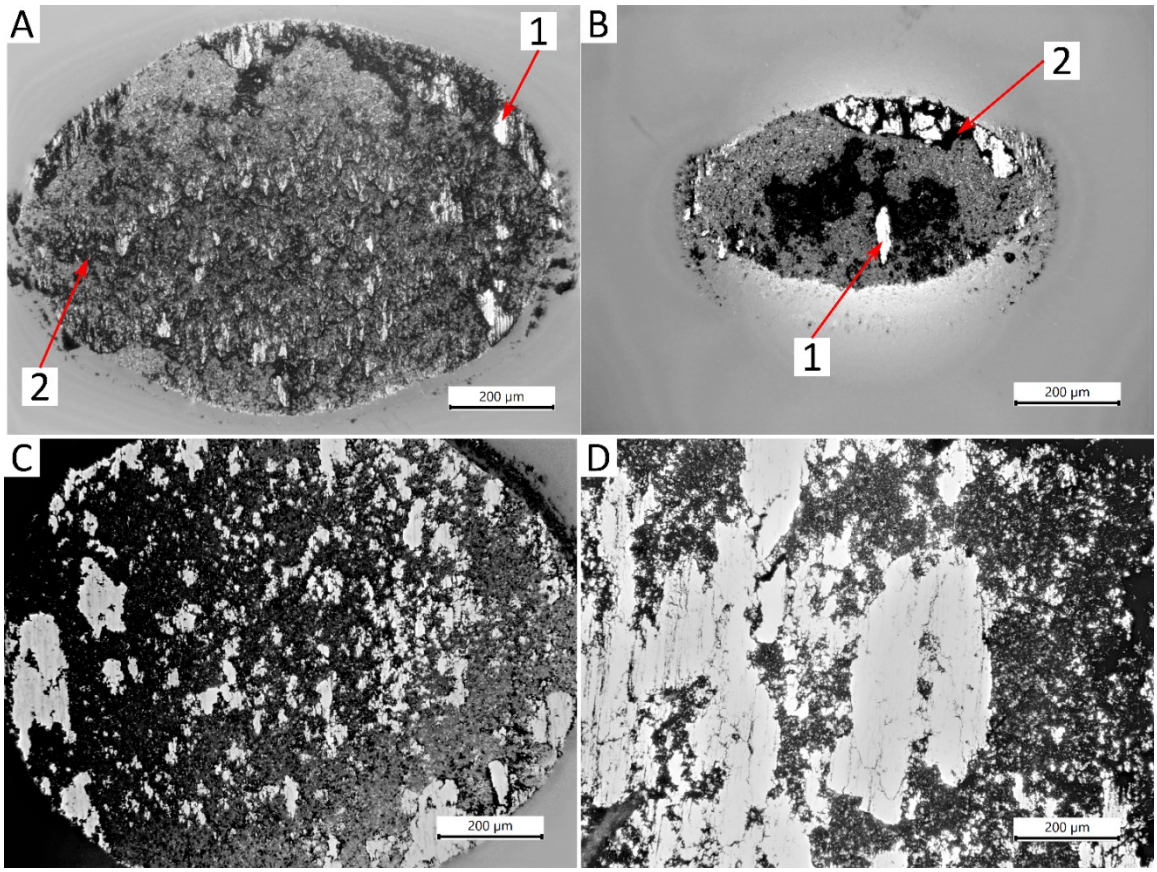

Figure 30: Optical micrographs of the worn surfaces of the ball counterparts after sliding wear testing against the HVOF-sprayed Cantor Run2 (A), Al_0(CrMnFeNi) Run1 (B), Al_{10}(CrMnFeNi) Run2 (C) and Al_{14}(CrMnFeNi) Run1 (D) coatings. Labels: 1 = transferred metal; 2 = tribo-oxidized cluster.

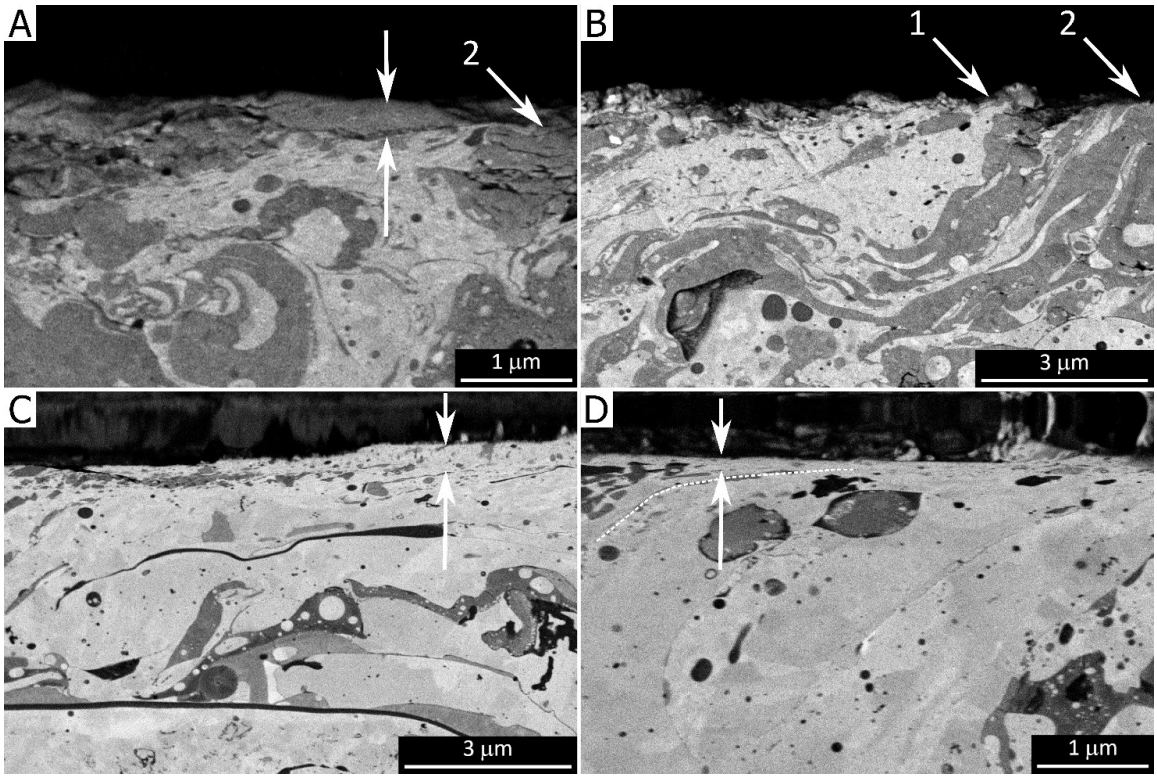

Figure 31: SEM micrographs (backscattered electrons) of the cross-sections of the ball-on-disc wear tracks on the HVOF-sprayed Cantor Run2 (A, B) and Al_{14}(CrMnFeNi) Run1 (C, D) coatings. The arrows in panel A indicate an oxide tribofilm; those in panel C indicate a plastically deformed layer of retransferred debris; the arrows in panel D indicate a plastically deformed surface layer, with the dashed line indicating the direction of surface plastic flow. Labels: 1 = plastically extruded metal lip; 2 = oxide inclusion exposed to the surface.

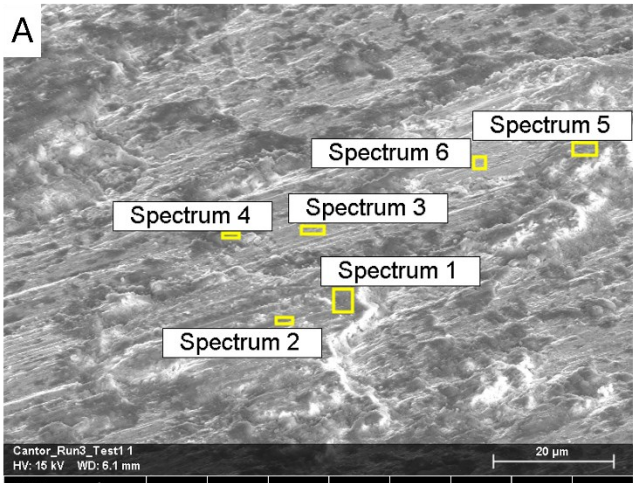

EDX results (wt.%)	O	Al	Si	Cr	Mn	Fe	Co	Ni
Spectrum 1	30.9	0.4	0.3	12.9	11.3	13.7	15.1	15.4
Spectrum 2	23.3	0.3	0.3	15.1	12.9	15.3	16.3	16.5
Spectrum 3	23.4	0.3	0.4	15.3	12.9	14.8	16.2	16.6
Spectrum 4	23.6	0.3	0.4	15.6	12.8	15.3	16.1	15.9
Spectrum 5	23.6	0.2	0.4	14.9	13.1	14.9	16.1	16.8
Spectrum 6	23.4	0.3	0.4	15.0	12.7	15.1	16.4	16.7

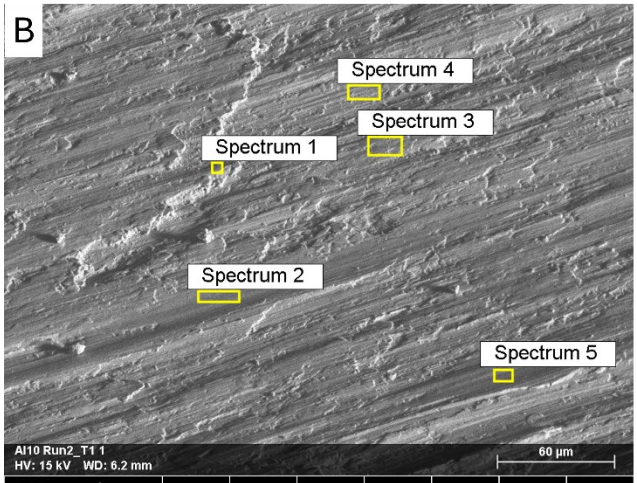

EDX results (wt.%)	O	Al	Si	Cr	Mn	Fe	Ni
Spectrum 1	18.7	5.5	0.1	15.2	14.8	32.3	13.5
Spectrum 2	22.0	6.7	0.1	18.4	18.4	24.9	9.4
Spectrum 3	13.9	5.6	0.1	16.3	15.9	35.1	13.1
Spectrum 4	7.5	5.4	0.1	17.3	17.8	36.8	15.3
Spectrum 5	18.0	5.9	0.1	17.8	17.3	29.7	11.2

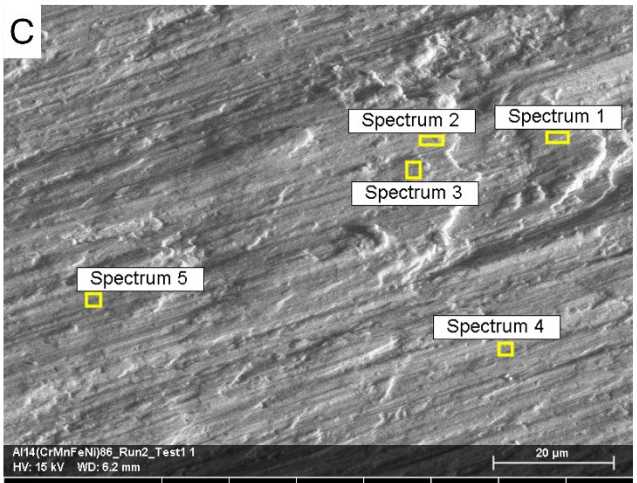

EDX results (wt.%)	O	Al	Si	Cr	Mn	Fe	Ni
Spectrum 1	9.2	7.7	0.2	17.3	16.3	36.0	13.2
Spectrum 2	8.5	7.2	0.1	16.7	15.9	37.3	14.3
Spectrum 3	8.5	8.0	0.2	16.9	16.3	36.3	13.8
Spectrum 4	4.6	6.0	0.2	16.9	18.0	38.7	15.7
Spectrum 5	9.7	8.7	0.1	15.5	16.0	36.3	13.7

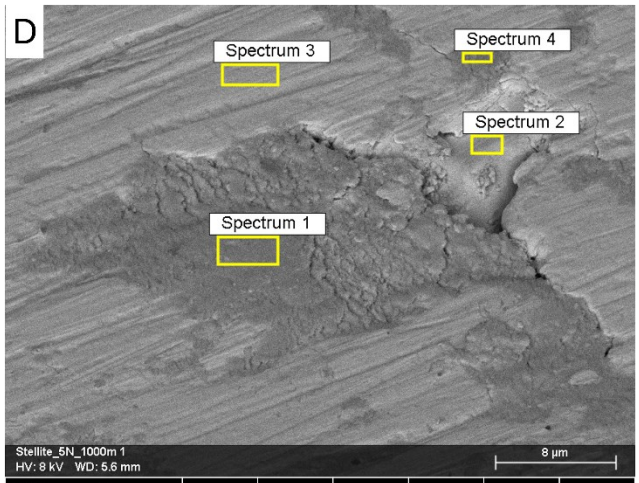

EDX results (wt.%)	O	Al	Si	Cr	Co	W
Spectrum 1	35.6	0.4	0.9	27.0	33.9	2.3
Spectrum 2	5.1	-	2.0	30.3	58.4	4.2
Spectrum 3	1.6	-	1.7	30.3	62.3	4.0
Spectrum 4	35.0	0.4	1.1	26.6	34.7	2.2

Figure 32: Cross-sectional backscattered-electron SEM micrographs of the HVOF Cantor Run2 (A), Al_{10}(CrMnFeNi) Run2 (B), Al_{14}(CrMnFeNi) Run2 (C), and Stellite (D) coatings with quantitative results from EDX analyses performed at the locations marked on the micrographs.

On the polished cross-section of Al_{14}(CrMnFeNi) coating, two characteristic surface features were identified. Figure 31C shows a slightly brighter layer, likely corresponding to a sheared lip of metal detached and re-deposited onto the worn surface. Figure 31D reveals ductile shearing of the metallic phase, with material dragged along the sliding direction, forming a thin surface layer. Compared with the HEA coatings, the Stellite coating exhibited a much

narrower wear track (Figure 33A), characterized by the absence of severe ductile tearing and by the presence of small pits and shallow abrasive grooves (Figure 33B).

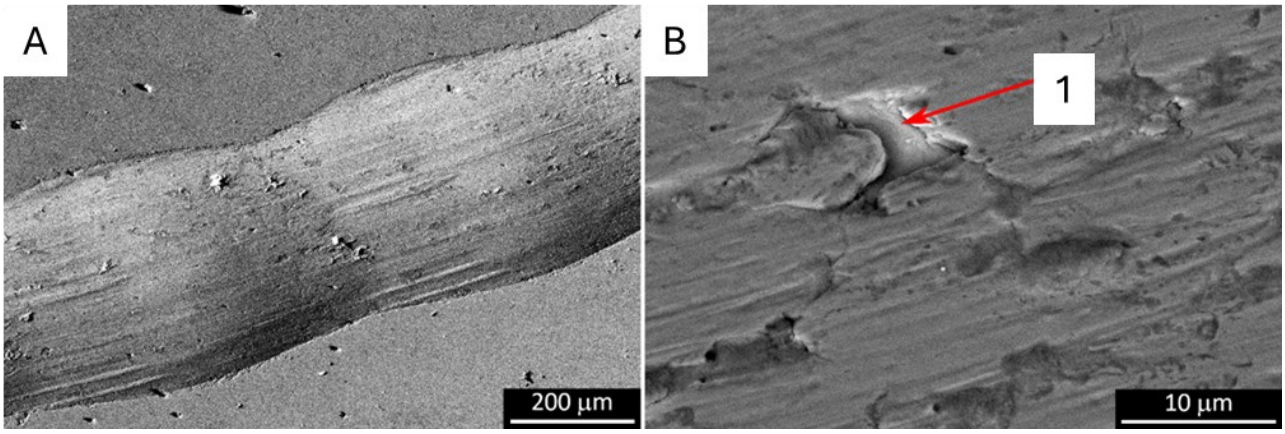

Figure 33: SEM micrographs (secondary electrons) of the ball-on-disc wear tracks on Stellite coating (A, B). A overview; B detail. Label 1 = micro-pit.

These tribological observations can be rationalized by considering the competing roles of phase constitution, oxide inclusions, and near-surface deformation. The progressive increase in specific wear rate from the Cantor to the Al-containing HEAs indicates that higher fractions of the BCC phase, together with a reduced occurrence of oxide inclusions at the surface, favour adhesive-dominated material removal under the present sliding conditions. Consequently, overall sliding resistance did not correlate simply with bulk or as-deposited hardness: coatings with higher measured hardness, i.e. Al_{14}(CrMnFeNi), suffered greater wear because the contact produced extensive plastic flow and adhesive transfer that overwhelmed any benefit from a harder matrix[124], [154]–[157].

Dense, well-bonded oxide inclusions that remained stable under contact acted protectively by bearing part of the load, interrupting the continuity of the ductile metal phase, and limiting the size of metal fragments removable by single tearing events [158]. Where such stable oxides accumulated, tribo-oxidized debris formed compacted surface clusters that reduced direct metal-to-metal contact and thus lowered wear. Conversely, coatings with fewer or weaker oxide inclusions developed more extensive plastic deformation and larger-scale adhesive tearing, which produced the higher wear rates and extensive transferred lips of metal observed on the counterpart[159]–[161].

Stellite reference, based on the literature, it is known that during sliding it developed a hard, stress-induced surface layer that limited adhesive tearing and produced a much narrower wear track. The formation of this hard surface layer shifted the dominant wear mode toward slow delamination and mild abrasion, reducing wear loss even though steady-state friction increased[153], [162]. This highlights that stress-induced surface hardening (e.g.,

martensitic-like transformation or other transformation/twinning mechanisms) can be more effective at improving sliding wear resistance than as-deposited hardness alone.

Taken together, these findings suggest two practical design guidelines for HEA sliding applications: promote stable, well-distributed hard inclusions or oxide phases that can sustain contact loads without catastrophic fragmentation, to reduce adhesive tearing and enable the formation of protective tribo-layers[158]; and target alloying strategies or microstructures that enable stress-induced surface hardening (TRIP/TWIP or transformation mechanisms) during sliding, rather than relying solely on higher as-deposited hardness[163]. Finally, the observed decrease in friction with increasing adhesive wear (and lower oxide content) can be attributed to the larger extent of metallic transfer and smoother metal–metal contact produced by severe adhesive flow, whereas oxide-rich surfaces tend to sustain higher tangential forces despite offering better wear protection[164], [165].

3.5. a. Electrochemical polarization results

The electrochemical polarization curves (Figure 34) showed that Cantor coatings had the highest rest potential, and their anodic behaviour featured an initial pseudo-passive stage at current densities of 10^{-6} – 10^{-5} A/cm^2, lasting up to an anodic overpotential of +200 mV vs. OCP. This was followed by transpassivation, with a rapid current increase to the order of 10^{-2} A/cm^2.

For the HVOF-sprayed Al_x(CrMnFeNi) coatings, both electrochemical nobility and the range of pseudo-passivity decreased progressively with increasing Al content. The Al_0(CrMnFeNi) coatings still exhibited some pseudo-passivity, but the current was less stable, with frequent spikes suggesting transient formation of metastable pits; breakdown occurred at approximately +100 mV vs. OCP. The Al_{10}(CrMnFeNi) and Al_{14}(CrMnFeNi) coatings were less noble and showed nearly continuous anodic activation with minimal pseudo-passive behaviour.

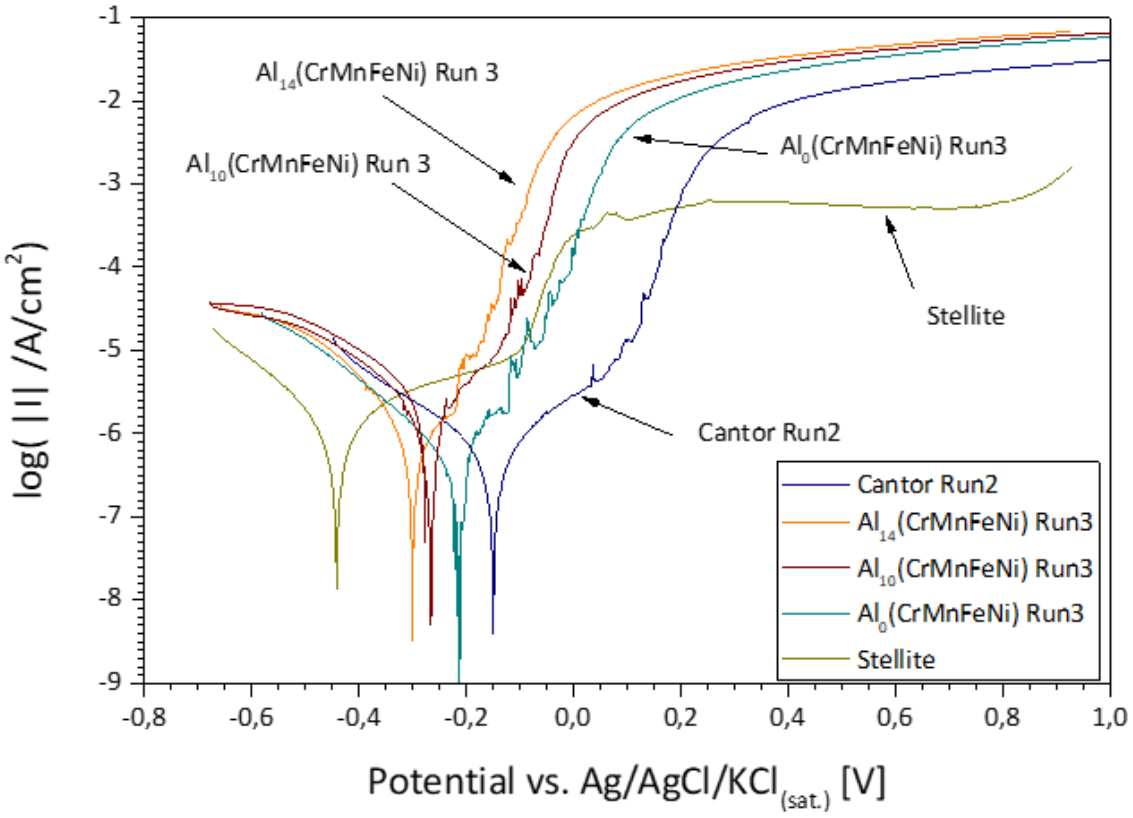

Figure 34: Representative electrochemical polarization curves for the metal coated material / deposition process combination explored in this work.

These trends were reflected in the corrosion current densities and corrosion potentials derived from Tafel analysis (Figure 35A, B). The Cantor and Al_0(CrMnFeNi) coatings exhibited low corrosion current densities, 0.4–0.6 µA/cm², with E_{Corr} around -150 mV vs.

Ag/AgCl/KCl(sat.) for Cantor and -220 to -270 mV for Al_0(CrMnFeNi). Al_{10}(CrMnFeNi) and Al_{14}(CrMnFeNi) coatings showed slightly higher corrosion current densities, rarely exceeding 1 µA/cm².

The HVOF-sprayed Stellite reference was less noble than all HVOF-sprayed HEA samples (Figure 34, Figure 35B), with a higher corrosion current density (~1.5 µA/cm²). However, it exhibited a wider pseudo-passive range (~350 mV), and after the initial breakdown, current density increased only to ~5×10^{-4} A/cm², rising further only at the highest overpotentials.

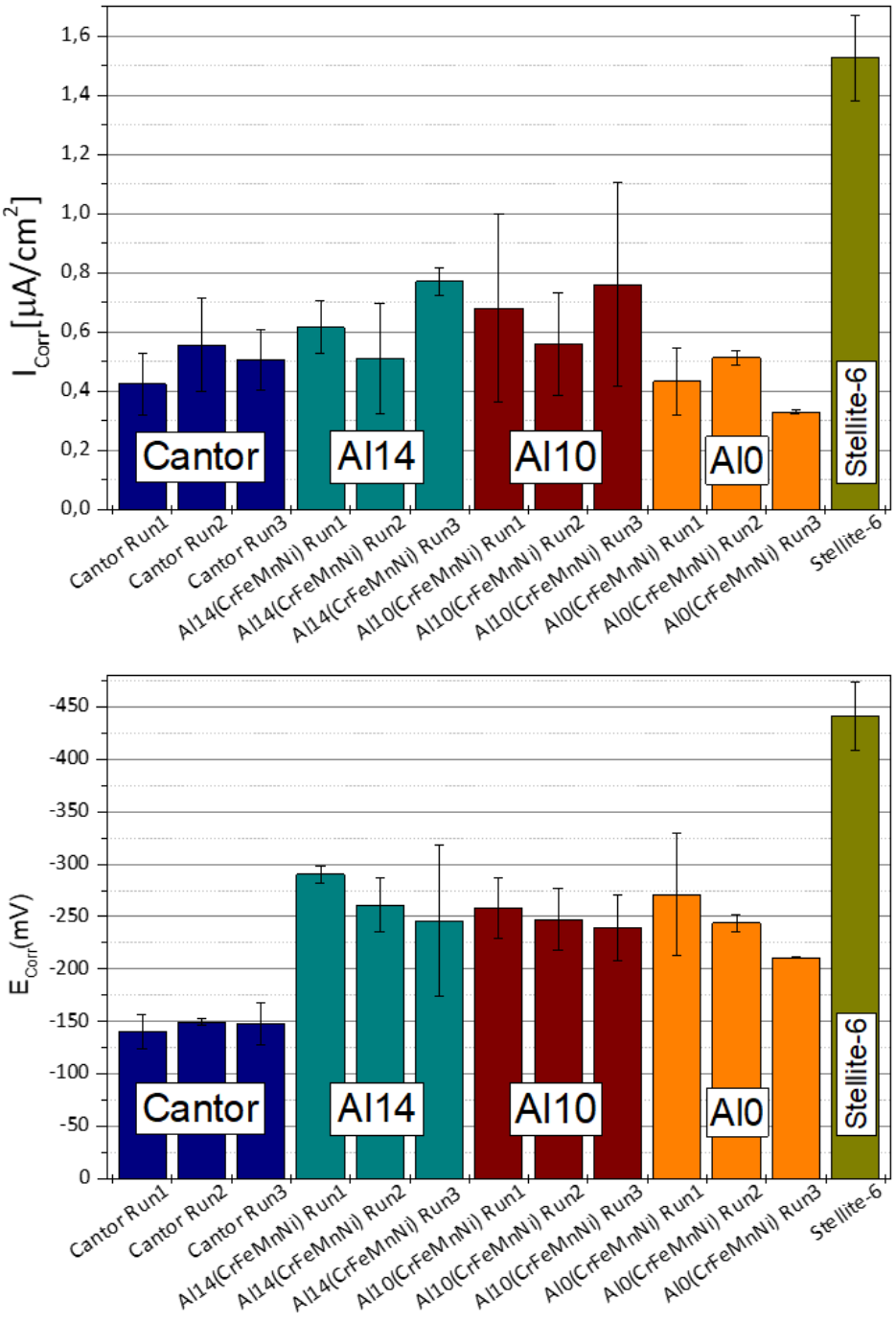

Figure 35: Corrosion current density (I_{Corr}) and corrosion potential (E_{Corr}) values for all the metal coatings.

Cross-sectional analysis of the corroded coatings (Figure 36) revealed that the upper portions of the HVOF-sprayed HEA coatings developed a severely damaged layer at the end of the anodic polarization stage (Figure 36). A mostly metallic layer remained on the outer surface, indicating that corrosion was more severe immediately below the surface, with attack propagating through lamellar boundaries and individual lamellae, leaving behind a skeleton of oxide inclusions and residual metal strips. Penetration was likely favoured by defects in the interlamellar oxide inclusions and at the oxide-metal interfaces. Spinel-type oxides, being electrically conductive, may have acted as cathodes, accelerating anodic dissolution of the metal. The mechanism was probably akin to crevice corrosion: limited oxygen access to the coating interior hindered passivation, promoting metal dissolution just below the outer “skin” (Figure 36).

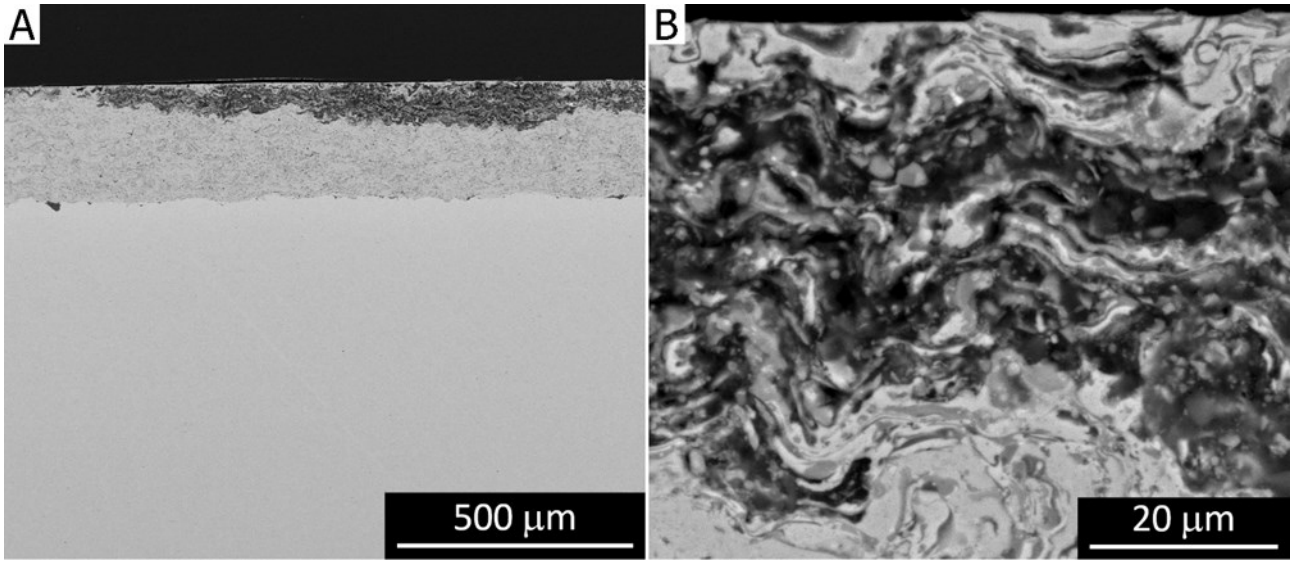

Figure 36: SEM micrographs (backscattered electrons) of the cross-sections of Al_{14}(CrMnFeNi) Run1 coating after the electrochemical polarization test: overview (A) and detail (B).

The results showed that the corrosion resistance of the HEA coatings worsened with increasing Al content. This is consistent with literature findings for bulk HEAs[166]–[170]: corrosion current density increases with Al addition, and passivation ability deteriorates. This behaviour is attributed to the formation of a 2-phase microstructure (BCC + FCC), which promotes galvanic coupling and destabilizes the passive film. The corrosion current density values of the HVOF HEA coatings (Figure 35) are comparable to those reported for bulk transition metal-based HEAs with and without Al, typically 10^{-8} to 10^{-7} A/cm^2 in aqueous NaCl solutions[167], [170]. Similarly, other thermally sprayed HEA coatings, such as HVOF-sprayed equiatomic AlCrFeCoNi[171], show corrosion current densities of ~10^{-7} A/cm^2.

The correspondence between these literature values and the present results supports the conclusion that the early breakdown observed here is primarily governed by coating-specific microstructural features rather than intrinsic alloy chemistry alone.

Overall, these observations indicate that the deposition process and microstructural features strongly influence corrosion behaviour. The lamellar structure in HVOF coatings allows corrosive agents to penetrate along interlamellar boundaries, and the oxide inclusions can exacerbate metal dissolution if they are electrically conductive, since in this case they would generate galvanic couples where the metal likely acts as the anode. Although it is not possible to establish experimentally whether this is the case, it is noted that spinel oxides of transition metals, such as those found in the present coatings (Section 3.3) often exhibit some electrical conductivity. A mostly metallic outer layer remains, highlighting that the most severe corrosion occurs beneath the surface. Considering these findings, the reduced passivation behaviour observed in the polarization curves, particularly the early loss of pseudo-passivity in Al-rich compositions, can be attributed to the interplay between lamellar defects, oxide inclusions, and microstructural heterogeneity introduced by the HVOF process. Future research could explore whether modifications in feedstock powder treatment or post-deposition annealing could improve corrosion resistance by promoting full recrystallization and homogenization of the microstructure.

3. b. Cermet coatings

3.1. b. Size distribution, microstructure, and phase composition of the powders

The powders obtained through the High-Energy Ball Milling (HEBM) process (Figure 37) exhibited a morphology characterized by slightly angular particles, most of which, however, maintained an overall equiaxed shape. This specific morphology results from the dynamic equilibrium established during HEBM between particle fracturing and cold-welding events, which continuously compete to achieve a state of mechanical and chemical balance. Such a balance promotes the formation of aggregates with a homogeneous internal composition. Despite their irregular appearance, the powders demonstrated adequate flowability, ensuring a stable and uniform feed during the subsequent thermal spraying operations.

The particle size analysis revealed that all powders exhibited rather similar distributions, consistent with the nominally expected values. Their characteristic parameters are summarized in Table 11. Among the different compositions, the Al_0(CrMnFeNi)+60TiC powder showed slightly smaller d_{10} and d_{50} values, indicating the presence of finer fragments, as visible in Figure 37C. In contrast, the AlCuCrFeNi+60TiC powder displayed a marginally narrower distribution range (smaller d_{10}–d_{90} span), suggesting a more uniform particle size distribution compared with the other systems.

Table 11: Density by helium pycnometry and characteristic values (10th, 50th, and 90th percentiles) of the particle size distributions of the HEBM feedstock powders.

Powder	**Density [g/cm^3]**	**d_{10} [µm]**	**d_{50} [µm]**	**d_{90} [µm]**
Cantor+60TiC	6.07	18	35	62
Al_0(CrMnFeNi)+60TiC	5.89	16	31	55
Al_{14}(CrMnFeNi)+60TiC	5.59	18	35	61
AlCuCrFeNi+60TiC	6.89	21	33	53

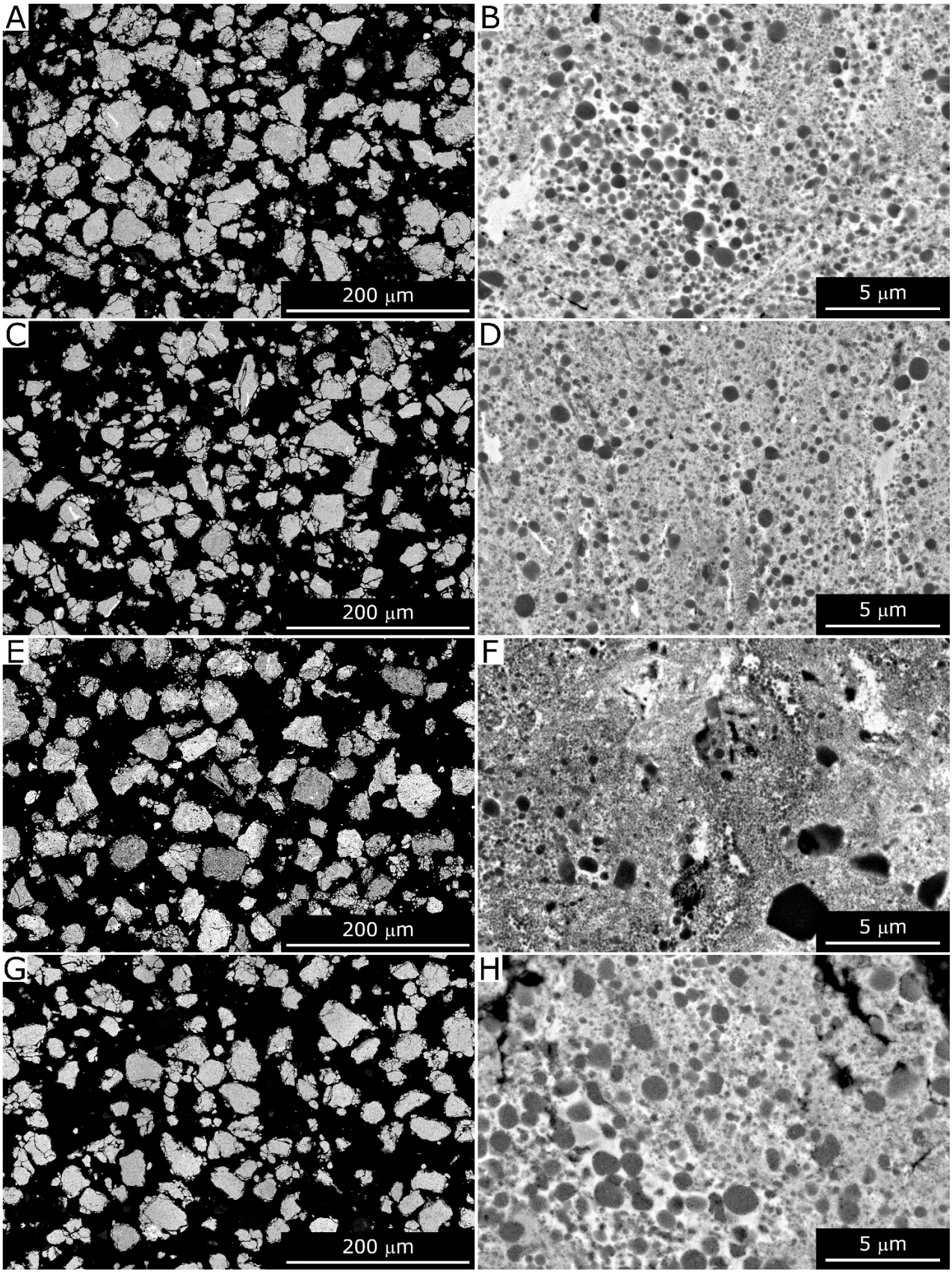

Figure 37: Backscattered-electrons SEM micrographs of the HEBM feedstock powders: Cantor+60TiC (A, B), Al0(CrMnFeNi)+60TiC (C, D), Al14(CrMnFeNi)+60TiC (E, F), AlCuCrFeNi+60TiC (G, H). Overviews (A, C, E, G) and details (B, D, F, H).

When observed at higher magnification (Figure 37B, D, F, H), the powders revealed a uniform distribution of the hard-phase particles, which could be easily identified by their darker contrast in backscattered-electron imaging. No interfacial voids or detachment were detected between the hard phase and the surrounding metallic matrix, suggesting good interfacial cohesion. The hard-phase particles exhibited a broad size distribution, ranging from micrometric to submicrometric and even nanometric dimensions, confirming the high degree of refinement induced by the milling process.

The EDX spectra (Figure 38: spectra 1, 2, 5) confirmed that titanium represented the main component of the carbide phase, whereas molybdenum appeared only occasionally as an impurity (notably in spectrum 1). Minor signals from matrix elements such as Cr, Mn, Fe, Ni, and Al were also present. These can be attributed to the finite dimensions of the X-ray generation volume, which under the given experimental conditions extended approximately 1.3 µm in depth and 0.7 µm in radius, overlapping partially with the matrix. The quantitative data reported in Table 12 indicate that, in certain cases (particularly spectrum 2), the chromium content relative to the other matrix elements (Al, Mn, Fe, Ni) was higher than expected from the nominal composition (see, for comparison, spectrum 4). This observation suggests that Cr, being the element with the second-highest affinity for carbon after Ti, might have partially participated in the carbide formation process and become dissolved within the TiC lattice.

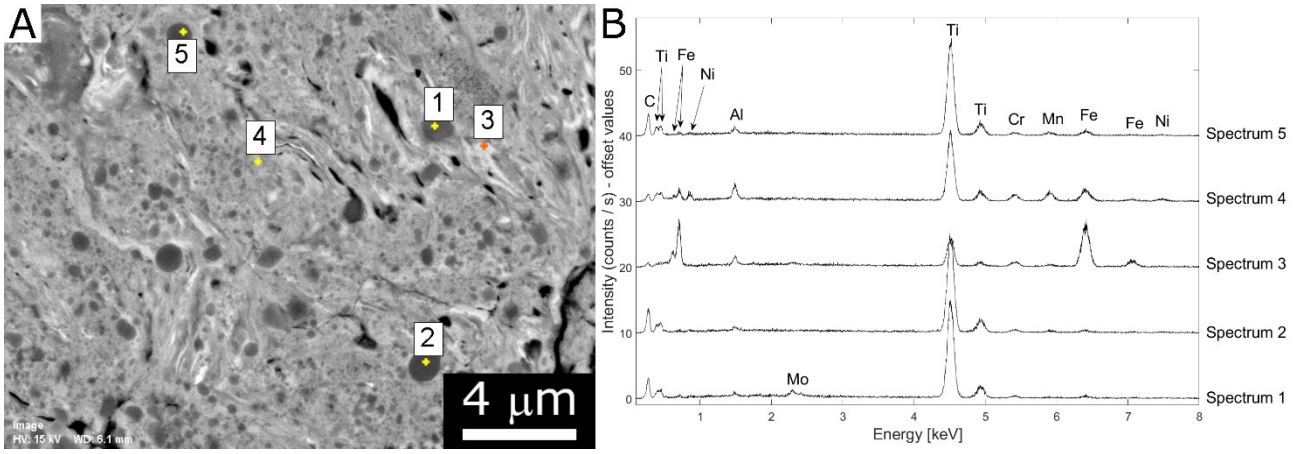

Figure 38: High-magnification backscattered-electron SEM micrograph of the Al14(CrMnFeNi)+60TiC powder (A) with corresponding EDX spectra (B).

Table 12: Quantitative results from the EDX spectra shown in Figure 38B, in mass% (normalized to 100).

Spectrum	C	O	Al	Ti	Cr	Mn	Fe	Ni	Mo
1	11.6	1.5	0.7	76.2	2.5	0.4	3.8	0.7	2.5
2	13.8	1.1	0.8	73.2	3.4	2.0	4.2	1.5	0.0
3	2.0	0.4	2.0	17.4	4.1	1.8	70.8	0.7	0.9
4	3.6	1.0	3.3	46.8	7.2	11.6	20.4	6.1	0.0
5	12.3	0.6	1.3	68.5	3.2	3.7	8.2	1.8	0.4

The overall composition of the powders, summarized in Table 13, confirmed good agreement with the nominal formulations. Minor deviations were associated with the presence of impurities such as Mo, W, and Nb, likely originating from residuals of previously processed hardmetal systems in the same production equipment. The metallic matrix appeared relatively homogeneous in all samples (Figure 37B, D, F, H), indicating that the mechanical energy transferred during HEBM was sufficient to promote interdiffusion among the metallic elements. Nonetheless, some small-scale compositional inhomogeneities could still be observed as faint streaks of varying contrast in the backscattered-electron images. As an example, spectrum 3 corresponds to a Fe-rich area in the $Al_{14}(Cr_{20}Mn_{25}Fe_{40}Ni_{15})$ matrix, although similar features were detected in all powders, suggesting that minor segregation phenomena occurred during milling.

In the case of the Al_{14}(CrMnFeNi)+60TiC powder, the carbon content was slightly below the nominal range (approximately 9–10 wt.%).

Table 13: Overall composition of the powders, computed by quantitative analysis on EDX spectra acquired on 400× micrographs and elemental analysis. Results were normalized to 100.

Element	Cantor+60TiC	Al_0(CrMnFeNi)+60TiC	Al_{14}(CrMnFeNi)+60TiC	AlCuCrFeNi+60TiC
Carbon[1]	9.27±0.20	N/A[2]	7.10±0.05	10.44±0.37
Nitrogen[1]	0.19±0.01	0.09±0.01	0.20±0.01	0.10±0.01
Oxygen[1]	0.75±0.01	0.51±0.01	0.69±0.02	0.39±0.01
Aluminum	0.17±0.03	0.51±0.07	3.58±0.23	2.32±0.17
Titanium	35.75±0.39	40.52±0.66	42.34±0.22	37.40±0.24
Chromium	9.82±0.22	10.29±0.07	9.46±0.22	8.69±0.09
Manganese	8.99±0.11	12.15±0.38	6.44±0.05	0.67±0.01
Iron	14.75±0.25	27.07±0.46	23.02±0.16	11.75±0.15
Cobalt	9.94±0.08	-	-	-
Nickel	10.06±0.04	8.56±0.41	6.63±0.27	17.99±0.45
Copper	-	-	-	10.25±0.40
Molybdenum	-	0.32±0.16	0.31±0.06	-
Tungsten	-	-	0.23±0.13	-
Niobium	0.31±0.06	-	-	-

[1] Measured by elemental analysis

[2] Not measured due to instrument malfunction

X-ray diffraction analyses (Figure 39) confirmed that TiC was the predominant hard phase in all powder compositions. The small presence of other elements such as Cr in the carbide

phase, as suggested by EDX data, can be attributed to limited substitutional solubility within the TiC lattice, without the formation of distinct secondary phases. No peaks corresponding to unreacted Ti or graphite were detected, indicating that the carbide formation reaction was essentially complete during the HEBM process. The only exception was the Al_{14}(CrMnFeNi)+60TiC powder, which exhibited unreacted Ti consistent with the carbon deficiency noted in the chemical analysis.

As already discussed in Section 3.1.a., the appearance of a BCC fraction in mechanically alloyed high-entropy systems is consistent with our earlier observations; the behaviour previously identified in purely metallic powders (Figure 39A,B) reappears here in the cermet powders as well, confirming that the severe plastic deformation and lattice disorder generated during HEBM promote the formation of a metastable BCC component even in alloys that are thermodynamically expected to be predominantly FCC. The large number of defects and the associated internal stresses, evidenced by the considerable broadening of the diffraction peaks, may have destabilized the densely packed FCC structure, favouring the formation of the less compact BCC phase. Additionally, the incomplete homogenization of the alloying elements at the end of milling could have locally enriched certain regions in Fe or other BCC-stabilizing elements, further promoting this structural transformation.

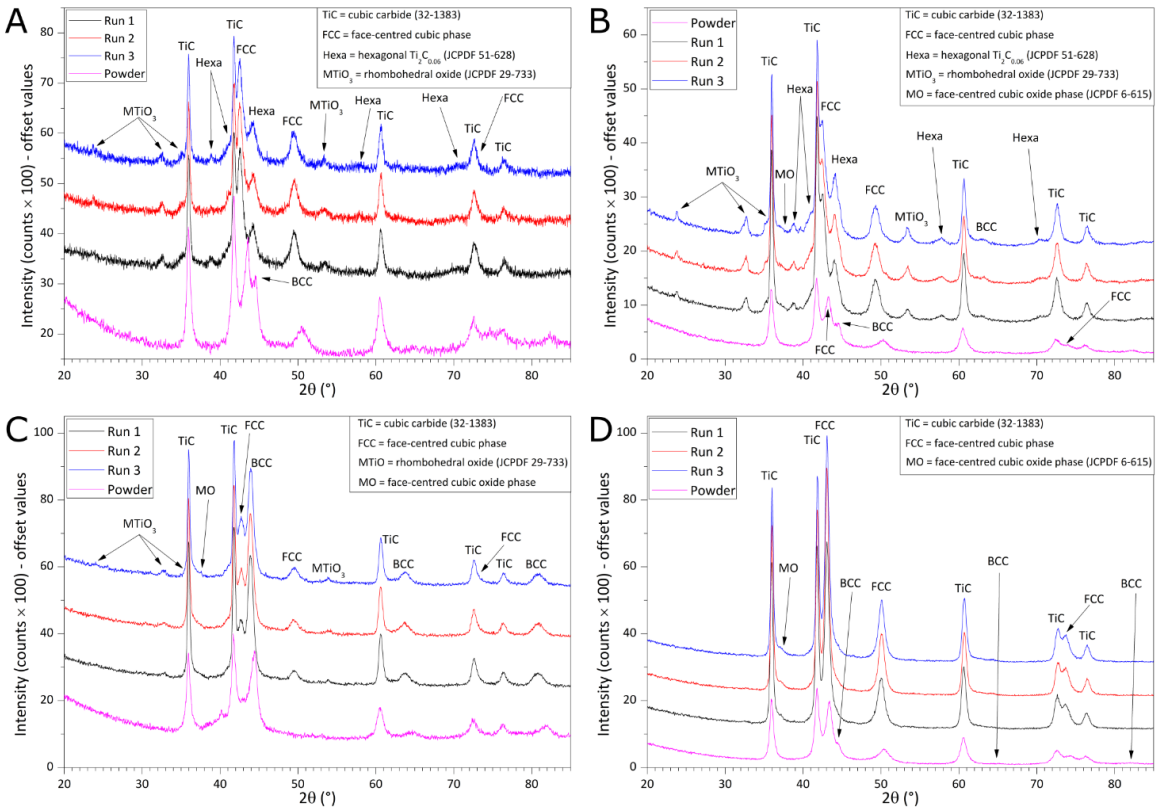

Figure 39: XRD patterns of the HEBM feedstock powders and the corresponding HVOF-sprayed coatings: Cantor+60TiC (A), Al0(CrMnFeNi)+60TiC (B), Al14(CrMnFeNi)+60TiC (C), AlCuCrFeNi+60TiC (D).

Quantitative phase analysis by Rietveld refinement in Table 14 revealed some variability in TiC content among the different compositions. However, when considering the relative densities of the phases, the resulting TiC volume fractions were all reasonably close to the nominal value of 60 vol.%. It should be noted that these results are to be regarded as semi-quantitative, as the accuracy of the refinement is inherently limited by the uncertainties associated with the structure factors of the analysed phases. This limitation is particularly relevant for the FCC and BCC random solid solutions typical of High-Entropy Alloys, since the details of their unit cell, which are needed to compute the structure factor, are not known with the same accuracy as for more conversional and widely studied alloys. This is also true for TiC containing minor substitutional elements such as Cr, which introduce a deviation from the well-documented lattice of pure TiC.

Table 14: Quantitative phase composition (in wt.%) of the feedstock powders and the coatings by Rietveld refinement of the XRD patterns.

Sample	**FCC**	**BCC**	**TiC**	**Ti**	**TiC_{1-x}**	**MO**	**$MTiO_3$**
Cantor+60TiC powder	52.4±0.3	8.2±0.4	39.4±0.6	-	-	-	-
Cantor+60TiC Run1	39.6±0.3	-	29.1±0.2	-	23.6±0.4	-	7.7±0.5
Cantor+60TiC Run2	41.1±0.3	-	28.9±0.2	-	21.8±0.4	-	8.2±0.6
Cantor+60TiC Run3	37.4±0.3	-	27.8±0.2	-	26.2±0.5	-	8.6±0.6
Al_0(CrMnFeNi)+60TiC Powder	33.5±0.4	8.8±0.4	57.7±0.2	-	-	-	-
Al_0(CrMnFeNi)+60TiC Run1	34.5±0.3	2.0±0.1	36.8±0.2	-	15.5±0.4	3.5±0.9	7.7±0.3
Al_0(CrMnFeNi)+60TiC Run2	31.3±0.2	2.5±0.4	34.4±0.2	-	18.6±0.4	4.0±0.4	9.2±0.3
Al_0(CrMnFeNi)+60TiC Run3	29.7±0.4	2.5±0.4	33.5±0.2	-	19.8±0.4	4.4±0.9	10.1±0.3
Al_{14}(CrMnFeNi)+60TiC Powder	7.8±0.3	33.1±0.3	42.9±0.2	16.2±0.7	-	-	-
Al_{14}(CrMnFeNi)+60TiC Run1	20.5±0.5	27.3±0.3	38.2±0.2	-	3.8±0.5	8.1±0.8	2.1±0.4
Al_{14}(CrMnFeNi)+60TiC Run2	20.8±0.5	25.7±0.3	36.1±0.2	-	3.9±0.5	10.9±0.9	2.6±0.5
Al_{14}(CrMnFeNi)+60TiC Run3	20.3±0.4	25.2±0.2	34.1±0.2	-	4.6±0.5	12.4±0.9	3.4±0.5
AlCuCrFeNi+60TiC Powder	49.7±0.4	1.8±0.2	48.5±0.2	-	-	-	-
AlCuCrFeNi+60TiC Run1	43.4±0.2	0.5±0.1	46.6±0.1	-	1.1±0.1	7.9±0.5	0.5±0.2
AlCuCrFeNi+60TiC Run2	44.7±0.2	0.6±0.1	45.4±0.1	-	0.5±0.2	8.5±0.3	0.3±0.1
AlCuCrFeNi+60TiC Run3	44.3±0.2	0.7±0.6	45.0±0.2	-	0.6±0.1	9.1±0.3	0.4±0.1

3.2. b. Microstructure and phase composition of the coatings

For each powder composition, the three coatings produced under varying gas flow rates did not reveal significant microstructural differences, a trend consistent with what was already observed for the purely metallic coatings in Section 3.2.a. Overall, the findings indicate that HVOF-sprayed coatings fabricated from the same feedstock powder show minimal variation, even when deposited under different processing conditions. Infrared pyrometer measurements were used to extrapolate the maximum spraying temperature (Tmax). The results revealed comparable maximum temperature values across all powders and deposition runs, ranging between 400 and 500 °C. This observation can be qualitatively appreciated in Figure 40, using the Cantor+60TiC samples as an example. Quantitative analysis of coating thickness and porosity (Table 7) confirmed that variations among the different deposition runs were generally small or negligible for all four materials. Consequently, for the sake of clarity, only one representative coating is shown in Figure 41 for each system: Al_0(CrMnFeNi)+60TiC (panels A–C), Al_{14}(CrMnFeNi)+60TiC (panels D–F), and AlCuCrFeNi+60TiC (panels G–I). All coatings displayed remarkably low porosity, with values consistently below 1% (Table 7). In particular, the AlCuCrFeNi+60TiC coatings exhibited porosity that was nearly undetectable in the “Run1” and “Run2” conditions, suggesting a particularly dense microstructure for this feedstock.

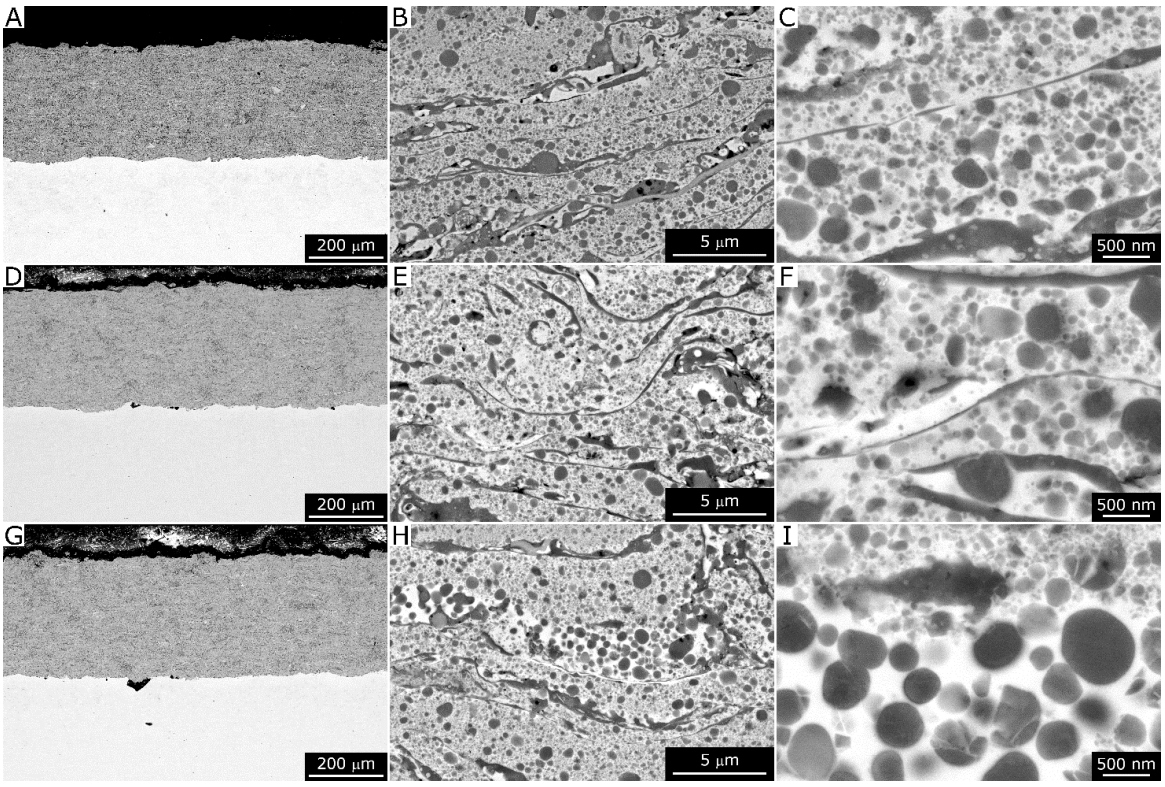

Figure 40: Backscattered-electrons SEM micrographs of the Cantor+60TiC coatings: Run1 (A-C), Run2 (D-F), and Run3 (G-I). Overviews (A, D, G), intermediate- (B, E, H) and high-magnification (C, F, I) views.

Table 15: Porosity and thickness (mean ± standard deviation) of all coatings by image analysis, and deposition efficiency.

Sample ID	Porosity (%)	Thickness [µm]	Thickness/pass [µm]	Deposition efficiency (%)
Cantor+60TiC Run1	0.38±0.24	294±13	7.5	53.0
Cantor+60TiC Run2	0.74±0.49	332±11	8.5	60.8
Cantor+60TiC Run3	0.20±0.09	307±11	7.9	58.3
Al_{14}(CrFeMnNi)+60TiC Run1	0.22±0.03	363±10	9.3	64.1
Al_{14}(CrFeMnNi)+60TiC Run2	0.23±0.04	339±8	8.7	55.5
Al_{14}(CrFeMnNi)+60TiC Run3	0.33±0.04	326±11	8.4	57.1
Al_{0}(CrFeMnNi)+60TiC Run1	0.18±0.03	323±21	8.3	59.8
Al_{0}(CrFeMnNi)+60TiC Run2	0.21±0.08	310±20	7.9	58.7
Al_{0}(CrFeMnNi)+60TiC Run3	0.23±0.09	281±18	7.2	55.6
AlCuCrFeNi+60TiC Run1	0.17±0.04	321±15	8.2	59.9
AlCuCrFeNi+60TiC Run2	0.14±0.04	311±15	8.0	56.9
AlCuCrFeNi+60TiC Run3	0.16±0.04	308±13	7.9	55.1

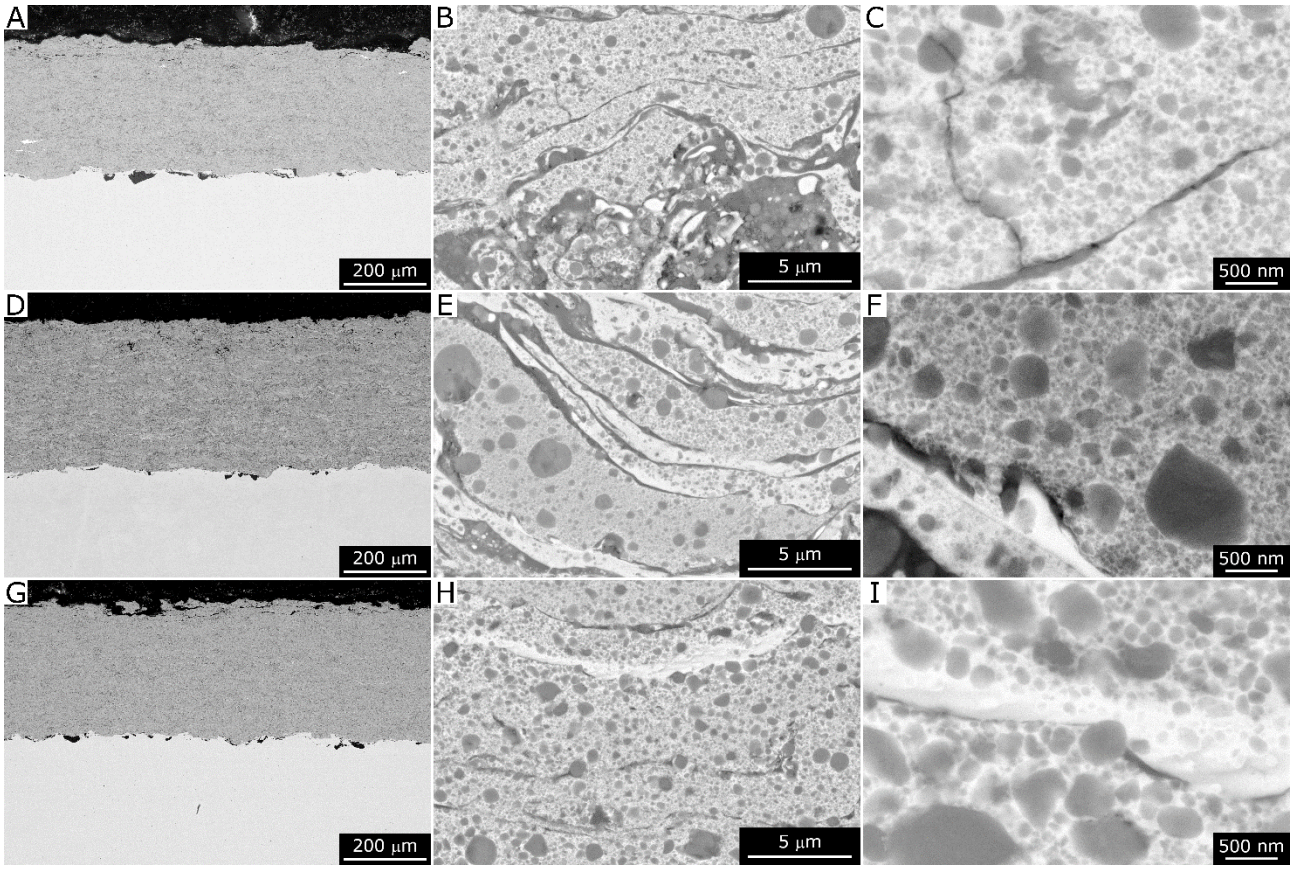

Figure 41: Backscattered-electrons SEM micrographs of the Al0(CrMnFeNi)+60TiC Run2 (A-C), Al14(CrMnFeNi)+60TiC Run1 (D-F), and AlCuCrFeNi+60TiC Run1 (G-I) coatings. Overviews (A, D, G), intermediate- (B, E, H) and high-magnification (C, F, I) views.

Deposition efficiencies, calculated from the samples' weight change as described in Section 2.2, ranged mostly between 50% and 60% (Table 15). An exception was the Cantor+60TiC system, where a slight decrease in deposition efficiency was observed at higher gas flow rates (from Run1 to Run3). This trend is likely attributable to increased particle rebounding caused by higher impact velocities under elevated gas flow. Nevertheless, these efficiencies

remain within a range suitable for industrial production, comparable to the 60% efficiency obtained with commercial WC-CoCr powders.

All coatings also contained oxide inclusions, most notably observed as dark stringers along lamellar boundaries in the SEM micrographs (Figure 40B, C, E, F, H, I and Figure 41B, C, E, F, H, I). EDX analyses in Figure 42 confirmed that these oxides were rich in Ti. Their formation likely followed a mechanism in which the metallic matrix was primarily melted during HVOF spraying, as suggested by the high degree of flattening of the lamellae. Under these conditions, a portion of TiC may have partially dissolved in the molten matrix. The dissolved Ti then migrated to particle surfaces, either in-flight or immediately after deposition[172], where it reacted with oxidizing agents such as entrained atmospheric oxygen[173] or water vapor from the H_2–O_2 combustion. In all coating systems, Ti exhibited the strongest thermodynamic affinity toward both carbon and oxygen, alongside aluminium, promoting the formation of these oxide inclusions.

Table 16: Chemical composition of the coatings (mass%, normalized to 100) measured by EDX analysis on areas imaged at 400×: mean ± standard deviation.

Element	**Cantor+60TiC**			**Al_0(CrMnFeNi)+60TiC**		
	Run1	*Run2*	*Run3*	*Run1*	*Run2*	*Run3*
Carbon	7.94±0.11	7.75±0.02	7.88±0.02	9.89±0.12	9.43±0.07	9.12±0.05
Oxygen	5.45±0.21	5.90±0.26	6.20±0.19	7.70±0.19	7.77±0.06	8.29±0.16
Aluminum	0.07±0.02	0.10±0.04	0.09±0.07	0.40±0.04	0.36±0.03	0.31±0.03
Silicon	0.22±0.03	0.23±0.03	0.20±0.01	0.35±0.01	0.29±0.04	0.26±0.01
Titanium	31.72±0.30	31.78±0.23	31.32±0.03	32.01±0.21	32.37±0.10	32.29±0.26
Chromium	9.64±0.09	9.66±0.13	9.76±0.08	9.05±0.12	9.14±0.08	9.08±0.13
Manganese	8.72±0.08	8.67±0.16	8.45±0.10	8.90±0.13	8.89±0.13	8.59±0.11
Iron	14.91±0.13	14.97±0.05	15.13±0.09	24.06±0.20	24.04±0.20	24.24±0.18
Cobalt	10.37±0.23	10.27±0.07	10.25±0.06	-	-	-
Nickel	10.39±0.04	10.13±0.16	10.21±0.14	7.54±0.17	7.54±0.04	7.62±0.15
Molybdenum	-	-	-	0.10±0.02	0.16±0.02	0.20±0.08
Tungsten	0.12±0.04	0.09±0.04	0.13±0.06	-	-	-
Niobium	0.47±0.04	0.44±0.09	0.40±0.03	-	-	-
Element	**Al_{14}(CrMnFeNi)+60TiC**			**AlCuCrFeNi+60TiC**		
	Run1	*Run2*	*Run3*	*Run1*	*Run2*	*Run3*
Carbon	6.44±0.06	6.21±0.06	6.16±0.43	11.44±0.11	10.34±0.11	10.38±0.42
Oxygen	8.20±0.07	8.46±0.28	9.65±0.15	5.39±0.32	5.62±0.17	5.16±0.13
Aluminum	3.04±0.04	3.06±0.04	2.95±0.06	1.93±0.01	1.87±0.03	1.97±0.04
Silicon	0.10±0.03	0.08±0.02	0.12±0.03	0.22±0.01	0.29±0.02	0.08±0.03
Titanium	37.66±0.02	37.64±0.18	37.23±0.35	33.21±0.14	33.28±0.14	33.30±0.23
Chromium	9.02±0.07	9.18±0.07	8.91±0.23	8.41±0.04	8.31±0.04	8.45±0.03
Manganese	5.69±0.09	5.63±0.06	5.04±0.19	0.49±0.06	0.49±0.05	0.48±0.04
Iron	22.61±0.08	22.59±0.32	22.49±0.22	11.40±0.14	11.68±0.26	11.65±0.19
Nickel	6.88±0.09	6.76±0.11	7.06±0.27	17.67±0.15	17.99±0.22	18.35±0.12
Copper	-	-	-	9.83±0.13	10.14±0.15	10.19±0.12
Molybdenum	0.25±0.01	0.32±0.08	0.24±0.02	-	-	-
Tungsten	0.10±0.04	0.07±0.06	0.15±0.02	-	-	-

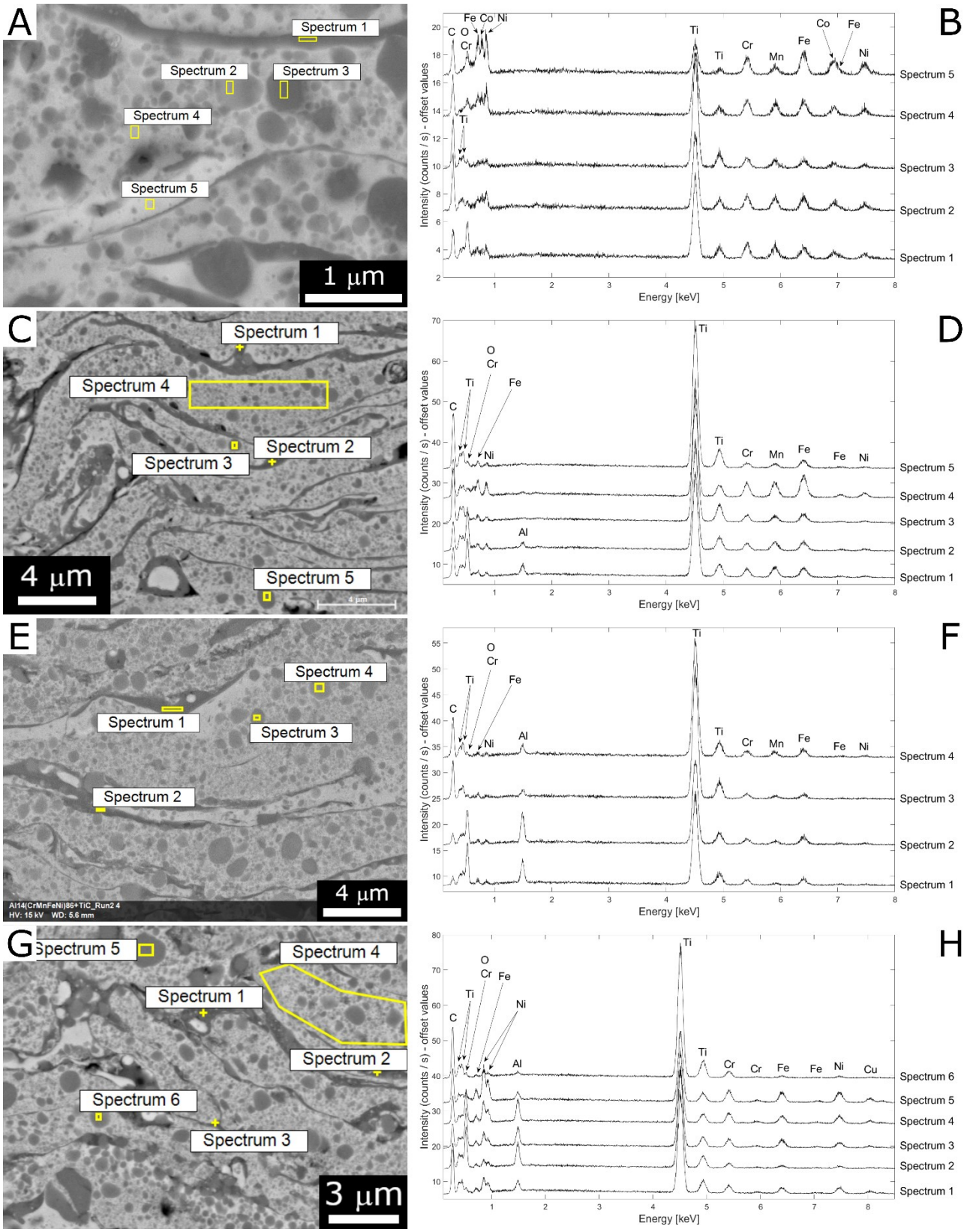

Figure 42: Backscattered-electrons SEM micrographs of the Cantor+60TiC Run2 (A), Al0(CrMnFeNi)+60TiC Run1 (C), Al14(CrMnFeNi)+60TiC Run2 (E), and AlCuCrFeNi+60TiC Run3 (G) coatings, with corresponding EDX spectra (B, D, F, H).

Qualitatively, the Al_{14}(CrMnFeNi)+60TiC coatings appeared slightly more oxidized (Figure 41E), whereas the AlCuCrFeNi+60TiC coatings contained comparatively fewer oxides

(Figure 41H). The other two compositions exhibited intermediate oxide contents (Figure 41B and Figure 40B, E, H). Volumetric quantification of oxide inclusions via image analysis was not feasible due to the similar backscattered-electron contrast between the oxides and TiC, preventing reliable greyscale thresholding. Nevertheless, EDX spectroscopy suggested that the AlCuCrFeNi+60TiC coatings had the lowest oxygen content (~5 wt.%), whereas the Al_{14}(CrMnFeNi)+60TiC coatings exhibited the highest (~8 wt.%) (Table 16). Despite this oxidation, the overall chemical composition remained largely consistent with that of the feedstock powders (compare Table 13 and Table 16), with minor inclusions of W, Mo, and Nb that are not expected to significantly influence coating properties.

Even accounting for Ti-based oxide formation and partial carbide dissolution, the coatings preserved most of the original TiC particles, including the finest ones, as evident in Figure 40C, F, I and Figure 41C, F, I. In some cases, the EDX spectra highlighted an intensified Cr peak within certain TiC particles compared to the surrounding matrix, confirming the occasional incorporation of Cr into the carbide lattice observed in the powders (Figure 42G, H: spectrum 6).

XRD analyses confirmed that TiC remained the primary phase in all coatings (Figure 3). However, semi-quantitative Rietveld refinement (Table 14) indicated a reduction in TiC content relative to the powders. Additionally, a hexagonal decarburized TiC_{1-x} phase was detected in all coatings except AlCuCrFeNi+60TiC, suggesting that the decrease in TiC resulted from a combination of oxidation, dissolution, and decarburization. The Cantor+60TiC and Al_0(CrMnFeNi)+60TiC coatings, which exhibited the largest TiC losses, correspondingly contained the highest amounts of TiC_{1-x}. In contrast, the AlCuCrFeNi+60TiC coatings showed minimal TiC_{1-x} formation and lower carbon loss, suggesting a lower degree of carbide alteration by any of the possible mechanisms.

The observed variations in TiC retention may be linked to the narrower particle size distribution of the AlCuCrFeNi+60TiC feedstock (Section 3.1.b.), which reduced the fraction of fine particles susceptible to overheating and oxidation, and/or to the specific matrix composition. In particular, aluminium appears to play a key role in limiting decarburization, as TiC loss and TiC_{1-x} formation were consistently lower in the Al-containing matrices.

Regarding the matrix, HVOF spraying promoted melting and re-solidification, reducing the BCC fraction induced by HEBM and shifting the phase composition toward FCC-dominant structures. Indeed, the Cantor+60TiC and Al_0(CrMnFeNi)+60TiC coatings contained negligible BCC content (≤2.5 wt.%), whereas AlCuCrFeNi+60TiC was almost purely FCC (<1 wt.% BCC). The Al_{14}(CrMnFeNi)+60TiC coatings retained both BCC and FCC phases,

with FCC accounting for ~45% of the matrix. Rapid quenching from the molten state likely facilitated FCC retention, despite thermodynamic expectations.

Oxides were also detected in XRD patterns (Figure 39A–C) as sub-stoichiometric Ti_2O_3 or ilmenite-type $MTiO_3$ phases, with M representing transition metals such as Fe or Ni. Unlike the metallic systems discussed earlier, where oxide formation predominantly involved the metallic constituents, the cermet compositions exhibit a markedly different oxidation behaviour. Owing to their high TiC content, the strong oxygen affinity of Ti makes it the primary oxide-forming element in all cases, even in formulations containing Al; as also suggested by the EDX analyses, Ti systematically dominates the oxide chemistry, a trend that could not be directly appreciated in the individual articles due to the absence of a side-by-side comparison. Nevertheless, aluminium, when present, can still be incorporated into these oxides, which may contribute to protecting TiC from decarburization and thus to the reduced TiC loss observed in Al-containing formulations.

3.3. b. Micro- and nano-mechanical properties

Vickers micro-indentation tests revealed that the coatings exhibited hardness values in the range of approximately 750 to 900 HV (Table 17). Among the investigated systems, the Cantor+60TiC coatings displayed the highest hardness, being the only samples with values approaching 900 HV, while the other compositions showed hardness values mostly between 750 and 800 HV. The differences in hardness can be interpreted as the combined effect of compositional variations and microstructural features, including the degree of TiC retention, the fraction of oxide inclusions, and the distribution of residual stresses induced by the HVOF process.

Table 17: Vickers microhardness (HV) by depth-sensing Vickers micro-indentation, elastic modulus (EIT) by spherical nano indentation and critical loads (LC) by scratch testing (mean ± standard deviation).

Sample ID	$HV_{0.3}$	E_{IT} [GPa]	L_c [N]
Cantor+60TiC Run1	884±91	238±6	12.1±1.3
Cantor+60TiC Run2	933±102	223±5	13.4±1.5
Cantor+60TiC Run3	904±97	219±5	13.4±1.4
Al_0(CrMnFeNi)+60TiC Run1	745±81	201±5	8.7±0.7
Al_0(CrMnFeNi)+60TiC Run2	786±82	208±6	9.0±1.0
Al_0(CrMnFeNi)+60TiC Run3	816±70	197±3	10.1±0.6
Al_{14}(CrMnFeNi)+60TiC Run1	747±80	191±5	12.0±1.4
Al_{14}(CrMnFeNi)+60TiC Run2	813±60	205±6	9.4±2.0
Al_{14}(CrMnFeNi)+60TiC Run3	740±73	191±5	10.0±1.6
AlCuCrFeNi+60TiC Run1	772±78	209±5	13.6±2.3
AlCuCrFeNi+60TiC Run2	793±64	229±5	14.6±2.1
AlCuCrFeNi+60TiC Run3	819±77	228±6	13.0±1.1

The elastic modulus values were generally around 200 GPa (Table 17). Although the elastic modulus is not a direct measure of toughness, previous investigations [174] demonstrated that, in thermal-sprayed coatings, the depth-sensing indentation technique tends to yield lower apparent moduli for brittle materials. This is due to the occurrence of microcracking or inelastic failure beneath the indenter during the loading phase, which leads to an underestimation of the true elastic response.

The differences in toughness among the samples were more clearly evidenced by the scratch tests. As shown in previous work on TiC-based hardmetals [175], variations in critical load obtained in progressive loading mode correlate well with the coatings' resistance to brittle fracture under functional conditions, such as abrasion. Optical inspection of the scratch tracks (Figure 43) revealed that the critical load (LC) for these coatings corresponded to the onset of systematic chipping along the track edges. It is essential to distinguish such continuous chipping from isolated events, which, according to ISO 20502, represent localized failures not followed by further damage propagation. These isolated

events are typical of thermal-sprayed coatings, where random defects, including pores or weakly bonded splats, may act as local stress concentrators leading to premature micro-failure.

Taking this into account, it is evident from Figure 43 that the Cantor+60TiC coatings (panel A) and the AlCuCrFeNi+60TiC coatings (panel D) exhibited markedly higher critical loads for the onset of chipping compared to the Al_0(CrMnFeNi)+60TiC (panel B) and Al_{14}(CrMnFeNi)+60TiC (panel C) coatings. This observation was confirmed quantitatively by the mean LC values reported in Table 17, where the Al_0(CrMnFeNi)+60TiC and Al_{14}(CrMnFeNi)+60TiC coatings generally exhibited critical loads between 8 and 10 N, whereas the Cantor+60TiC and AlCuCrFeNi+60TiC coatings reached higher LC values, in the range of 12 to 14 N. These results clearly indicate that the Al_{14}(CrMnFeNi)+60TiC coatings were indeed more brittle than the others, and that a similar behaviour was also observed for the Al_0(CrMnFeNi)+60TiC ones.

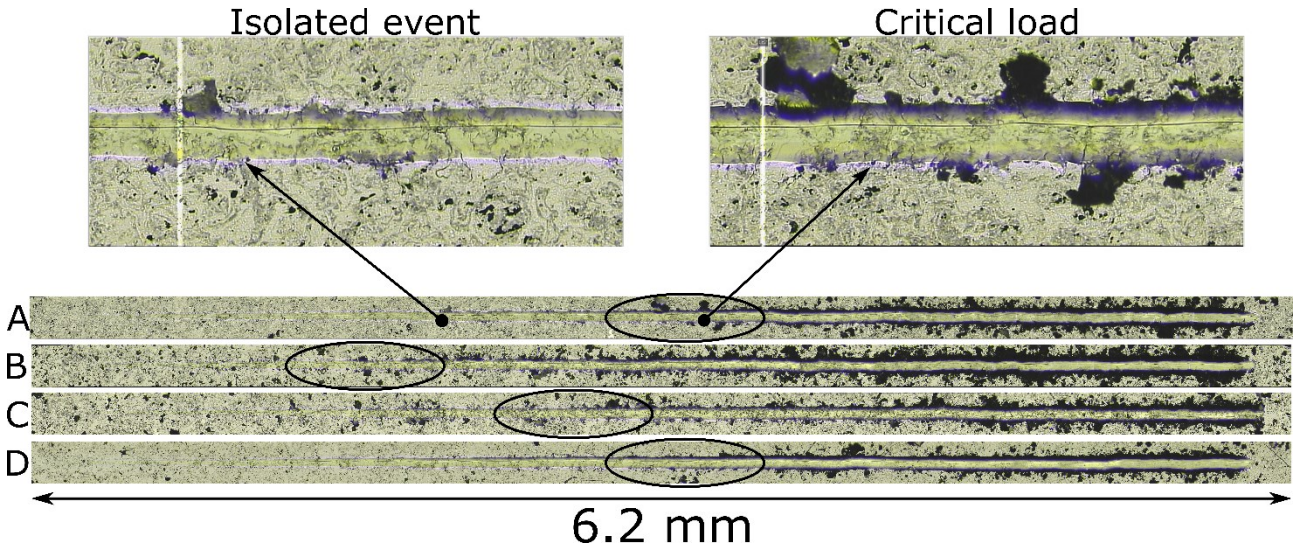

Figure 43: Stitching of optical images showing overviews of scratch tracks on samples Cantor+60TiC Run2 (A), Al0(CrMnFeNi)+60TiC Run2 (B), Al14(CrMnFeNi)+60TiC Run1 (C), and AlCuCrFeNi+60TiC Run2 (D). Magnified details show the criterion to identify a critical load, differentiating it from an isolated event caused by local inhomogeneities unavoidable in a thermal spray coating.

As for the metallic coatings, a deeper understanding of the coatings' fine-scale mechanical response was obtained through high-speed nanoindentation tests on selected samples. In fact, once again, this technique, by enabling a very high number of indentations, allows the identification of distinct mechanical phases through statistical deconvolution using a Gaussian Mixture Model (GMM), as illustrated in Figure 45. The resulting "mechanical phases" correspond to regions in the material that are mechanically homogeneous, though not necessarily coinciding with specific crystallographic phases.

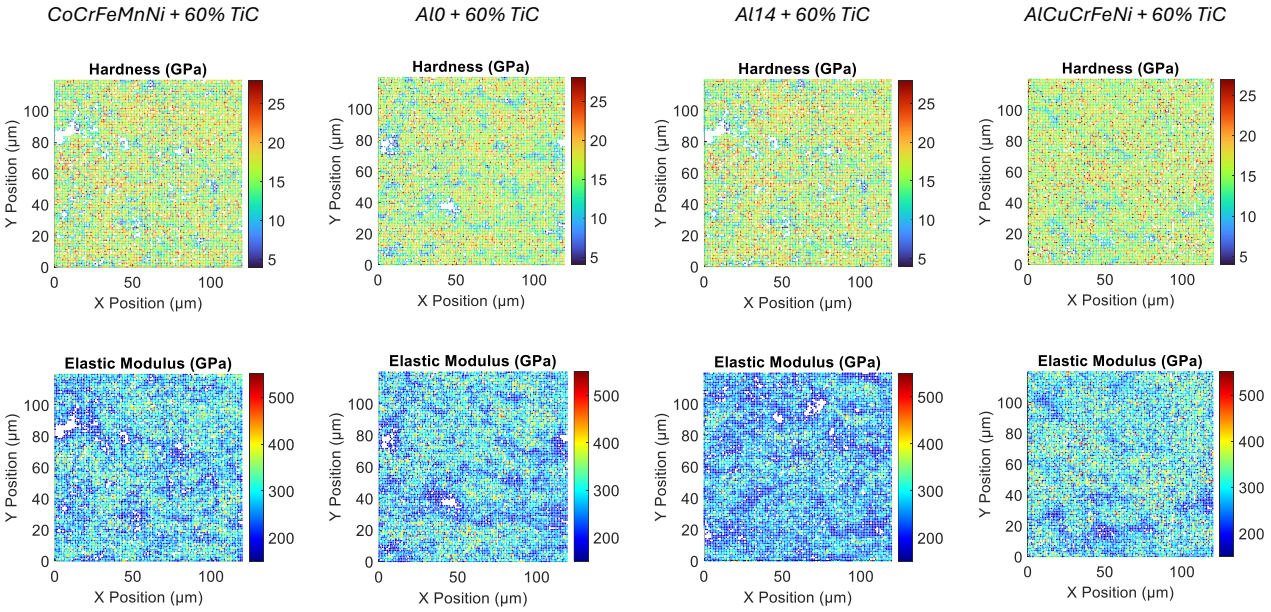

Figure 44: Hardness and elastic modulus maps obtained from high-speed nanoindentation with 1 µm spacing between indents. Note: the represented areas are cropped from the actual map sizes, and all samples have been standardized to the same region of interest (ROI) to illustrate comparative differences effectively.

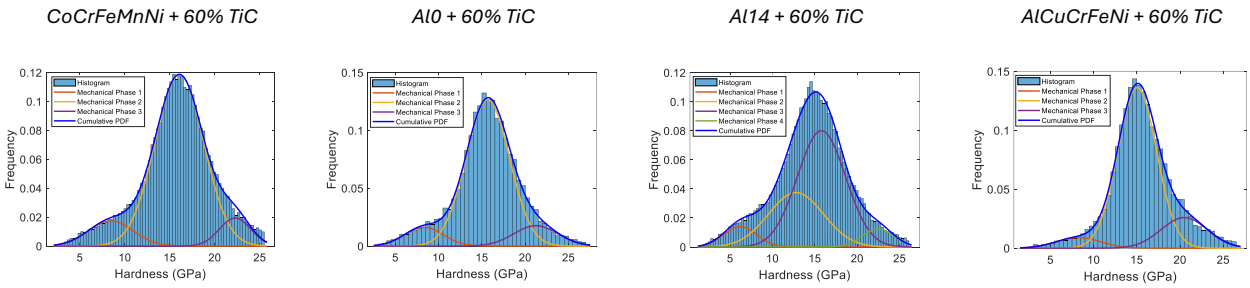

Figure 45: Distributive curves of indentation hardness obtained by high-speed nanoindentation on the four samples, analysed with the GMM algorithm: in each image, the histogram with the fractions of indentations included in each range of values, the histogram-fitting curve, cumulative individual distributions, and the Gaussian fit of individual distributions are shown.

The Al_{14}(CrMnFeNi)+60TiC coating was selected as a representative example due to its complex and comprehensive mechanical behaviour, which makes it a suitable reference for interpreting the results obtained from other coatings. In this sample, four main mechanical phases were identified (Table 18). The first, with an average nano-hardness of about 6.2 GPa, can be attributed to the softer, ductile FCC phase of the metallic matrix. The second phase, showing a hardness of approximately 12.8 GPa, corresponds to the harder BCC phase, typical of Al-rich regions. The third mechanical phase, which contained most of the indentation data, exhibited an intermediate hardness of about 15.8 GPa and likely represented the combined response of the matrix and fine TiC particles, whose sizes fall in the nano- or submicron range. This behaviour is consistent with previous studies on high-speed nanoindentation[145], in which statistical analysis of large datasets allows distinguishing between mixed (interfacial) and intrinsic phase responses. The fourth

mechanical phase corresponded to indents located entirely within the largest TiC particles, yielding a hardness of about 22.4 GPa. This value aligns well with the lower bound of the literature range for TiC hardness (2600–3200 HV)[176], [177], confirming the accuracy and reliability of the present analysis, despite the possible influence of the surrounding matrix on the measured response.

As shown in Table 18, coatings characterized by a purely or nearly purely FCC matrix did not exhibit the second mechanical phase associated with BCC. Nonetheless, the hardness values corresponding to the FCC phase (first distribution) and the TiC particles (fourth distribution) were comparable across all coatings, corroborating the interpretation of the data and suggesting that the intrinsic properties of the TiC phase were essentially unaffected by the surrounding metallic matrix.

Table 18: Results of GMM deconvolution to identify mechanical phases from high-speed nanoindentation data.

Sample	E_{IT} [GPa]				H_{IT} [GPa]			
	Phase 1	Phase 2	Phase 3	Phase 4	Phase 1	Phase 2	Phase 3	Phase 4
Cantor +60TiC Run3	169±34	-	270±50	370±35	8.4±2.5	-	16.1±2.7	22.3±1.8
Al_0(CrMnFeNi) +60TiC Run3	207±37	-	276±51	391±29	8.3±2.2	-	15.7±2.5	21.2±2.6
Al_{14}(CrMnFeNi) +60TiC Run3	143±20	216±33	275±33	346±19	6.2±2	12.8±3.2	15.8±2.8	22.4±1.9
AlCuCrFeNi +60TiC Run3	221±41	-	283±54	399±27	8.27±1.7	-	15.0±2.1	20.5±2.2

This apparent increase in hardness can be attributed to three main factors. Firstly, the indentation size effect leads to higher hardness values at small penetration depths, as typical in nanoindentation testing[178]. Secondly, even the nanoindentations primarily falling on the metallic regions were likely influenced by the presence of nearby TiC or TiC_{1-x} particles, whose fine distribution within the matrix increased local constraint and thus apparent hardness. Finally, the high strain rates characteristic of high-speed nanoindentation (on the order of 3 s^{-1}) [145] are known to enhance the measured hardness and modulus of strain-rate-sensitive phases. This is particularly relevant for CoCrFeMnNi-based alloys, such as the Cantor composition, whose mechanical response is strongly dependent on strain rate, temperature, and grain size[179].

The higher hardness observed in the BCC phase of the Al_{14}(CrMnFeNi)+60TiC coatings, likely accompanied by reduced ductility, offers a plausible explanation for their lower toughness and critical load values obtained in the scratch tests. Additionally, the comparatively high Fe content in both the Al_{14}(CrMnFeNi)+60TiC and Al_0(CrMnFeNi)+60TiC

coatings may have contributed to their brittle behaviour. This interpretation is consistent with previous findings on simpler metallic systems, where Fe-rich matrices were found to be more brittle than Ni-rich ones [99], [101], [136]. Such behaviour thus appears to be systematic and recurrent, extending to both HEA and non-HEA formulations.

3.4. b. Sliding and abrasive wear behaviour

In both sliding (Figure 46) and abrasive (Figure 47) wear tests, the coatings exhibited a ranking that closely mirrored the trend observed in the scratch experiments. The Al_0(CrMnFeNi)+60TiC and Al_{14}(CrMnFeNi)+60TiC compositions, regardless of the deposition parameters employed, displayed higher specific wear rates compared with the Cantor+60TiC and AlCuCrFeNi+60TiC coatings. This correspondence between scratch and wear performance highlights the strong connection between coating brittleness and tribological behaviour. Moreover, the incorporation of TiC within the HEA matrix consistently reduced the wear rate by at least one order of magnitude, confirming the strong strengthening effect provided by the ceramic phase (3.4.a.). Interestingly, the overall wear-rate hierarchy imposed by the HEA matrix itself remained essentially unchanged, irrespective of the presence or absence of the TiC reinforcement.

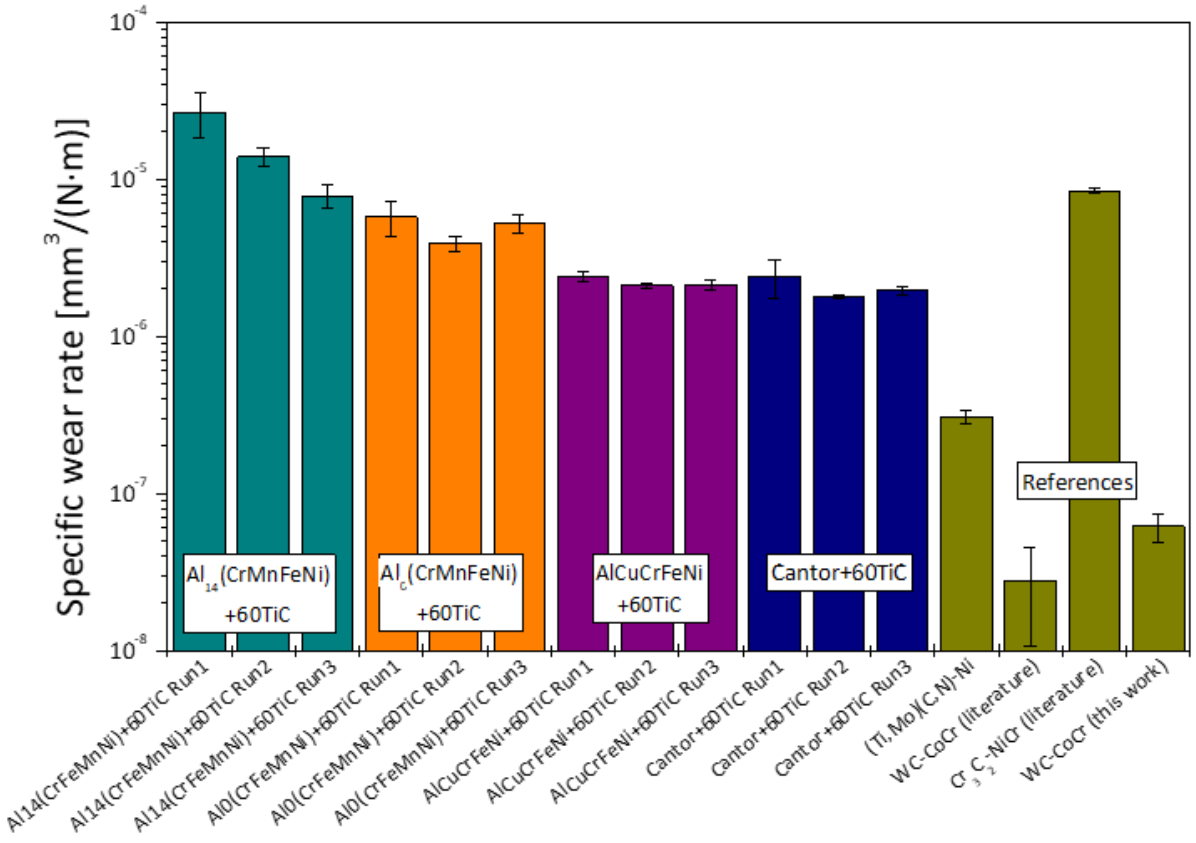

Figure 46: Specific wear rates measured by ball-on-disc testing on all hardmetal coatings, compared to reference data measured under similar conditions in [175] *((Ti,Mo)(C,N)-Ni) and* [136] *(WC-CoCr and Cr3C2-NiCr).*

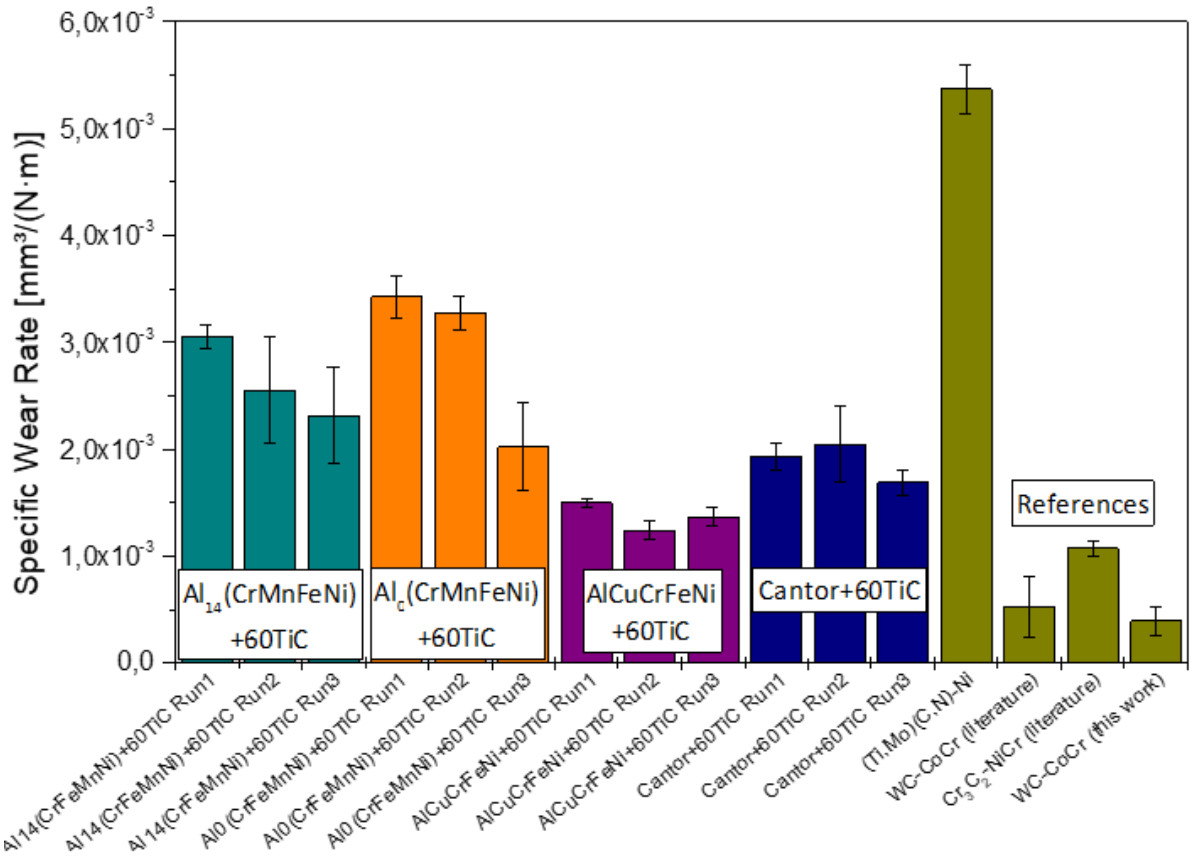

Figure 47: Specific wear rates measured by steel-wheel abrasion testing on all hardmetal coatings, compared to reference data measured under similar conditions in [175] *((Ti,Mo)(C,N)-Ni) and* [136] *(WC-CoCr and Cr3C2-NiCr).*

Under sliding wear conditions, the surfaces of the Al_0(CrMnFeNi)+60TiC (Figure 48C, D) and Al_{14}(CrMnFeNi)+60TiC (Figure 48E, F) coatings were characterized by the presence of numerous micropits, some of which are highlighted in the micrographs. The dominant wear mechanism in these coatings was therefore surface fatigue, associated with the nucleation and propagation of fatigue cracks leading to micropitting. Such a mechanism tends to progress more rapidly in brittle materials, where the ability to dissipate strain energy through plastic deformation at the crack tip is limited, thus promoting easier crack growth. In contrast, the comparatively tougher Cantor+60TiC (Figure 48A, B) and AlCuCrFeNi+60TiC (Figure 48G, H) coatings exhibited very few micropits even under the relatively severe contact conditions employed, characterized by high initial Hertzian contact pressures. In these tougher coatings, wear mainly took the form of abrasive grooving, likely due to their hardness being somewhat below 1000 HV (Section 3.3.b.), which is lower than that typically reported for conventional hardmetal coatings.

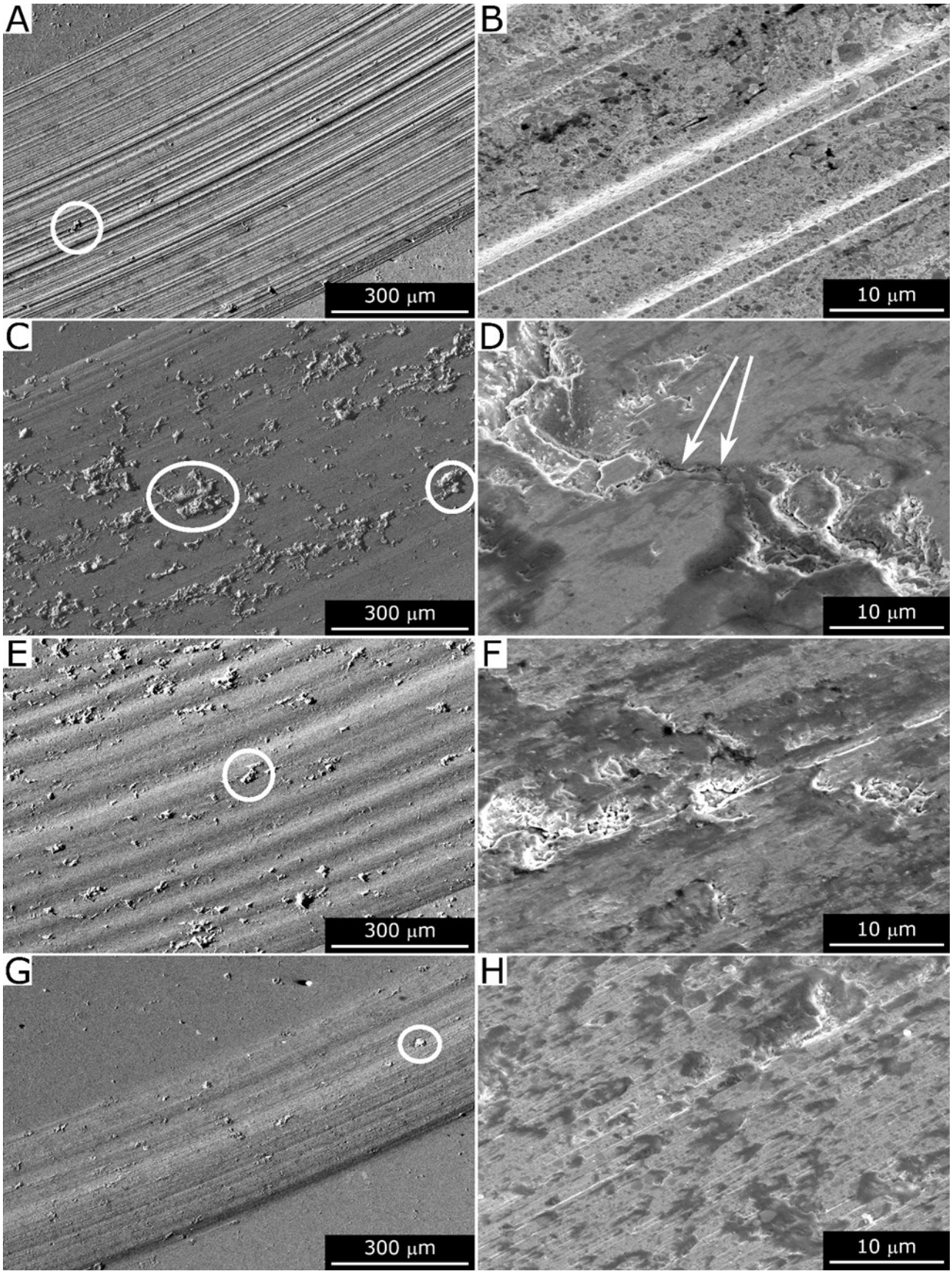

Figure 48: SEM micrographs of the ball-disc wear tracks produced on samples Cantor+60TiC Run3 (A, B), Al0(CrMnFeNi)+60TiC Run1 (C, D), Al14(CrMnFeNi)+60TiC Run3 (E, F), and AlCuCrFeNi+60TiC Run3 (G, H). Overviews (A, C, E, G) and magnified views (B, D, F, H). Circles indicate micropits; arrows in panel D indicate a crack.

In addition to fatigue and abrasion, some tribo-oxidation also occurred during sliding, as indicated by the presence of oxide clusters on the worn surfaces, often located within the pits (Figure 49A, B: spectra 1, 3, 4; Figure 49C, D: spectra 1, 2). The composition of these tribologically induced oxides differed from that of the oxide inclusions observed in Figure 42. While the inclusions were enriched in titanium, the tribo-oxidized clusters exhibited an elemental composition more closely resembling that of the bulk coating. Raman spectroscopy further confirmed this difference (Figure 50): the tribo-oxidized clusters were primarily composed of spinel-type mixed oxides, whereas the inclusions mainly consisted of titanium sub-oxides and ilmenite-type phases. This evidence suggests that the clusters formed through a low-speed tribo-oxidation process [180], involving the fine debris generated during sliding. Due to their high surface-to-volume ratio, these small debris particles reacted readily with oxygen, leading to the oxidation of all metallic constituents. This mechanism differs substantially from the high-temperature, spontaneous oxidation observed during deposition, where oxidation is limited to the most reactive element (Ti). A slightly higher Al content was also detected in the tribo-oxidized clusters (Figure 49), which can be attributed to the embedment of debris from the Al_2O_3 counterbody; however, aluminium never became the dominant constituent, since the specific wear rate of the alumina balls remained lower than that of the coatings.

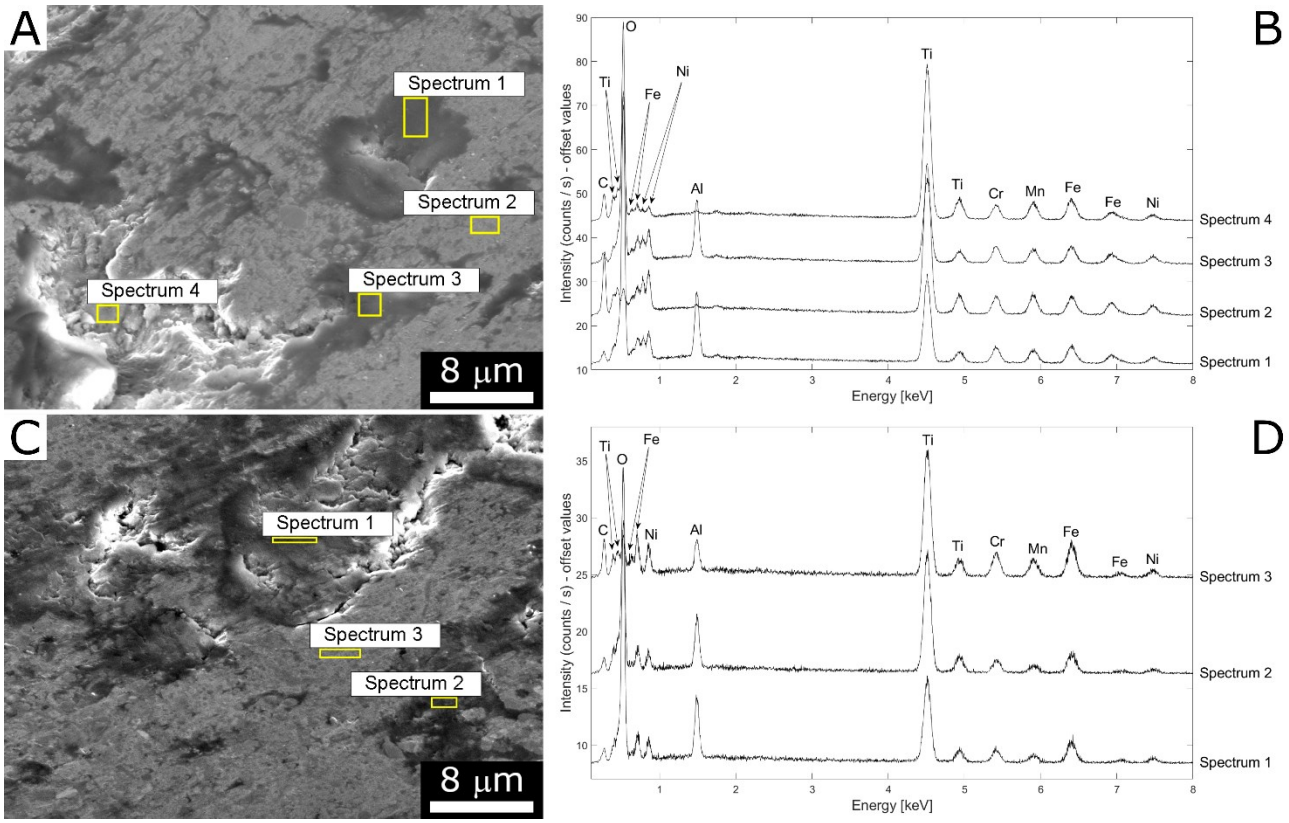

Figure 49: SEM micrographs of the worn surfaces of the Cantor+60TiC Run 2 (A) and Al14(CrMnFeNi)+60TiC Run3 (C) samples after the ball-on disc test, with corresponding EDX spectra (B, D).

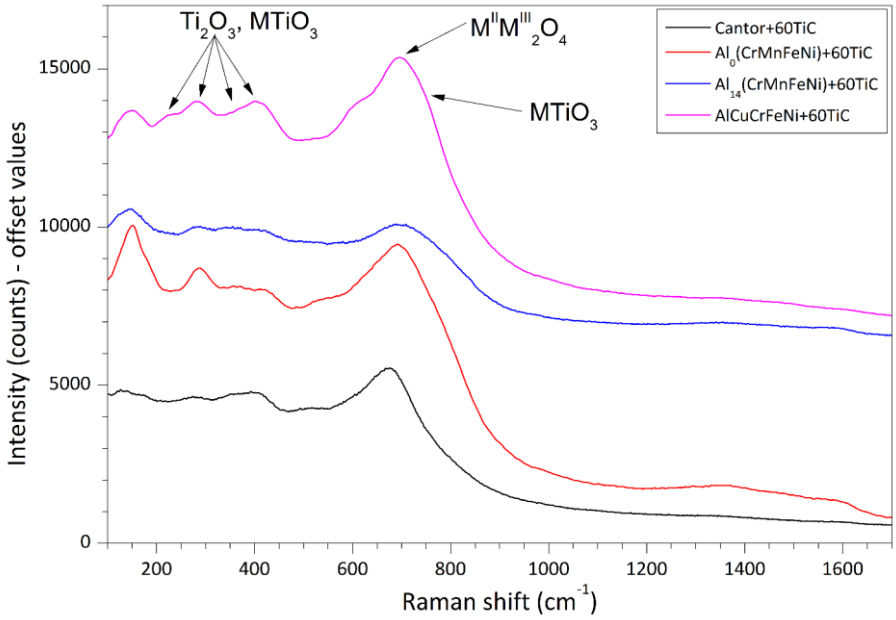

Figure 50: Representative micro-Raman spectra acquired on oxide clusters found on the ball-on-disc sliding wear tracks of samples Cantor+60TiC Run 2, Al0(CrMnFeNi)+60TiC Run1, Al14(CrMnFeNi)+60TiC Run1, and AlCuCrFeNi+60TiC.

The dry particle abrasion tests revealed a combined ductile–brittle wear mechanism across all samples (Figure 51A, C, E). The alumina particles, propelled by the rotating wheel in a high-stress abrasion configuration[99], produced indentation, ploughing, and wedging or chipping on the coating surfaces. Cross-sectional micrographs at higher magnification

(Figure 52B, D, F) showed fragmented Al_2O_3 particles embedded in the surface and chipping away the coating material. Notably, the damage did not extend deeply below the surface, as the overview images (Figure 52A, C, E) revealed no cracks penetrating the interior of the coating.

Although the overall worn surface morphologies appeared broadly similar, some qualitative differences could still be discerned. As shown in Figure 51D, direct brittle fracture occurred more frequently in the coatings identified as more brittle through scratch testing, such as Al_0(CrMnFeNi)+60TiC and Al_{14}(CrMnFeNi)+60TiC. Conversely, the tougher coatings tended to fail through ductile mechanisms, as evidenced by the presence of plastically deformed regions followed by local delamination (Figure 51B and F, arrows), indicative of low-cycle fatigue.

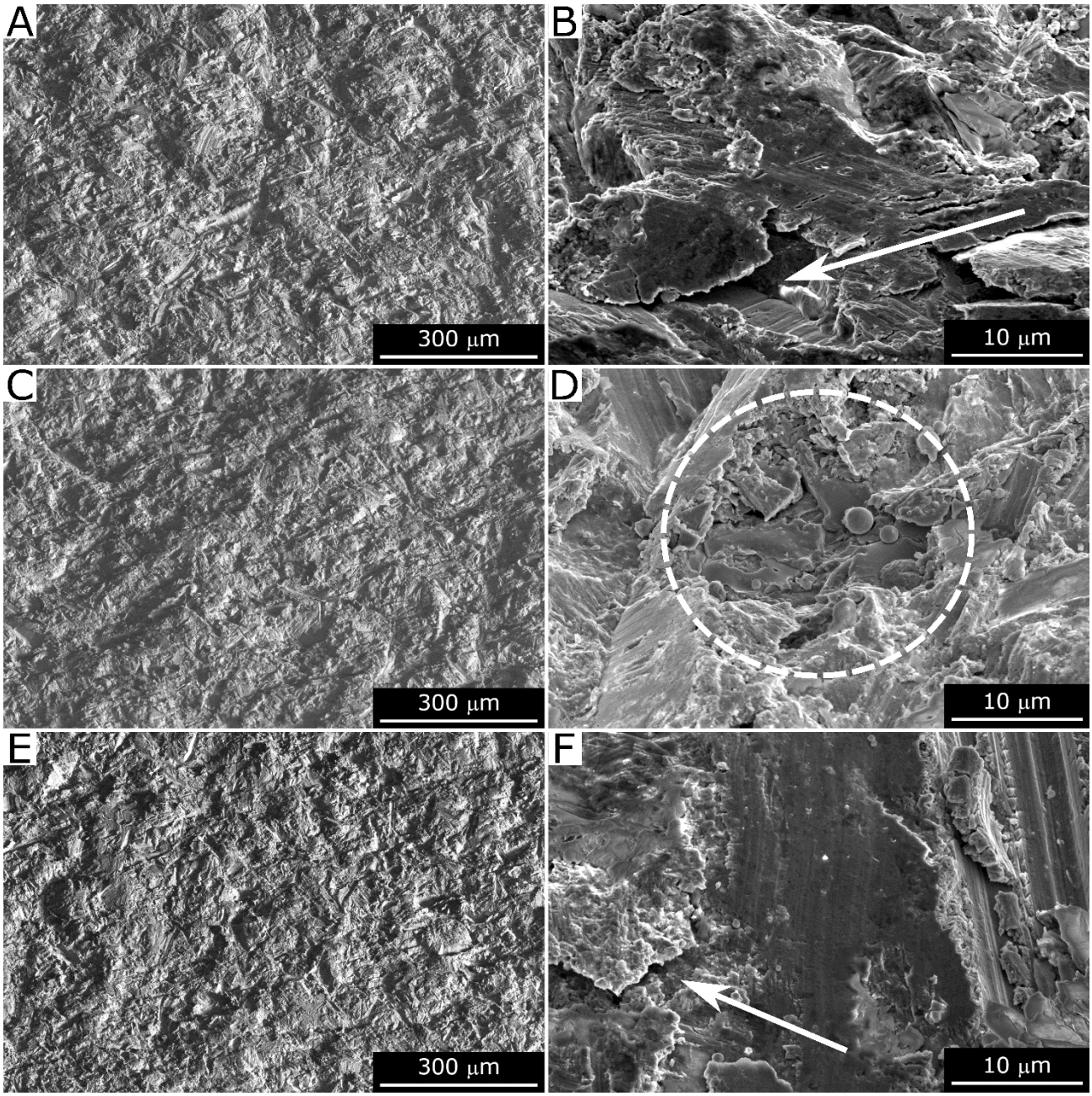

Figure 51: SEM micrographs of the surfaces of the abrasion tracks produced on samples Cantor+60TiC Run2 (A, B), Al_{14}(CrMnFeNi)+60TiC Run1 (C, D), and AlCuCrFeNi+60TiC Run2 (E, F). Overviews (A, C, E) and magnified views (B, D, F). The circle in panel D indicates a brittle fracture area; arrows in panels B and F indicate delamination of plastically fatigued areas.

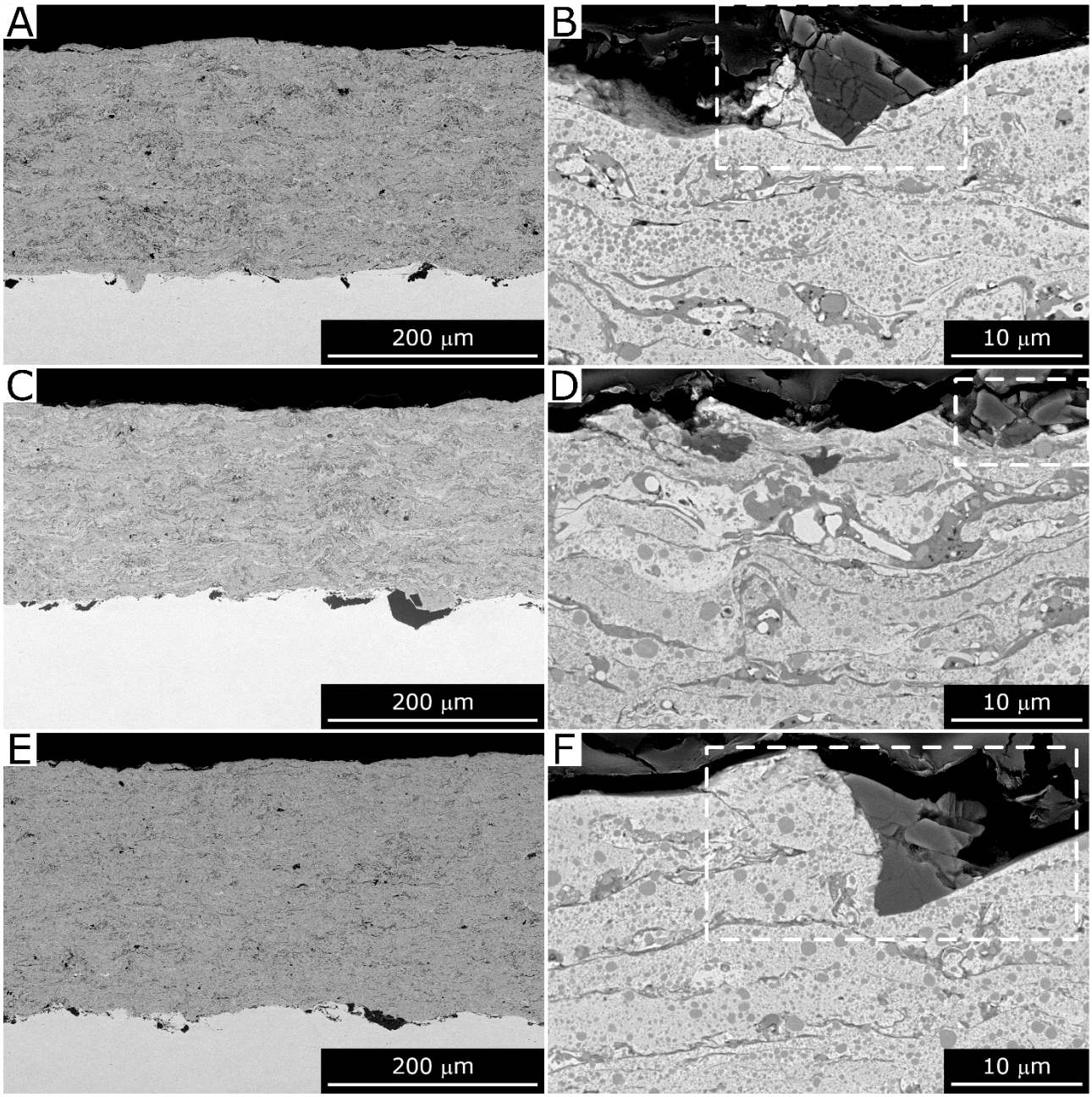

Figure 52: Backscattered-electrons SEM micrographs of the cross-sections of the abrasion tracks produced on samples Cantor+60TiC Run2 (A, B), Al14(CrMnFeNi)+60TiC Run1 (C, D), and AlCuCrFeNi+60TiC Run2 (E, F). Overviews (A, C, E) and magnified views (B, D, F). Dashed rectangles in panels B, D, F show embedded fragments of abrasive particles indenting into and chipping the coatings.

When compared to reference data obtained in this and previous studies, the specific wear rates measured for the Cantor+60TiC and AlCuCrFeNi+60TiC coatings under sliding conditions (Figure 46) were intermediate between those typical of HVOF-sprayed WC–CoCr and Cr_3C_2–NiCr coatings. The WC–CoCr coating tested here displayed a wear rate only slightly higher than that reported in [136], despite differences in test geometry, confirming the reliability of the measurement. The Al_0(CrMnFeNi)+60TiC coatings showed wear rates like those of Cr_3C_2–NiCr, whereas the Al_{14}(CrMnFeNi)+60TiC coatings performed even worse. All the present samples, however, exhibited lower sliding wear resistance than

HVOF-sprayed (Ti,Mo)(C,N)–Ni coatings[175]. These results thus indicate that further optimization of the HEA matrix composition is needed to achieve an appropriate compromise between toughness, necessary to limit surface fatigue, and hardness, which governs the resistance to abrasive grooving.

In contrast, under high-stress abrasive conditions (Figure 47), the performance ranking changed slightly. The Cantor+60TiC and, especially, the AlCuCrFeNi+60TiC coatings exhibited specific wear rates comparable to those reported in [137] for HVOF-sprayed Cr_3C_2–NiCr, and significantly better than those of (Ti,Mo)(C,N)–Ni coatings. The WC–CoCr coating tested in this work also showed a specific wear rate in line with previous data. Particularly remarkable is the similarity between the performance of the AlCuCrFeNi+60TiC and Cr_3C_2–NiCr coatings. In previous studies on TiC-based hardmetals with simpler Ni- or Fe-based matrices [99], [101], [136], [175], the steel-wheel test consistently resulted in poorer performance compared to Cr_3C_2–NiCr due to the intrinsic brittleness of those materials. The present results therefore demonstrate that the AlCuCrFeNi+60TiC coatings, characterized by a low oxide content and a ductile HEA-based FCC matrix, represent a significant improvement in this respect. Further developments aimed at coupling such toughness with slightly increased hardness could yield even better results. In particular, the design of FCC matrices exhibiting twinning-induced or transformation-induced plasticity (TWIP or TRIP effects) appears to be a promising route to achieve the desired balance between hardness and toughness[135], [181].

3.5. b. Electrochemical polarization results

The polarization curves obtained for all coatings exhibited very similar shapes, in sharp contrast with the conspicuous differences observed among the metallic HEA coatings with different compositions. This indicates that the presence of the TiC particles largely affects the electrochemical response, so that, in a cermet coating, the matrix composition has much less relevance on the electrochemical response. Moreover, the deposition parameters also did not significantly influence the polarization response, at least within the parameter ranges investigated in this study (Figure 53). In each case, the anodic branches presented an initial activation stage, which was used to perform the Tafel extrapolation. Specifically, the linear regions of both the anodic and cathodic branches, located approximately between 0.05 and 0.1 V above and below the open circuit potential, were fitted linearly, and the intersection of these extrapolations provided the corrosion potential (E_{Corr}) and the corrosion current density (I_{Corr}), as summarized in Table 19.

Table 19: Corrosion potential (E_{Corr}) and corrosion current density (I_{Corr}) values (average ± half-difference) obtained by Tafel extrapolation from the electrochemical polarization curves.

Sample ID	E_{Corr} [V]	I_{Corr} [μA/cm²]
Cantor+60TiC Run1	-0.447±0.004	5.19±0.58
Cantor+60TiC Run2	-0.410±0.006	4.01±0.22
Cantor+60TiC Run3	-0.385±0.005	3.55±0.14
Al_0(CrMnFeNi)86+60TiC Run1	-0.433±0.003	9.71±0.09
Al_0(CrMnFeNi)86+60TiC Run2	-0.418±0.002	8.15±0.26
Al_0(CrMnFeNi)86+60TiC Run3	-0.414±0.011	10.01±0.51
Al_{14}(CrMnFeNi)+60TiC Run1	-0.463±0.025	11.13±1.50
Al_{14}(CrMnFeNi)+60TiC Run2	-0.443±0.003	6.94±0.49
Al_{14}(CrMnFeNi)+60TiC Run3	-0.467±0.019	6.97±0.16
AlCuCrFeNi+60TiC Run1	-0.261±0.043	4.28±1.29
AlCuCrFeNi+60TiC Run2	-0.321±0.003	2.71±0.02
AlCuCrFeNi+60TiC Run3	-0.293±0.019	2.99±0.40

The measured corrosion potentials were generally comprised between –0.50 and –0.45 V vs. Ag/AgCl/KCl(sat.), except for the AlCuCrFeNi+60TiC coatings, which showed slightly nobler values around –0.30 V. Corrosion current densities were mostly in the 3–10 μA/cm² range, although systematic variations with composition were evident. Specifically, the Al_0(CrMnFeNi)+60TiC and Al_{14}(CrMnFeNi)+60TiC samples displayed higher current densities (≈7–11 μA/cm²), while the Cantor+60TiC and AlCuCrFeNi+60TiC coatings exhibited lower values (≈3–5 μA/cm²).

At overpotentials greater than +0.1 V vs. OCP, the anodic polarization curves entered a pseudo-passive regime, characterized by a gradual increase in current density in the 10^{-5}–

10^{-4} A/cm² range. This quasi-passive behaviour persisted until approximately –0.05 V vs. Ag/AgCl/KCl(sat.), where a marked increase in current density indicated the breakdown of passivity and the onset of transpassive dissolution. Such a sequence of activation, pseudo-passivation, and breakdown was analogous to that previously observed in TiC-based hardmetal coatings with simpler, non-HEA matrices[99], [101], [136], while it differs e.g. from the behaviour of the Al_{14}(CrMnFeNi) metallic coating, which exhibited almost no pseudo-passivity. This means that the TiC particles and, probably, the presence of Ti and C dissolved in the matrix during the HVOF spraying process had a major effect on the electrochemical response of the system.

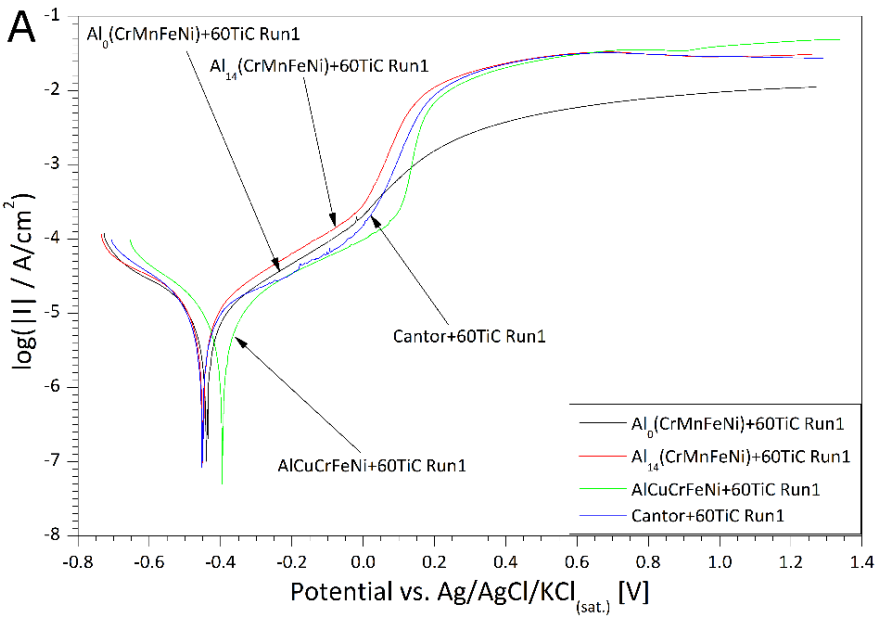
A
Al0(CrMnFeNi)+60TiC Run1
Al14(CrMnFeNi)+60TiC Run1
Cantor+60TiC Run1
AlCuCrFeNi+60TiC Run1
log(|I| / A/cm2)
Potential vs. Ag/AgCl/KCl(sat.) [V]
Al0(CrMnFeNi)+60TiC Run1
Al14(CrMnFeNi)+60TiC Run1
AlCuCrFeNi+60TiC Run1
Cantor+60TiC Run1

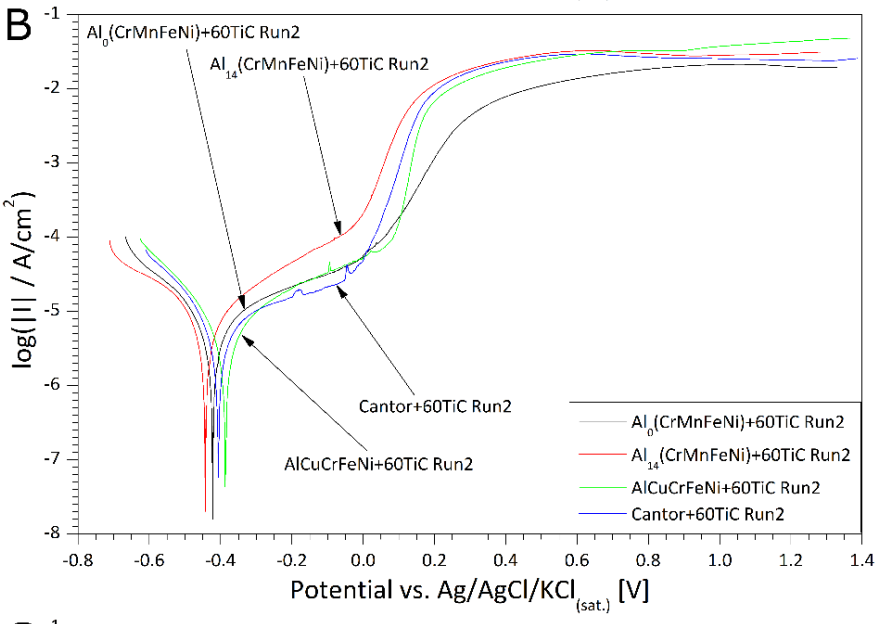
B
Al0(CrMnFeNi)+60TiC Run2
Al14(CrMnFeNi)+60TiC Run2
Cantor+60TiC Run2
AlCuCrFeNi+60TiC Run2
log(|I| / A/cm2)
Potential vs. Ag/AgCl/KCl(sat.) [V]
Al0(CrMnFeNi)+60TiC Run2
Al14(CrMnFeNi)+60TiC Run2
AlCuCrFeNi+60TiC Run2
Cantor+60TiC Run2

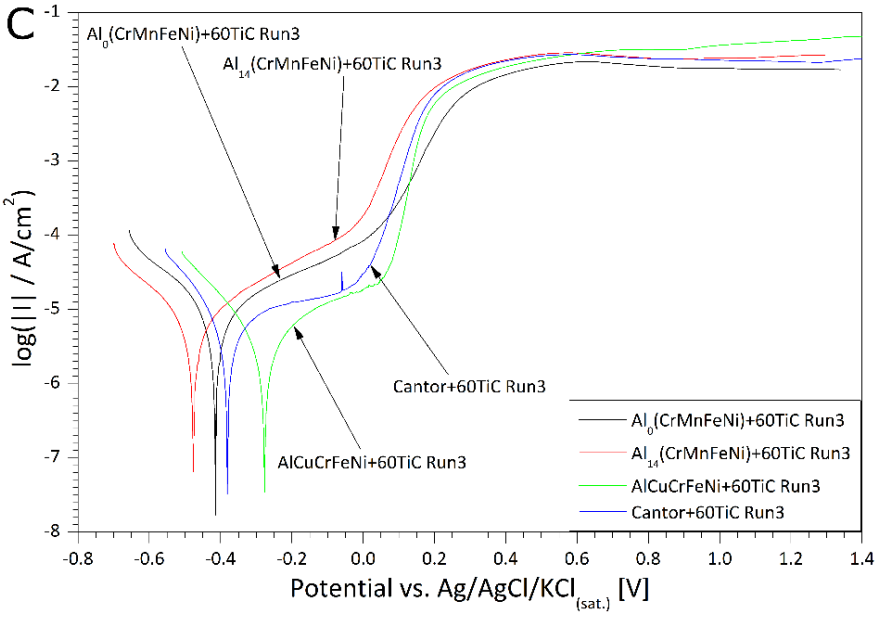
C
Al0(CrMnFeNi)+60TiC Run3
Al14(CrMnFeNi)+60TiC Run3
Cantor+60TiC Run3
AlCuCrFeNi+60TiC Run3
log(|I| / A/cm2)
Potential vs. Ag/AgCl/KCl(sat.) [V]
Al0(CrMnFeNi)+60TiC Run3
Al14(CrMnFeNi)+60TiC Run3
AlCuCrFeNi+60TiC Run3
Cantor+60TiC Run3

Figure 53: Electrochemical polarization curves for all deposition runs of each of the 4 coating materials: Run 1 (A), Run 2 (B), and Run 3 (C).

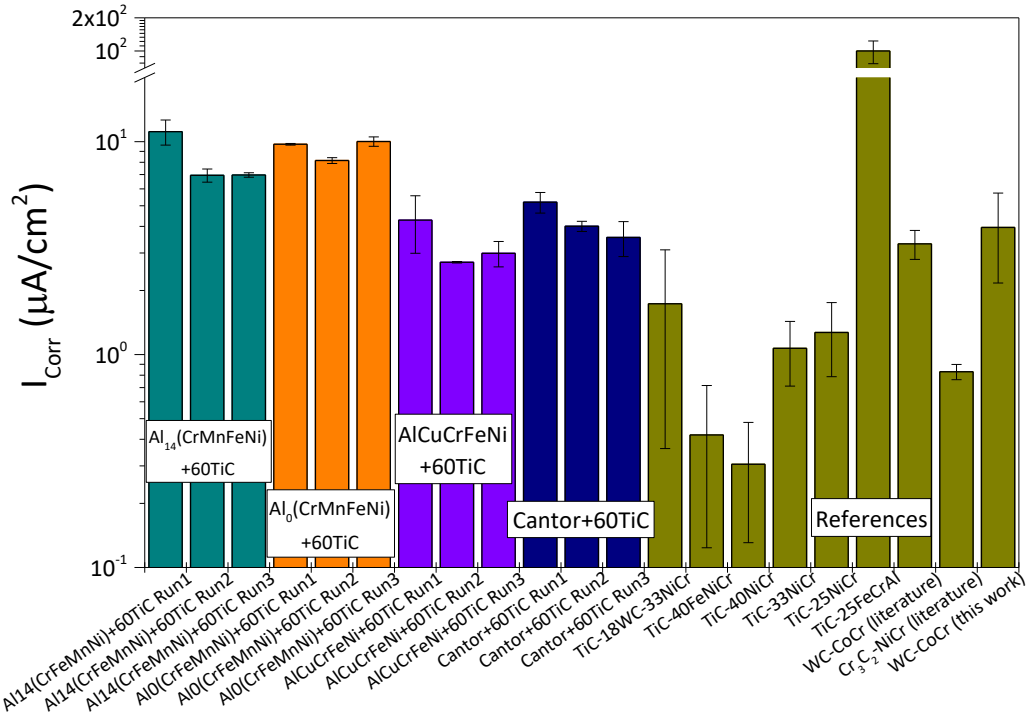

Figure 54: Corrosion current density (I_{Corr}) values for all the hardmetal coatings.

SEM cross-sectional analysis of the coatings after polarization testing confirmed that corrosion progressed through selective dissolution of the metallic matrix, while the TiC phase remained comparatively stable (Figure 55). The resulting morphology was characterized by a uniformly advancing corrosion front, leaving behind fine TiC particles “floating” within a corroded matrix (Figure 55A, C, E, G). Only isolated splats appeared partially unaffected, likely due to local compositional heterogeneities. EDX spectra collected from the corroded areas (Figure 56, spectra 1 and 3) showed intensified oxygen peaks and a marked depletion of matrix elements such as Mn, Fe, and Ni, compared with spectra acquired from uncorroded regions (spectra 2 and 4). The Cr signal, in contrast, became relatively stronger, suggesting that corrosion led to the formation of Cr-enriched oxides, consistent with a selective leaching of Fe, Mn, and Ni during transpassive dissolution. Minor peaks corresponding to Si, S, Ca, and Cl were attributed to polishing residues and to the interaction with the NaCl-containing electrolyte.

Among the different compositions, noticeable differences in the extent of substrate corrosion were observed after the tests. The Al_0(CrMnFeNi)+60TiC and AlCuCrFeNi+60TiC coatings (Figure 55C and G) exhibited significant substrate attack, while the Cantor+60TiC and Al_{14}(CrMnFeNi)+60TiC coatings (Figure 55A and E) remained largely intact. In particular, the Al_0(CrMnFeNi)+60TiC coating showed blistering, likely due to pressure build-up from

corrosion products accumulating at the coating–substrate interface. As the corrosion front advanced, the remaining intact coating layer became thinner and increasingly porous, enabling electrolyte penetration and the onset of localized galvanic or crevice corrosion at the substrate. Despite this evident morphological degradation, the polarization curves did not reflect any substantial differences in current density, even in the transpassive region. This observation suggests that the overall current was dominated by the transpassive dissolution of the matrix, while substrate corrosion, though visually significant, contributed only marginally to the measured current because of its limited exposed area. Therefore, the polarization data can be regarded as representative of the coating's intrinsic electrochemical behaviour.

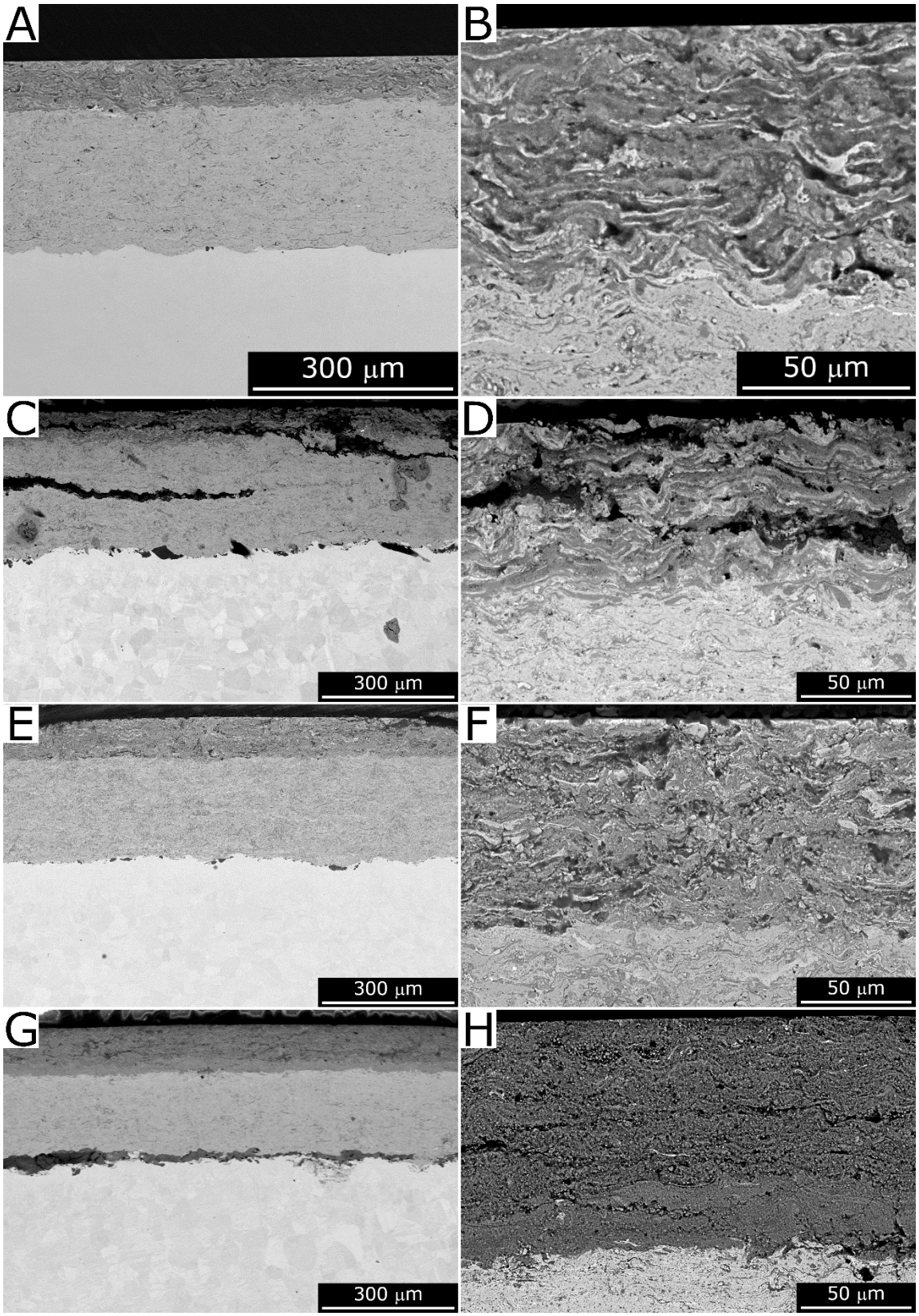

Figure 55: Backscattered-electron SEM micrographs of polished cross-sections of the Cantor+60TiC Run 1 (A, B), Al0(CrMnFeNi)+60TiC (C, D) Run3, Al14(CrMnFeNi)+60TiC Run3 (E, F) and AlCuCrFeNi+60TiC (G, H) samples after electrochemical polarization testing.

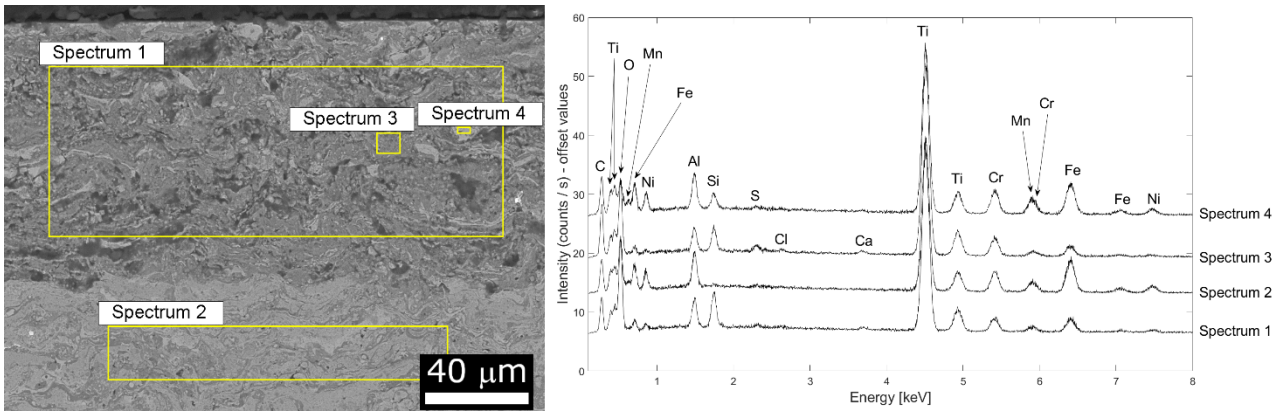

Figure 56: Backscattered-electron SEM micrograph of the polished cross-section of Al_{14}(CrMnFeNi)+60TiC Run3 after electrochemical polarization testing, and the corresponding EDX spectra.

The electrochemical behaviour of the coatings can be further interpreted by comparing the potentials of the individual phases. According to reference [182], the equilibrium potentials of stoichiometric TiC and sub-stoichiometric $TiC_{0.9}$ in 3.5 wt.% NaCl are +0.050 V and +0.105 V vs. Ag/AgCl/KCl(sat.), respectively. These values are significantly higher than the corrosion potentials measured for the coatings, implying that TiC acted as a cathodic phase during polarization. Conversely, HEAs in Al–Cr–Mn–Fe–Co–Ni–Cu systems typically display corrosion potentials between –0.2 and –0.5 V [167], [169], [183]–[186], consistent with the present measurements. Thus, the HEA matrices were anodic with respect to TiC, and the anodic branches of the curves mainly reflected their dissolution behaviour.

When compared with bulk HEAs reported in the literature [167], [169], [183]–[186], the coatings showed an earlier breakdown of passivity and higher pseudo-passive current densities. Bulk HEAs generally exhibit passive current densities below 10^{-5} A/cm² and can maintain passivity up to potentials near 1 V, while the present coatings experienced breakdown at significantly lower potentials. Such differences likely arise from the composite nature and microstructure of the coatings. For example, HEAs with high Cu content, such as AlCuCrFeNi, are known to exhibit poor passivation due to galvanic coupling between Cu-rich and less noble regions [167], [185], while Al-rich HEAs forming BCC+FCC dual phases, such as Al_{14}(CrMnFeNi), also show impaired passivation [167], [169]. Interestingly, in the present study, the expected disparities among compositions were less pronounced: materials predicted to perform poorly (e.g., AlCuCrFeNi) showed improved behaviour, while those expected to passivate effectively (e.g., Cantor-type HEA) exhibited somewhat reduced performance.

This general trend is also reflected in the electrochemical polarization curves obtained in this work (Figure 34). The Cantor coatings displayed the highest rest potential and

developed a short pseudo-passive region, with current densities in the 10^{-6}–10^{-5} A/cm² range up to roughly +200 mV vs. OCP, before entering rapid transpassivation. In contrast, the Al_x(CrMnFeNi) series showed a progressive loss of electrochemical nobility and pseudo-passivity with increasing Al content: Al_0(CrMnFeNi) still formed an unstable pseudo-passive film with frequent metastable pit events, whereas Al_{10} and Al_{14} exhibited nearly continuous activation with minimal passivation. These observations are consistent with the earlier breakdown potentials and higher pseudo-passive current densities measured for the coatings.

This “levelling” effect among the different coatings likely stems from their cermet nature. The impact quenching associated with the HVOF process probably minimized solute segregation, particularly Cu segregation, known to disrupt passivation in bulk HEAs. The dissolution of small amounts of Ti and C from TiC into the metallic matrix, as reported previously for similar systems [99], [166], may have also enhanced corrosion resistance by modifying the matrix chemistry. On the other hand, the limited presence of pores and oxide inclusions could locally hinder passivation compared with dense bulk materials.

Most importantly, the electrochemical behaviour of the coatings appears to have been dominated by micro-galvanic interactions between the anodic HEA matrix and the cathodic TiC particles. These local galvanic couples accelerated matrix oxidation, promoting the formation of passive films even in matrices that would otherwise remain active. Consequently, all coatings exhibited pseudo-passive regions of similar shape and magnitude, regardless of composition. However, these same galvanic effects also facilitated the eventual breakdown of passivity under increasing anodic overpotentials.

This mechanism contrasts with that observed in WC–CoCr hardmetals, where the apparent breakdown of passivity at high potentials actually results from accelerated oxidation of WC, while the CoCr matrix remains passive up to very high overpotentials [187]–[189]. In the present TiC-based systems, by contrast, the breakdown corresponded to a genuine loss of passivity in the metallic matrix, as evidenced by the microstructural observations in Figure 55. Moreover, while the anodic current densities of pure TiC and $TiC_{0.9}$ remain below 10^{-4} A/cm² even at +1 V, the coatings investigated here reached values above 10^{-2} A/cm², confirming that the TiC phase contributed negligibly to the overall current despite its large surface fraction.

Finally, although the polarization curves of all samples followed the same general trend, minor differences could still be discerned as a function of matrix composition. The AlCuCrFeNi+60TiC and Cantor+60TiC coatings consistently showed slightly lower current densities within the pseudo-passive region and lower corrosion current densities in the Tafel analysis (Table 19), indicating a modestly improved corrosion resistance. On the other hand, variations in deposition parameters did not yield any measurable effect on the electrochemical performance, confirming that composition was the main controlling factor.

3.6. b. Chronoamperometry tests

To assess the longer-term stability of the (pseudo-)passive state, chronoamperometric tests were performed on the “Run3” samples from both series. The analysis was restricted to these samples because the previously discussed polarization results showed no significant influence of process parameters. The first overpotential selected for the chronoamperometric test, +0.15 V vs. E_{Corr}, fell within the pseudo-passive region of the polarization curves in Figure 53.

At this applied potential, the current density dropped rapidly within the first two minutes of testing (Figure 57), which is typical of a passivating system. In agreement with the polarization results of Figure 53, the inset in Figure 57 shows that the initial current densities of the AlCuCrFeNi+60TiC and Cantor+60TiC coatings were lower than those of the Al_0(CrMnFeNi)+60TiC and Al_{14}(CrMnFeNi)+60TiC coatings. However, after the initial decrease, the current density of the AlCuCrFeNi+60TiC and Cantor+60TiC coatings stabilized at higher levels. The minimum value of approximately 10^{-6} A/cm² can be attributed to the growth of the pseudo-passive layer, but the subsequent slow increase throughout the test suggests progressive destabilization of this layer in the chloride-rich environment.

In contrast, the current densities of the Al_0(CrMnFeNi)+60TiC and Al_{14}(CrMnFeNi)+60TiC coatings became negative (slightly above -1×10^{-5} A/cm²), i.e. cathodic, and although they slowly increased during the test, they remained negative until its conclusion. This indicates that the early-stage passive film was sufficiently stable and protective to increase the practical nobility of the samples: at a fixed potential of +0.15 V above their initial OCP, the samples themselves became cathodic relative to the reference electrode. In other words, the passive film made the samples so noble that the imposed potential effectively acted as a cathodic overpotential. Thus, despite their initially higher current densities, the Al_0(CrMnFeNi)+60TiC and Al_{14}(CrMnFeNi)+60TiC samples exhibited far superior long-term stability.

Accordingly, at the end of the test, the Al_0(CrMnFeNi)+60TiC and Al_{14}(CrMnFeNi)+60TiC coatings showed no corrosion visible to the naked eye. By contrast, reddish corrosion products were observed on the AlCuCrFeNi+60TiC and Cantor+60TiC coatings, and their chronoamperometric curves displayed not only positive and increasing current densities but also spike-like transients indicative of pit formation. Consistently, the Cantor+60TiC coating, whose curve exhibited more current spikes, showed more reddish corrosion products.

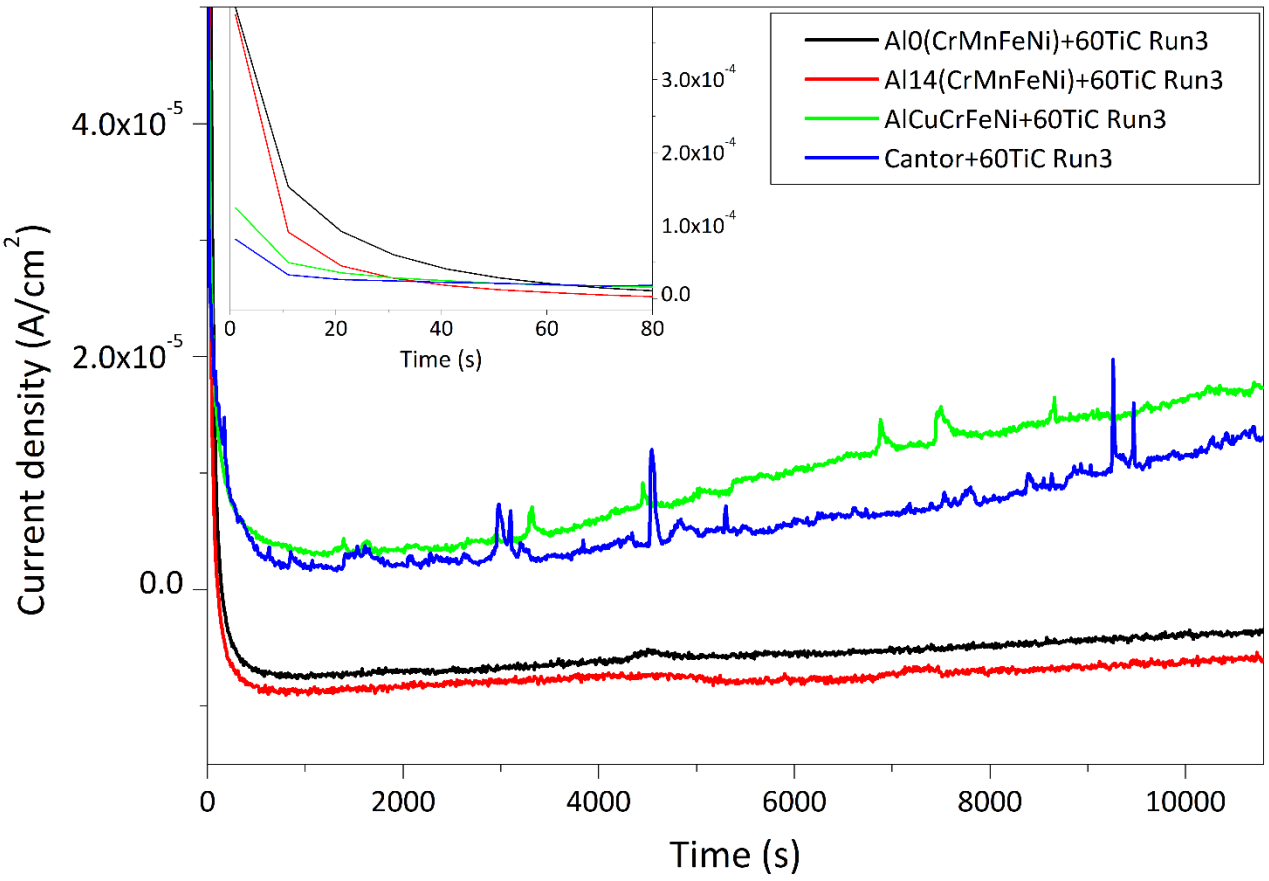

Figure 57: Chronoamperometric curves (current density vs. time) recorded at a fixed overpotential of +0.15 V vs. OCP on the AlCuCrFeNi+60TiC Run3, Cantor+60TiC Run3, Al_0(CrMnFeNi)+60TiC Run3 and Al_{14}(CrMnFeNi)+60TiC Run3 samples.

SEM+EDX analysis of the Cantor+60TiC and AlCuCrFeNi+60TiC surfaces after chronoamperometry at +0.15 V vs. OCP revealed localized accumulations of Fe-, O-, and Cl-rich corrosion products (Figure 58: spectra 1–4, 6). Micro-Raman spectra (Figure 59A, spectra 1 and 2) confirmed the presence of hematite and magnetite, with peak assignments following de Faria et al [190]. These products originated from substrate corrosion: pits developing in the coating allowed the electrolyte to penetrate and attack the underlying substrate, following a crevice corrosion mechanism. The polarization curve of the Cantor+60TiC coating (Figure 53) also exhibited spikes consistent with transient pit nucleation.

Fe-based corrosion products were less common on the AlCuCrFeNi+60TiC coating, consistent with the fewer current spikes seen in its chronoamperometric curve (Figure 57). One pit is shown in Figure 59B (spectrum 2).

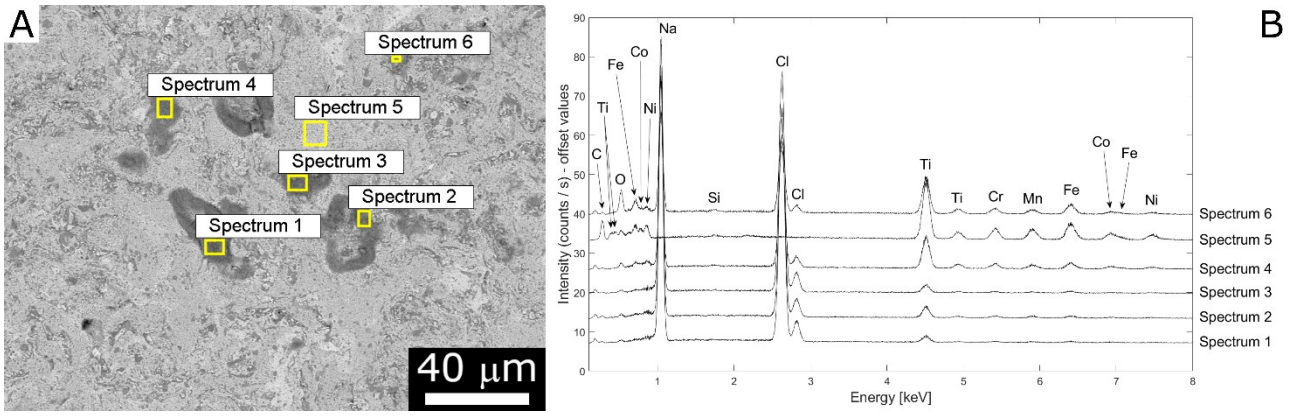

Figure 58: SEM micrograph acquired on the surface of the Cantor+60TiC Run3 sample after the chronoamperometric test at +0.15 V vs. OCP (A), and the corresponding EDX spectra (B).

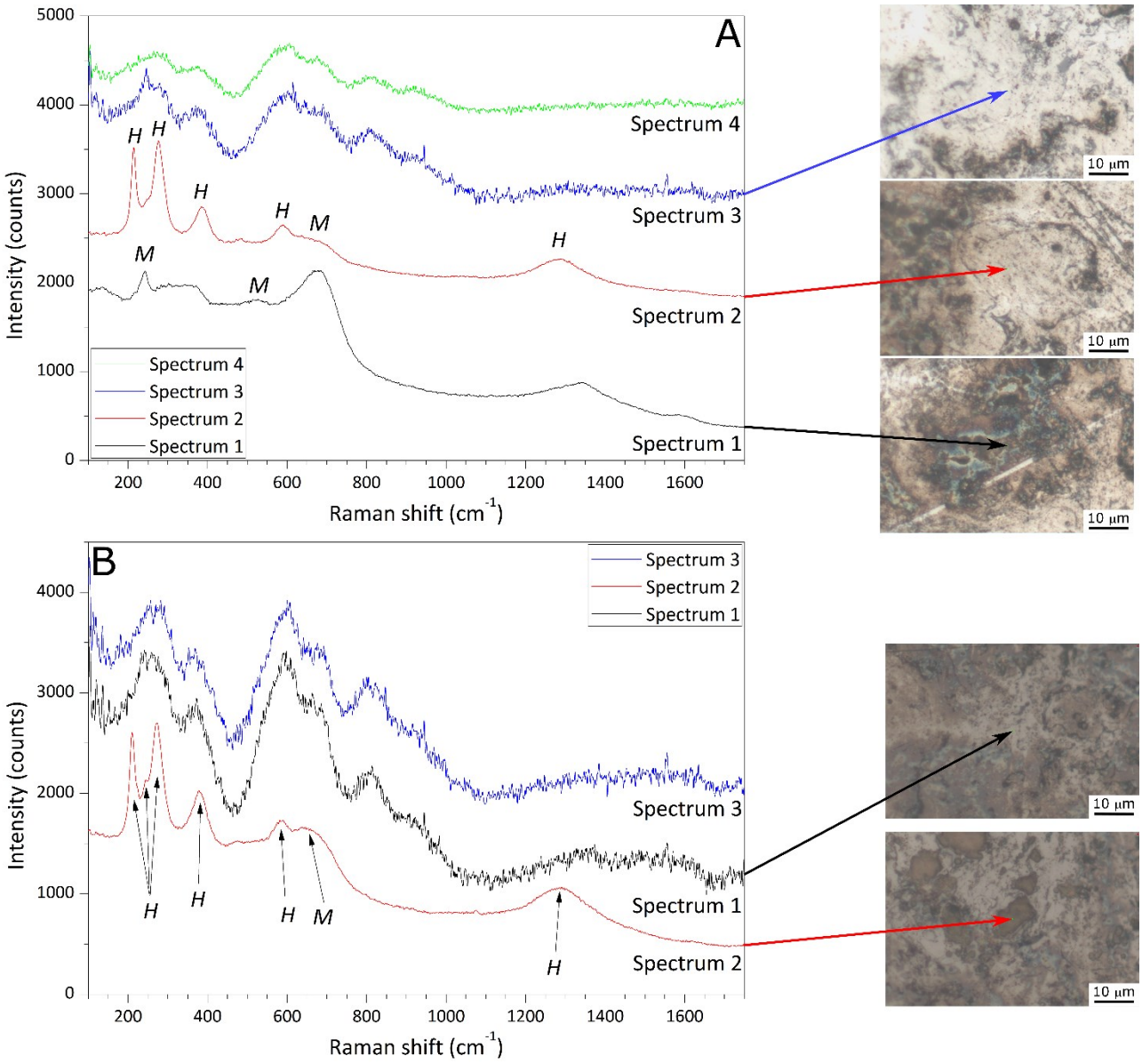

Figure 59: Micro-Raman spectra acquired on the surfaces of the Cantor+60TiC Run3 (A) and AlCuCrFeNi+60TiC Run3 (B) samples after the chronoamperometric tests at +0.15 V vs. OCP, with optical micrographs of the acquisition locations of the spectra. Spectrum 4 in panel A and spectrum 3 in panel B were acquired outside the tested area. Labels: H = hematite; M = magnetite.

Cross-sectional analysis of the AlCuCrFeNi+60TiC coating confirmed that although overall damage was limited, some interconnected pathways, visible as darker regions due to increased porosity and corrosion product presence, had formed across the coating (Figure 60E, F: circled in E and indicated by arrows in F). The electrolyte thereby reached the substrate, producing corrosion products at the interface (Figure 60F: circle). In backscattered electron mode, these corrosion products appear slightly brighter than the embedded alumina grit residue. EDX maps (Figure 61) show oxygen-rich, Fe-containing regions on the substrate lacking Al, confirming Fe-based corrosion products (circled in panels A–D). Additionally, Fe-rich spots within interconnected pores in the coating (Figure 61D: arrows) indicate upward transport of Fe-containing corrosion products, explaining their presence on the outer surface.

In contrast, SEM cross-sections of the Al_0(CrMnFeNi)+60TiC coating after chronoamperometry at +0.15 V vs. OCP showed no significant corrosion in the coating or at the substrate interface. The coating in the tested region (Figure 60A) was indistinguishable from unaffected areas (Figure 60C). No interconnected porous paths or corrosion products were found at the interface (Figure 60B, matching Figure 60D). This contrasts sharply with the same sample after polarization testing (Figure 55C, D). This difference confirms that the selective matrix leaching observed after polarization (Figure 55) resulted from passive-film breakdown, as stated in Section 3.5.b.; it did not occur while the pseudo-passive film remained reasonably stable. Because substrate corrosion products appeared after chronoamperometry in samples that did not show substrate corrosion after polarization (e.g., Cantor+60TiC), and vice versa (e.g., Al_0(CrMnFeNi)+60TiC), substrate corrosion in the two test types was unrelated. During polarization, substrate corrosion initiated only in the transpassive regime; in the pseudo-passive regime, pits large enough to expose the substrate could not form within the short duration of the polarization test (≤10 min at 0.0005 V/s). Thus, substrate corrosion did not influence the polarization response near the rest potential or within the pseudo-passive region (Section 3.5.b.) and did not affect the corrosion current density or E_{Corr} values in Table 19. Furthermore, substrate corrosion was not caused by pre-existing interconnected pores; if it were, the same sample would have displayed substrate corrosion in both tests.

AlCuCrFeNi+60TiC Run3 sample developed fewer pits and corrosion products than the Cantor+60TiC sample after chronoamperometry at +0.15 V vs. OCP, most Raman spectra obtained from the tested surface corresponded to the characteristic spectrum of titanium carbide (Figure 59B, spectrum 1), which also appeared outside the corroded region (Figure

59B, spectrum 3). Similarly, on the Cantor+60TiC surface, TiC spectra were found where the signal was collected away from pits (Figure 59A, spectrum 4).

TiC has a rock-salt FCC structure without Raman-active modes, but defects such as C vacancies, unavoidable in materials produced by HEBM and then thermally sprayed, break symmetry and generate Raman activity[191], [192]. TiC was detected wherever the surface was not covered by thick corrosion products, because the spacing between TiC particles was below the lateral resolution of micro-Raman (~1 μm). The metallic matrix does not produce Raman signals. The observation of the TiC spectrum in unpitted regions implies that the passive film was thinner than the penetration depth of the laser and thus undetectable. Thin passive films are generally more desirable: thicker films tend to be more porous and less protective[170].

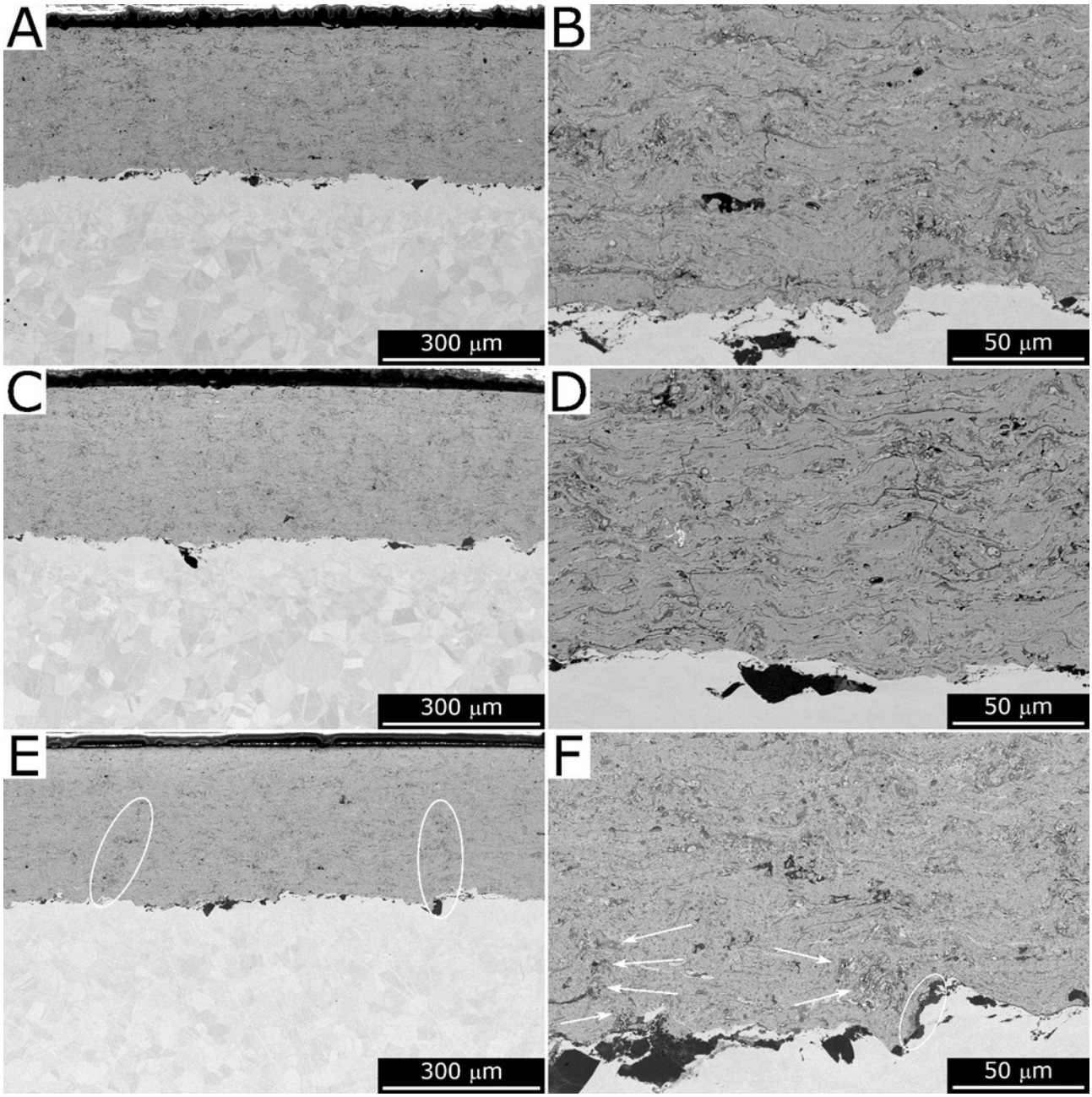

Figure 60: Cross-sectional SEM micrographs of coated samples after chronoamperometric tests at +0.15 V vs. OCP: Al_0(CrMnFeNi)+60TiC Run3 sample in the tested region (A, B) and in a region away from the test area (C, D), and AlCuCrFeNi+60TiC Run3 sample in the tested region (E, F) – overviews (A, C, E) and details of the interface with the substrate (B, D, F). In panel E, the circles indicate interconnected paths; in panel F, the circle indicates Fe-based corrosion products on the substrate and the arrows indicate interconnected paths.

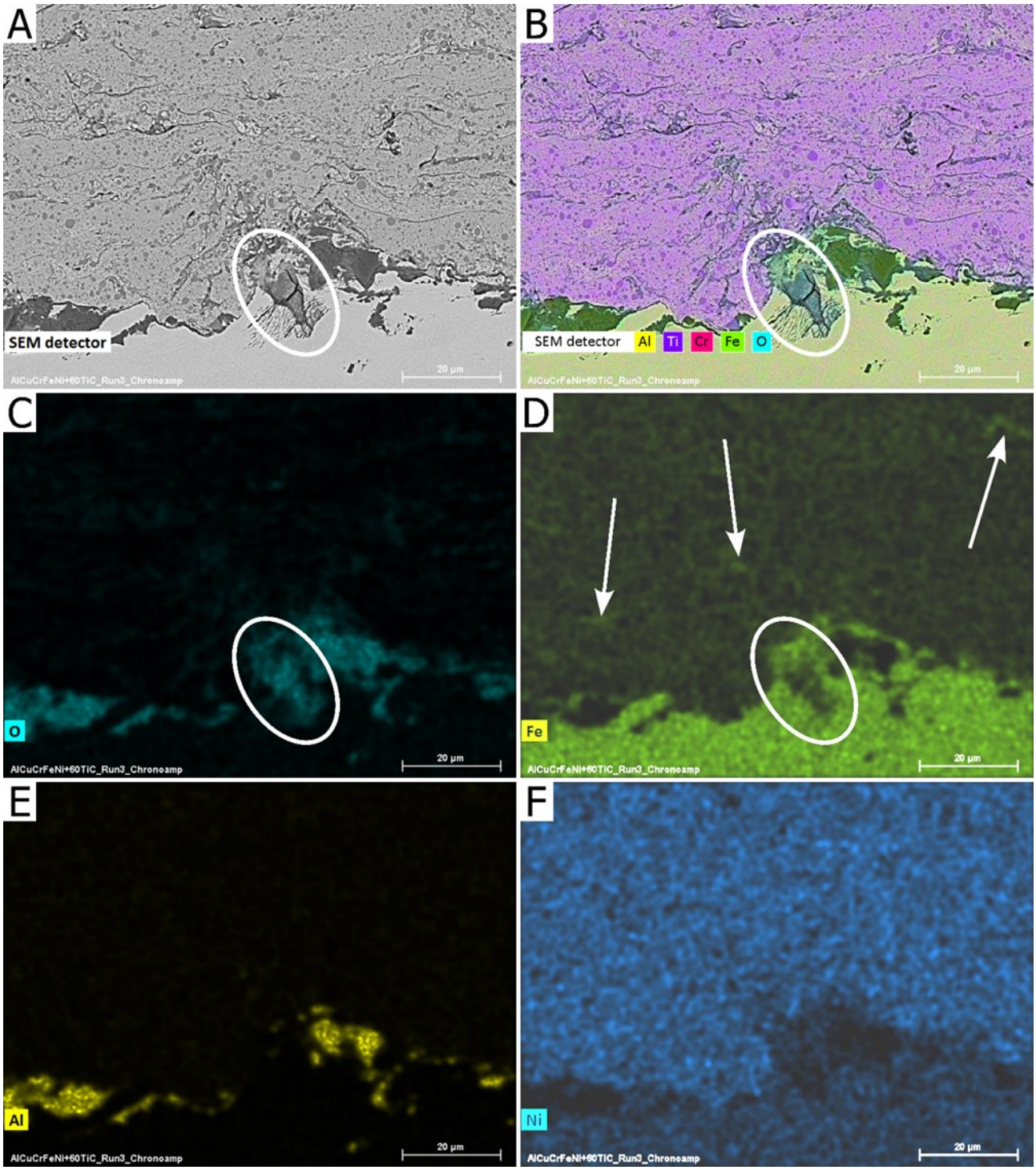

Figure 61: Cross-sectional SEM micrograph of the AlCuCrFeNi+60TiC Run3 sample after the chronoamperometry test at +0.15 V vs. OCP (A), and the corresponding EDX maps: overall map (B) and maps of oxygen (C), iron (D), aluminium (E) and nickel (F).

Because micro-Raman spectroscopy could not determine the pseudo-passive film composition, XPS was performed on the Al_0(CrMnFeNi)+60TiC and Al_{14}(CrMnFeNi)+60TiC samples after chronoamperometry at +0.15 V vs. OCP. XPS probes <10 nm depth. XPS was not performed on the AlCuCrFeNi+60TiC and Cantor+60TiC coatings because the large (1 mm²) sampling area of the instrument might have included substrate corrosion products, preventing reliable interpretation of the passive film composition.

The XPS results (Figure 62) show that in the Al_0(CrMnFeNi)+60TiC sample the dominant signals were from Fe 2p and Ti 2p (Figure 62A, B). In the Al14(CrMnFeNi)+60TiC sample, Fe 2p, Cr 2p, and Ti 2p were the strongest components (Figure 9C–E). Fe and Cr existed entirely as Fe_2O_3 and Cr_2O_3, indicating these oxides were responsible for matrix passivation. The Ti signal was stronger due to the high TiC fraction and included a dominant TiO_2 component (passivating the TiC particles) and a secondary Ti^0 component (likely from partial TiC decarburization, as shown previously). The absence of Fe^0 and Cr^0 may reflect their lower signal intensities or the nanometric thickness of the oxide film on TiC, which allowed detection of underlying Ti^0. Thus, part of the TiO_2 signal may also originate from the matrix, meaning the matrix passive film likely consisted of mixed Fe^{3+}–Cr^{3+}–Ti^{4+} oxides. This supports the idea that Ti dissolved into the matrix during spraying contributed to its passivation. Signals from Ni, Mn, and Al (in Al_{14}(CrMnFeNi)+60TiC) were negligible, indicating they were not major passive-film constituents.

The fact that TiC particles carried a thinner oxide film than the matrix is consistent with the corrosion potentials of stoichiometric and substoichiometric TiC (Section 3.5.b.). TiC remained cathodic at +0.15 V above the initial OCP, corresponding to an absolute potential <0 V vs. Ag/AgCl/KCl(sat.), meaning its tendency to form oxide during chronoamperometry was low; it acted predominantly as a cathode.

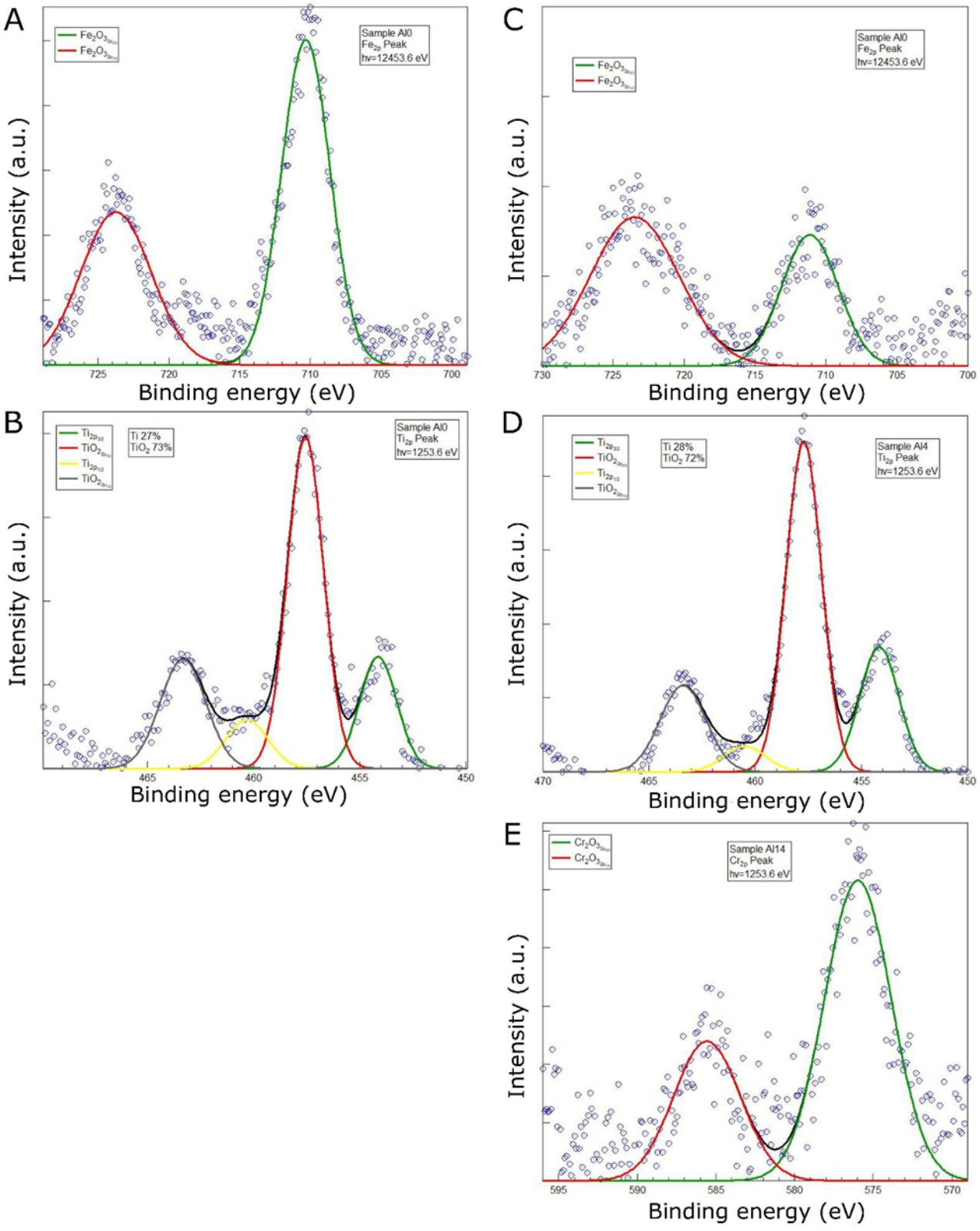

Figure 62: XPS spectra acquired on coating surfaces after the chronoamperometry tests at +0.15 V vs. OCP: Fe2p (A) and Ti2p (B) spectra of the Al_0(CrMnFeNi)+60TiC sample; Fe2p (C), Ti2p (D), and Cr2p (E) spectra of the Al_{14}(CrMnFeNi)+60TiC sample.

To evaluate the stability limits of the passive films on the Al_0(CrMnFeNi)+60TiC and Al_{14}(CrMnFeNi)+60TiC samples, additional chronoamperometric tests were conducted at overpotentials of +0.20 V and +0.25 V vs. OCP (Figure 63). Both values lie within the

pseudo-passive region of the curves in Figure 53 but impose harsher conditions than +0.15 V.

All curves at these higher overpotentials still showed a rapid initial current drop (first 100–200 s), but the overall behaviour differed from that at +0.15 V. At +0.20 V, the Al_0(CrMnFeNi)+60TiC sample initially exhibited slightly cathodic current densities but then returned to anodic values and later showed a sudden increase by two orders of magnitude. At +0.25 V, its current density remained anodic and increased continuously, ending around 2×10^{-4} A/cm².

The Al_{14}(CrMnFeNi)+60TiC sample never became cathodic. At +0.20 V, its current increased steadily, exceeding values recorded for the Al_0(CrMnFeNi)+60TiC sample before the latter's sudden jump. At +0.25 V, its current density was several orders of magnitude higher from the beginning and rapidly rose to ~4×10^{-3} A/cm².

Thus, increasing the overpotential above +0.15 V vs. OCP destabilized the passive layers of both compositions. The Al_{14}(CrMnFeNi)+60TiC coating, likely due to its dual-phase (BCC + FCC) matrix, degraded more readily.

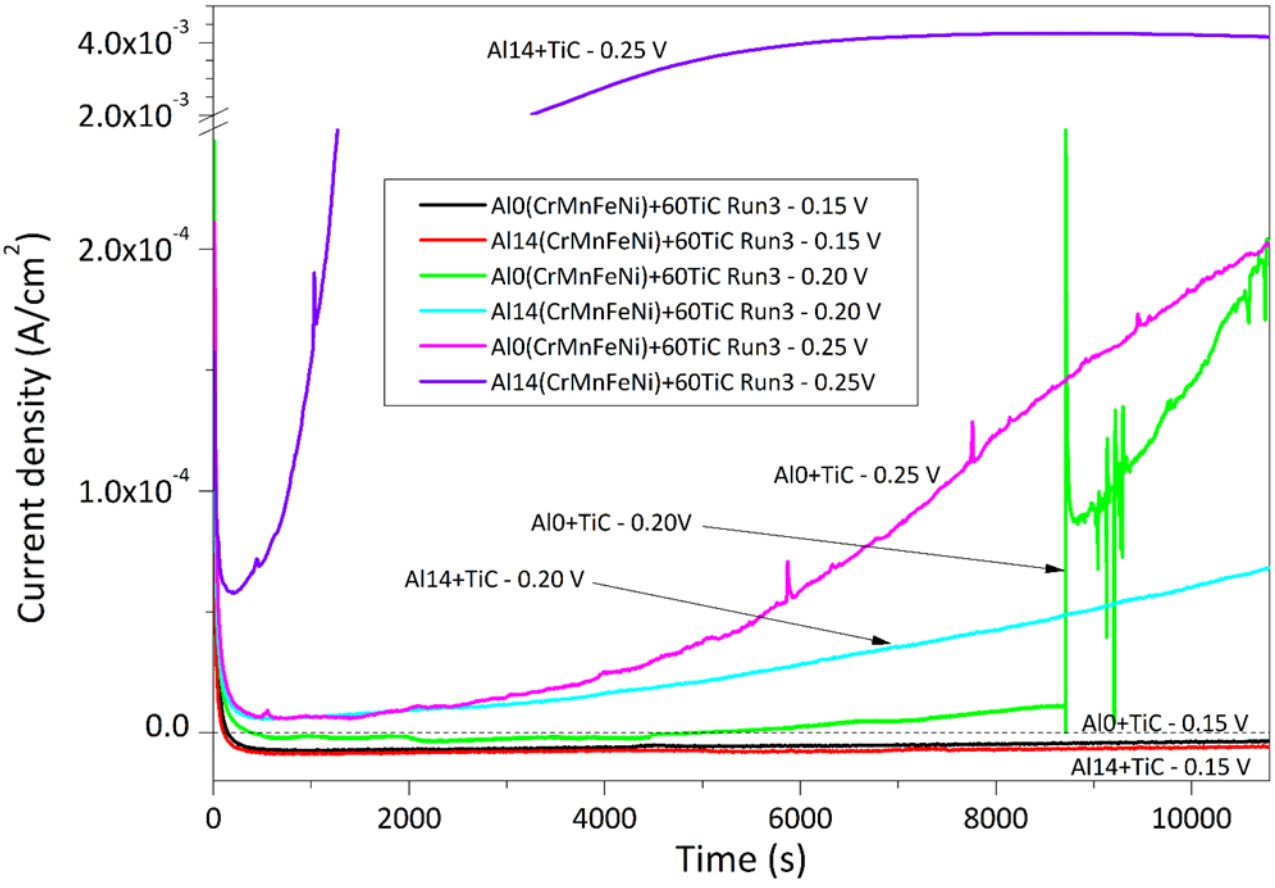

Figure 63: Chronoamperometric curves recorded on the Al_0(CrMnFeNi)+60TiC Run3 and Al_{14}(CrMnFeNi)+60TiC Run3 samples at fixed overpotentials of +0.15 V vs. OCP, +0.20 V vs. OCP, +0.25 V vs. OCP.

SEM micrographs (Figure 64) reveal that passive-film cracking triggered interlamellar corrosion, with severity proportional to the recorded current densities. Damage remained limited after testing at +0.20 V (Al_{14}: Figure 64A–B; Al_0: Figure 64E–F). At low magnification, no macroscopic defects were visible (Figure 64A, E). However, the electrolyte penetrated lamellar boundaries and corroded the matrix in specific lamellae (circled in panels A and F). Higher magnification (Figure 64B, F) shows unsupported TiC particles due to matrix dissolution. Corresponding EDX spectra (Figure 65A, C) show that Ti peaks remained similar in corroded and unaffected areas, while Cr, Mn, Fe, and Ni peaks decreased in corroded regions. Cr peaks increased relatively to Mn, Fe, and Ni, indicating selective dissolution of the latter three, consistent with the selective dissolution observed in Section 3.5.b. Pre-existing oxide inclusions (spectrum 3) contained more Ti (and some Al) but far less Cr, Mn, Fe, and Ni than the corroded regions.

Although the substrate interface appeared intact (Figure 64A, E), detailed images, particularly for Al_0(CrMnFeNi)+60TiC, revealed isolated corrosion spots. Figure 65B and C show needle-like Fe-, O-, and Cl-rich corrosion products (spectra 4 and 5), easily distinguished from Al_2O_3 grit residues through their backscattered electron contrast level and the EDX spectra (compare with spectrum 6). These features suggest that the rising current during the test corresponded to the onset of substrate corrosion: the electrolyte, after selectively dissolving specific lamellae, eventually formed an interconnected path through the coating. This agrees with observations from polarization tests (Section 3.5.b., Figure 55C–D) and supports the conclusion that substrate corrosion did not result from pre-existing porosity but rather from the time-dependent development of through-thickness pathways. Higher overpotentials accelerated this process.

Corrosion at lamellar boundaries was more severe at +0.25 V (Figure 64C–D, G–H), matching the higher currents of Figure 63. The Al_0(CrMnFeNi)+60TiC sample (Figure 64G–H) developed pronounced interlamellar routes extending deep into the coating. The Al_{14}(CrMnFeNi)+60TiC sample (Figure 64C–D) suffered even more extensive interlamellar attack. As the current densities increased, the corrosion morphology progressively approached that seen after transpassive corrosion in the polarization tests (Figure 55 and Figure 56). In all cases, the primary mechanism triggered by passive-film breakdown was the penetration of the electrolyte along lamellar boundaries followed by selective dissolution of the metallic matrix, progressing from the boundary inward. Local substrate corrosion also reappeared, and reddish corrosion products were visible on the surfaces of samples tested at +0.25 V vs. OCP.

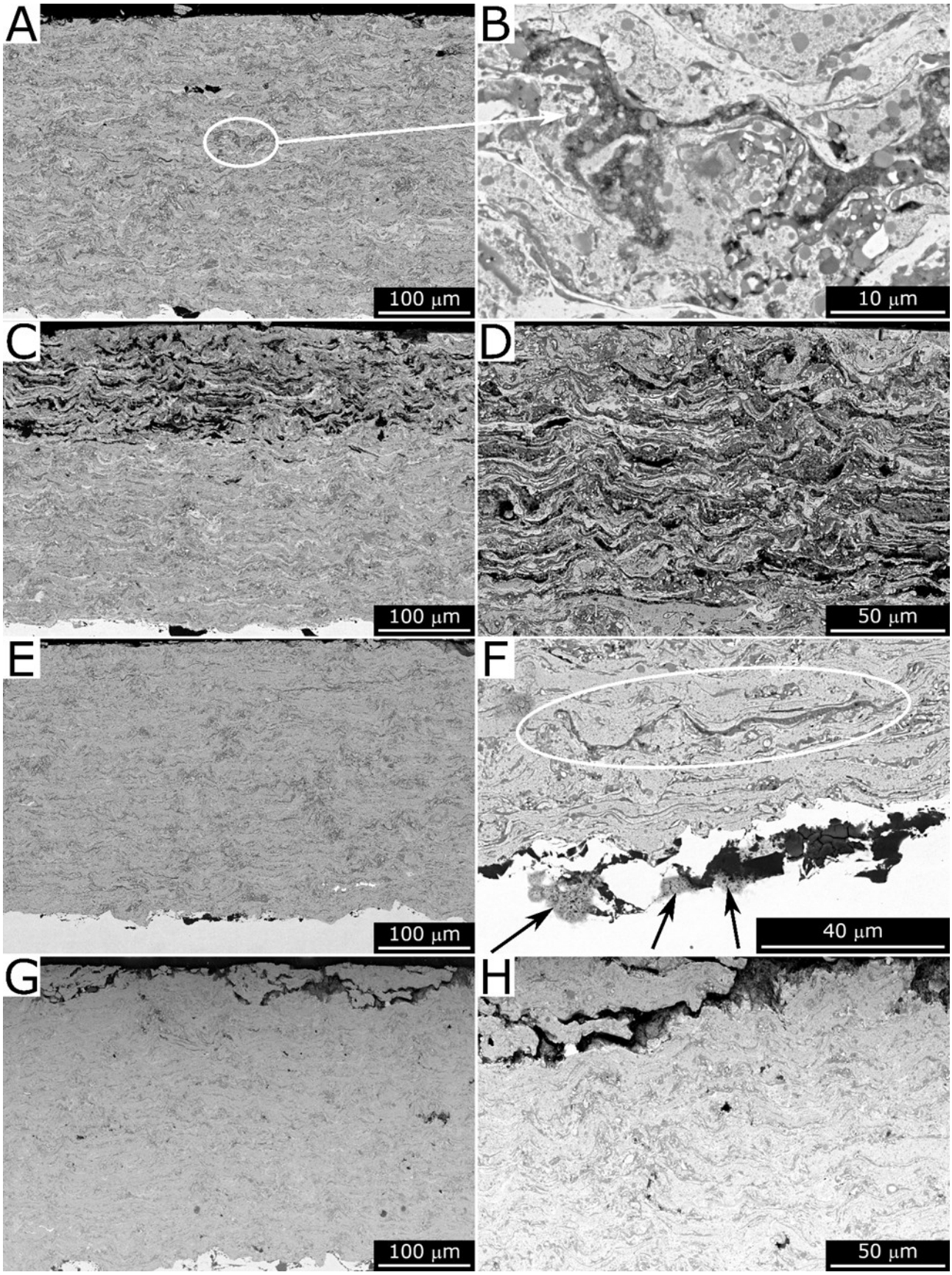

Figure 64: Cross-sectional SEM micrographs of the Al14(CrMnFeNi)+60TiC Run3 (A-D) and Al0(CrMnFeNi)+60TiC (E-H) samples after chronoamperometric tests at +0.20 V (A-B, E-F) and +0.25 V vs. OCP (C-D, G-H): overviews (A, C, E, G) and details of the corroded area (B, D, F, H). The circles in panels A and F indicate corroded lamellae; the arrows in panel F indicate substrate corrosion.

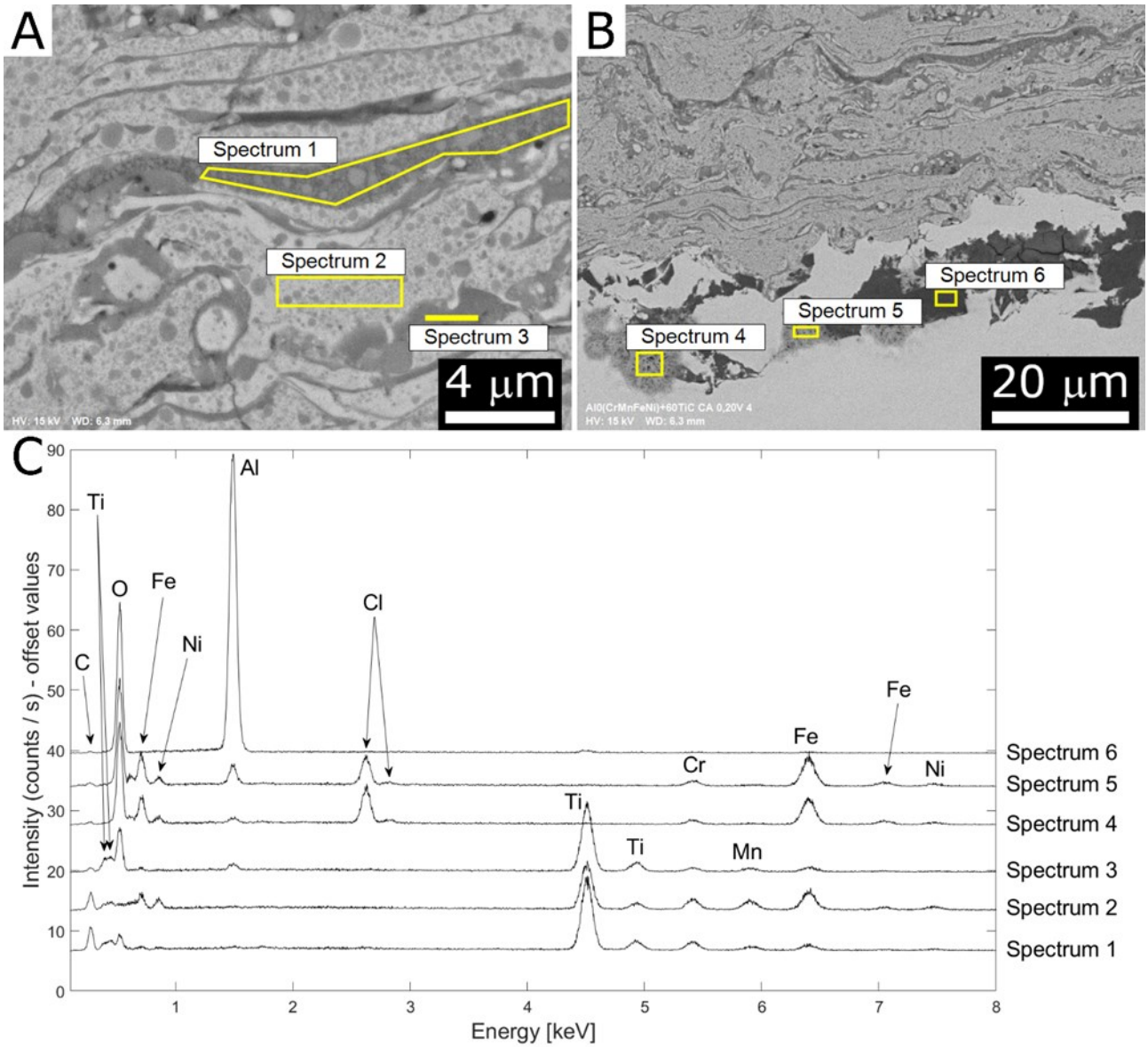

Figure 65: Cross-sectional SEM micrographs of the Al_0(CrMnFeNi)+60TiC Run3 sample after the chronoamperometric test at +0.20 V (A-B) and corresponding EDX spectra (C).

Conclusions

This PhD Thesis set out to design, deposit and characterise new thermal spray coatings capable of eliminating cobalt and tungsten while maintaining, and where possible improving, the functional performance traditionally provided by Stellite overlays and WC–CoCr hardmetal systems. The work addressed two complementary material families: metallic high-entropy alloy (HEA) coatings and HEA–TiC cermet coatings, both produced through high-energy ball milling and deposited via high-velocity oxy-fuel (HVOF) spraying. These material systems were chosen in response to two critical industrial drivers: the increasing pressure to reduce the dependence on Critical Raw Materials (CRMs), particularly Co and W, now formally recognised as strategically vulnerable by the European Commission; and the well-documented health hazards associated with cobalt-containing binders, which have been linked to carcinogenicity and environmental risks. Recent reviews of global supply chains and occupational exposure confirm the urgency of developing CRM-free alternatives that remain competitive in demanding wear- and corrosion-dominated environments.

From a microstructural and physico-chemical perspective, the metallic HEA coatings produced in this work demonstrate the viability of the selected design strategy. HVOF deposition of mechanically alloyed Cantor-type and cobalt-free $Al_x(CrMnFeNi)_{100-x}$ HEAs produced dense, low-porosity coatings with homogeneous microstructures, consistent with recent studies showing that HEA powders, even when produced by mechanical alloying rather than gas atomisation, can serve as robust feedstocks for thermal spray technologies. The evolution of phase composition with aluminum content followed the behaviour widely documented for this alloy system: Cantor and Al_0(CrMnFeNi) promote stable FCC matrices with relatively high toughness, whereas Al-rich variants tend to develop dual FCC/BCC or predominantly BCC microstructures due to ordering phenomena and lattice distortions. This structural shift is directly reflected in the mechanical properties: hardness increases steadily as the matrix transitions from FCC to mixed FCC/BCC and finally to BCC structures, a trend supported by numerous reports in the HEA literature where aluminum acts as a strong solid-solution strengthener but reduces ductility. High-speed nanoindentation mapping carried out in this thesis confirmed the presence of distinct mechanical populations: soft FCC, harder BCC, and interfacial regions, with local property variations mirroring those observed in bulk HEAs and thermally sprayed HEA coatings examined in recent works.

Importantly, mechanical performance alone does not dictate industrial applicability. Corrosion testing in 3.5 wt.% NaCl demonstrated that both cobalt-containing (Cantor) and

cobalt-free Al_0(CrMnFeNi) and Al_{10}(CrMnFeNi) coatings exhibit corrosion resistance comparable to stainless steels and conventional Ni-based overlays. Several publications have highlighted similar passivation behaviour in HEAs with balanced Cr/Ni ratios, confirming that the corrosion response of these alloys is governed more by passive-film stability and microstructural homogeneity than by the presence of Co or W. The results of this thesis therefore reinforce the feasibility of HEAs as CRM-free functional coatings for corrosive environments.

Parallel research explored CRM-free hardmetal-type coatings based on HEA–TiC cermets. All four compositions synthesised: Cantor+60TiC, Al_0(CrMnFeNi)+60TiC, Al_{14}(CrMnFeNi)+60TiC and AlCuCrFeNi+60TiC; could be deposited via HVOF as dense coatings with a fine dispersion of TiC. This aligns with earlier studies demonstrating that TiC-based cermets offer a promising path for reducing reliance on WC and Co while maintaining high hardness. Structural analyses revealed that TiC remained the dominant ceramic phase after deposition, although limited decarburisation (TiC_{1-x} formation) and oxide inclusions were observed, consistent with high-temperature spray processes. The matrices retained the trends observed in their monolithic HEA counterparts: FCC-dominated matrices (Cantor, Al_0(CrMnFeNi) and AlCuCrFeNi) exhibited enhanced ductility, whereas BCC/B2-rich matrices (e.g., Al_{14}(CrMnFeNi)) delivered higher hardness at the expense of brittleness. Such structure–property relationships are widely discussed in the cermet literature, where the balance between matrix toughness and ceramic reinforcement dictates the final performance.

Micromechanical mapping revealed four main mechanical populations: soft FCC metallic regions, harder BCC-rich regions, mixed interfacial zones and very hard TiC particles. The high nanohardness values measured for the metallic phases, greater than typical bulk HEAs, can be attributed to indentation size effects, constraint from finely distributed ceramic phases, and the high strain-rate nature of the mapping technique. These factors collectively contribute to the high macroscopic hardness of the coatings but also accentuate the need to control interlamellar brittleness to prevent crack propagation under service conditions.

Tribological performance revealed a nuanced landscape. Under sliding wear (ball-on-disc), all HEA–TiC cermets displayed higher specific wear rates than WC–CoCr benchmarks and remained inferior to advanced (Ti,Mo)(C,N)–Ni systems reported in recent studies. The dominant damage mechanisms: microabrasion, interfacial fatigue, and localised brittle fracture; are consistent with failure modes commonly observed in TiC-based and high-

ceramic-fraction cermets. These findings underscore that improving matrix toughness is essential if HEA–TiC cermets are to match the sliding wear resistance of WC–CoCr.

However, the behaviour under high-stress abrasion (steel-wheel abrasion) was more encouraging. Coatings such as Cantor+60TiC and particularly AlCuCrFeNi+60TiC displayed specific wear rates comparable to Cr_3C_2–NiCr and significantly better TiC-based cermets with conventional matrices. The promising behaviour of AlCuCrFeNi+60TiC highlights a key insight: HEA matrices, when optimised for ductility and strain hardening, can confer a level of toughness that mitigates brittle fracture during severe abrasive loading. This represents a substantial step towards CRM-free hardmetals tailored for abrasive environments.

The corrosion behaviour of the HEA–TiC coatings was generally acceptable for industrial deployment. Variations in corrosion current densities and potentials were more strongly influenced by oxide inclusions, splat-boundary quality and deposition conditions than by the exact HEA chemistry. The presence of a high-volume fraction of TiC did not intrinsically deteriorate the corrosion resistance, provided that the coatings remained dense and that galvanic interactions were stabilised by protective passive layers. These findings are consistent with recent studies on TiC- and TiCN-based cermets, which highlight the decisive role of coating density and surface passivation. The incorporation of TiC can even promote a pseudo-passivation behaviour that further enhances corrosion resistance.

From a broader technological perspective, the overall results confirm several key conclusions. First, cobalt replacement in WC-based systems is already feasible using Ni-rich or compositionally complex binders, without sacrificing tribological or corrosion performance. Second, full replacement of both Co and W is technically achievable using TiC-based cermets with HEA or NiCr matrices, although further development is required, particularly in improving sliding wear behaviour, before these materials can be considered possible substitutes. Third, the synergistic combination of HEA design principles, advanced powder engineering and high-kinetic thermal spray deposition forms a powerful platform for developing next-generation protective coatings aligned with circular-economy objectives and tightening regulatory constraints. These findings are consistent with contemporary literature advocating HEA-based coatings as promising candidates for sustainable, high-performance surface engineering.

To move these systems closer to industrial adoption, several research directions emerge naturally from the results. Future work should explore HEA matrices designed to exploit transformation-induced plasticity (TRIP) or twinning-induced plasticity (TWIP), as these

mechanisms could provide the toughening required to close the sliding-wear performance gap. Alloying strategies for fine-tuning FCC/BCC/B2 phase equilibria should be refined further, and powder engineering approaches, such as hybrid atomised–milled powders and controlled particle size distributions, should be optimised to reduce oxidation, porosity and carbide decarburisation during spraying. More complex tribological tests involving impact, cyclic loading, variable temperature, or combined wear–corrosion interactions will be essential for benchmarking against advanced WC–CoCr and Cr_3C_2–NiCr coatings. Finally, post-deposition treatments such as laser remelting, heat treatments, or hot isostatic pressing could be used to heal interlamellar defects and stabilise the microstructure.

In conclusion, this thesis demonstrates that it is technically feasible to design, manufacture and validate cobalt- and tungsten-free thermal spray coatings capable of approaching, and in certain cases matching, the performance of current industrial benchmarks. It provides both detailed property data for specific compositions and generalisable design principles that can inform the next generation of sustainable, high-performance protective coatings. The work therefore represents a significant contribution to the ongoing transition towards coatings that are safer, more resource-efficient, and compliant with emerging environmental and regulatory frameworks.

Bibliography

[1] K. Holmberg and A. Erdemir, “Influence of tribology on global energy consumption, costs and emissions,” *Friction*, vol. 5, no. 3, pp. 263–284, Sep. 2017, doi: 10.1007/S40544-017-0183-5/METRICS.

[2] “European Commission. (2020). The European Green Deal. EUR-Lex - 52019DC0640 - EN - EUR-Lex.” https://eur-lex.europa.eu/legal-content/EN/TXT/?uri=CELEX%3A52019DC0640 (accessed Aug. 07, 2025).

[3] L. Pawlowski, “The Science and Engineering of Thermal Spray Coatings: Second Edition,” *Sci. Eng. Therm. Spray Coatings Second Ed.*, pp. 1–626, Mar. 2008, doi: 10.1002/9780470754085.

[4] Y. Y. Özbek, N. Canikoğlu, and M. Ipek, “The mechanical properties and wear resistance of HVOF sprayed WC-Co coatings,” *Acta Phys. Pol. A*, vol. 129, no. 4, pp. 600–603, Apr. 2016, doi: 10.12693/APHYSPOLA.129.600.

[5] “European Chemicals Agency (ECHA). (2023). Chromium Trioxide Authorization List. .” https://echa.europa.eu/-/echa-proposes-restrictions-on-chromium-vi-substances-to-protect-health (accessed Aug. 07, 2025).

[6] “REACH Regulation - European Commission.” https://environment.ec.europa.eu/topics/chemicals/reach-regulation_en (accessed Aug. 07, 2025).

[7] P. O. of the E. Union, “Study on the review of the list of critical raw materials : final report.,” Sep. 2017, doi: 10.2873/876644.

[8] E. P. George, D. Raabe, and R. O. Ritchie, “High-entropy alloys,” *Nat. Rev. Mater.*, vol. 4, no. 8, pp. 515–534, Aug. 2019, doi: 10.1038/S41578-019-0121-4.

[9] P. L. Conway, T. Klaver, J. Steggo, and E. Ghassemali, “High entropy alloys towards industrial applications High-throughput screening and experimental investigation,” *Mater. Sci. Eng. A*, vol. 830, p. 142297, 2022, doi: 10.1016/j.msea.2021.142297.

[10] D. Attinger *et al.*, “Surface engineering for phase change heat transfer: A review,” *MRS Energy Sustain.*, vol. 1, no. 1, p. E4, Dec. 2014, doi: 10.1557/MRE.2014.9.

[11] J.R. Davis, “Surface Engineering for Corrosion and Wear Resistance,” *Surf. Eng. Corros. Wear Resist.*, Mar. 2001, doi: 10.31399/ASM.TB.SECWR.9781627083157.

[12] T. S. Eyre, “Wear characteristics of metals,” *Tribol. Int.*, vol. 9, no. 5, pp. 203–212, Oct. 1976, doi: 10.1016/0301-679X(76)90077-3.

[13] B. Bhushan, “Modern Tribology Handbook, Two Volume Set,” *Mod. Tribol. Handbook, Two Vol. Set*, Dec. 2000, doi: 10.1201/9780849377877/MODERN-TRIBOLOGY-HANDBOOK-TWO-VOLUME-SET-BHARAT-BHUSHAN.

[14] P. Fauchais, A. Vardelle, P. Fauchais, and A. Vardelle, “Thermal Sprayed Coatings Used Against Corrosion and Corrosive Wear,” *Adv. Plasma Spray Appl.*, Mar. 2012, doi: 10.5772/34448.

[15] “J. R. Davis, ‘Handbook of Thermal Spray Technology,’ ASM International, 2004. - References - Scientific Research Publishing.” https://www.scirp.org/reference/referencespapers?referenceid=871658 (accessed Aug. 07, 2025).

[16] S. Amin and H. Panchal, “A Review on Thermal Spray Coating Processes,” *Int. J. Curr. Trends Eng. Res.*, vol. 2, pp. 556–563, 2016, Accessed: Aug. 07, 2025. [Online]. Available: http://www.ijcter.com

[17] Irene Garcia Cano, “New Trends in Thermal Spray Technology.” https://www.researchgate.net/publication/326266036_New_Trends_in_Thermal_Spray_Technology (accessed Aug. 07, 2025).

[18] “HVOF vs HVAF coating equipment comparison WCCoCr quality cost system.” https://kermetico.com/hvaf-vs-hvof-coating (accessed Aug. 07, 2025).

[19] V. K. Champagne, “The Cold Spray Materials Deposition Process: Fundamentals and Applications V. K. Champagne Woodhead Publishing.” https://www.libreriauniversitaria.it/cold-spray-materials-deposition-process/book/9781845691813?srsltid=AfmBOopb92q3KHxJHoimFXH_EN0xVRf1idTJ35VQR5GfkQYldzCZm5bs (accessed Aug. 07, 2025).

[20] J. Villafuerte, “Modern Cold Spray: Materials, Process, and Applications,” *Mod. Cold Spray Mater. Process. Appl.*, pp. 1–429, Aug. 2015, doi: 10.1007/978-3-319-16772-5/COVER.

[21] “Critical Raw Materials Act - European Commission.” https://single-market-economy.ec.europa.eu/sectors/raw-materials/areas-specific-interest/critical-raw-materials/critical-raw-materials-act_en (accessed Aug. 07, 2025).

[22] J. A. Picas, M. Punset, M. Teresa Baile, E. Martín, and A. Forn, “Properties of WC-CoCr based coatings deposited by different HVOF thermal spray processes,” in *Plasma Processes and Polymers*, 2009. doi: 10.1002/ppap.200932402.

[23] N. Espallargas, “Introduction to thermal spray coatings,” *Futur. Dev. Therm. Spray*

Coatings Types, Des. Manuf. Appl., pp. 1–13, Jan. 2015, doi: 10.1016/B978-0-85709-769-9.00001-4.

[24] P. R. Rajendran *et al.*, “Optimisation of HVOF Spray Process Parameters to Achieve Minimum Porosity and Maximum Hardness in WC-10Ni-5Cr Coatings,” *Coatings*, vol. 12, no. 3, Mar. 2022, doi: 10.3390/COATINGS12030339.

[25] M. H. Basiri and M. Mosallaee, “Optimizing the properties of nano WC-10Co-4Cr HVOF coatings by using RSM,” *Surf. Eng.*, vol. 40, no. 9–10, pp. 1010–1021, Sep. 2024, doi: 10.1177/02670844241299869.

[26] M. Ksiazek, I. Nejman, and L. Boron, “Investigation on microstructure, mechanical and wear properties of hvof sprayed composite coatings (Wc–co + cr) on ductile cast iron,” *Materials (Basel).*, vol. 14, no. 12, Jun. 2021, doi: 10.3390/MA14123282.

[27] I. Shishkovsky, N. Kakovkina, and V. Sherbakof, “Mechanical properties of NiCrBSi self-fluxing alloy after LPBF with additional heating,” *Procedia CIRP*, vol. 94, pp. 217–221, Jan. 2020, doi: 10.1016/J.PROCIR.2020.09.041.

[28] L. A. Cabrera Maynez, C. Maynez, and L. Alejandra, “Design and Development of a High Velocity Oxy-Fuel Thermal Spray Gun Recommended Citation”, Accessed: Aug. 07, 2025. [Online]. Available: https://digitalcommons.utep.edu/open_etd

[29] L. Bortolotti *et al.*, “Effect of powder morphology on tribological performance of HVAF-sprayed WC-CoCr coatings,” *Surf. Coatings Technol.*, vol. 505, p. 132090, Jun. 2025, doi: 10.1016/J.SURFCOAT.2025.132090.

[30] M. Oksa, E. Turunen, T. Suhonen, T. Varis, and S. P. Hannula, “Optimization and Characterization of High Velocity Oxy-fuel Sprayed Coatings: Techniques, Materials, and Applications,” *Coatings 2011, Vol. 1, Pages 17-52*, vol. 1, no. 1, pp. 17–52, Sep. 2011, doi: 10.3390/COATINGS1010017.

[31] W. Tillmann, S. Kuhnt, I. T. Baumann, A. Kalka, E. C. Becker-Emden, and A. Brinkhoff, “Statistical Comparison of Processing Different Powder Feedstock in an HVOF Thermal Spray Process,” *J. Therm. Spray Technol.*, vol. 31, no. 5, pp. 1476–1489, Jun. 2022, doi: 10.1007/S11666-022-01392-2/FIGURES/10.

[32] J. He and J. M. Schoenung, “A review on nanostructured WC-Co coatings,” *Surf. Coatings Technol.*, vol. 157, no. 1, pp. 72–79, Aug. 2002, doi: 10.1016/S0257-8972(02)00141-X.

[33] S. Joshi and P. Nylen, “Advanced Coatings by Thermal Spray Processes,” *Technol. 2019, Vol. 7, Page 79*, vol. 7, no. 4, p. 79, Nov. 2019, doi:

10.3390/TECHNOLOGIES7040079.

[34] K. Fan *et al.*, “Influence of WC Particle Size on the Mechanical Properties and Residual Stress of HVOF Thermally Sprayed WC–10Co–4Cr Coatings,” *Mater. 2022, Vol. 15, Page 5537*, vol. 15, no. 16, p. 5537, Aug. 2022, doi: 10.3390/MA15165537.

[35] P. L. Fauchais, J. V. R. Heberlein, and M. I. Boulos, “Thermal spray fundamentals: From powder to part,” *Therm. Spray Fundam. From Powder to Part*, pp. 1–1566, Jan. 2014, doi: 10.1007/978-0-387-68991-3.

[36] G. Mittal and S. Paul, “Suspension and Solution Precursor Plasma and HVOF Spray: A Review,” *J. Therm. Spray Technol. 2022 315*, vol. 31, no. 5, pp. 1443–1475, Mar. 2022, doi: 10.1007/S11666-022-01360-W.

[37] M. Sauter, A. Killinger, A. Grebhardt, and C. Bonten, “High Velocity Flame Spraying (HVOF) of Ceramic – Polymer Composite Filaments,” *Therm. Spray 2022 Proc. from Int. Therm. Spray Conf.*, vol. 84369, pp. 432–436, May 2022, doi: 10.31399/ASM.CP.ITSC2022P0432.

[38] M. Sauter *et al.*, “High temperature properties of nichrome resistant heaters – A systematic comparison of APS, suspension and filament HVOF sprayed coatings,” *Surf. Coatings Technol.*, vol. 496, p. 131594, Jan. 2025, doi: 10.1016/J.SURFCOAT.2024.131594.

[39] A. R. Lopez, B. Hassan, W. L. Oberkampf, R. A. Neiser, and T. J. Roemer, “Computational Fluid Dynamics Analysis of a Wire-Feed, High-Velocity Oxygen Fuel (HVOF) Thermal Spray Torch,” *J. Therm. Spray Technol.*, vol. 7, no. 3, pp. 374–382, 1998, doi: 10.1361/105996398770350855/METRICS.

[40] P. Fauchais, G. Montavon, and G. Bertrand, “From powders to thermally sprayed coatings,” *J. Therm. Spray Technol.*, vol. 19, no. 1–2, pp. 56–80, Jan. 2010, doi: 10.1007/S11666-009-9435-X/FIGURES/21.

[41] M. Vardelle, A. Vardelle, and P. Fauchais, “Spray parameters and particle behavior relationships during plasma spraying,” *J. Therm. Spray Technol.*, vol. 2, no. 1, pp. 79–91, Mar. 1993, doi: 10.1007/BF02647426/METRICS.

[42] L. Pawlowski, “Materials Used for Spraying,” *Sci. Eng. Therm. Spray Coatings*, pp. 1–51, Mar. 2008, doi: 10.1002/9780470754085.CH1.

[43] B. Kolman, J. Forman, J. Dubský, and P. Chráska, “Homogeneity studies of powders and plasma sprayed deposits,” *Mikrochim. Acta*, vol. 114–115, no. 1, pp. 335–342, Dec. 1994, doi: 10.1007/BF01244560/METRICS.

[44] A. ÜNal, “Production of rapidly solidified aluminium alloy powders by gas atomisation and their applications,” *Powder Metall.*, vol. 33, no. 1, pp. 53–64, Jan. 1990, doi: 10.1179/POM.1990.33.1.53.

[45] A. Nouri and A. Sola, “Powder morphology in thermal spraying,” *J. Adv. Manuf. Process.*, vol. 1, no. 3, p. e10020, Jul. 2019, doi: 10.1002/AMP2.10020;SUBPAGE:STRING:ABSTRACT;WEBSITE:WEBSITE:AICHE;REQUESTEDJOURNAL:JOURNAL:2637403X;WGROUP:STRING:PUBLICATION.

[46] L. M. Berger, “Application of hardmetals as thermal spray coatings,” *Int. J. Refract. Met. Hard Mater.*, vol. 49, no. 1, pp. 350–364, Mar. 2015, doi: 10.1016/J.IJRMHM.2014.09.029.

[47] P. K. Mehrotra, “Powder Processing and Green Shaping,” *Compr. Hard Mater.*, vol. 1, pp. 213–235, 2014, doi: 10.1016/B978-0-08-096527-7.00007-6.

[48] R. M. German, “Consolidation Techniques,” *Compr. Hard Mater.*, vol. 1, pp. 237–263, 2014, doi: 10.1016/B978-0-08-096527-7.00008-8.

[49] J. E. Blendell and W. Rheinheimer, “Solid-State Sintering,” *Encycl. Mater. Tech. Ceram. Glas. Vol. 1-3*, vol. 1, pp. V1-249-V1-257, Jan. 2021, doi: 10.1016/B978-0-12-803581-8.12084-3.

[50] C. Suryanarayana, “Mechanical alloying and milling,” *Prog. Mater. Sci.*, vol. 46, no. 1–2, pp. 1–184, Jan. 2001, doi: 10.1016/S0079-6425(99)00010-9.

[51] F. Pougoum *et al.*, “Effect of high-energy ball-milling on the characteristics of Fe3Al-based HVOF coatings containing boride and nitride phases,” *Wear*, vol. 358–359, pp. 97–108, Jul. 2016, doi: 10.1016/J.WEAR.2016.04.001.

[52] Randall M. German, “Sintering Theory and Practice | Wiley.” https://www.wiley.com/en-us/Sintering+Theory+and+Practice-p-9780471057864 (accessed Aug. 08, 2025).

[53] Y. Y. Santana *et al.*, “Characterization and residual stresses of WC–Co thermally sprayed coatings,” *Surf. Coatings Technol.*, vol. 202, no. 18, pp. 4560–4565, Jun. 2008, doi: 10.1016/J.SURFCOAT.2008.04.042.

[54] L. Pawlowski, “Suspension and solution thermal spray coatings,” *Surf. Coatings Technol.*, vol. 203, no. 19, pp. 2807–2829, Jun. 2009, doi: 10.1016/J.SURFCOAT.2009.03.005.

[55] P. Fauchais, R. Etchart-Salas, V. Rat, J. F. Coudert, N. Caron, and K. Wittmann-Ténèze, “Parameters controlling liquid plasma spraying: Solutions, sols, or

suspensions," *J. Therm. Spray Technol.*, vol. 17, no. 1, pp. 31–59, 2008, doi: 10.1007/S11666-007-9152-2.

[56] A. Meghwal, A. Anupam, B. S. Murty, C. C. Berndt, R. S. Kottada, and A. S. M. Ang, "Thermal Spray High-Entropy Alloy Coatings: A Review," *J. Therm. Spray Technol. 2020 295*, vol. 29, no. 5, pp. 857–893, May 2020, doi: 10.1007/S11666-020-01047-0.

[57] R. Unabia, R. Candidato, and L. Pawłowski, "Current Progress in Solution Precursor Plasma Spraying of Cermets: A Review," *Met. 2018, Vol. 8, Page 420*, vol. 8, no. 6, p. 420, Jun. 2018, doi: 10.3390/MET8060420.

[58] M. F. Bonilauri *et al.*, "Deposition of high-velocity oxygen-fuel (HVOF) coatings on laser-powder bed fused (L-PBF) parts subjected to in-situ laser remelting treatments," *Surf. Coat. Technol.*, vol. 510, pp. 1–27, Aug. 2025, doi: 10.1016/J.SURFCOAT.2025.132250.

[59] K. Malamousi, K. Delibasis, and S. Kamnis, "Real-Time Thermal Spray Process Monitoring Using Convolution Neural Network Deep Learning Architectures," *J. Therm. Spray Technol.*, vol. 33, no. 1, pp. 17–32, Feb. 2024, doi: 10.1007/S11666-024-01713-7/FIGURES/10.

[60] S. Liscano, L. Gil, and M. H. Staia, "Effect of sealing treatment on the corrosion resistance of thermal-sprayed ceramic coatings," *Surf. Coatings Technol.*, vol. 188–189, no. 1-3 SPEC.ISS., pp. 135–139, Nov. 2004, doi: 10.1016/J.SURFCOAT.2004.08.009.

[61] J. R. . Davis, *Nickel, cobalt, and their alloys*. ASM International, 2000.

[62] D. Zhang, S. J. Harris, and D. G. McCartney, "Microstructure formation and corrosion behaviour in HVOF-sprayed Inconel 625 coatings," *Mater. Sci. Eng. A*, vol. 344, no. 1–2, pp. 45–56, Mar. 2003, doi: 10.1016/S0921-5093(02)00420-3.

[63] C. Huang, J. Wang, J. Yan, and L. Liao, "Evaluation of corrosion and wear performance of Fe-based coating and hastelloy C276 in H2S environment on 304 stainless steel substrate," *Colloids Surfaces A Physicochem. Eng. Asp.*, vol. 674, p. 131871, Oct. 2023, doi: 10.1016/J.COLSURFA.2023.131871.

[64] C. R. C. Lima, M. J. X. Belém, H. D. C. Fals, and C. A. D. Rovere, "Wear and corrosion performance of Stellite 6® coatings applied by HVOF spraying and GTAW hotwire cladding," *J. Mater. Process. Technol.*, vol. 284, p. 116734, Oct. 2020, doi: 10.1016/J.JMATPROTEC.2020.116734.

[65] M. S. Sahith, G. Giridhara, and R. S. Kumar, "Development and analysis of thermal

barrier coatings on gas turbine blades – A Review," *Mater. Today Proc.*, vol. 5, no. 1, pp. 2746–2751, Jan. 2018, doi: 10.1016/J.MATPR.2018.01.060.

[66] "(PDF) Safety from failure of thermally sprayed hardmetal coatings in high-temperature applications." https://www.researchgate.net/publication/390929222_Safety_from_failure_of_thermally_sprayed_hardmetal_coatings_in_high-temperature_applications (accessed Aug. 08, 2025).

[67] I. Konyashin *et al.*, "Wettability of tungsten carbide by liquid binders in WC–Co cemented carbides: Is it complete for all carbon contents?," *Int. J. Refract. Met. Hard Mater.*, vol. 62, pp. 134–148, Jan. 2017, doi: 10.1016/J.IJRMHM.2016.06.006.

[68] M. Oksa, P. Auerkari, J. Salonen, and T. Varis, "Nickel-based HVOF coatings promoting high temperature corrosion resistance of biomass-fired power plant boilers," *Fuel Process. Technol.*, vol. 125, pp. 236–245, Sep. 2014, doi: 10.1016/J.FUPROC.2014.04.006.

[69] B. Schnyder *et al.*, "Investigation of the electrochemical behaviour of WC-Co hardmetal with electrochemical and surface analytical methods," *Surf. Sci.*, vol. 566–568, no. 1-3 PART 2, pp. 1240–1245, Sep. 2004, doi: 10.1016/J.SUSC.2004.06.102.

[70] J. A. Picas, M. Punset, E. Rupérez, S. Menargues, E. Martin, and M. T. Baile, "Corrosion mechanism of HVOF thermal sprayed WC-CoCr coatings in acidic chloride media," *Surf. Coatings Technol.*, vol. 371, pp. 378–388, Aug. 2019, doi: 10.1016/J.SURFCOAT.2018.10.025.

[71] H. Wang, F. Tang, J. Chen, M. Xing, X. Liu, and X. Song, "Corrosion behavior of WC-η coatings in molten zinc," *Corros. Sci.*, vol. 199, p. 110192, May 2022, doi: 10.1016/J.CORSCI.2022.110192.

[72] J. Yuan, Q. Zhan, J. Huang, S. Ding, and H. Li, "Decarburization mechanisms of WC–Co during thermal spraying: Insights from controlled carbon loss and microstructure characterization," *Mater. Chem. Phys.*, vol. 142, no. 1, pp. 165–171, Oct. 2013, doi: 10.1016/J.MATCHEMPHYS.2013.06.052.

[73] D. A. Stewart, P. H. Shipway, and D. G. McCartney, "Microstructural evolution in thermally sprayed WC–Co coatings: comparison between nanocomposite and conventional starting powders," *Acta Mater.*, vol. 48, no. 7, pp. 1593–1604, Apr. 2000, doi: 10.1016/S1359-6454(99)00440-1.

[74] L. Zhao, M. Maurer, F. Fischer, R. Dicks, and E. Lugscheider, "Influence of spray

parameters on the particle in-flight properties and the properties of HVOF coating of WC-CoCr," *Wear*, vol. 257, no. 1–2, pp. 41–46, Jul. 2004, doi: 10.1016/J.WEAR.2003.07.002.

[75] G. Bolelli *et al.*, "Tribology of HVOF-and HVAF-sprayed WC-10Co4Cr hardmetal coatings: A comparative assessment," 2015, doi: 10.1016/j.surfcoat.2015.01.048.

[76] C. Chen, A. Feng, Y. Wei, Y. Wang, X. Pan, and X. Song, "Effects of WC particles on microstructure and wear behavior of laser cladding Ni60 composite coatings," *Opt. Laser Technol.*, vol. 163, p. 109425, Aug. 2023, doi: 10.1016/J.OPTLASTEC.2023.109425.

[77] H. Wang *et al.*, "Grain size effect on wear resistance of WC-Co cemented carbides under different tribological conditions," *J. Mater. Sci. Technol.*, vol. 35, no. 11, pp. 2435–2446, Nov. 2019, doi: 10.1016/J.JMST.2019.07.016.

[78] K. O. Méndez-Medrano, C. J. Martínez-González, F. Alvarado-Hernández, O. Jiménez, V. H. Baltazar-Hernández, and H. Ruiz-Luna, "Microstructure and Properties Characterization of WC-Co-Cr Thermal Spray Coatings," *J. Miner. Mater. Charact. Eng.*, vol. 06, no. 04, pp. 482–497, 2018, doi: 10.4236/JMMCE.2018.64034.

[79] BP, "Statistical Review of World Energy", Accessed: Aug. 08, 2025. [Online]. Available: www.bp.com/statisticalreview.

[80] "Regulation - 2017/821 - EN - EUR-Lex." https://eur-lex.europa.eu/eli/reg/2017/821/oj/eng (accessed Aug. 08, 2025).

[81] "Cobalt Statistics and Information | U.S. Geological Survey." https://www.usgs.gov/centers/national-minerals-information-center/cobalt-statistics-and-information (accessed Aug. 08, 2025).

[82] M. Grohol and C. Veeh, "Study on the critical raw materials for the EU 2023 : final report," p. 152, 2023.

[83] R. M. Lunn, S. S. Mehta, G. D. Jahnke, A. Wang, M. S. Wolfe, and B. R. Berridge, "Cancer Hazard Evaluations for Contemporary Needs: Highlights from New National Toxicology Program Evaluations and Methodological Advancements," *J. Natl. Cancer Inst.*, vol. 114, no. 11, pp. 1441–1448, Nov. 2022, doi: 10.1093/JNCI/DJAC164.

[84] "IARC Monographs on the Identification of Carcinogenic Hazards to Humans – INTERNATIONAL AGENCY FOR RESEARCH ON CANCER." https://monographs.iarc.who.int/ (accessed Aug. 08, 2025).

[85] M. Suh, C. M. Thompson, G. P. Brorby, L. Mittal, and D. M. Proctor, "Inhalation cancer

risk assessment of cobalt metal," *Regul. Toxicol. Pharmacol.*, vol. 79, pp. 74–82, 2016, doi: 10.1016/j.yrtph.2016.05.009.

[86] R. Lauwerys and D. Lison, "Health risks associated with cobalt exposure — an overview," *Sci. Total Environ.*, vol. 150, no. 1–3, pp. 1–6, Jun. 1994, doi: 10.1016/0048-9697(94)90125-2.

[87] undefined, "Toxicology studies of cobalt metal in F344/N rats and B6C3F1/N mice and toxicology and carcinogenesis studies of cobalt metal in F344/NTac rats and B6C3F1/N mice (inhalation studies).," *Natl. Toxicol. Program Tech. Rep. Ser.*, no. 581, p. NTP-TR, Dec. 2014, doi: 10.22427/NTP-TR-581.

[88] "Committee for Risk Assessment - ECHA." https://echa.europa.eu/about-us/who-we-are/committee-for-risk-assessment (accessed Aug. 08, 2025).

[89] G. Bolelli *et al.*, "Sliding and abrasive wear behaviour of HVOF- and HVAF-sprayed Cr3C2–NiCr hardmetal coatings," *Wear*, vol. 358–359, pp. 32–50, Jul. 2016, doi: 10.1016/J.WEAR.2016.03.034.

[90] V. Matikainen *et al.*, "A Study of Cr3C2-Based HVOF- and HVAF-Sprayed Coatings: Microstructure and Carbide Retention," *J. Therm. Spray Technol.*, vol. 26, no. 6, pp. 1239–1256, Aug. 2017, doi: 10.1007/S11666-017-0578-X/TABLES/8.

[91] Š. Houdková, F. Zahálka, M. Kašparová, and L. M. Berger, "Comparative study of thermally sprayed coatings under different types of wear conditions for hard chromium replacement," *Tribol. Lett.*, vol. 43, no. 2, pp. 139–154, Aug. 2011, doi: 10.1007/S11249-011-9791-9/FIGURES/19.

[92] M. Grimm, S. Conze, L. M. Berger, G. Paczkowski, T. Lindner, and T. Lampke, "Microstructure and Sliding Wear Resistance of Plasma Sprayed Al2O3-Cr2O3-TiO2 Ternary Coatings from Blends of Single Oxides," *Coatings 2020, Vol. 10, Page 42*, vol. 10, no. 1, p. 42, Jan. 2020, doi: 10.3390/COATINGS10010042.

[93] G. Bolelli *et al.*, "Properties of WC–FeCrAl coatings manufactured by different high velocity thermal spray processes," *Surf. Coatings Technol.*, vol. 247, pp. 74–89, May 2014, doi: 10.1016/J.SURFCOAT.2014.03.021.

[94] L. M. Berger *et al.*, "Microstructure and properties of HVOF-sprayed chromium alloyed WC–Co and WC–Ni coatings," *Surf. Coatings Technol.*, vol. 202, no. 18, pp. 4417–4421, Jun. 2008, doi: 10.1016/J.SURFCOAT.2008.04.019.

[95] J. M. Guilemany, J. Nutting, J. R. Miguel, and Z. Dong, "Microstructure characterization of WC-Ni coatings obtained by HVOF thermal spraying," *Scr. Metall.*

Mater., vol. 33, no. 1, pp. 55–61, Jul. 1995, doi: 10.1016/0956-716X(95)00045-W.

[96] D. G. Bhosale, T. R. Prabhu, and W. S. Rathod, “Sliding and erosion wear behaviour of thermal sprayed WC-Cr3C2-Ni coatings,” *Surf. Coatings Technol.*, vol. 400, p. 126192, Oct. 2020, doi: 10.1016/J.SURFCOAT.2020.126192.

[97] B. Song, J. W. Murray, R. G. Wellman, Z. Pala, and T. Hussain, “Dry sliding wear behaviour of HVOF thermal sprayed WC-Co-Cr and WC-CrxCy-Ni coatings,” *Wear*, vol. 442–443, p. 203114, Feb. 2020, doi: 10.1016/J.WEAR.2019.203114.

[98] G. Bolelli, L. M. Berger, M. Bonetti, and L. Lusvarghi, “Comparative study of the dry sliding wear behaviour of HVOF-sprayed WC–(W,Cr)2C–Ni and WC–CoCr hardmetal coatings,” *Wear*, vol. 309, no. 1–2, pp. 96–111, Jan. 2014, doi: 10.1016/J.WEAR.2013.11.001.

[99] V. Testa *et al.*, “Corrosion and wear performances of alternative TiC-based thermal spray coatings,” *Surf. Coatings Technol.*, vol. 438, p. 128400, May 2022, doi: 10.1016/J.SURFCOAT.2022.128400.

[100] P. Sassatelli, “MATERIALI E PROCESSI SOSTENIBILI PER RIVESTIMENTI PROTETTIVI TERMOSPRUZZATI,” 2025, Accessed: Sep. 04, 2025. [Online]. Available: https://tesidottorato.depositolegale.it/handle/20.500.14242/142999

[101] G. Bolelli *et al.*, “Properties of HVOF-sprayed TiC-FeCrAl coatings,” *Wear*, vol. 418–419, pp. 36–51, Jan. 2019, doi: 10.1016/J.WEAR.2018.11.002.

[102] J. W. Yeh *et al.*, “Nanostructured High-Entropy Alloys with Multiple Principal Elements: Novel Alloy Design Concepts and Outcomes,” *Adv. Eng. Mater.*, vol. 6, no. 5, pp. 299–303, May 2004, doi: 10.1002/ADEM.200300567.

[103] B. Cantor, I. T. H. Chang, P. Knight, and A. J. B. Vincent, “Microstructural development in equiatomic multicomponent alloys,” *Mater. Sci. Eng. A*, vol. 375–377, no. 1-2 SPEC. ISS., pp. 213–218, Jul. 2004, doi: 10.1016/J.MSEA.2003.10.257.

[104] J. W. Yeh, “Recent progress in high-entropy alloys,” vol. 31, no. no.6, pp. 633–648, 2006, Accessed: Aug. 11, 2025. [Online]. Available: https://inis.iaea.org/records/7f3gk-s8e75

[105] J. W. Yeh, “Alloy design strategies and future trends in high-entropy alloys,” *JOM*, vol. 65, no. 12, pp. 1759–1771, Dec. 2013, doi: 10.1007/S11837-013-0761-6/FIGURES/12.

[106] D. B. Miracle and O. N. Senkov, “A critical review of high entropy alloys and related concepts,” *Acta Mater.*, vol. 122, pp. 448–511, Jan. 2017, doi:

10.1016/J.ACTAMAT.2016.08.081.

[107] D. B. Miracle, J. D. Miller, O. N. Senkov, C. Woodward, M. D. Uchic, and J. Tiley, “Exploration and Development of High Entropy Alloys for Structural Applications,” *Entropy 2014, Vol. 16, Pages 494-525*, vol. 16, no. 1, pp. 494–525, Jan. 2014, doi: 10.3390/E16010494.

[108] M. H. Tsai and J. W. Yeh, “High-entropy alloys: A critical review,” *Mater. Res. Lett.*, vol. 2, no. 3, pp. 107–123, 2014, doi: 10.1080/21663831.2014.912690.

[109] J. W. Yeh, “Physical Metallurgy of High-Entropy Alloys,” *JOM*, vol. 67, no. 10, pp. 2254–2261, Oct. 2015, doi: 10.1007/S11837-015-1583-5/FIGURES/16.

[110] Y. F. Kao, S. K. Chen, T. J. Chen, P. C. Chu, J. W. Yeh, and S. J. Lin, “Electrical, magnetic, and Hall properties of AlxCoCrFeNi high-entropy alloys,” *J. Alloys Compd.*, vol. 509, no. 5, pp. 1607–1614, Feb. 2011, doi: 10.1016/J.JALLCOM.2010.10.210.

[111] J. W. Yeh, S. Y. Chang, Y. Der Hong, S. K. Chen, and S. J. Lin, “Anomalous decrease in X-ray diffraction intensities of Cu–Ni–Al–Co–Cr–Fe–Si alloy systems with multi-principal elements,” *Mater. Chem. Phys.*, vol. 103, no. 1, pp. 41–46, May 2007, doi: 10.1016/J.MATCHEMPHYS.2007.01.003.

[112] K. Y. Tsai, M. H. Tsai, and J. W. Yeh, “Sluggish diffusion in Co–Cr–Fe–Mn–Ni high-entropy alloys,” *Acta Mater.*, vol. 61, no. 13, pp. 4887–4897, Aug. 2013, doi: 10.1016/J.ACTAMAT.2013.04.058.

[113] M. H. Tsai, J. W. Yeh, and J. Y. Gan, “Diffusion barrier properties of AlMoNbSiTaTiVZr high-entropy alloy layer between copper and silicon,” *Thin Solid Films*, vol. 516, no. 16, pp. 5527–5530, Jun. 2008, doi: 10.1016/J.TSF.2007.07.109.

[114] M.-H. Tsai *et al.*, “Thermal Stability and Performance of NbSiTaTiZr High-Entropy Alloy Barrier for Copper Metallization,” *J. Electrochem. Soc.*, vol. 158, no. 11, p. H1161, Oct. 2011, doi: 10.1149/2.056111JES/XML.

[115] S. Ranganathan, “Alloyed pleasures: Multimetallic cocktails,” 2003.

[116] S. V Divinski, A. Pokoev, N. Esakkiraja, and A. Paul, “A Mystery of ‘Sluggish Diffusion’ in High-Entropy Alloys: The Truth or a Myth?,” 2018, doi: 10.4028/www.scientific.net/DF.17.69.

[117] J. Dąbrowa and M. Danielewski, “State-of-the-Art Diffusion Studies in the High Entropy Alloys,” *Met. 2020, Vol. 10, Page 347*, vol. 10, no. 3, p. 347, Mar. 2020, doi: 10.3390/MET10030347.

[118] P. I. Odetola *et al.*, “Exploring high entropy alloys: A review on thermodynamic design

and computational modeling strategies for advanced materials applications," *Heliyon*, vol. 10, no. 22, p. e39660, Nov. 2024, doi: 10.1016/J.HELIYON.2024.E39660.

[119] O. N. Senkov, D. B. Miracle, K. J. Chaput, and J. P. Couzinie, "Development and exploration of refractory high entropy alloys—A review," *J. Mater. Res. 2018 3319*, vol. 33, no. 19, pp. 3092–3128, Oct. 2018, doi: 10.1557/JMR.2018.153.

[120] O. N. Senkov, G. B. Wilks, D. B. Miracle, C. P. Chuang, and P. K. Liaw, "Refractory high-entropy alloys," *Intermetallics*, vol. 18, no. 9, pp. 1758–1765, Sep. 2010, doi: 10.1016/J.INTERMET.2010.05.014.

[121] A. Meghwal, A. Anupam, B. S. Murty, C. C. Berndt, R. S. Kottada, and A. S. M. Ang, "Thermal Spray High-Entropy Alloy Coatings: A Review," *J. Therm. Spray Technol. 2020 295*, vol. 29, no. 5, pp. 857–893, May 2020, doi: 10.1007/S11666-020-01047-0.

[122] V. R. Srivatsav, S. Ragunath, N. Radhika, and M. A. Khan, "Exploring the potential of gas atomized high entropy alloys in thermal spray coatings – a comprehensive review," *J. Mater. Chem. A*, vol. 12, no. 43, pp. 29432–29468, Nov. 2024, doi: 10.1039/D4TA04512B.

[123] M. Löbel, T. Lindner, T. Lampke, and C. Kohrt, "Development of wear-resistant High-Entropy alloy coatings produced by thermal spray technology," *Proc. Int. Therm. Spray Conf.*, vol. 1, pp. 200–204, 2017, doi: 10.31399/ASM.CP.ITSC2017P0200.

[124] R. Bhaskaran Nair *et al.*, "High-Entropy Alloy Coatings Deposited by Thermal Spraying: A Review of Strengthening Mechanisms, Performance Assessments and Perspectives on Future Applications," *Met. 2023, Vol. 13, Page 579*, vol. 13, no. 3, p. 579, Mar. 2023, doi: 10.3390/MET13030579.

[125] M. Kumaravel, S. Bagherifard, and M. Guagliano, "Advancements in Deposition of High Entropy Alloys Using Cold Spray Technology," *J. Therm. Spray Technol.*, vol. 34, no. 1, pp. 1–36, Feb. 2025, doi: 10.1007/S11666-024-01879-0/FIGURES/23.

[126] X. Ma, P. Ruggiero, R. Bhattacharya, O. N. Senkov, and A. K. Rai, "Evaluation of New High Entropy Alloy as Thermal Sprayed Bondcoat in Thermal Barrier Coatings," *J. Therm. Spray Technol.*, vol. 31, no. 4, pp. 1011–1020, Apr. 2022, doi: 10.1007/S11666-021-01279-8/FIGURES/11.

[127] M. Zhang, Y. Zhang, P. Dai, L. Zhao, L. Wu, and S. Li, "Study on the Process Parameters and Corrosion Resistance of FeCoNiCrAl High Entropy Alloy Coating Prepared by Atmospheric Plasma Spraying," *Materials (Basel).*, vol. 18, no. 7, p. 1396, Apr. 2025, doi: 10.3390/MA18071396/S1.

[128] *Cobalt, Antimony Compounds, and Weapons-grade Tungsten Alloy*. International Agency for Research on Cancer, 2023.

[129] T. A. Owoseni, M. Gupta, S. V. Joshi, M. Ingmar, and T. Varis, “Wear and Corrosion of HVAF and HVOF-Sprayed WC-CoCr Coatings on Aluminum Alloy,” *J. Therm. Spray Technol.*, vol. 34, no. 2, pp. 970–991, Mar. 2025, doi: 10.1007/S11666-024-01894-1/FIGURES/19.

[130] G. Bolelli *et al.*, “HVOF deposition of TiC-based hardmetal coatings with High-Entropy Alloy (HEA) matrix,” *Surf. Coatings Technol.*, vol. 512, p. 132386, Sep. 2025, doi: 10.1016/J.SURFCOAT.2025.132386.

[131] G. Bolelli *et al.*, “Deposition of High-Entropy Alloy (HEA) coatings by HVOF and cold gas spray,” *J. Alloys Compd.*, vol. 1039, p. 183050, Sep. 2025, doi: 10.1016/J.JALLCOM.2025.183050.

[132] B. Cantor, “Multicomponent high-entropy Cantor alloys,” *Prog. Mater. Sci.*, vol. 120, p. 100754, Jul. 2021, doi: 10.1016/J.PMATSCI.2020.100754.

[133] N. D. Stepanov, D. G. Shaysultanov, R. S. Chernichenko, M. A. Tikhonovsky, and S. V. Zherebtsov, “Effect of Al on structure and mechanical properties of Fe-Mn-Cr-Ni-Al non-equiatomic high entropy alloys with high Fe content,” *J. Alloys Compd.*, vol. 770, pp. 194–203, Jan. 2019, doi: 10.1016/J.JALLCOM.2018.08.093.

[134] C. Ng *et al.*, “Phase stability and tensile properties of Co-free Al 0.5CrCuFeNi2 high-entropy alloys,” *J. Alloys Compd.*, vol. 584, pp. 530–537, 2014, doi: 10.1016/J.JALLCOM.2013.09.105.

[135] Y. F. Ye, Q. Wang, J. Lu, C. T. Liu, and Y. Yang, “High-entropy alloy: challenges and prospects,” *Mater. Today*, vol. 19, no. 6, pp. 349–362, Jul. 2016, doi: 10.1016/J.MATTOD.2015.11.026.

[136] G. Bolelli *et al.*, “TiC–NiCr thermal spray coatings as an alternative to WC-CoCr and Cr3C2–NiCr,” *Wear*, vol. 450–451, p. 203273, Jun. 2020, doi: 10.1016/J.WEAR.2020.203273.

[137] L. R. Gehlen *et al.*, “Tribological and electrochemical performances of HVOF sprayed NbC-NiCr coatings,” *Surf. Coatings Technol.*, vol. 474, p. 130098, Dec. 2023, doi: 10.1016/J.SURFCOAT.2023.130098.

[138] S. A. Krishna, N. Noble, N. Radhika, and B. Saleh, “A comprehensive review on advances in high entropy alloys: Fabrication and surface modification methods, properties, applications, and future prospects,” *J. Manuf. Process.*, vol. 109, pp. 583–

606, Jan. 2024, doi: 10.1016/J.JMAPRO.2023.12.039.

[139] G. Bolelli *et al.*, “Pre-treatment of Selective Laser Melting (SLM) surfaces for thermal spray coating,” *Surf. Coatings Technol.*, vol. 441, p. 128533, Jul. 2022, doi: 10.1016/J.SURFCOAT.2022.128533.

[140] V. Testa *et al.*, “Alternative metallic matrices for WC-based HVOF coatings,” *Surf. Coatings Technol.*, vol. 402, p. 126308, Nov. 2020, doi: 10.1016/J.SURFCOAT.2020.126308.

[141] T. Degen, M. Sadki, E. Bron, U. König, and G. Nénert, “The HighScore suite,” *Powder Diffr.*, vol. 29, no. S2, pp. S13–S18, Dec. 2014, doi: 10.1017/S0885715614000840.

[142] B. H. Toby and R. B. Von Dreele, “GSAS-II: The genesis of a modern open-source all purpose crystallography software package,” *J. Appl. Crystallogr.*, vol. 46, no. 2, pp. 544–549, Apr. 2013, doi: 10.1107/S0021889813003531.

[143] B. H. Toby, “EXPGUI, a graphical user interface for GSAS,” *urn:issn:0021-8898*, vol. 34, no. 2, pp. 210–213, Apr. 2001, doi: 10.1107/S0021889801002242.

[144] S. Gražulis *et al.*, “Crystallography Open Database (COD): an open-access collection of crystal structures and platform for world-wide collaboration,” *Nucleic Acids Res.*, vol. 40, no. D1, pp. D420–D427, Jan. 2012, doi: 10.1093/NAR/GKR900.

[145] E. Rossi, J. M. Wheeler, and M. Sebastiani, “High-speed nanoindentation mapping: A review of recent advances and applications,” *Curr. Opin. Solid State Mater. Sci.*, vol. 27, no. 5, p. 101107, Oct. 2023, doi: 10.1016/J.COSSMS.2023.101107.

[146] W. C. Oliver and G. M. Pharr, “An improved technique for determining hardness and elastic modulus using load and displacement sensing indentation experiments,” *J. Mater. Res.*, vol. 7, no. 6, pp. 1564–1583, Jun. 1992, doi: 10.1557/JMR.1992.1564.

[147] H. Besharatloo and J. M. Wheeler, “Influence of indentation size and spacing on statistical phase analysis via high-speed nanoindentation mapping of metal alloys,” *J. Mater. Res.*, vol. 36, no. 11, pp. 2198–2212, Jun. 2021, doi: 10.1557/S43578-021-00214-5/FIGURES/7.

[148] P. Sudharshan Phani and W. C. Oliver, “A critical assessment of the effect of indentation spacing on the measurement of hardness and modulus using instrumented indentation testing,” *Mater. Des.*, vol. 164, p. 107563, Feb. 2019, doi: 10.1016/J.MATDES.2018.107563.

[149] “ASTM G99 – 17: Standard Test Method for Wear Testing with a Pin-on-Disk Apparatus,” *Annual Book of ASTM Standards*. 2020.

[150] A. V. Naumkin, A. Kraut-Vass, S.W. Gaarenstroom, and C.J. Powell, “NIST X-ray Photoelectron Spectroscopy Database,” 2000. Accessed: Dec. 07, 2025. [Online]. Available: https://doi.org/10.18434/T4T88K

[151] D. Luo *et al.*, “Tribological Behavior of High Entropy Alloy Coatings: A Review,” *Coatings 2022, Vol. 12, Page 1428*, vol. 12, no. 10, p. 1428, Sep. 2022, doi: 10.3390/COATINGS12101428.

[152] S. Gorsse, M. H. Nguyen, O. N. Senkov, and D. B. Miracle, “Corrigendum to database on the mechanical properties of high entropy alloys and complex concentrated alloys, data in brief 21 (2018) 2664–2678,” *Data Br.*, vol. 32, p. 106216, Oct. 2020, doi: 10.1016/J.DIB.2020.106216.

[153] P. Sassatelli *et al.*, “Properties of HVOF-sprayed Stellite-6 coatings,” *Surf. Coatings Technol.*, vol. 338, pp. 45–62, Mar. 2018, doi: 10.1016/J.SURFCOAT.2018.01.078.

[154] S. Sabarinath, V. Raj, L. V. Nair, V. Thomas, N. Ogunlakin, and V. S. Saji, “High entropy alloy (HEA) coatings for tribological applications - a review,” *Results Eng.*, vol. 27, p. 105695, Sep. 2025, doi: 10.1016/J.RINENG.2025.105695.

[155] F. Zhang *et al.*, “Recent developments in CoCrFeNi-based high entropy alloy coatings: Design, synthesis, and properties,” *J. Alloys Compd.*, vol. 1018, p. 179193, Mar. 2025, doi: 10.1016/J.JALLCOM.2025.179193.

[156] S. Li, Y. Sun, Z. Liu, L. Zhou, T. Wu, and Y. Bai, “Evolution of tribological properties of laser cladding 3D transition metal high entropy alloy coatings,” *J. Mater. Sci.*, vol. 60, no. 9, pp. 4118–4147, Mar. 2025, doi: 10.1007/S10853-025-10695-Y/FIGURES/12.

[157] T. Zirari and V. Trabadelo, “A review on wear, corrosion, and wear-corrosion synergy of high entropy alloys,” *Heliyon*, vol. 10, no. 4, p. e25867, Feb. 2024, doi: 10.1016/J.HELIYON.2024.E25867.

[158] D. Kumar, “Recent advances in tribology of high entropy alloys: A critical review,” *Prog. Mater. Sci.*, vol. 136, p. 101106, Jul. 2023, doi: 10.1016/J.PMATSCI.2023.101106.

[159] P. Patel *et al.*, “Microstructural and Tribological Behavior of Thermal Spray CrMnFeCoNi High Entropy Alloy Coatings,” *J. Therm. Spray Technol.*, vol. 31, no. 4, pp. 1285–1301, Apr. 2022, doi: 10.1007/S11666-022-01350-Y/FIGURES/15.

[160] J. Nohava, B. Bonferroni, G. Bolelli, and L. Lusvarghi, “Interesting aspects of indentation and scratch methods for characterization of thermally-sprayed coatings,”

Surf. Coatings Technol., vol. 205, no. 4, pp. 1127–1131, Nov. 2010, doi: 10.1016/J.SURFCOAT.2010.08.086.

[161] S. Gorsse, M. H. Nguyen, O. N. Senkov, and D. B. Miracle, “Database on the mechanical properties of high entropy alloys and complex concentrated alloys,” *Data Br.*, vol. 21, pp. 2664–2678, Dec. 2018, doi: 10.1016/J.DIB.2018.11.111.

[162] D. H. E. Persson, S. Jacobson, and S. Hogmark, “Antigalling and low friction properties of a laser processed Co-based material,” *J. Laser Appl.*, vol. 15, no. 2, pp. 115–119, May 2003, doi: 10.2351/1.1514218.

[163] S. Qiu *et al.*, “Influence of lattice distortion on stacking fault energies of CoCrFeNi and Al-CoCrFeNi high entropy alloys,” *J. Alloys Compd.*, vol. 846, p. 156321, Dec. 2020, doi: 10.1016/J.JALLCOM.2020.156321.

[164] J. A. R. Wesmann and N. Espallargas, “Effect of atmosphere, temperature and carbide size on the sliding friction of self-mated HVOF WC–CoCr contacts,” *Tribol. Int.*, vol. 101, pp. 301–313, Sep. 2016, doi: 10.1016/J.TRIBOINT.2016.04.032.

[165] J. A. R. Wesmann, S. Kuroda, and N. Espallargas, “The Role of Oxide Tribofilms on Friction and Wear of Different Thermally Sprayed WC-CoCr,” *J. Therm. Spray Technol.*, vol. 26, no. 3, pp. 492–502, Feb. 2017, doi: 10.1007/S11666-017-0522-0/METRICS.

[166] Y. Fu, J. Li, H. Luo, C. Du, and X. Li, “Recent advances on environmental corrosion behavior and mechanism of high-entropy alloys,” *J. Mater. Sci. Technol.*, vol. 80, pp. 217–233, Jul. 2021, doi: 10.1016/J.JMST.2020.11.044.

[167] Y. Qiu, S. Thomas, M. A. Gibson, H. L. Fraser, and N. Birbilis, “Corrosion of high entropy alloys,” *npj Mater. Degrad.*, vol. 1, no. 1, pp. 1–18, Dec. 2017, doi: 10.1038/S41529-017-0009-Y;SUBJMETA.

[168] J. Y. Zhang *et al.*, “High-Entropy Alloys: A Critical Review of Aqueous Corrosion Behavior and Mechanisms,” *High Entropy Alloy. Mater.*, vol. 1, no. 2, pp. 195–259, Sep. 2023, doi: 10.1007/S44210-023-00021-Z/TABLES/1.

[169] Y. Shi, B. Yang, X. Xie, J. Brechtl, K. A. Dahmen, and P. K. Liaw, “Corrosion of Al xCoCrFeNi high-entropy alloys: Al-content and potential scan-rate dependent pitting behavior,” *Corros. Sci.*, vol. 119, pp. 33–45, May 2017, doi: 10.1016/J.CORSCI.2017.02.019.

[170] M. Izadi, M. Soltanieh, S. Alamolhoda, S. M. S. Aghamiri, and M. Mehdizade, “Microstructural characterization and corrosion behavior of AlxCoCrFeNi high entropy

alloys," *Mater. Chem. Phys.*, vol. 273, p. 124937, Nov. 2021, doi: 10.1016/J.MATCHEMPHYS.2021.124937.

[171] M. Löbel *et al.*, "Microstructure and Corrosion Properties of AlCrFeCoNi High-Entropy Alloy Coatings Prepared by HVAF and HVOF," *J. Therm. Spray Technol.*, vol. 31, no. 1–2, pp. 247–255, Jan. 2022, doi: 10.1007/S11666-021-01255-2.

[172] S. Deshpande, S. Sampath, and H. Zhang, "Mechanisms of oxidation and its role in microstructural evolution of metallic thermal spray coatings—Case study for Ni–Al," *Surf. Coatings Technol.*, vol. 200, no. 18–19, pp. 5395–5406, May 2006, doi: 10.1016/J.SURFCOAT.2005.07.072.

[173] C. M. Hackett, G. S. Settles, and J. D. Miller, "On the gas dynamics of HVOF thermal sprays," *J. Therm. Spray Technol.*, vol. 3, no. 3, pp. 299–304, Sep. 1994, doi: 10.1007/BF02646278.

[174] G. Bolelli *et al.*, "Tribology of HVOF- and HVAF-sprayed WC–10Co4Cr hardmetal coatings: A comparative assessment," *Surf. Coatings Technol.*, vol. 265, pp. 125–144, Mar. 2015, doi: 10.1016/J.SURFCOAT.2015.01.048.

[175] G. Bolelli *et al.*, "Wear resistance of HVOF- and HVAF-sprayed (Ti,Mo)(C,N)–Ni coatings from an agglomerated and sintered powder," *Wear*, vol. 512–513, p. 204550, Jan. 2023, doi: 10.1016/J.WEAR.2022.204550.

[176] "Springer Handbook of Condensed Matter and Materials Data," *Springer Handb. Condens. Matter Mater. Data*, 2005, doi: 10.1007/3-540-30437-1.

[177] F. Cardarelli, "Ceramics, Refractories, and Glasses," *Mater. Handb.*, pp. 883–1012, 2018, doi: 10.1007/978-3-319-38925-7_10.

[178] W. D. Nix and H. Gao, "Indentation size effects in crystalline materials: A law for strain gradient plasticity," *J. Mech. Phys. Solids*, vol. 46, no. 3, pp. 411–425, Mar. 1998, doi: 10.1016/S0022-5096(97)00086-0.

[179] Z. Han *et al.*, "The deformation behavior and strain rate sensitivity of ultra-fine grained CoNiFeCrMn high-entropy alloys at temperatures ranging from 77 K to 573 K," *J. Alloys Compd.*, vol. 791, pp. 962–970, Jun. 2019, doi: 10.1016/J.JALLCOM.2019.03.373.

[180] G. Straffelini, "Friction and Wear : Methodologies for Design and Control," 2016.

[181] H. Y. Diao, R. Feng, K. A. Dahmen, and P. K. Liaw, "Fundamental deformation behavior in high-entropy alloys: An overview," *Curr. Opin. Solid State Mater. Sci.*, vol. 21, no. 5, pp. 252–266, Oct. 2017, doi: 10.1016/J.COSSMS.2017.08.003.

[182] V. A. Shvets, V. A. Lavrenko, V. N. Talash, A. D. Panasyuk, and Y. B. Rudenko, “Anodic Polarization of Titanium Carbide TiC x in 3% NaCl Solution in the Homogeneity Range,” *Powder Metall. Met. Ceram. 2016 557*, vol. 55, no. 7, pp. 469–476, Nov. 2016, doi: 10.1007/S11106-016-9829-5.

[183] H. Wu, L. Wang, S. Zhang, C. L. Wu, C. H. Zhang, and X. Y. Sun, “Corrosion and cavitation erosion behaviors of laser clad FeNiCoCr high-entropy alloy coatings with different types of TiC reinforcement,” *Surf. Coatings Technol.*, vol. 471, p. 129910, Oct. 2023, doi: 10.1016/J.SURFCOAT.2023.129910.

[184] X. Zhang *et al.*, “Influence of remelting and annealing treatment on corrosion resistance of AlFeNiCoCuCr high entropy alloy in 3.5% NaCl solution,” *J. Alloys Compd.*, vol. 775, pp. 565–570, Feb. 2019, doi: 10.1016/J.JALLCOM.2018.10.081.

[185] Y. J. Hsu, W. C. Chiang, and J. K. Wu, “Corrosion behavior of FeCoNiCrCux high-entropy alloys in 3.5% sodium chloride solution,” *Mater. Chem. Phys.*, vol. 92, no. 1, pp. 112–117, Jul. 2005, doi: 10.1016/J.MATCHEMPHYS.2005.01.001.

[186] R. F. Zhao, B. Ren, B. Cai, Z. X. Liu, G. P. Zhang, and J. jian Zhang, “Corrosion behavior of CoxCrCuFeMnNi high-entropy alloys prepared by hot pressing sintered in 3.5% NaCl solution,” *Results Phys.*, vol. 15, p. 102667, Dec. 2019, doi: 10.1016/J.RINP.2019.102667.

[187] A. M. Human and H. E. Exner, “The relationship between electrochemical behaviour and in-service corrosion of WC based cemented carbides,” *Int. J. Refract. Met. Hard Mater.*, vol. 15, no. 1–3, pp. 65–71, 1997, doi: 10.1016/S0263-4368(96)00014-5.

[188] A. M. Human and H. E. Exner, “Electrochemical behaviour of tungsten-carbide hardmetals,” *Mater. Sci. Eng. A*, vol. 209, no. 1–2, pp. 180–191, May 1996, doi: 10.1016/0921-5093(95)10137-3.

[189] A. M. Human, B. Roebuck, and H. E. Exner, “Electrochemical polarisation and corrosion behaviour of cobalt and Co(W,C) alloys in 1 N sulphuric acid,” *Mater. Sci. Eng. A*, vol. 241, no. 1–2, pp. 202–210, Jan. 1998, doi: 10.1016/S0921-5093(97)00492-9.

[190] D. L. A. de Faria, S. Venâncio Silva, M. T. de Oliveira, D. L. A. de Faria, S. Venâncio Silva, and M. T. de Oliveira, “Raman microspectroscopy of some iron oxides and oxyhydroxides,” *JRSp*, vol. 28, no. 11, pp. 873–878, 1997, doi: 10.1002/(SICI)1097-4555(199711)28:11.

[191] S. Pellegrino, P. Trocellier, L. Thomé, S. Miro, J. M. Costantini, and E. Jouanny,

"Raman investigation of ion irradiated TiC and ZrC," *Nucl. Instruments Methods Phys. Res. Sect. B Beam Interact. with Mater. Atoms*, vol. 454, pp. 61–67, Sep. 2019, doi: 10.1016/J.NIMB.2019.02.012.

[192] M. V Klein, J. A. Holy, and W. S. Williams, "Raman scattering induced by carbon vacancies in TiCx," *Phys. Rev. B*, vol. 17, no. 4, pp. 1546–1556, Feb. 1978, doi: 10.1103/PhysRevB.17.1546.

Ringraziamenti

Se ripenso al ragazzo che fino ai diciotto anni non voleva nemmeno sentir parlare di università, mi viene da sorridere. Evidentemente non avevo ancora capito che la curiosità avrebbe avuto la meglio sulla pigrizia. Per fortuna, al momento giusto, ho fatto la scelta che mi ha portato fin qui; e no, non è stato un erroe di compilazione del modulo di iscrizione.

Dopo la magistrale sono arrivati dieci mesi di assegno di ricerca, una sorta di "tempo supplementare" che mi ha fatto capire che la partita non era ancora finita. Poi il dottorato: tre anni intensi, tra rivestimenti, trattamenti superficiali, campioni da preparare e risultati da interpretare con più o meno ottimismo a seconda delle giornate.

Il lavoro si è concentrato principalmente sul progetto europeo CoBrain, dedicato alla ricerca di rivestimenti alternativi all'utilizzo di Cromo VI e Cobalto. Un tema complesso e attuale, che mi ha insegnato quanto sia importante coniugare prestazioni e responsabilità. In laboratorio ho imparato che quando un esperimento non funziona non è un fallimento… è "un'interessante opportunità di approfondimento" (che detta così suona decisamente meglio).

In questi anni sono successe tante cose. Sono nate amicizie vere, costruite tra una prova sperimentale e una pausa caffè che durava più del previsto. È nata Agata, che con il suo arrivo ha riempito la famiglia di una gioia nuova e ha ricordato a tutti noi quanto sia potente un sorriso. Mi sono sposato con Marta, il progetto meglio riuscito della mia carriera, e insieme abbiamo iniziato un capitolo ancora più importante. La vita, nel frattempo, ha iniziato a galoppare… e cerchiamo di starle dietro.

Da cinque mesi ho intrapreso una nuova avventura in Ferrari, dove ho incontrato persone straordinarie con cui condividere questo percorso. È un ambiente che richiede precisione, passione e spirito di squadra: qualità che ho imparato a coltivare negli anni di studio e ricerca.

Al di là dei titoli e delle tappe accademiche, ciò che conta davvero sono le persone. I rapporti costruiti, le difficoltà affrontate, le risate, le discussioni, le soddisfazioni condivise. Anche i momenti più duri, col tempo, riescono a strappare un sorriso: perché hanno contribuito a farmi crescere.

Un grazie sincero a chi mi ha guidato nel percorso di ricerca, per la fiducia, il rigore e l'esempio. Grazie ai colleghi con cui ho condiviso il laboratorio: tra prove riuscite e altre "creative", siamo cresciuti insieme.

Grazie agli amici di sempre e a quelli incontrati lungo la strada: anche quando il tempo è poco, sapere che ci siete fa la differenza. Grazie ai compagni di squadra, perché lo sport è stato equilibrio, sfogo e scuola di vita. Mi ha insegnato che si cade, ci si rialza e si riparte, magari brontolando un po', ma si riparte.

Un grazie immenso alla mia famiglia.

Ai nonni, per l'affetto incondizionato e per avermi sempre fatto sentire a casa.

Agli zii e ai cugini, per la leggerezza e le risate che rendono tutto più semplice.

Ad Agata, che con la sua energia e la sua dolcezza ha portato una luce nuova nelle nostre vite.

A Pol, perché tra silenzi strategici ci siamo sempre capiti.

A Laura, un punto di riferimento silenzioso ma fondamentale, una di quelle persone che rendono tutto più sereno solo con la loro presenza.

Mamma e papà, qui le parole si fanno piccole. Mi avete insegnato il valore dell'impegno, della coerenza e della responsabilità. Se oggi affronto le sfide con fiducia è perché ho sempre saputo di avere alle spalle un sostegno solido.

E infine Marta. Sei stata accanto a me nei momenti di entusiasmo e in quelli di fatica, quando lo stress era tanto e le scadenze correvano più veloci di noi. Mi hai sopportato, sostenuto e riportato con i piedi per terra quando serviva. Oggi sei mia moglie, compagna di vita e di sogni. Se guardo al futuro con serenità è perché lo immagino insieme a te.

A tutti voi va il mio grazie più sincero.

Ogni traguardo raggiunto porta il mio nome, ma dentro c'è un pezzo di ciascuno di voi.

Il percorso continua, con qualche responsabilità in più e qualche capello in meno, ma con la stessa curiosità di sempre e con la certezza che ciò che conta davvero sono le persone con cui scegli di condividerlo.